Ancient carbon utilization in Arctic marine waters and sediments

Dissertation

Zur Erlangung des Doktorgrades

der Naturwissenschaften

Dr. rer. nat.

am

Fachbereich Geowissenschaften

der Universität Bremen

Vorgelegt von:

Manuel Ruben

Bremen

Oktober 2023

This work will be carried out from June 2020 to October 2023 in the Marine Geochemistry Group at the Alfred Wegener Institute for Polar and Marine Research, Bremerhaven, in cooperation with the Organic Geochemistry Group at MARUM - Center for Marine Environmental Sciences, University of Bremen, the Biogeochemistry Group at the Max Planck Institute for Marine Microbiology, Bremen, the Joint Research Group for Deep-Sea Ecology and Deep-Sea Ecology and Technology at the Alfred Wegener Institute and the Max Planck Institute for Marine Microbiology, Bremen, and the Marine Chemistry & Geochemistry Group at Woods Hole Oceanographic Institution, Woods Hole. This project was funded within the framework of the Alfred Wegener Institute's internal INSPIRES 2020 call under the POV IV research program.

Gutachter/Reviewers:

Prof. Dr. Gesine Mollenhauer

Prof. Dr. Jordon Hemingway

Date of the colloquium: 29th of February 2024

"Life is Like a Box of Chocolates,

You Never Know What You're Gonna Get"

Forrest Gump (1994)

Table of Contents

Abstract

This thesis is at the interface of biogeochemistry, microbiology and sedimentology. It focuses on the question of whether microorganisms are able to utilize ancient organic carbon from both bedrock and permafrost soils for their metabolism and biosynthesis when these OC deposits get remobilized and enter the Arctic Ocean. In addition, it attempts to provide a basis for assessing how changing organic carbon fluxes in a warming climate and over geological time scales may influence feedback mechanisms and the global climate. The core of the thesis is radiocarbon analysis using ^{14}C as an inverse tracer, tracking organic carbon from substrate to microbial biomass and emitted metabolic end products. The thesis consists of four chapters:

The first manuscript shows the publication "Fossil organic carbon utilization in marine Arctic fjord sediments by subsurface microbes", published on June 1, 2023 in Nature Geoscience (DOI: https://doi.org/10.1038/s41561-023-01198-z). Addresses the utilization of ancient rock or petrogenic organic carbon in Arctic fjord sediments supplied by glacial meltwater streams. By radiocarbon analysis of intact polar lipid fatty acids of living microorganisms, it was estimated that local bacteria utilize between 5 ± 2 % and 55 ± 6% (average 25 ± 16 %) of petrogenic organic carbon for their biosynthesis. This suggests that previously sequestered organic carbon has the potential to contribute to natural greenhouse gas emissions over geological timescales if mobilized, for example, by glacial erosion.

The second manuscript "Release and microbial utilization of fossil carbon from eroding permafrost coastlines: fueling the short-term carbon cycle" was submitted to Global Biogeochemical Cycles on July 7, 2023 (AGU journal submission 2023GB007910). The study involves an incubation experiment that quantifies the release of fossil carbon from Yedoma (permafrost soil) incubated in seawater, linking dissolved inorganic carbon (quantity and ^{14}C content) and microbial communities. The data presented indicate that organic carbon from the Yedoma is readily utilized by both marine and previously dormant soil microorganisms. During the three months of incubation, approximately 2.8 ± 0.3 % of the incubated organic carbon is released, of which 88 ± 12 % is derived from a fossil source within the Yedoma soil. This study quantifies for the first time the amount of fossil organic carbon released from permafrost soils into seawater and suggests that increasing coastal erosion of permafrost soils will have a positive greenhouse gas emission feedback in a warming climate.

The third manuscript is a draft describing additional work on the sedimentary remnants of the incubation experiment (described in manuscript 2) using ramped pyrolysis-oxidation with ^{14}C analysis of the emitted

gases. The data obtained indicate that this type of analysis is not suitable for investigating (ancient) organic carbon utilization in the context of an incubation experiment with isotopically very homogeneous sample material (subfractions). The observed inter-sample variability in both thermograms and associated ^{14}C signatures show a greater difference than the apparent changes over the three months of incubation. Thus, other analytical methods are encouraged to investigate the bioavailability of permafrost organic carbon after redeposition on the seafloor, e.g. as in manuscript 4. However, due to its strong isotopic homogeneity, it was possible to show that no modern subfraction was present in the experiment of manuscript 2, thus verifying its results that the emitted dissolved inorganic carbon came from a fossil source.

The fourth manuscript is a draft of a downcore study in the Canadian Arctic, targeting greenhouse gas emissions from redeposited permafrost soils on the seafloor in the nearshore zone. It combines the approaches of manuscripts 1 and 2, using dissolved inorganic carbon quantification to determine the flux and sources of released carbon using C isotopy ($\delta^{13}C$ and $F^{14}C$), while linking it to microbial communities, geochemical zonation, and membrane lipid isotopy ($\delta^{13}C$ and $F^{14}C$). The presented data suggest that in the nearshore zone, about 48 ± 5 % of the escaping dissolved inorganic carbon is derived from recent marine primary production, although they contribute only about 4 ± 4 % of the OC in the sediments. About half of the escaping dissolved inorganic carbon was attributed to the deep Yedoma permafrost deposits (38 ± 10 %) and the active layer including recent terrestrial primary production (15 ± 12 %), which contribute 41 ± 22% and 55 ± 22%, respectively, to the sedimentary OC pool. Membrane lipid analysis further suggests that bacteria used on average 16 ± 4 % active layer, 11 ± 3% Yedoma, and 73 ± 6 % marine OC for their biosynthesis in the uppermost 24 cm. This indicates that OC derived from permafrost soil is remineralized after redeposition to the seafloor and contributes to the permafrost carbon feedback.

Kurzfassung

Das Doktoratsprojekt liegt an der Schnittstelle von Biogeochemie, Mikrobiologie und Sedimentologie. Es ist auf die Frage fokussiert, ob Mikroorganismen in der Lage sind, urzeitlichen organischen Kohlenstoff aus Gestein und Permafrostböden für ihren Stoffwechsel und ihre Biosynthese zu nutzen, wenn diese in den Arktischen Ozean gelangen. Um diese Fragestellung zu bearbeiten wird versucht, eine Wissensgrundlage zu schaffen welche eine Beurteilung erlaubt, wie sich ändernde Flüsse von organischem Kohlenstoff in einem sich erwärmenden Klima und über geologische Zeitskalen auf Rückkopplungsmechanismen des globalen Klimas auswirken können. Der Schwerpunkt der Arbeit liegt auf der Radiokarbonanalyse unter Verwendung von ^{14}C als inverser Tracer, um den organischen Kohlenstoff

vom Substrat in die mikrobielle Biomasse und in die emittierten Stoffwechselendprodukte zu verfolgen. Die Arbeit besteht aus vier Kapiteln:

Das erste Manuskript "Fossil organic carbon utilization in marine Arctic fjord sediments by subsurface microbes" wurde am 1. Juni 2023 in der Fachzeitschrift Nature Geoscience veröffentlicht (DOI: https://doi.org/10.1038/s41561-023-01198-z). Dieses beschäftigt sich mit der mikrobiellen Verstoffwechslung urzeitlichen Gesteins- oder petrogenen organischen Kohlenstoffs in Arktischen Fjordsedimenten, eingetragen durch Gletscherschmelzwasserströmen. Durch die Radiokarbonanalyse von Membranlipid-Fettsäuren lebendiger Mikroorganismen wurde abgeschätzt, dass die lokalen sedimentäre Bakterien zwischen 5 ± 2% und 55 ± 6% (im Durchschnitt 25 ± 16%) des petrogenen organischen Kohlenstoffs für ihre Biosynthese nutzen. Dies zeigt, dass zuvor in Gestein gespeicherter organischer Kohlenstoff das Potential hat, über geologische Zeitskalen zu natürlichen Treibhausgasemissionen beizutragen, wenn dieser durch z. B. Gletscherverwitterung mobilisiert wird.

Das zweite Manuskript "Release and microbial utilization of fossil carbon from eroding permafrost coastlines: fueling the short-term carbon cycle" wurde am 7. Juli 2023 bei Global Biogeochemical Cycles eingereicht (AGU Journal Submission 2023GB007910). Das Manuskript beschreibt ein Inkubationsexperiment, welches die Freisetzung von fossilem Kohlenstoff aus Yedoma (Permafrostboden) in Meerwasser quantifiziert und den Zusammenhang zwischen gelöstem anorganischem Kohlenstoff (Menge und ^{14}C-Gehalt) und Mikroorganismen herstellt. Die vorgelegten Daten zeigen, dass der organische Kohlenstoff aus dem Yedoma sowohl von marinen als auch von zuvor inaktiven Bodenmikroorganismen genutzt werden kann. Über die drei monatige Inkubationszeit wurde etwa 2,8 ± 0,3% des inkubierten organischen Kohlenstoffs freigesetzt, wovon 88 ± 12% aus einer fossilen Quelle im Yedoma-Boden stammen. Diese Arbeit liefert zum ersten Mal quantitative Daten zur Freisetzung organischen Kohlenstoffs aus Permafrostböden ins Meerwasser, was auf eine positive Rückkopplung von zunehmender Erosion der Küstenpermafrostböden und Treibhausgasen in einem erwärmenden Klima hinweist.

Das dritte Manuskript umfasst einen Entwurf, der zusätzliche Arbeiten an den sedimentären Rückständen des Inkubationsexperiments beschreibt (wie in Manuskript 2 beschrieben), wobei „Ramped Pyrolyse und Oxidation“ mit ^{14}C-Analyse an den emittierten Gasen angewandt wurde. Die erhaltenen Daten zeigen, dass die Art der Analyse nicht geeignet ist, um die Nutzung von (urzeitlichen) organischen Kohlenstoffs mit einem Inkubationsexperiment zu untersuchen. Sowohl die beobachtete intra-Proben Variabilität der Thermogramme als auch der entsprechenden ^{14}C-Signaturen zeigen größere Unterschiede als die

messbaren Veränderungen über die drei Monate der Inkubationszeit. Daher werden andere Analysemethoden empfohlen, um die Bioverfügbarkeit von organischem Kohlenstoff aus Permafrostböden nach der Wiederablagerung in Meeresböden zu untersuchen, z. B. wie in Manuskript 4.

Das vierte Manuskript ist ein Entwurf einer Sedimentkernstudie in der kanadischen Arktis, die auf Treibhausgasemissionen aus wieder abgelagerten Permafrostböden auf dem Meeresboden in der küstennahen Zone abzielt. Hierzu werden die Ansätze der Manuskripte 1 und 2 kombiniert, indem gelöster anorganischer Kohlenstoff quantifiziert wird, um den Fluss aus dem Sediment zu quantifizieren und die Quellen des freigesetzten Kohlenstoffs durch Isotopenanalyse ($\delta^{13}C$ und $F^{14}C$) zu bestimmen. Zusätzlich wird dies mit mikrobiellen Gemeinschaften, geochemischer Zonierung und Membran-Lipid-Isotopie ($\delta^{13}C$ und $F^{14}C$) in Verbindung gebracht. Die erhobenen Daten deuten darauf hin, dass in der küstennahen Zone etwa 48 ± 5 % des aus dem Meeresboden entweichenden indem gelöster anorganischer Kohlenstoff aus rezenter mariner Primärproduktion stammt, obwohl diese nur etwa 4 ± 4 % des organischen Kohlenstoffs in den Sedimenten beitragen. Etwa die Hälfte des entweichenden gelösten anorganischen Kohlenstoff konnte den Yedoma Permafrostablagerungen (38 ± 10 %) und der aktiven Schicht, mit rezenter terrestrischer Primärproduktion (15 ± 12 %) zugeschrieben werden, welche 41 ± 22 % bzw. 55 ± 22 % zum sedimentären organischen Kohlenstoff beitragen. Die Analyse der Membranlipide deutet ferner darauf hin, dass die Bakterien in den obersten 24 cm durchschnittlich 16 ± 4 % aus der aktiven Schicht, 11 ± 3 % aus Yedoma und 73 ± 6 % aus marinem organischen Kohlenstoff, für ihre Biosynthese nutzten. Dies deutet darauf hin, dass aus dem Permafrostboden stammender organischer Kohlenstoff nach der Wiederablagerung auf dem Meeresboden mikrobiell abgebaut wird und zur Kohlenstoffrückkopplung des Permafrosts beiträgt.

Introduction

Scientific Background

The effects of anthropogenic climate change are expected to have tremendous and far-reaching impacts not only on local communities (Hunt & Watkiss, 2010) but also on people around the world (Burrows & Kinney, 2016). It is predicted to not only cause socioeconomic changes (da Silva, 2004) but also affect the very basis of livelihoods in terms of agricultural production (Adams et al., 1998), water security (Haddeland et al., 2014), and fisheries (Brander, 2010). In addition to the human consequences, the natural world is also heavily impacted, with widespread changes being triggered around the globe (Pachauri et al., 2014) some of which may become irreversible on human time scales, so-called tipping points (Lenton et al., 2019). The main driver of anthropogenic climate change is the release of greenhouse gas emissions into the atmosphere, primarily from fossil fuel combustion, agriculture, and land-use change (IPCC, 2007). Despite the importance of global atmospheric carbon concentrations for our future, the amount of organic carbon (OC) stored in soils, rocks, oceans, and the biosphere is many times greater than the climate-determining carbon pool in the atmosphere (Bird et al., 2001; Fahey et al., 2010; Sabine & Tanhua, 2010; Sundquist & Visser, 2005). Although the size of these pools varies widely in orders of magnitude, they are in equilibrium over long time scales (Sarmiento, 2013). The OC stored in permafrost soils and sedimentary rocks is for the most part not actively cycled (Guillemette et al., 2017).

One of the regions most affected by climate change is the Arctic, where temperatures are rising about four times faster than the global average (Rantanen et al., 2022), leading to unprecedented rates of glacier melt and permafrost thaw (IPCC, 2019). Rising atmospheric and sea surface temperatures, sea level rise, and declining sea ice lead to increasing rates of tidewater glacier retreat and coastal permafrost erosion, resulting in dramatic changes along coastlines (Irrgang et al., 2022). Causing the mobilization of both glacial bedrock (Bendixen et al., 2017) and permafrost soils (Winterfeld et al., 2018) at faster rates. While tidewater glaciers and permafrost soils have very different origins, the climatically enhanced melting and thawing increases both influx of nutrients and carbon form glaciers and ice-sheets (Bhatia, Kujawinski, et al., 2013; Herraiz-Borreguero et al., 2016; Hodson et al., 2017; Hood et al., 2015; Raiswell et al., 2016; Shadwick et al., 2013; Wadham et al., 2013; Yager et al., 2016), as well from eroding permafrost coast lines (Couture et al., 2018; Fritz et al., 2017; Irrgang et al., 2022; Jong et al., 2020; Lantuit et al., 2012; Tanski et al., 2016; Terhaar et al., 2021) to the ocean.

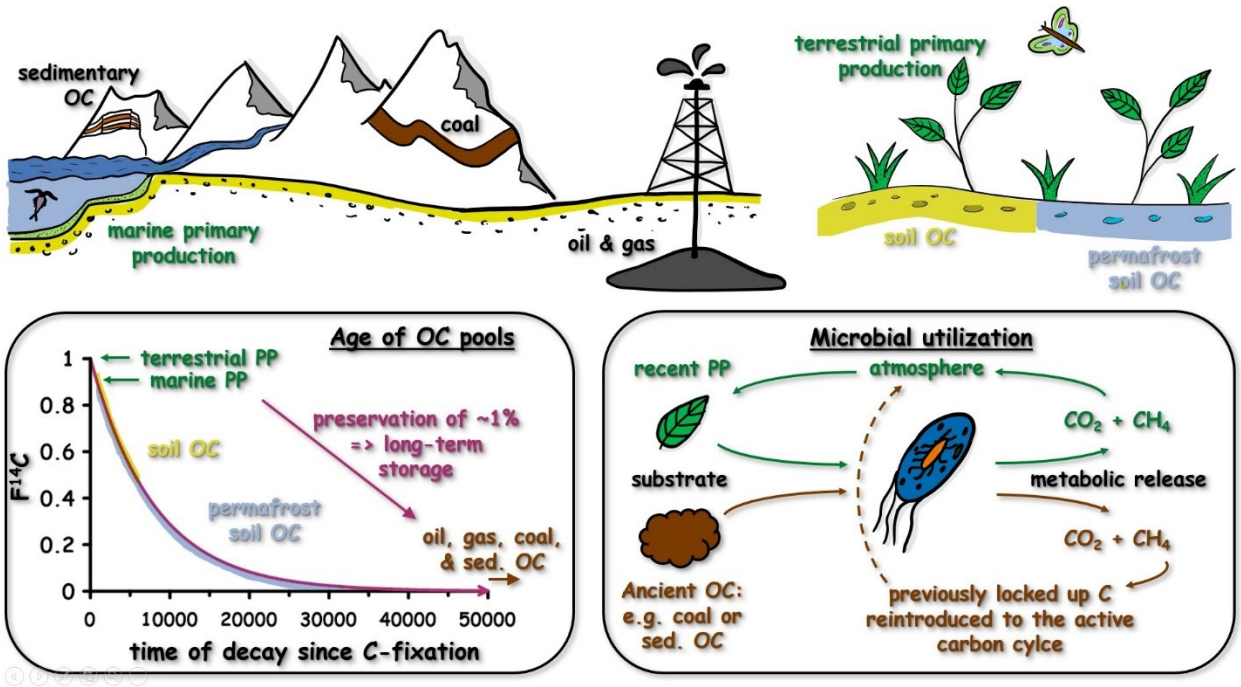

Figure 1: Different global organic carbon (OC) pools and their respective ages (lower left panel). The degradation of OC over time causes labile compounds to be consumed or degraded by, for example, microbes or light, leading to the accumulation of more recalcitrant compounds within deposits over time. Long-term preservation of ~1% of OC from primary production (pp) in oil, gas, coal, or sedimentary OC resulted in a drawdown of atmospheric CO_2 over millions of years. Depending on whether or not microbes can use ancient OC as a substrate, there may be a feedback mechanism between mobilized ancient carbon deposits and the atmosphere, reintroducing previously sequestered carbon into the active carbon cycle.

OC previously stored in sedimentary rocks and permafrost soils can be considered old, fossil, or ancient based on the time of its biosynthesis (Figure 1). Traditionally, ancient carbon has been considered a non-bioavailable substrate for present-day organisms because it was synthesized, deposited, and has already undergone diagenesis thousands to millions of years ago (Guillemette et al., 2017). However, since the turn of the millennium, several studies have identified a wide range of different generic ancient carbon sources in diverse environments that are bioavailable despite their high age (Bardgett et al., 2007; Cui, Bianchi, Jaeger, et al., 2016; Cui, Bianchi, Savage, et al., 2016; Hood et al., 2015; Horan et al., 2017; Petsch et al., 2001, 2003; Slater et al., 2006; Wakeham et al., 2006). Thus, the entire concept of decreasing bioavailability with increasing age is challenged, although different ecosystems and locations appear to influence the potential for microbial use of ancient carbon (Bogard et al. 2019; Marín-Spiotta et al. 2014; McCallister et al. 2004; McCallister et al. 2012). OC from both glacial sedimentary bedrock and permafrost soils is eroded, during aquatic transport and after redeposition in newly formed sediments, the remobilized OC can be accessed by microorganisms, but the extent to which microorganisms can utilize the remobilized carbon is highly debated (Bardgett et al., 2007; Cui, Bianchi, Jaeger, et al., 2016; Cui,

Bianchi, Savage, et al., 2016; Hood et al., 2015; Petsch et al., 2001, 2003; Slater et al., 2006; Wakeham et al., 2006). The key hypothesis of this debate is that the bioavailability of ancient carbon would indicate the release of ancient (old or fossil) carbon, in the form of the greenhouse gases CO_2 and CH_4, back into the active carbon cycle via microbial utilization after remobilization of, for example, sedimentary rock or permafrost soil (Figure 2; Guillemette et al., 2017).

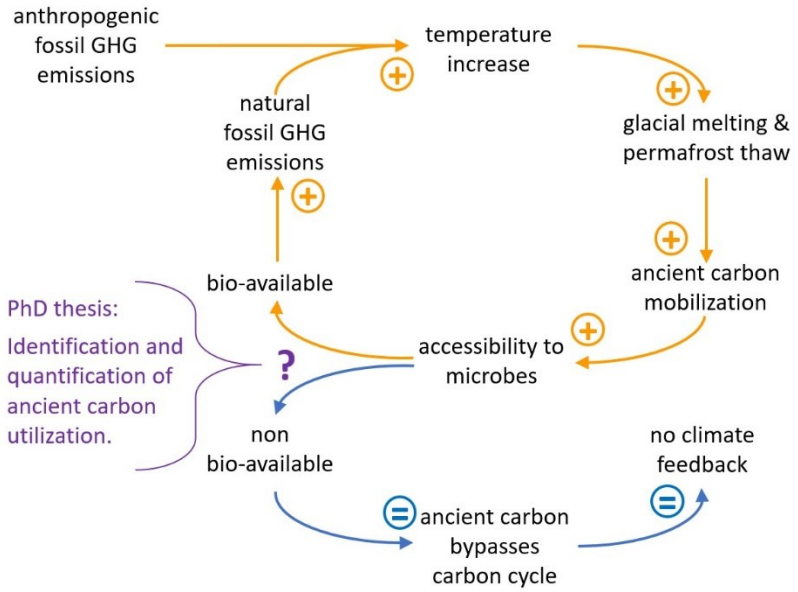

Figure 2: The purpose of the thesis in relation to the positive feedback mechanism of anthropogenic fossil greenhouse gas (GHG) emissions, rising global temperatures, increased melt and thaw, and the possibility of whether or not microbes can utilize the ancient carbon.

However, mobilized ancient carbon is still widely considered to be inert and is therefore not part of today's carbon cycle models. Improving our understanding of the availability of ancient carbon to subsurface and aquatic microbial communities is critical to understanding it as part of the global short- and long-term carbon cycle. As with increased supply, the availability of ancient carbon would represent an increasing source of carbon in a warming climate, which may need to be considered in new climate models (Guillemette et al., 2017). Although the remobilization of ancient OC is a natural process, it is expected to be accelerated by anthropogenic climate change. The rate of re-introduction of ancient carbon to the atmosphere depends strongly on two factors: 1) the rate of erosion and 2) the bioavailability of eroded OC, both of which are poorly constrained. However, the implications are of great importance because increased thawing of high-latitude permafrost soils, permafrost mobilization, and coastal erosion (IPCC, 2019; Irrgang et al., 2022), as well as increased runoff rates from glaciers (Delaney & Adhikari, 2020) and ice sheets (Bendixen et al., 2017), would lead to catalyzing positive feedback loops triggered by anthropogenic climate change.

To address these issues, my dissertation investigates the bioavailability and hence the carbon release potential of meltwater-derived, glacial petrogenic OC (OC_{petro}) after seafloor deposition, and permafrost soil OC (OC_{PS}) both in the water column and after seafloor deposition. Although the drivers and causes of increased permafrost and glacial carbon fluxes to the ocean are similar, the mechanisms, organic carbon quality, and reservoir size differ substantially. Therefore, the generic types are discussed separately.

Organic Carbon in the Arctic Ocean

The Arctic Ocean was chosen as the study region because it is currently considered an important global carbon sink (Parmentier et al., 2013). It is strongly influenced by terrestrial inputs; as an intercontinental ocean, it contains only about 1 % of the global ocean volume, while the discharge of several major rivers accounts for about 10 % of global freshwater runoff (Lammers et al., 2001). Its outer edges are defined by extensive shallow shelf areas where the burial of OC from marine production is estimated to be as low as 1% of the primary production (Stein et al., 2004). Within the sediments, this highly available marine OC is expected to be degraded primarily in the uppermost oxygenated layer (Boetius & Damm, 1998; Brüchert et al., 2018). Brüchert et al. (2018) estimate that the aerobic degradation of OC in the topmost 50 cm of Siberian shelf sediments averages 86 %. They further highlight the uncertainty in the relative contributions of marine and terrestrial OC degradation within these rapidly remineralizing aerobic top layers (Brüchert et al., 2018). The relative contributions of terrestrial OC have been shown to decrease with distance from estuaries (Vonk et al., 2014), coasts (Grotheer et al., 2020), and glacial termini (Szczuciński et al., 2009), with a marked difference between deltaic and non-deltaic sediments. On average, terrestrial OC accounts for about 10% of the total OC input to Arctic Ocean sediments, but it is estimated that 90% of it is protected from degradation and thus sequestered in the sediment (Macdonald et al., 2015). Therefore, its bioavailability is expected to be low compared to OC from recent marine primary production. On the other hand, other studies suggest that terrestrial OC remineralization in the Arctic seafloor is the dominant source of most methane in the Arctic Ocean (Semiletov et al., 2011). This conflicting view of the fate of (often ancient) terrestrial OC in Arctic sediments is particularly important given the vast amount of OC stored in North American and Eurasian permafrost soils (Tarnocai et al., 2009) and sedimentary bed rock (Galy et al., 2008) that are eroded by glaciers (Herman et al., 2021) and their high vulnerability to Arctic amplification (IPCC, 2019).

This terrestrial OC is supplied by the major Arctic rivers that drain the majority of the terrestrial area underlain by permafrost (Olefeldt et al., 2016), which directly borders the Arctic Ocean (Lantuit et al., 2012) and is directly eroded at the coastlines (Irrgang et al., 2022). Similarly, the heavily glaciated

archipelagos of Norway, Russia, and Canada, as well as the Greenland ice sheet, all border or lie within the Arctic Ocean (Dowdeswell et al., 1997). While glacially eroded bedrock and permafrost soils are eroded primarily on land, enormous amounts of their OC will eventually end up in the Arctic Ocean (Drenzek et al., 2007; Terhaar et al., 2021). Uncertainty about the fate of OC delivered to the Arctic Ocean leads to speculation, if the Arctic Ocean will transition from a carbon sink to a carbon source in the coming decades (IPCC, 2019). This makes the Arctic Ocean an ideal study region to investigate the bioavailability of ancient carbon. For my Ph.D. thesis, I focused on three main regions with different approaches, which were:

1. Hornsund Fjord, Svalbard – Petrogenic OC utilization in marine sediments
2. Russian shelf – Permafrost soil OC bioavailability in the ocean
    a. Quantification of ancient CO_2 release from eroding coast lines
    b. Temporal evolution of ancient OC_{PS} bioavailability of POC entering the ocean
3. Beaufort Sea, Herschel Island, Canada – spatial and temporal availability of OC_{PS} in near shore zone

Glacial Organic Carbon

Glaciers and ice sheets cover about 11% of the world's land mass (Smith et al., 2015), of which 69% are located in the polar regions, including the world's two ice sheets (IPCC, 2019). In Antarctica, cumulative mass loss has been observed in the Antarctic Peninsula and West Antarctic Ice Sheet since 1992, and has accelerated since 2006 (IPCC, 2019). This region alone was reported to have lost -112 ± 12 Gt yr^{-1} between 2003 and 2013 (Martín-Español et al., 2016), despite an increase in snowfall since the 1930s (Goodwin et al., 2016). Of the total Antarctic ice sheet, approximately half is subject to bed melting (Siegert et al., 2018), which accounts for ~65 Gt of meltwater annually (Pattyn, 2010). While the East Antarctic Ice Sheet appears to be relatively stable in mass (Martín-Español et al., 2016), its northern hemisphere counterpart, the Greenland Ice Sheet, shows an increasing acceleration of ice loss in the last two decades compared to the 1990s (Bamber et al., 2018). The mass loss increased dramatically from -75.1 ± 29.4 Gt yr^{-1} between 1900-1983 to -186.4 ± 18.9 Gt yr^{-1} between 2003-2010, representing an astounding 248% increase in mass loss within the last century (Kjeldsen et al., 2015). Projected climate change in the coming decades is expected to further increase glacial retreat and accelerate runoff from ice sheets (Zemp et al., 2019) and alpine glaciers (Adhikari & Marshall, 2013).

The increase in glacier discharge includes not only ice and water, but also sediment due to increased glacier bedrock erosion, subglacial fluvial erosion, and paraglacial denudation associated with increased

ice and water fluxes (Herman et al., 2021). Subglacial sediment deposits may play a critical role in the sediment output of glaciers. In a warming climate, these deposits are expected to be exported more extensively due to increased meltwater runoff, but also formed more extensively due to new bedrock erosion (Bendixen et al., 2017). However, short- and long-term changes can show significant differences, making it notoriously difficult to predict sediment supply by glaciers and ice sheets (Herman et al., 2021). Nevertheless, alpine glaciers in Patagonia and Alaska have been reported to have increased sediment discharge with increasing ice velocity (Herman et al., 2015; Koppes et al., 2009, 2010; Koppes & Hallet, 2006). While erosion rates of polar glaciers and ice sheets have traditionally been assumed to be negligible (Cuffey et al., 2000; Thomson et al., 2013), within the last decade several authors have pointed to high sediment loads at glacier outlets (Bendixen et al., 2017; Cowton et al., 2012; Young et al., 2016). Recent estimates suggest that the Greenland Ice Sheet alone accounts for about 8% of the global suspended sediment load exported to the oceans (Overeem et al., 2017). Glacial sediment production provides important fertilizers such as iron, phosphorus, silica, and carbon to downstream ecosystems, thereby influencing chemical cycles (Hawkings et al., 2017; St. Pierre et al., 2019; Wadham et al., 2019). Globally, OC_{petro} accounts for approximately 90% of OC on Earth (Galy et al., 2008), highlighting the need to understand its potential role in the global carbon cycle with increased export rates from glaciers and ice sheets due to anthropogenic climate change (Herman et al., 2021). It is particularly noteworthy that even if global greenhouse gas emissions were to cease immediately, deglaciation would continue throughout the 21st century because glaciers and ice sheets, such as Greenland's, are currently in disequilibrium and would continue to experience increased mass loss (Box et al., 2022). This leads to an ever-increasing export of not only ice and water, but also OC-bearing sediments. Glacial erosion rates are a function of subglacial strata (Boulton, 1979) and OC-bearing sedimentary rocks can be expected to be preferentially eroded relative to igneous and metamorphic rocks, highlighting the importance of our understanding of OC_{petro} bioavailability. Potentially as yet undiscovered metabolic pathways (Vinšová et al., 2022) may allow microbes to utilize OC_{petro} with major implications for global carbon budgets, even if these processes would only utilize a very small fraction of this pool. Hood et al. (2015) estimated that glacial meltwater streams will export an additional 78 Tg of OC to aquatic ecosystems by 2050 due to climate-induced glacier retreat. However, this study largely ignored particulate OC. Many retreating glaciers terminate in fjord systems, and several studies have shown that glacier-derived OC can be highly bioavailable despite its high age (Hood et al., 2009, 2015). This further emphasizes the importance of investigating the utilization potential of these ancient OC-rich materials.

Fjord systems can be considered as miniature oceans, and therefore offer the potential to study marine processes in a defined space (Skei, 1983). They are often sedimentary depocenters adjacent to glaciers and have the highest carbon burial rates of any marine environment normalized to their area, burying approximately 11% of the OC sequestered in the oceans annually (Smith et al., 2015). Within the first few kilometers of glacier termini, vertical fluxes of particulate matter are very high, exporting OC to the seafloor (Szczuciński & Zajączkowski, 2012). Arctic fjords are generally characterized by high to very high sedimentation rates due to glacial runoff (Bianchi et al., 2018; Witold Szczuciński et al., 2009). High amounts of both biogenic and petrogenic OC are exported to local sediments (Walinsky et al., 2009). Although turbidity is high in these systems, primary production is also very high, up to 216 g C m^{-2} a^{-1} in some fjords (Smoła et al., 2017), and provides energy to higher trophic levels, albeit with high spatial and temporal variability (Bourgeois et al., 2016). Spring blooms can produce large amounts of highly bioavailable organic matter within days to weeks (Calleja et al., 2017). Despite the high rates of primary production in fjords, Paulsen et al. (2017) found that heterotrophic bacterial consumption is not sustained by this alone, but relies on OC from glacial runoff. This study further reports that different bacterial communities are present depending on the origin of the water masses, indicating a strong control of the OC source on heterotrophic microbial communities (Paulsen et al., 2017). This is consistent with reports of changes in bacterial, archaeal, and fungal communities influenced by glacial meltwater (Gutiérrez et al., 2015). While several studies have addressed the use of meltwater-derived OC by microbes during aquatic transport (Hemingway et al., 2019; Hood et al., 2009; Paulsen et al., 2017), prior to our work in Hornsund Fjord, no studies have investigated the use of meltwater-derived OC_{petro} after redeposition on the seafloor (Manuscript 1). In the first work package of my Ph.D. project, I investigated the microbial utilization of ancient OC_{petro} delivered to sediments by retreating glaciers in Hornsund Fjord, Svalbard. The goals were to determine: 1) whether or not OC_{petro} is bioavailable in the sediments after redeposition; 2) to what extent do microbes utilize OC_{petro}.

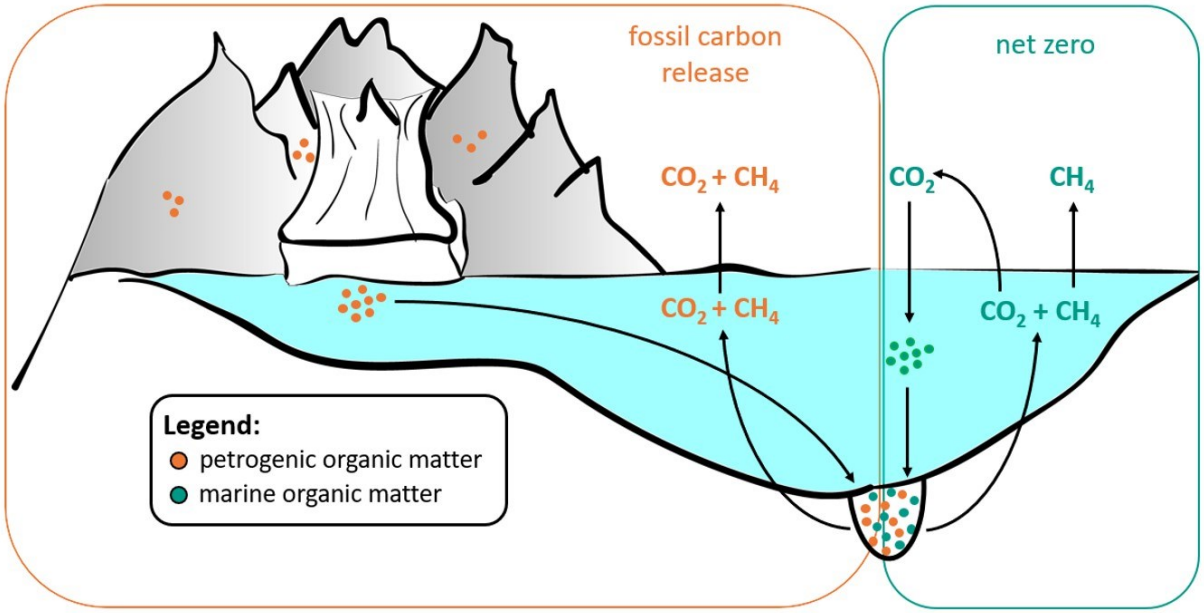

Figure 3: Organic carbon sources in a fjord system, supplying organic matter to the sediments from marine primary production and petrogenic organic matter from glacial bedrock erosion. Indicating both scenarios of either fossil carbon release form petrogenic organic matter utilization or net zero scenario under exclusive marine organic matter utilization.

Permafrost Organic Carbon

The term permafrost has been defined as permanently frozen ground for a duration of at least two consecutive years (Van Everdingen, 1998). Permafrost covers approximately 25% of the land surface of the Northern Hemisphere (Tarnocai et al., 2009), extending over an area of ~30 million km² (Chadburn et al., 2017) and penetrating up to 600 m below the present surface (Barry & Gan, 2011). Soils in this area are estimated to store ~1700 PgC, which is approximately twice the size of the current atmospheric carbon reservoir (Olefeldt et al., 2016). The uppermost 3 m of the northern circumpolar region store ~ 1000 PgC (Mishra et al., 2021), spanning diverse morphological and vegetative areas (Treat et al., 2018). Another ca. 210 PgC are stored in ice-rich (up to 90 %vol.) Yedoma complexes, which on average have the highest OC content (2-4 %wt.) of all permafrost strata (Mishra et al., 2021; Strauss et al., 2013, 2017; Wild et al., 2019). This exceptionally high ice content makes Yedoma particularly vulnerable to rapid thawing and causes the remobilization of large amounts of previously frozen OC (Olefeldt et al., 2016; Strauss et al., 2017). By 2100, Yedoma is estimated to release 5-10 Tg of DOC annually, which is equivalent to 19 to 26 % of the annual dissolved OC export from the Arctic Ocean (Drake et al., 2015). The total permafrost carbon feedback from Yedoma is estimated to increase by 50% by 2100 (Strauss et al., 2017; Turetsky et al., 2019; Walter Anthony et al., 2018).

In general, OC_{PS} is very different from the previously discussed OC_{petro}. While OC_{petro} is millions of years old, OC_{PS} is "only" a few thousand years old (Guillemette et al., 2017; Schirrmeister et al., 2013). The vulnerable Yedoma deposits were formed during the Pleistocene, when large areas of Eurasia, Alaska, and northwestern Canada were unglaciated and large amounts of OC from local tundra vegetation were retained in the formed soils due to low temperatures and subsequently preserved rather than microbially degraded as in temperate or tropical soils (Schirrmeister et al., 2013). Common features of Yedoma deposits are their fine-grained nature, high ice abundance, syngenetic ice wedges, cryostructures such as horizontal ice bands and dense ice lenses, and a variety of Pleistocene fossil remains (Strauss et al., 2017). The grain size of the mineral particles ranges from silt to fine sand, and the ice content is generally ~30-40 %vol., including ice wedges up to ~90 %vol. ice (Strauss et al., 2013). OC stored in the deposits is present in both dissolved (Fritz et al., 2015) and particulate (Guo et al., 2007) states. In particular, dissolved OC_{PS} has been reported to be highly bioavailable and rapidly microbially utilized after permafrost thaw (Rogers et al., 2021) demonstrating the potential of OC_{PS} for permafrost carbon feedback.

The high vulnerability of Yedoma to climate warming and subsequent remobilization compared to other permafrost deposits is due to 1) the properties of the ground ice and 2) its large spatial extent and thickness (Olefeldt et al., 2016). This system has not only local but also global significance, as it has been identified as one of the major global tipping points (Lenton, 2012). The main processes behind Yedoma degradation are 1) active layer thickening (Hinkel & Nelson, 2003), 2) thermokarst and thermoerosion due to rapid thawing (Ulrich et al., 2014), 3) increased unfrozen water and ground warming (Kurylyk et al., 2016), and 4) thermoerosion along water body shorelines (Günther et al., 2013; Jones et al., 2011; Kanevskiy et al., 2016). Some estimates suggest widespread cold season temperature anomalies of +40°C in permafrost regions (Farquharson et al., 2019), highlighting the expected changes due to climate change in these regions. The thawing and development of thermokast lakes in the Yedoma regions, which cover an area of ~1095 million km² (Matthews et al., 2020), are estimated to have already released up to ~2.5 PgC since pre-industrial times at a rate of 14-18 TgC per year (Elder et al., 2018; Strauss et al., 2017; Walter Anthony et al., 2016). Nearshore thermokast lakes may be converted to lagoons over time by coastal erosion, altering local geochemical cycles (Angelopoulos et al., 2020). Neighboring Arctic coasts are characterized by high variability in geomorphology and resistance to thawing and erosion. The main drivers of coastal erosion are wave energy, coastal morphology, cryolithology, solar radiation, and the ground thermal regime, with the main drivers of these processes being increases in air and sea temperature, sea ice retreat, sea level rise, wave climatology, and storm intensity and seasonality (Irrgang et al., 2022). The high rates of coastal erosion of up to several tens of meters per year (Vonk et al., 2012)

and the resulting high terrestrial OC export to Arctic shelf sediments emphasize the importance to study whether or not microbial processes degrade the permafrost derived OC during the lateral across shelf transport and its bioavailability after redeposition in marine sediments.

Despite the critical importance of these processes and their implications for global carbon cycle models, as well as their potential subsequent impact on global policy, these processes remain understudied. In the terrestrial environment, a number of different studies, including laboratory incubations, have been conducted to investigate carbon release from thawing permafrost soils. However, to date, only two studies have investigated the degradation of permafrost soils in the ocean (Tanski et al., 2019, 2021), focusing primarily on carbon release during lateral transport in the water column, but ignoring its fate after redeposition and the age of the released carbon. This is despite the fact that the release of old OC from previously frozen permafrost deposits is particularly important for the permafrost carbon feedback (Liljedahl et al., 2017; Nauta et al., 2015; Schuur et al., 2015; Tanski et al., 2019, 2021; Walter Anthony et al., 2018; Woodcroft et al., 2018; Yumashev et al., 2019). Furthermore, sedimentary microbial communities have been shown to be able to degrade a wider range of different substrates compared to water column communities (Arnosti, 2008, 2011). Therefore, even if carbon release is limited in the water column, the same substrate may release more carbon when deposited on the seafloor. Despite these important implications for the global climate system, virtually nothing is known about the long-term bioavailability of permafrost OC after redeposition on the seafloor, with only indirect estimates of redeposition and use having been made to date (Grotheer et al., 2020; Vonk et al., 2014; Winterfeld et al., 2018).

Methodological Approach

Despite the strong generic differences between OC_{petro} and OC_{PS}, both have in common their high age, which distinguishes them from recently synthesized OC. From this point forward, both OC_{petro} and OC_{PS} will be referred to as ancient carbon, while recently synthesized OC will be referred to as modern. Similar to ancient carbon substrates, modern OC can have a wide range of origins from both terrestrial and aquatic sources. To distinguish ancient from modern OC, radiocarbon dating is a very reliable tool. The natural abundance of radiocarbon ^{14}C in the atmosphere and its incorporation into biomass during carbon fixation, followed by its radioactive decay, allows a robust separation between modern and ancient OC (Feng et al., 2013; Galy et al., 2015; Hinojosa et al., 2014; Mollenhauer & Eglinton, 2007; Rieley et al., 1991; Schwab et al., 2020; Shah et al., 2008; Tao et al., 2015; Vonk et al., 2012; Vonk et al., 2014; White et al., 2008). Radiocarbon has a half-life of 5730 years (Stuiver & Polach, 1977). Current state-of-the-art

analysis allows for accurate measurements to about six (~30000 years) to ten (~50000 years) half-lives before present, using gas or graphite as targets (Mollenhauer et al., 2021). This property makes ^{14}C an ideal inverse tracer (absence is determined in comparison to traditional tracers such as ^{13}C) to study ancient carbon use (Figure 4).

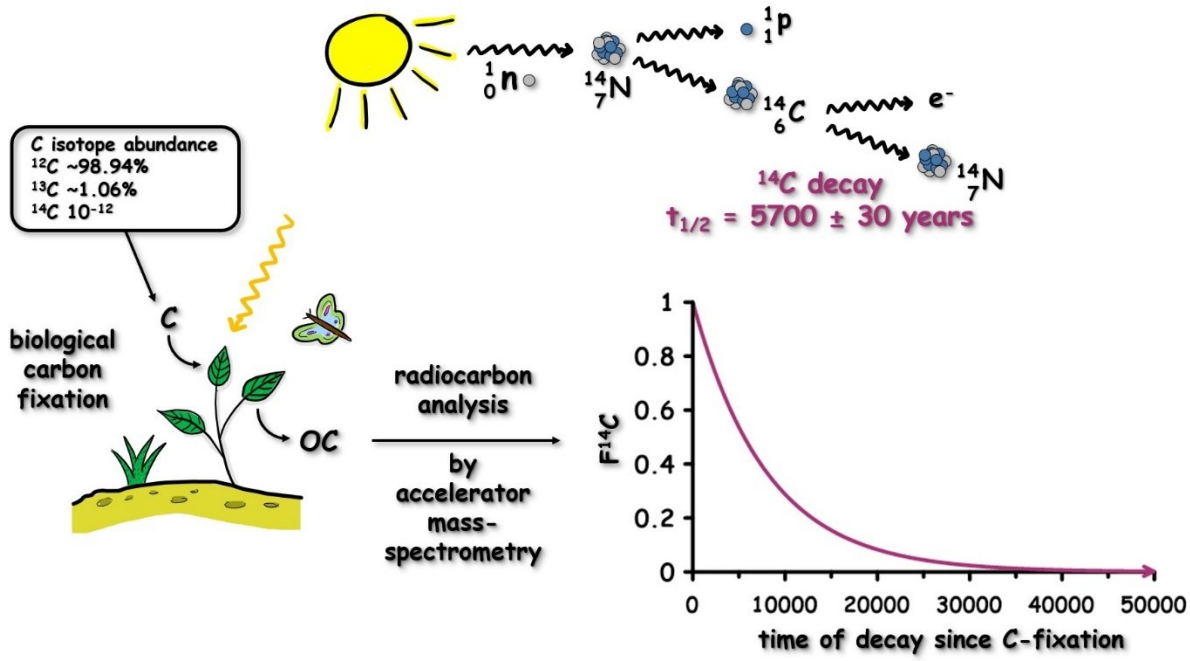

Figure 4: Radiocarbon (^{14}C) is a radionuclide produced naturally by cosmic rays reacting with nitrogen. ^{14}C decays back to its parent isotope nitrogen with a half-life ($t_{1/2}$) of about 5700 years. During biological carbon fixation, the isotopic carbon composition of the environment is incorporated into the biomass (OC). By performing radiocarbon analysis using accelerator mass spectrometry, the time since C fixation can be determined by producing a "fraction of modern carbon" ($F^{14}C$) value, this age is given in "^{14}C years". $F^{14}C$ indicates the abundance of ^{14}C atoms in a substance relative to a standard value of 1950 ($F^{14}C=1$). Due to nuclear testing, global $F^{14}C$ values after 1950 may have elevated values >1.

However, due to the pooled deposition of modern and ancient substrates in sediments and soils, bulk OC dating may not be sufficient for adequate source determination. More in-depth tools such as biomarker analysis and compound-specific radiocarbon analysis are often required to distinguish between different sources of ancient and modern OC at a site (Eglinton et al., 1996, 1997; Kusch et al., 2010). Compound-specific radiocarbon analysis, in particular, can be a powerful tool for determining the radiocarbon signature, age, and/or residence time of OC contributing to a local OC pool such as sediments (Kusch et al., 2010). As valuable as these findings are, they do not necessarily allow to infer the bioavailability of the OC (Guillemette et al., 2017), especially since the biomarkers used for compound specific analysis are selected for their comparatively high resistance to degradation processes (Bianchi & Canuel, 2011). Nevertheless, the compound-specific radiocarbon analysis can be used to identify specific radiocarbon

signatures ($F^{14}C$) for specific subfractions of the OC pool, allowing the assignment of specific $F^{14}C$ as end members (Wei et al., 2021). In order to investigate the bioavailability of ancient substrates, this thesis required the use of a combination of radiocarbon analysis approaches, including: 1) intact polar lipid-derived fatty acids as indicators of living biomass, 2) dissolved inorganic carbon to determine the substrate origin of released CO_2 in an aquatic environment (Figure 5), 3) gas fractions of different thermal stability produced by ramped pyrolysis-oxidation, and 4) bulk analysis. The individual approaches of the four work packages (details in Chapters 2-5) are described in detail below:

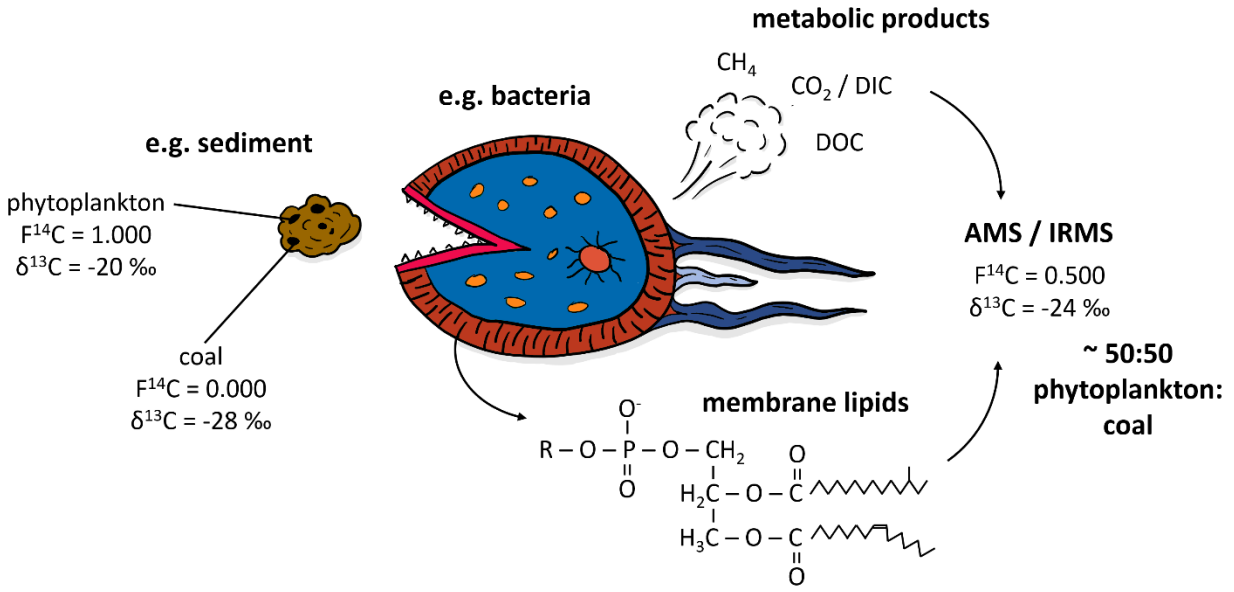

Figure 5: Organic carbon (OC) in deposits such as sediments can be composed of materials from different sources, such as phytoplankton or coal. To understand which of these OC substrates are used by e.g. bacteria in the sediments, isotopic analysis can be performed using accelerator mass spectrometry (AMS; $F^{14}C$) and isotope ratio mass spectrometry (IRMS; $\delta^{13}C$). By analyzing: 1) their metabolic products such as methane (CH_4), carbon dioxide (CO_2), dissolved inorganic carbon (DIC), or dissolved organic carbon (DOC); or 2) biomass such as membrane lipids; the average substrate can be determined. In this example, the membrane lipids and metabolic products indicate that the bacteria are using phytoplankton and coal in a 50:50 ratio for their energy needs.

For the first work package, I used a combined approach of biomarker analysis, lipidomics, and radiocarbon analysis of bulk organic matter and specific compounds, in particular intact polar lipids. The radioactive decay of ^{14}C allows a clear distinction between modern and ancient organic matter based on their respective radiocarbon signatures. ^{14}C is an ideal tracer to determine heterotrophic carbon substrates used by microbial communities, as ^{14}C is transferred from the substrate to the using organism during biomass assembly (Petsch et al., 2001). Intact polar lipids are indicative of living biomass because these membrane lipids tend to lose their headgroups within days to weeks after cell lysis (Harvey et al., 1986; Logemann et al., 2011). These lipids were extracted from sediments using a modified Bligh and Dyer

method, and their fatty acid radiocarbon signatures were determined to characterize substrate utilization. This approach has been used successfully in several studies over the past two decades (Petsch et al., 2001; Slater et al., 2006; White et al., 2005). I applied this approach to a distal-proximal profile of three sediment cores in Hornsund Fjord, Svalbard. The study area was chosen because of its binary origin of OC from OC_{petro} and OC from marine primary production, which allowed the application of a distinctive two endmember isotope mixing model. Using this approach, I determined the percentage of OC_{petro} used for microbial biosynthesis by subsurface bacteria in local marine fjord sediments.

In the second work package, I investigated the use of ancient carbon from Siberian Yedoma permafrost soils during lateral transport in the Arctic shelf seas. For this purpose, I set up a laboratory experiment in which Yedoma permafrost soil from the Lena Delta was incubated for three months at ~2°C under aerobic conditions with authentic Arctic coastal seawater, which I was able to collect from the Arctic during the cruise Arctic Century in September 2021. By determining pH, DIC concentrations, and radiocarbon over the course of the experiment, I was able to simulate microbial utilization during shelf transport, co-occurring ancient carbon degradation and CO_2 release, and determine an overwhelming release of CO_2 from fossil OC. Applying radiocarbon analysis to DIC instead of CO_2 allowed for more robust measurements due to reduced contamination by atmospheric CO_2. Additional DNA extraction and sequestration of the microbial community allowed for the identification of the microbiota that used the fossil OC.

In the third work package, I used the solid phase of the incubation experiment from work package two to estimate the bioavailability of the permafrost OC after redeposition on the seafloor. For this purpose, I performed ramped pyrolysis-oxidation with subsequent radiocarbon analysis on the produced and collected CO_2 gas. The radiocarbon analysis of individual fractions released by the method (different temperature intervals) was used to investigate changes in OC over the time of the experiment. This method had the advantage of not only providing information on the thermal activation energy (an indicator of organic matter lability) for different lability fractions within the sediments, but also of determining the age of the respective fractions. Thus, using this method, I was able to determine how much of the redeposited permafrost OC may be accessible to sedimentary microbial communities, as well as their radiocarbon signature, thereby further constraining whether or not a positive feedback loop can be expected from increasing Arctic coastal erosion.

The fourth work package aimed to investigate the degradation of OC_{PS} after deposition in nearshore sediments. To this end, I performed a combined approach of work packages one and two on two sediment

cores from Herschel Island, Canada. I used biomarker and bulk parameter-based characterization of OC input to the sediment to determine the sources of sedimentary OC. This was followed by IPL-FA extraction and radiocarbon analysis to determine the substrate used by sedimentary bacteria and combined with radiocarbon analysis of porewater DIC to estimate a carbon flux from the sediment to the water column, including the age of the released carbon.

Declaration of (Co-) Author Contributions

This cumulative dissertation is a collection of four first-author manuscripts. In the following, the individual (co-) author contributions to the scientific articles and the status of the manuscripts are reported.

Manuscript 1: Fossil organic carbon utilization in marine Arctic fjord sediments by subsurface microbes

Manuel Ruben, Jens Hefter, Florence Schubotz, Walter Geibert, Martin Butzin, Torben Gentz, Hendrik Grotheer, Matthias Forwick, Witold Szczuciński, Gesine Mollenhauer

Published: 1st June 2023 in Nature Geoscience; DOI: https://doi.org/10.1038/s41561-023-01198-z

M. Ruben and G. Mollenhauer designed and planned the study. T. Gentz, M. Forwick, and W. Szczuciński carried out the sample collections in the field. Sample preparation for organic biomarkers, bulk analysis, compound extractions, and purifications were performed by M. Ruben and J. Hefter. Sedimentary age-models were determined by W. Geibert and W. Szczuciński. Modeled surface DIC age model was set up by M. Butzin. Compound specific radiocarbon analysis and bulk parameter determination were performed by J. Hefter, T. Gentz, H. Grotheer, and M. Ruben. Intact polar lipid extraction, quantification, and analysis was performed by F. Schubotz and M. Ruben. All performed lab work was performed under the supervision and with the help of the lab personnel in the respective labs. Data analysis and archiving was done by M. Ruben. Manuscript writing and visualization were performed by M. Ruben with extensive help from G. Mollenhauer and assistance of the other co-authors. The personal contribution is estimated to exceed 85%.

Manuscript 2: Release and microbial utilization of fossil carbon from eroding permafrost coastlines: fueling the short-term carbon cycle

Manuel Ruben, Hannah Marchant, Matthias Wietz, Torben Gentz, Jens Strauss, Boris Koch, Gesine Mollenhauer

Submitted: 7th July 2023 to Global Biogeochemical Cycles, AGU journal submission 2023GB007910

M. Ruben, H. Marchant, and G. Mollenhauer designed and planned the study. Samples were collected in the field by M. Ruben and j. Strauss. Lab based work including the incubation experiment and data analysis was performed by M. Ruben, under the supervision and with the help of the lab personal in the respective labs. Radiocarbon analysis of the DIC samples was done by T. Gentz and M. Ruben. DNA data collection and analysis were headed by M. Wietz. Dissolved carbon and nitrogen analysis were performed by B. Koch and colleagues. Biogeochemical data analysis was performed by M. Ruben with extensive help from H. Marchant and G. Mollenhauer. Data archiving was performed by M. Wietz and M. Ruben. The manuscript was written by M. Ruben with extensive help from G. Mollenhauer, M. Wietz, and H. Marchant, as well as contributions of the other co-authors. The personal contribution is estimated to exceed 80%.

Manuscript 3: ^{14}C age distribution in organic matter fractions separated by Ramped Pyrolysis-Oxidation from permafrost soils incubated in seawater

Manuel Ruben, Valier Galy, Hannah Marchant, Torben Gentz, Gesine Mollenhauer

In preparation for Geophysical Research Letters

M. Ruben, V. Galy, H. Marchant, and G. Mollenhauer designed and planned the study. Samples were taken, prepared, and analyzed by M. Ruben. Data analysis and evaluation were performed by M. Ruben. The manuscript was written by M. Ruben with extensive contributions by V. Galy and G. Mollenhauer. Lab based work was performed under the supervision and with the help of the lab personnel in the respective labs. The personal contribution is estimated to exceed 90%.

Manuscript 4: Release and remineralization of permafrost organic carbon after redeposition on the ocean floor

Manuel Ruben, Jens Hefter, Torben Gentz, Florence Schubotz, Bingbing Wei, Bo Liu, Michael Fritz, Anna Irrgang, Anabel von Jackowski, Walter Geibert, Gesine Mollenhauer

In preparation for Nature Geoscience

M. Ruben designed and planned the study. Samples were taken in the field by M. Ruben and M. Fritz. Biogeochemical sample preparation, extraction, and purification was done by M. Ruben. Measurements of biogeochemical parameters were performed by M. Ruben, J. Hefter, T. Gentz, and F. Schubotz, under the supervision and with the help of the lab personnel in the respective labs. M. Fritz and A. Irrgang provideD the bathymetric model and essential insight into the study region. DNA extraction analysis and quantification were performed by A. von Jackowski. Fluxes were determined by M. Ruben and B. Liu. The

endmember analysis was performed by B. Wei and M. Ruben. The sedimentary age model was produced by W. Geibert. The manuscript was written by M. Ruben with extensive contributions by G. Mollenhauer, B. Wei, and A. von Jackowski, and supported by the other co-authors. The personal contribution is estimated to exceed 75%.

Manuscript 1

Fossil organic carbon utilization in marine Arctic fjord sediments by subsurface microbes

Published: 1st June 2023 in Nature Geoscience; DOI: https://doi.org/10.1038/s41561-023-01198-z

Authors

Manuel Ruben[1,2], Jens Hefter[1], Florence Schubotz[3], Walter Geibert[1], Martin Butzin[1,3], Torben Gentz[1], Hendrik Grotheer[1,3], Matthias Forwick[4], Witold Szczuciński[5], Gesine Mollenhauer[1,2,3]

Affiliation

[1] Alfred Wegener Institut, Helmholtz Centre for Polar- and Marine-Research, Am Handelshafen 12, 27570 Bremerhaven, Germany
[2] University of Bremen, Bibliothekstraße 1, 28359 Bremen, Germany
[3] MARUM - Center for Marine Environmental Sciences, University of Bremen, Leobener Str. 8, 28359 Bremen, Germany
[4] UiT The Arctic University of Norway, Department of Geosciences, Postboks 6050 Langnes, NO-9037 Tromsø, Norway
[5] Geohazards Research Unit, Institute of Geology, Adam Mickiewicz University, Poznań
Bogumiła Krygowskiego 12, 61-680 Poznań, Poland

Corresponding authors

Corresponding authors are Manuel Ruben (manuel.ruben@awi.de) and Gesine Mollenhauer (Gesine.mollenhauer@awi.de), to whom correspondence and requests for materials should be addressed.

Abstract

Rock-derived or petrogenic organic carbon has traditionally been regarded as being non-bioavailable and bypassing the active carbon cycle when eroded. However, it has become apparent that this organic carbon might not be so inert, especially in fjord systems where petrogenic organic carbon influxes can be high, making its degradation another potential source of greenhouse gas emissions. The extent to which subsurface microbes use this organic carbon is not well constrained, despite its potential impacts on global carbon cycling. Here we performed compound-specific radiocarbon analyses on intact polar lipid-fatty acids of live microbes from marine sediments in Hornsund Fjord, Svalbard. By this means, we estimate that local bacterial communities utilize between 5 ± 2% and 55 ± 6% (average of 25 ± 16%) of petrogenic organic carbon for their biosynthesis, providing evidence for the important role of petrogenic organic carbon as a substrate after sediment redeposition. We hypothesize that the lack of sufficient recently synthesized organic carbon from primary production forces microbes into utilization of petrogenic organic

carbon as an alternative energy source. The input of petrogenic organic carbon to marine sediments and subsequent utilization by subsurface microbes represents a natural source of fossil greenhouse gas emissions over geological time scales.

Rock-derived or petrogenic organic carbon

Shales and other sedimentary deposits store around 90% of global organic carbon (OC; Galy et al., 2008). However, this fossil rock-derived or petrogenic organic carbon (OC_{petro}) has been widely neglected as a potential microbial substrate and source of fossil greenhouse gases (GHG; Guillemette et al., 2017). Traditionally, OC_{petro} has not been included in studies of the active carbon cycle as the majority of it was synthesized, deposited, and degraded millions of years ago and is commonly regarded as non-bioavailable (Guillemette et al., 2017). However, within the last two decades, several studies have investigated the availability of OC_{petro} from different sources as a substrate for microbes, painting a more diverse picture of its bioavailability (Cui et al., 2017; Guillemette et al., 2017; Hemingway et al., 2018; Petsch et al., 2001; Wakeham et al., 2006). Globally, OC_{petro} oxidation is estimated to account for release of 40 to 100 x 10^6 tC annually (Petsch, 2014), opposing the effects of OC burial (France-Lanord & Derry, 1997) and silicate weathering (Berner & Caldeira, 1997). Thus, a proper assessment of OC_{petro} bio-availability and the role of microbes become increasingly important as more evidence of GHG release from OC_{petro} into the atmosphere is discovered (Thomas M Blattmann, 2022; Hemingway et al., 2018; Hilton et al., 2014; Horan et al., 2017; Soulet et al., 2021).

Previous work focused on dissolved organic carbon (OC) from glacial runoff, showing it to be highly bio-available, despite its old age (Hemingway et al., 2019; Hood et al., 2009). Although microbial communities may play a crucial role in glacial nutrient and carbon cycling (Kohler et al., 2020), the extent to which the particulate OC supplied by glaciers can be utilized by microbes after its redeposition is virtually unexplored. According to conservative estimates, fjords bury about 18 Mt of OC annually (~11% of marine carbon burial; Smith et al., 2015). Globally, about 11% of landmasses are covered by polar ice sheets and alpine glaciers (Hood et al., 2015), eroding into the underlying bedrocks (Bennett & Glasser, 2011), including OC rich strata. Increasing temperatures at high latitudes (IPCC, 2019) are expected to increase runoff and sediment exported from both polar glaciers (Delaney & Adhikari, 2020) and ice-sheets (Bendixen et al., 2017) to downstream depositional environments, thus increasing OC_{petro} fluxes in the upcoming decades (Szczuciński et al., 2009). At marine-terminating glaciers, the bulk of this OC_{petro} is deposited within a distance of several kilometers from glacier termini (Szczuciński & Zajączkowski, 2012), with a strong dominance of particulate OC over dissolved OC exported from ice sheets (Bhatia et al., 2013).

However, OC_{petro} deposition is not limited to fjords but may supply 40 – 50% of OC buried in Arctic Ocean sediments (Drenzek et al., 2007). It is therefore of interest whether this vast pool of remobilized OC_{petro} can be microbially degraded, and a proper budget and assessment of its rates are necessary to understand impacts on the global carbon cycle.

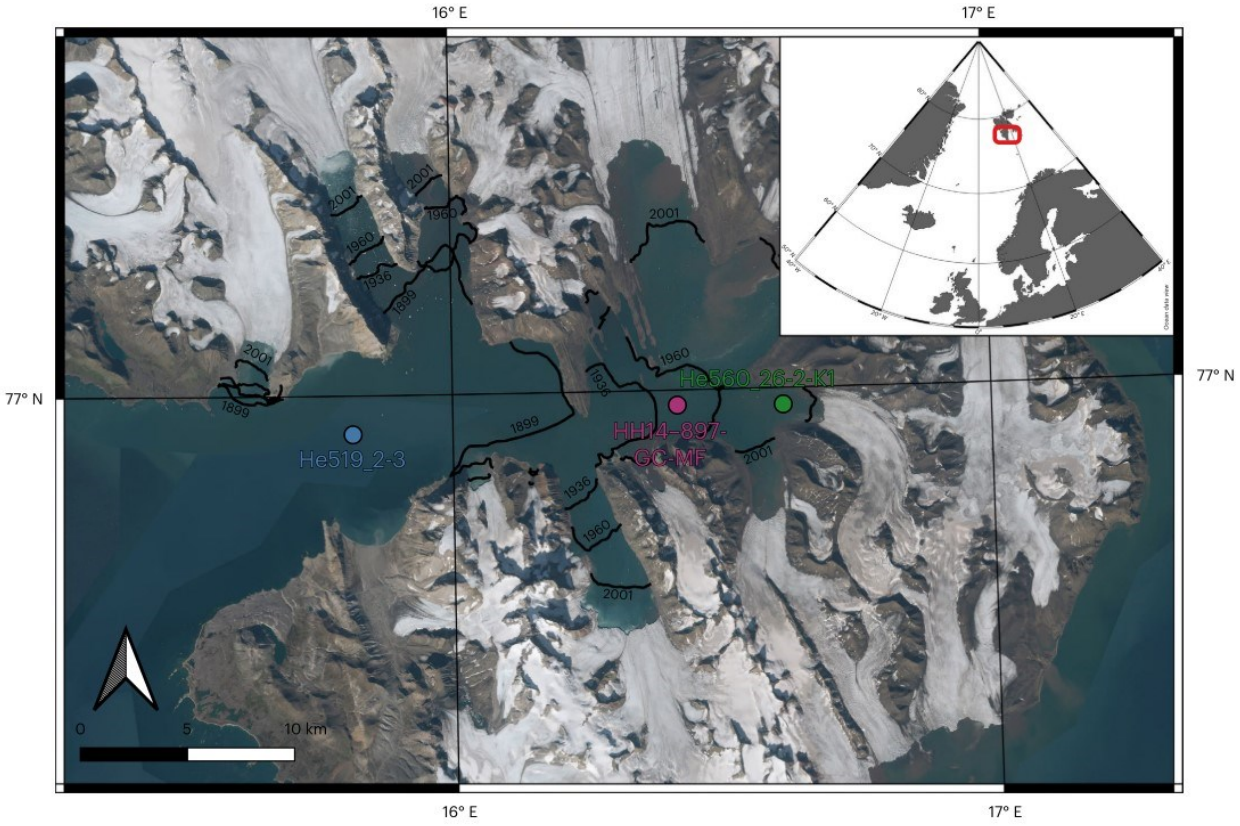

Figure 6: ***Map of Hornsund Fjord in Svalbard with core locations****. Core locations with respect to reconstructed retreating glacier termini lines in black of the years 1899, 1936, 1960, and 2001 (modified after Błaszczyk et al. 2013(Błaszczyk et al., 2013)). The location of marine influenced main basin short core He519_2-3 is shown in blue, that of central Brepollen long core HH14-897-GC-MF in purple, and that of glacier termini core He560_26-2-K1 in green. The map was extracted from a satellite imagery mosaic prepared by the Norwegian Polar Institute, based on Copernicus Sentinel data 2020.*

Organic carbon dynamics in Hornsund fjord

To investigate this process, we analyzed three sediment cores, two short and one long, from Hornsund Fjord, Svalbard (Figure 6). Hornsund's marine-influenced main basin is separated from the tidewater-glacier dominated inner basin, Brepollen, by a shallow sill. The Brepollen basin was formed during the last century following the post Little Ice Age deglaciation (Błaszczyk et al., 2013). The most marine influenced core (27 cm long core He519_2-3) was retrieved from the center of the main basin at a depth of 202 m. It records the sedimentary history from approximately 1950s to 2018 CE. A gravity core was collected in the Brepollen basin center (149 cm long core HH14-897-GC-MF) at a water depth of 140 m, archiving the time

span from 1960s to 2014 CE. The 23 cm long core, He560_26-2-K1, was taken ~1 km from the glacier termini at a water depth of 46 m, covering the time period from about 2012 to 2020 CE (details in methods).

The catchment geology of the Hornsund fjord is very diverse (Birkenmajer, 1990). The majority of sediments supplied to the fjord comes from the eastern part of the drainage basin, build of OC-rich Paleogene mudstones and sandstones formed in continental shelf sea environment (details in supplement; Birkenmajer, 1990; Włodarska-Kowalczuk et al., 2019) . The area is mainly glacier-covered (Błaszczyk et al., 2013), however, these strata extend northward. The better exposure displays some low- to mid-grade coal seams, however, representing only a minor portion of the rock volume (<170 m thick unit; Ćmiel & Fabiańska, 2004; Harland, 1997). Since the late 19th century, the local glaciers have been retreating rapidly at rates of several tens of meters to more than 100 m annually (Błaszczyk et al., 2013), simultaneously shifting the sedimentary depocenter alongside the glacier termini position (Szczuciński et al., 2017). Sediment accumulation rates in the studied core locations varied from more than 10 cm to a few mm per year with respect to distance from retreating glacier termini. Average total OC (TOC) contents range between 1.3 ± 0.1 to 1.9 ± 0.1 wt.% and are constant throughout the individual cores independent of glacial proximity (Figure 7 a). The origin of the OC was assessed using several geochemical parameters and biomarker indices including bulk $\delta^{13}C$, fatty acid based terrestrial aquatic ratio (TAR; Meyers, 1997), BIT-Index as a soil OC marker (Hopmans et al., 2004), *n*-alkane carbon preference index (CPI) as an indicator for degradation/thermal maturity (Figure 7 c-f; details in methods; Bray & Evans, 1961), and bulk radiocarbon ($F^{14}C$) signature (Figure 8 b, d, f). Contributions to the OC pool by terrestrial plants and soils can be neglected based on both the low TAR- ratio and BIT-index, which reflects exclusively input of fresh, soil-derived organic matter and is not sensitive to old mature terrestrial OC from source rock (Hopmans et al., 2004). Based on the above mentioned biogeochemical parameters, all three cores show a homogenous OC composition consisting of a mixture of two types of material: 1) young, freshly synthesized, labile marine organic matter (OC_{marine}) from primary production and 2) old, thermally very mature, supposedly non-bioavailable, OC_{petro} eroded from organic rich sedimentary rocks in the fjord catchment (Włodarska-Kowalczuk et al., 2019). Further evidence for a petrogenic origin of much of the organic matter is provided by the infinite compound-specific radiocarbon ages of long-chain *n*-alkanes extracted from the central Brepollen core (Table S 1). Even though primary production rates in Hornsund are similar (Piwosz et al., 2009) to other fjord systems with marine-terminating glaciers (Meire et al., 2017), the relative abundance of sedimentary OC_{marine} (f_{marine}) is rather low and increases with increasing distance to the glacier termini. The f_{marine}-value was estimated using an isotope mass balance based on

$F^{14}C$ of the bulk TOC, with two endmembers: one modern OC_{marine} ($F^{14}C$~1=modern) and one fossil OC_{petro} ($F^{14}C$=0=fossil; details in methods). The short core in the vicinity of glacier termini and the long core in the center of the Brepollen basin both have low f_{marine}-values of 2 ± 2% to 11 ± 2%. By contrast, in the short core (He519_2-3) from the fjord main basin, the f_{marine} ranges from 42 ± 2% at the core top to 26 ± 6% at the bottom. Overall, the TOC age is primarily controlled by the input of OC_{marine} as this input is the main difference between the OC deposited in the main basin versus the Brepollen basin.

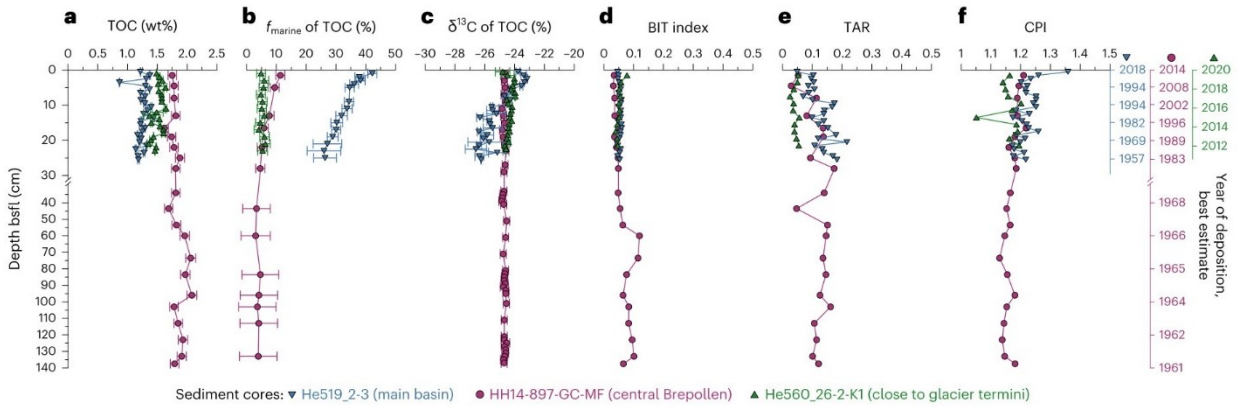

Figure 7: ***Bulk organic matter parameters and biomarker indices plotted against depth and year of deposition A.D****. Figure displays total organic carbon content (TOC; a), contribution of marine organic carbon to TOC (fmarine; b), stabile carbon isotope composition of organic carbon ($\delta^{13}C$; c), branched and isoprenoid tetraether index (BIT; d), terrestrial aquatic ratio (TAR; e), and carbon preference index (CPI; f) for the three analyzed sediment cores. Data are presented in all subpanels as mean values. Given uncertainties in subpanels a) and c) are based on standard deviations of duplicate measurements of each sample; uncertainties in subpanel b) display propagated 1σ errors form bulk radiocarbon measurements, sediment age model and surface dissolved inorganic carbon age model (details in methods). The deposition years are best estimates of the sediment age models (uncertainties and details in supplement).*

Compound specific radiocarbon analysis

Due to the characteristic $F^{14}C$ signature of the two pools, we were able to use ^{14}C as an inverse tracer (absence of ^{14}C) under the assumption that the isotopic signature of the substrate (i.e. in sediments) will be passed on through the heterotrophic utilization into the synthesized biomass (Petsch et al., 2001). Following the approach of Petsch et al. (2001), we assessed the bioavailability of these two OC pools in the sediment cores by radiocarbon analyses of the fatty acid (FA) side chains of intact polar lipids (IPL), extracted with a modified Bligh and Dyer approach (Slater et al., 2006). Bacterial IPLs have been reported to decay within days to weeks after cell lysis and are therefore regarded as indicators for living microbiota (Logemann et al., 2011). Bacterially produced FAs $C_{br\text{-}15:0}$ and $C_{16:1\ n\text{-}7}$ (Wakeham et al., 2006) were purified into single compound fractions and subsequently radiocarbon dated. With this approach, we were able to identify the average $F^{14}C$ signature of the substrate utilized by bacteria in the sediment (Wakeham et

al., 2006). To ensure bacterial FA origin, precursor lipids were determined by high pressure liquid chromatography coupled to mass spectrometry (HPLC-MS).

Using HPLC-MS, the dated $C_{br\text{-}15:0}$ and $C_{16:1\ n\text{-}7}$ FAs were found to derive from a diverse group of phospholipid precursors: mainly phosphatidylglycerol and phosphatidylethanolamine in the glacier termini and Brepollen long core and additionally phosphatidylcholine in the main basin core (Figure S 1). While most of these lipids can be assigned to sulfate-reducing bacteria (Seidel et al., 2013) or other sedimentary marine bacteria (Schubotz et al., 2011), minor contributions of potentially algae-derived betaine-lipids and phosphatidylcholine (<10%) could potentially lead to an increase in the measured $F^{14}C$ FA values and hence an underestimation of OC_{petro} degradation (details in supplement).

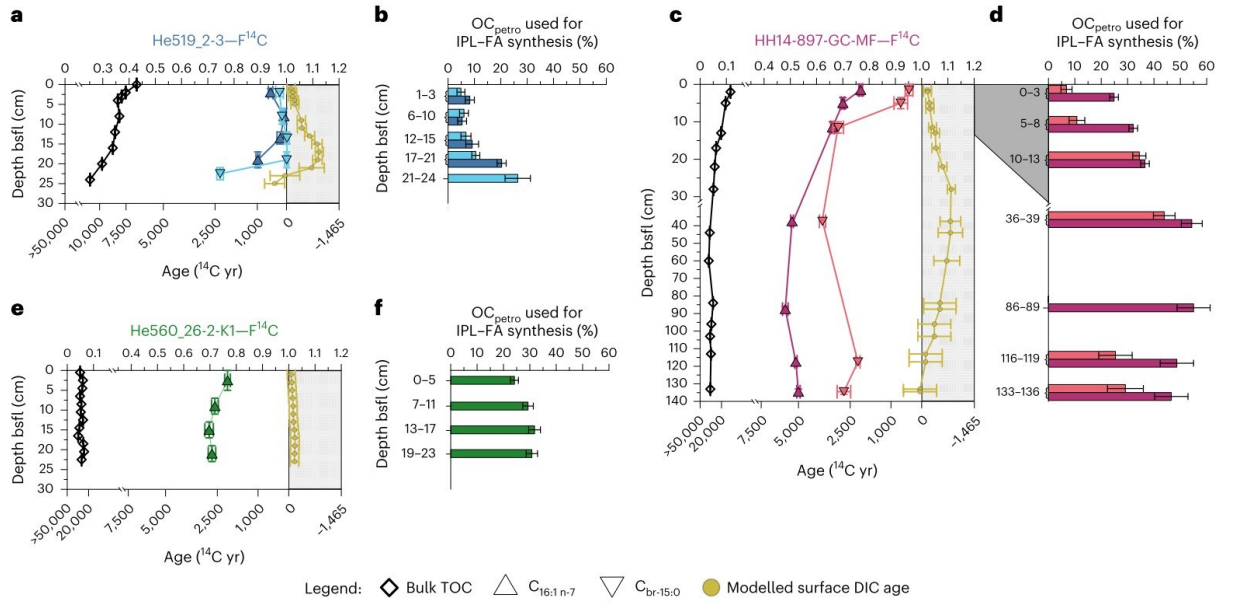

Figure 8: ***IPL-FA radiocarbon data and estimated OC_{petro} used for IPL-FA synthesis.*** *Subpanels are color coded and refer to data from sediment cores He519_2-3, HH14-897-GC-MF, and He560_26-2-K1 are shown in blue (a,b), purple (c,d), and green (e,f) respectively. Sub-panels a, c, and e display radiocarbon signatures of total organic carbon (TOC), modeled surface dissolved inorganic carbon (DIC) $F^{14}C$-signature, and intact polar lipid-fatty acids (IPL-FAs $C_{16:1\ n\text{-}7}$ and $C_{br\text{-}15:0}$) displayed as fraction modern carbon ($F^{14}C$) values and corresponding ^{14}C age. Values in gray-shaded area show elevated $F^{14}C$-values (>1), due to 1960-s above ground nuclear weapons tests, thus, giving the impression of apparent ages in ^{14}C years in the future. Data are presented as mean values for blank corrected measured (TOC, IPL-FA) and calculated values (surface DIC $F^{14}C$-signature and panels b,d,f). Sub-panels b, d, and f represent calculated percentages of OC_{petro} used for bacterial IPL-FA synthesis of $C_{16:1\ n\text{-}7}$ (dark colored) and $C_{br\text{-}15:0}$ (light colored). Values are estimated by an isotope mass balance using respective IPL-FA $F^{14}C$ signatures (panels a, c, and e) versus the endmembers of fossil petrogenic organic carbon (OC_{petro}; $F^{14}C$=0) and modeled surface DIC $F^{14}C$-signature in the calendar year of deposition (details in methods). Please note the different axis breaks in panels c and d. Vertical error bars of subpanels a, c, and e display depth intervals of analyzed sediments. Uncertainties in subpanels a, c, and e for bulk TOC, IPL-FA $C_{16:1\ n\text{-}7}$ and $C_{br\text{-}15:0}$ display propagated 1σ errors of measurements and blank correction (details in methods); uncertainties displayed in the modeled surface DIC $F^{14}C$-signatures are propagated 1σ errors from the sediment age model combined with an estimated $F^{14}C$ (DIC) uncertainty of 0.015. Uncertainties displayed in subpanels b, d, and f represent propagated 1σ uncertainties from subpanels a, c, and e of measured IPL-FAs ($C_{16:1\ n\text{-}7}$ and $C_{br\text{-}15:0}$) and modeled surface DIC age uncertainties.*

In the marine-influenced main basin core (He519_2-3), compound-specific $F^{14}C$ values for IPL-FAs within the topmost part of the core (< 15 cm; $F^{14}C$ = 0.939 ± 0.008 to 1.002 ± 0.009) agree closely with modeled surface dissolved inorganic carbon (DIC) values ($F^{14}C$ = 1.013 ± 0.015 to 1.116 ± 0.020), indicating an exclusive or at least strong preferential utilization of recently synthesized OC_{marine} (Figure 8 a). Further downcore (17-21 and 21-24 cm), the FAs diverge from modeled DIC signatures toward lower $F^{14}C$ values ($F^{14}C$ < 1.000 ± 0.007), indicating an increase in OC_{petro} utilization. Interestingly, this shift mirrors with a decrease of f_{marine} from 30-42% in the topmost 15 cm to less than 30% below. Nevertheless, OC_{marine} is the primary, but not exclusive substrate utilized by the sedimentary microbiome in sediment core He519_2-3 while an apparent shift towards increasing OC_{petro} utilization occurs downcore.

A different picture emerges at the glacier termini core (He560_26-2-K1, Figure 8 e). The $C_{16:1\ n-7}$ $F^{14}C$ values range between 0.767 ± 0.011 and 0.697 ± 0.016, which is far lower and outside the 2σ uncertainty of the modeled surface DIC $F^{14}C$ (ranging between 1.009 ± 0.015 and 1.023 ± 0.015). This indicates the substantial uptake of OC_{petro} into the bacterial membrane lipids. Unfortunately, sedimentary contents of $C_{br-15:0}$ were too low to perform compound-specific radiocarbon dating. IPL-FA data from the Brepollen long core (HH14-897-GC-MF, Figure 8 c) show $F^{14}C$ values similar to those from the He560 glacier termini core at the topmost interval. As depth increases, the IPL-FA signatures shift toward even lower $F^{14}C$ values reflecting increasing OC_{petro} utilization in sediments representing depositions closer to the glacier terminis. The values remain rather constant below 30 cm. This shift occurs alongside a decrease in the f_{marine} in the sediments – similar to the decrease in the main basin core. The pervasive offset in $F^{14}C$ values between $C_{16:1\ n-7}$ and $C_{br-15:0}$ can best be explained by different bacterial sources for these IPL-FAs that preferentially consume different types of organic matter (details in supplement).

The percentage of ancient carbon used for the microbial biosynthesis (Figure 8 b, d, f) was estimated with an isotope mass balance model, using a radiocarbon-free, fossil endmember for OC_{petro} ($F^{14}C$=0) and modern OC_{marine} endmember according to the reservoir age modeled at the respective depth intervals (details in methods). A pronounced difference between the two Brepollen cores to the main basin core is evident from this mass balance estimate. Within the top 15 cm of the main-basin core, OC_{petro} accounts for 5 ± 2% to 9 ± 2% of the utilized carbon, whereas in the Brepollen cores, OC_{petro} contributes up to 37 ± 2% in the topmost intervals. The most proximal core at the glacier termini is characterized by extremely high sedimentation rates, f_{marine} values consistently below 6 ± 2% throughout the core, and fairly constant OC_{petro} utilization (24 ± 2% to 32 ± 2%). On the contrary, in both the marine-influenced main basin short core and the central Brepollen basin long core, we can observe an increased utilization of OC_{petro} with

increasing depth and decreasing f_{marine}. The highest estimate of OC_{petro} utilization reached 55 ± 6% in the central Brepollen core in the depth interval of 86-89 cm, compared to the lowest OC_{petro} of only 5 ± 6% in the marine influenced main basin core (see above). Here, we show that even over short distances within one fjord system the microbial utilization of OC_{petro} can vary widely, suggesting both low and substantial fossil GHG emission potential from increasing glacial erosion.

Although we cannot directly identify the mechanisms for OC_{petro} utilization, we hypothesize that with decreasing abundance of fresh, labile OC_{marine}, microbes are forced to utilize OC_{petro} for their biosynthesis. For example, in the interval with the highest percentage of OC_{petro} utilized for lipid synthesis (HH14 86-89cm) the mass balance suggests that 55 ± 6% of utilized carbon originates from OC_{petro} when the abundance of labile OC_{marine} in the sediment is low (f_{marine}=5 ± 6%). In the topmost three dated intervals of the main basin core, OC_{petro} utilization is much lower but still accounts for 5 ± 2% to 9 ± 2% when f_{marine} is above 30%.

Under the assumption that sedimentary microbes use the same substrate for both their anabolic and catabolic pathways (Carlson et al., 2007), we estimate that heterotrophic remineralization of OC_{petro} accounts for between 5 ± 2% to 55 ± 6% of local microbiota's overall energy consumption. This remineralization leads to the conclusion that CO_2 (and CH_4) emitted from sediments as metabolic end-products originate in some part from fossil sources, which might be enhanced with increased mobilization of ancient organic-rich deposits in a warming climate.

Implications of OC_{petro} utilization

Our data indicate that OC_{petro} is indeed microbially utilized after deposition in Hornsund Fjord. These findings are in line with previous studies (Hemingway et al., 2018; Horan et al., 2017; Petsch et al., 2001; Soulet et al., 2021) and highlight that several parts of the world's OC_{petro} pools are part of the active carbon cycle, and that these may be affected by microbial processing and consumption. Glaciated fjord ecosystems similar to the Hornsund Fjord with often OC-rich (including coal bearing) bedrock in their drainage areas are fairly widespread and can be found in Svalbard (Kim et al., 2011), Alaska(Page et al., 1996), Greenland (Bojesen-Koefoed et al., 2012), Franz-Joseph-Land (Dibner et al., 1992), and Antarctica (Elliot et al., 2015). These ecosystems may likewise supply suitable substrates for microbial degradation to marine sediments. Recent studies of other glacial environments based on both modern glacial sediments (Vinšová et al., 2022), watershed analysis (Horan et al., 2017), and paleo CO_2 isotopic compositions (Thomas M Blattmann, 2022) indicate that similar utilization of old, previously "locked up" OC may also occur on shore, indicating the geographical pervasiveness of OC_{petro} utilization. Microbial

OC_{petro} utilization has also been reported from terrestrial shales (Petsch et al., 2001). These findings indicate that OC_{petro} utilization at the rock interface, after erosion and redeposition is likely to occur globally. The resulting fossil GHG emissions may be substantial on a geological time-scale – even if only a fraction of the OC_{petro} becomes re-mineralized after deposition or exposure.

Based on our data, we cannot estimate GHG fluxes resulting from OC_{petro} utilization in marine sediments. However, considering the size of the global OC_{petro} reservoir (Galy et al., 2008) further quantitative research into this topic seems to be mandated, both in terms of a global OC_{petro} flux from rivers, ice-sheets and glaciers, but also OC_{petro} utilization dynamics in sediments, soils and the water column. High latitude temperatures continue to rise up to four times more rapidly than in the rest of the world (Rantanen et al., 2022) and sediment export rates are expected to increase from both glaciers (Delaney & Adhikari, 2020) and ice-sheets (Bendixen et al., 2017) to downstream depositional environments. Next to oxidation of OC_{petro}, consequent ecosystem changes like increased fertilization of primary production (Bhatia et al., 2013) or turbidity (Szczuciński & Zajączkowski, 2012) are only two of the manifold associated changes impacting carbon cycling in the glacial environment. Considering a recent estimate of global atmospheric CO_2 concentrations increasing by 50 ppm due to fjord sediment mobilization during the last glacial maximum(Cui et al., 2022), a potential climate impact on decadal to centennial time-scale seems worth investigating. Therefore, in order to fully grasp the impact of glacial retreat on global carbon budgets, studying these processes in both marine and terrestrial settings may be needed, given the IPCC projections based on the low emission RCP2.6 scenario predict global glacial mass loss of 18% in 2100 relative to 2015, suggesting long lasting effects even in the event of zero anthropogenic GHG emissions (IPCC, 2019).

Methods

Sampling

The sediment cores analyzed in this study were taken on three separate expeditions in Hornsund Fjord, Svalbard. Gravity-core HH14-897-MF-GC was taken in October 2014 on board the Norwegian RV Helmer Hanssen in the central Brepollen basin. The two short cores were taken on the German RV Heincke during cruises He519 in September 2018 and He560 in August 2020. Core He519_2-3 was taken at the central main basin, whereas core He560_26-2-K1 was retrieved in the inner Brepollen basin (details in table S 2)

Both short cores were sliced on board RV Heincke, transferred into glass containers, and frozen at -20°C immediately after coring until analysis. The archive half of gravity-core HH14-897-MF-GC was stored at 4°C in the core repository at the Department of Geosciences, UiT The Arctic University of Norway prior to sampling in January 2019. After sampling, sediments were transferred into glass containers and stored at -20°C. Even though the long sediment core was not frozen immediately after coring, biomarkers, bulk parameters, compound-specific radiocarbon data, and IPL data show similar patterns as the second Brepollen basin core He560_26-2-K1. In particular, the matching IPL (details in supplement) and compound-specific radiocarbon data provide confidence that the data obtained from the Brepollen long core accurately reflect in-situ information and allows for OC_{petro} utilization estimates in the deeper core sections. Any potential storage effects would be expected to result in increased IPL concentrations and $F^{14}C$ values of IPL biased towards modern atmospheric values, which was not observed.

All glassware used was combusted at 450°C for 6 hours and equipment cleaned with solvents before usage for both sampling and laboratory activities.

Age models

The age models were established using the short-lived isotopes ^{210}Pb and ^{137}Cs. The ^{210}Pb in recent marine sediments is of twofold origin. The supported ^{210}Pb ($^{210}Pb_{sup}$) is continuously produced within the sediments by the decay of parent isotopes, while excess ^{210}Pb ($^{210}Pb_{ex}$) is delivered to the sediment from above, produced by ^{222}Rn decay in the atmosphere and the water column overlying the sediment. Sediment cores He519_2-3 and He560_26-2-K1 were analyzed at the Alfred-Wegener-Institute Bremerhaven, Germany, using a planar-type HPGE gamma spectrometer. Core HH14-897-GC-MF was measured at the Institute of Geology at Adam Mickiewicz University in Poznań, Poland using a gamma detector Canberra BE3830. The age models of the three cores were generated based on $^{210}Pb_{ex}$ using the

constant sedimentation – constant flux model (CFCS) and verified with penetration depth and peaks in ^{137}Cs isotope and historical information on the fjord deglaciation (Błaszczyk et al., 2013). However, alternative models were also considered and the resulting accumulation rates should be regarded as approximates as the particular assumptions behind each model were not fully met. The analysis was conducted with the help of the R-based *serac* code (Bruel & Sabatier, 2020; details in supplement; Figure S 4-6).

Surface DIC age model

Dissolved inorganic radiocarbon concentrations of surface water are simulated using the Finite-volumE Sea ice-Ocean Model FESOM2 (Danilov et al., 2017) equipped with radiocarbon (Lohmann et al., 2020). Radiocarbon is implemented in terms of $F^{14}C$, neglecting marine biological processes which play a minor role compared to circulation and radioactive decay (Fiadeiro, 1982; Toggweiler et al., 1989). Air-sea exchange fluxes of $^{14}CO_2$ in FESOM2 depend on wind speed and CO_2 solubility (Wanninkhof, 2014), and assume a surface water global-mean DIC concentration of 2.0 mol / m³. The model was spun up in a previous simulation to quasi steady-state conditions typical of 1850 CE (Lohmann et al., 2020). We continued the simulation to 2015 CE, using periodic climate forcing (Large & Yeager, 2009) and transient values of atmospheric CO_2 (Meinshausen et al., 2017) as well as of $F^{14}C$ (Graven et al., 2017). In the North Atlantic the simulated anthropogenic ^{14}C distribution is in line with observations (Butzin et al., 2021; Key et al., 2004). FESOM2 employs unstructured meshes with variable resolution, here featuring about 127,000 surface nodes and 47 layers. After the simulation the model results were remapped to regular geographical coordinates and evaluated at the surface level considering the grid cell nearest to Hornsund.

Total organic carbon and stable carbon isotope ratios

TOC concentrations of core HH14-897-MF-GC were measured at the Department of Quaternary Geology and Palaeogeography of the Adam Mickiewicz University. The analyses were performed with a vario MAX CNS elemental analyzer (Elementar, Germany). To determine the organic carbon content, prior to the analyses, samples were treated with 1 molar liquid hydrochloric acid (HCl) at room temperature for over a week (until no sign of reaction is visible) to remove carbonates. The $\delta^{13}C$ of bulk organic carbon in sediment was obtained using an Elemental Analyzer Flash EA 1112HT Series combined with an Isotopic Ratio Mass Spectrometer Thermo Delta V Advantage in a Continuous Flow mode. Results are expressed relative to Vienna PeeDee Belemnite. Methods are described in detail inWoszczyk et al. (2021). The preliminary results were presented by Szczuciński et al. (2017).

Both sediment cores He519_2-3 and He560_26-2-K1 were analyzed for TOC and $\delta^{13}C$ by continuous-flow elemental analyzer - isotope ratio mass spectrometer using a Thermo Finnigan Flash EA 2000 connected to a Delta V Plus isotope ratio mass spectrometer at MARUM Bremen, Germany, following the protocols of Werner & Brand (2001) and Brodie et al. (2011). Pretreatment involved sample homogenization and carbonate removal over night with 10% HCl or until no further gas development was visible. Afterwards the sample was neutralized with deionized water, freeze-dried, and weighed for analysis.

Bulk radiocarbon dating

Radiocarbon ages of the TOC were determined by accelerator mass spectrometry (AMS) at the MICADAS facility of the Alfred-Wegener-Institute in Bremerhaven, Germany. AMS dating was performed on graphite targets of 1 mg C, and sediment masses were chosen according to TOC concentrations. As a pre-treatment, samples were homogenized and carbonates were removed three times with 6M HCl at 60°C. Methodology and blank determination were performed as described by Mollenhauer et al. (2021).

Lipid Biomarkers

Lipid biomarkers were extracted from about 3 g of sediment using the method by Mollenhauer & Eglinton (2007) at the Alfred-Wegener-Institute in Bremerhaven, Germany and subsequently separated into four subfractions for alkanes, ketones, alcohols (containing glycerol dialkyl glycerol tetraethers: GDGTs), and fatty acids, as described in Wei et al. (2020). The subfractions of alkanes and fatty acids were quantified on a GC-FID on a setup as in Wei et al. (2020). GDGTs were quantified on a HPLC-MS setup as described in Wei et al. (2020), after the protocol of Hopmans et al. (2016). Known amounts of the internal standards squalane, C_{46}-GDGT, and 19-methylarachidic acid were added to the sediments before the extraction for the quantification of alkanes, GDGTs, and fatty acids, respectively.

Subsequently, biomarker indices were calculated as follows:

- Carbon preference index (CPI) indicating thermal maturity of OC, using the ratio of even to odd numbered *n*-alkanes after Bray & Evans (1961):

$$CPI = 0.5 * \left(\frac{C_{25} + C_{27} + C_{29} + C_{31} + C_{33}}{C_{24} + C_{26} + C_{28} + C_{30} + C_{32}} + \frac{C_{25} + C_{27} + C_{29} + C_{31} + C_{33}}{C_{26} + C_{28} + C_{30} + C_{32} + C_{34}}\right) \quad (1)$$

- Branched and Isoprenoid Tetraether (BIT) Index indicating input from terrestrial soils in the catchment area (and absence thereof in case of values near 0) after Hopmans et al. (2004):

$$BIT\ index = \frac{\text{GDGT I} + \text{GDGT II} + \text{GDGT III}}{Crenarchaeol + \text{GDGT I} + \text{GDGT II} + \text{GDGT II}} \quad (2)$$

- Terrestrial aquatic ratio (TAR) indicating the relative abundance of OC from terrestrial versus aquatic origin, using comparing short- and long-chain fatty acid concentrations after Meyers (1997):

$$TAR = \frac{C_{24:0} + C_{26:0} + C_{28:0}}{C_{12:0} + C_{14:0} + C_{16:0}} \quad (3)$$

Intact polar lipids

Intact polar lipids were extracted with a modified Bligh & Dyer (1959) approach, following the protocol by Slater et al. (2006); depth intervals of the individual cores were chosen to obtain at least 80 g of sediment to ensure sufficient FA recovery for subsequent radiocarbon analysis. The total lipid extracts were separated into three fractions via an activated (1% H_2O) silica column chromatography into 1) neutral lipids, 2) glyco lipids, and 3) polar lipids using 1) dichloromethane, 2) acetone, and 3) methanol to elute the fractions from the column, following the methodologies of Slater et al. (2006), Wakeham et al. (2006), and Akondi et al. (2017).

Aliquots of 1% of the polar lipid fractions were analyzed on a Bruker maXis Plus ultra- high-resolution quadrupole time-of-flight mass spectrometer (Q-TOF) with an electrospray ionization source coupled to Dionex Ultimate 3000RS ultra-high-pressure liquid chromatography at MARUM, Bremen. The analyses were carried out using hydrophilic interaction chromatography (Hilic) in positive mode to check the separation of phospholipids with improved chromatographic separation and detection as described in Wörmer et al. (2013).

Compound-specific radiocarbon analysis

Compound-specific radiocarbon analysis (CSRA) was performed on purified IPL-FA and *n*-alkanes from aliquots obtained by modified Bligh and Dyer extraction as described above. IPL-FA CSRA was performed

of all extracted depth intervals. CSRA of *n*-alkanes purified from the neutral fraction was limited to three depth intervals (0-3 cm; 86-89 cm; 133-136 cm) of core HH14-897-MF-GC. The *n*-alkane separation for CSRA was achieved following methods described by Meyer et al. (2019).

The polar lipid fractions were saponified at 80 °C with 1 mL of KOH (0.1 M) in MeOH:H_2O (9:1, v/v) for 2 h. Neutral lipids were removed with a liquid-liquid phase separation using hexane. The remaining solution was acidified and FA were extracted with a liquid-liquid phase separation using DCM. The FAs were converted into fatty acid methyl esters (FAME) overnight at 50°C in MeOH at a pH of 1 under a N_2 atmosphere. Subsequently, the FAMEs were separated from the MeOH phase by liquid-liquid phase separation using hexane and purified via passage through an activated (1% H_2O) silica column, eluting FAMEs with 4 mL DCM:HEX (2:1, v/v).

From both of the purified *n*-alkane and IPL-FAME fractions, single compounds were isolated using a GC coupled to a preparative fraction collector (PFC) with the setup described in Wei et al. (2021). CSRA was performed as gas measurements at the MICADAS facility of the Alfred-Wegener-Institute in Bremerhaven, Germany, following the protocol described in Mollenhauer et al. (2021).

Blank determination for CSRA was achieved in a two-step process. 1) Procedural blanks were run alongside the samples to ensure that no contamination from glassware, solvents, or reagents occurred during the extraction and wet chemical preparation. All blanks were free of those FA and *n*-alkane homologues that were subsequently isolated with PFC. 2) Procedural blanks for PFC and subsequent radiocarbon analysis were determined using FA and *n*-alkanes extracted from recent (apple peel) and fossil (Eocene Messel shale) laboratory internal standard materials, followed by subsequent radiocarbon age correction with according blanks as described in Winterfeld et al. (2018) and Sun et al. (2020).

Isotope mass balance

The isotope mass balance calculations used a 1) fossil and a 2) modern endmember:

1) $F^{14}C_{fossil}$
2) $F^{14}C_{modeled\ DIC}$

The fossil endmember was set to a constant $F^{14}C$ value of 0, as the OC_{petro} is expected to be radiocarbon free, as organic-rich rocks outcropping the hinterland of Hornsund were deposited in the Tertiary (Lewińska-Preis et al., 2009; Marshall et al., 2015). Further, compound specific radiocarbon analyses of isolated *n*-alkanes yielded $F^{14}C$ values near the detection limit, supporting the radiocarbon free

endmember definition (detail in supplement). The modern endmember was defined as equivalent to the modeled surface DIC radiocarbon signature based on the biomarker data. The biomarker data indicated that the organic matter originated exclusively from the fixation of DIC during photosynthesis and OC from primary production is assumed to have the same radiocarbon signature. $F^{14}C_{modeled\ DIC}$ values changed over time due to the rapid decrease in the $F^{14}C$ of the modeled surface DIC after the peak in atmospheric radiocarbon content resulting from above-ground nuclear weapons tests in the 1960s (Figure S 7). Therefore, for the calculations, the $F^{14}C_{modeled\ DIC}$ was adjusted according to the estimated year of sediment deposition, based on ^{210}Pb + ^{137}Cs age models as described above.

The isotopic mass balances were used to estimate the relative contribution of OC_{marine} (f_{marine}) to the bulk sedimentary OC and to calculate the percentage of OC_{marine} used for bacterial membrane lipid synthesis ($\%OC_{marine\text{-}synt}$) based on the $F^{14}C$ signatures of the bulk TOC ($F^{14}C_{bulk}$) and the dated single compound IPL-FAs ($F^{14}C_{IPL\text{-}FA}$). The general equation used for the calculations is:

$$F^{14}C_{Bulk} = f_{marine} * \ F^{14}C_{modeled\ DIC} + (1 - f_{marine}) * F^{14}C_{fossil} \quad (4)$$

$$F^{14}C_{IPL-FA} = \%OC_{marine-synt} * \ F^{14}C_{modeled\ DIC} + \left(100 - \%OC_{marine-synt}\right) * F^{14}C_{fossil} \quad (5)$$

Data availability

All obtained data are publicly available at the PANGEA data repository (https://doi.org/10.1594/PANGAEA.946019). Bulk data of core HH14-897-GC-MF, including bulk TOC and $\delta^{13}C$, ^{210}Pb, and ^{137}Cs measurements (https://doi.pangaea.de/10.1594/PANGAEA.946568) as well as the associated age model (https://doi.pangaea.de/10.1594/PANGAEA.946576) are available separately on PANGEA.

Acknowledgements

We thank the captains and crews of R/Vs Helmer Hanssen and Heincke, Steinar Iversen from UiT for this practical support during the cruise/expedition on RV Helmer Hanssen. We gratefully thank Elizabeth Bonk, Lea Phillips, Maylin Malter, Jenny Wendt, Palash Kumawat, and Laura Kattein for their help handling samples. Many thanks to Felix Mark and Nils Koschnick for providing core He560_26-2-K1. Dmitry Sidorenko is acknowledged for FESOM model support. Sara Schlagenhauff for linguistic help. We thank

Robert Hilton and Jordon Hemingway whose careful and constructive reviews helped improve the manuscript. The age control and basic data on core HH14-897-MF-GC were obtained within a Polish National Science Centre (NCN) grant No. 2013/10/E/ST10/00166 in cooperation with K. Apolinarska, A. Dominiczak, M. Forwick, W. Szczuciński and M. Woszczyk. We acknowledge funding by the Deutsche Forschungsgemeinschaft (DFG, German Science Foundation) under Germany's Excellence Strategy EXC 2077 390741603 supporting contributions from F.S. and H.G.; M. B. was supported by the German Federal Ministry of Education and Research (BMBF) through project PalMod and is additionally funded through DFG-ANR project MARCARA.

Authors contributions

All authors contributed extensively to the work presented in this paper.

Manuel Ruben, Gesine Mollenhauer, and Florence Schubotz designed the study; Matthias Forwick, Witold Szczuciński, Gesine Mollenhauer, and Torben Gentz collected and provided sample material; Manuel Ruben and Jens Hefter performed laboratory experiments; Manuel Ruben, Jens Hefter, Florence Schubotz, Martin Butzin, Witold Szczuciński, Walter Geibert, Torben Gentz, and Hendrik Grotheer collected and analyzed data; Manuel Ruben, Gesine Mollenhauer, and Florence Schubotz wrote the manuscript.

Competing interests

The authors declare no competing interests.

Supplementary Information

Intact polar lipids source assignments

All three cores were dominated by phospholipids with variable relative amounts. While phosphatidylethanolamine (PE) and phosphatidylglycerol (PG) dominated the Brepollen long core HH14-897-GC-MF and the glacier-front core He560_26-2-K1, the marine influenced main basin core He519_2-3 contained higher amounts of phosphatidylcholine (PC), followed by PG and PE (Figure S 1). Phosphatidyl-(*N*)-monomethylethanolamine (PME), Phosphatidyl-(*N,N*)-dimethylethanolamine (PDME), diphosphatidylglycerol (DPG) and lyso-DPG were detected in minor amounts in all cores. The aminolipids, betaine lipids (BL), were also present in all three cores with varying amounts but always <10%. PG and PE are the most common lipids found in bacteria (Sohlenkamp & Geiger, 2016) and are typically assigned to sulfate-reducing bacteria (with DPG) in marine sediments (Lipp & Hinrichs, 2009; Schubotz et al., 2011), although other gram-negative bacteria are also potential sources. The fatty acid distribution in PG, PE, and DPG support a bacterial source as $C_{16:1}$ fatty acids dominate these lipid classes as well as odd-numbered carbon fatty acids such as $C_{17:1}$ and $C_{br\text{-}15:0}$ (Figure S 2, note: the double bond and methyl-branch was not determined by HPLC-MS, but was identified by PLFA analyses via GC-MS). The assignment of PC to a bacterial source is not as straightforward as only 10% of all bacteria are estimated to possess the genes involved in its biosynthesis (Sohlenkamp et al., 2003) and PC - with BL- is more commonly assigned to phytoplankton (Dembitsky, 1996). The higher abundance of PC in the marine-influenced core could point to detrital remains of phytoplankton, however, the fatty acid distribution indicates that a large part of PC is likely of bacterial origin (Figure S 2). Similarly, BL contain fatty acids that point to bacterial sources, but a small contribution from detrital sources that bypassed degradation in these organic-rich likely methanogenic anoxic sediments cannot be excluded. It is to be expected that detrital contributions of phospholipids and betaine lipids decrease with sediment depth and age (Harvey et al., 1986; Logemann et al., 2011), however, it is possible that degradation in deeper methanogenic layers of organic rich sediments proceeds slower leading to a potential longer preservation of bacterial IPLs. The associated fatty acids $C_{16:1}$ and $C_{br\text{-}15:0}$ were chosen for compound specific radiocarbon analysis due to their predominant bacterial origin (Bianchi & Canuel, 2011) and their abundance in the extracted IPL fractions. The different radiocarbon signatures of $C_{16:1}$ and $C_{br\text{-}15:0}$ fatty acids are likely due to different abundances in source bacteria, both in terms of fatty acid abundances within single organisms but also in the relative abundances of bacterial strains within the subsurface community. However, further microbiological methods like 16S RNA would be needed to address differences on a community level.

Compound specific radiocarbon dating of *n*-alkanes

n-Alkanes were separated from the neutral fraction of the intact polar lipid extract by a second silica column chromatography, eluting the alkane fraction with hexane. From three depth intervals of sediment core HH14-897-GC-MF, purified samples of *n*-C_{19}, *n*-C_{20}, *n*-C_{21}, and *n*-C_{22} as well as combined *n*-$C_{26+28+30}$ and *n*-$C_{27+29+31}$ were collected using the GC-PFC used similarly as for intact polar lipid fatty acid purification. The purified splits were radiocarbon dated in the same manner as the intact polar lipid fatty acids using AMS at the MICADAS facility of the Alfred-Wegener-Institute in Bremerhaven, Germany.

The radiocarbon values obtained for all *n*-alkane samples indicate that a large part of the organic matter is derived from a radiocarbon free source (Table S 1). The $F^{14}C$ values are close to the detection-limit for gas measurements and can be considered to be $F^{14}C=0$ within 2σ uncertainties in almost all cases except for the samples of combined *n*-$C_{27+29+31}$, whose $F^{14}C$ values suggest minor contributions from younger materials (less than 3 % assuming a modern source; Mollenhauer et al., 2021). In combination with low CPI values (Figure S 3), the age of the *n*-alkanes supports the assumption that freshly synthesized OM from terrestrial vegetation contributes a negligible amount to sedimentary OM. These results further support the application of a two-endmember model for radiocarbon based isotopic mass balances calculations.

Sediment core age models

Core He519_2-3 (27 cm long) collected from the Hornsund fjord main basin revealed near-constant $^{210}Pb_{ex}$ in the topmost part, considered a surface mixed layer, and steadily decreasing activities below. The modeled accumulation rate is approximately 4.1 mm/yr. The isotope ^{137}Cs was detected throughout the core and its maximum may be related to the 1986 Chernobyl event. Due to deep sediment mixing, the age model can only be treated as an approximation, but all models confirm that the sediments are considerably younger than the ^{210}Pb extinction age and were deposited -or last mixed- within the era of

artificial radionuclides (

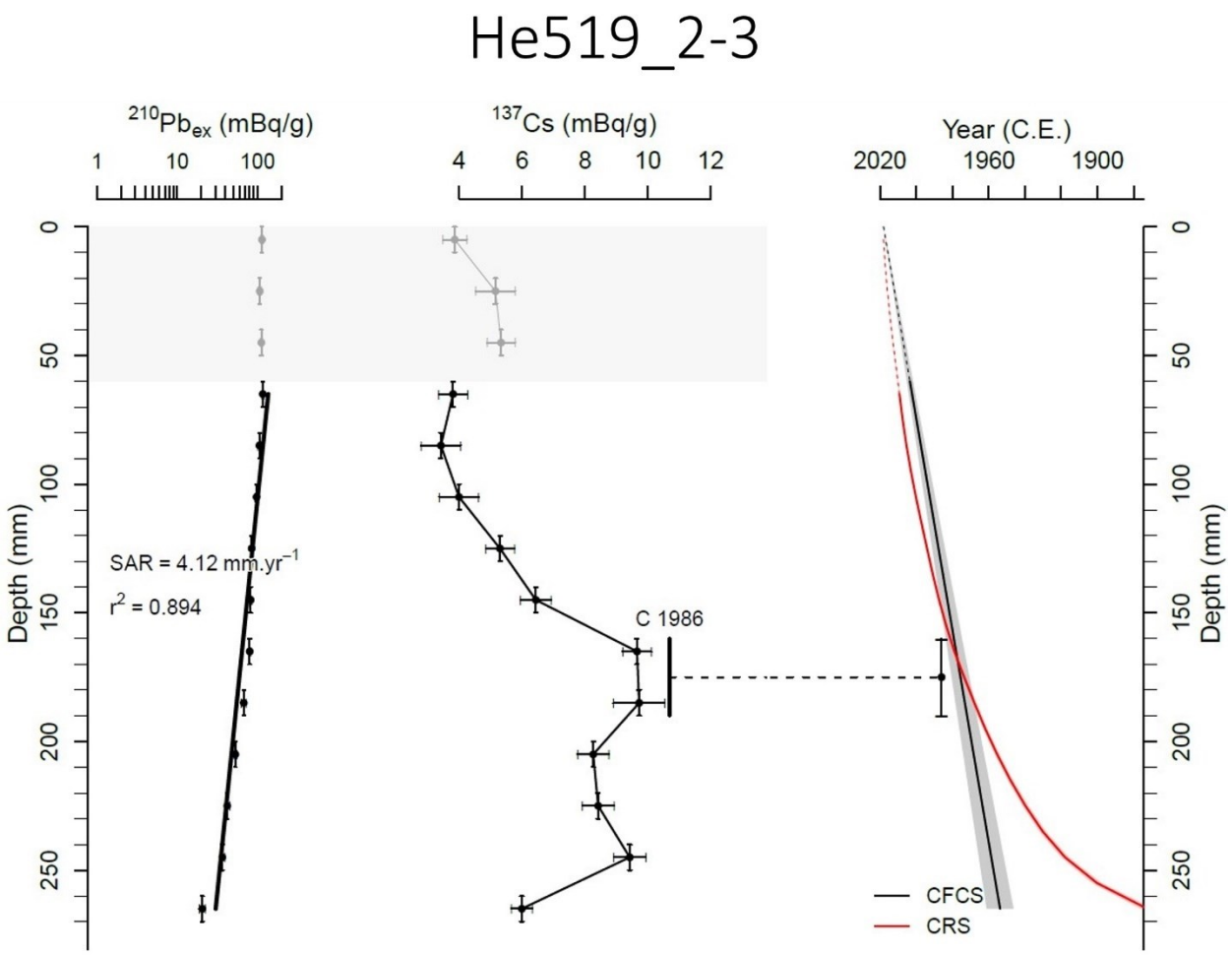

Figure S 4).

The longest core (154 cm) HH14-897-GC-MF was collected from an area in Brepollen that was deglaciated between 1936 and 1960. The $^{210}Pb_{ex}$ decreased with depth and revealed a rapid accumulation rate of approximately 147 mm/yr until around 1968, when the coring site was still close to the tidewater glacier termini, decreasing to approximately 8.1 mm/yr during the younger period (Figure S 5). The modeled sediment accumulation rates agreed with 1963 (nuclear weapon tests) and 1986 (Chernobyl) peaks in ^{137}Cs and the thickness of preserved sediment lamination.

The inner fjord sediment core He560-26-2-K1 (22 cm long), collected from an area in Brepollen, that was deglaciated during the last 50 years (Figure 6), showed $^{210}Pb_{ex}$ throughout, indicating recent rapid deposition. There was no clear depth trend in $^{210}Pb_{ex}$, and ^{137}Cs was present throughout. The calculated sediment accumulation rate was in the order of 25.5 mm/yr. $^{210}Pb_{sup}$ (^{226}Ra) measured via its daughter ^{214}Pb yielded an apparent cyclicity, which could be related to annual layering and respective accumulation

rate in the order of 30 mm/yr. Thus, the core is considered to comprise deposits accumulated within the last decade (Figure S 6).

Geological units

Please use the following geological map of Hornsund fjord, Svalbard, by the polish academy of science created by Birkenmajer (1990):

http://geoinfo.amu.edu.pl/sgp/wgs04/01Hornsund/M%20geol%20Hornsundu-HI.jpg

It displays the outcropping geological units which supply the local fjord sediments by glacial erosion. They likely include low- to mid-grade coal seems, however, they are likely in minority and no outcrops are documented. Moreover, due to the extensive glacial cover in the study area, the subglacial geology may be only extrapolated from adjacent exposed areas further north.

Supplementary Table

Table S 1: Radiocarbon signature and respective ages of n-alkanes.

sample label	target comment	$F^{14}C$	±1σ	Age (^{14}C)	±1σ
HH14-897-GC-MF 0-3cm	*n*-C_{19}	0.016	0.006	33322	2675
HH14-897-GC-MF 0-3cm	*n*-C_{20}	0.006	0.005	40883	5038
HH14-897-GC-MF 0-3cm	*n*-C_{21}	0.010	0.006	36860	3774
HH14-897-GC-MF 0-3cm	*n*-C_{22}	0.006	0.007	40594	5885
HH14-897-GC-MF 0-3cm	*n*-$C_{26+28+30}$	0.017	0.005	32797	2050
HH14-897-GC-MF 0-3cm	*n*-$C_{27+29+31}$	0.051	0.005	23868	704
HH14-897-GC-MF 86-89cm	*n*-C_{19}	0.003	0.005	47332	8100
HH14-897-GC-MF 86-89cm	*n*-C_{20}	0.002	0.005	50688	10673
HH14-897-GC-MF 86-89cm	*n*-C_{21}	0.006	0.006	41041	5262
HH14-897-GC-MF 86-89cm	*n*-C_{22}	0.004	0.006	44650	7636
HH14-897-GC-MF 86-89cm	*n*-$C_{26+C28+C30}$	0.001	0.004	52331	10160
HH14-897-GC-MF 86-89cm	*n*-$C_{27+C29+C31}$	0.018	0.004	32387	1780
HH14-897-GC-MF 133-136cm	*n*-C_{19}	0.003	0.004	46486	6268
HH14-897-GC-MF 133-136cm	*n*-C_{20}	0.002	0.004	49049	7751
HH14-897-GC-MF 133-136cm	*n*-C_{21}	0.013	0.004	34871	2102
HH14-897-GC-MF 133-136cm	*n*-C_{22}	0.001	0.004	52805	11536
HH14-897-GC-MF 133-136cm	*n*-$C_{26+28+30}$	0.003	0.003	46920	6014
HH14-897-GC-MF 133-136cm	*n*-$C_{27+29+31}$	0.027	0.004	29063	1074

Table S 2: Core ID, location, water depth and associated cruise reports of the analyzed sediment cores.

Core ID	Latitude [N]	Longitude [E]	Water depth [m]	Reference
HH14-897-GC-MF	76°59.555’	016°24.313’	140	Forwick et al. (2014)
He519_2-3	76° 58,957'	015° 49,194'	202	Mark et al. (2018)
He560_26-2-K1	76° 59,520‘	016° 33,898‘	46	Mark (2020)

Supplementary Figures

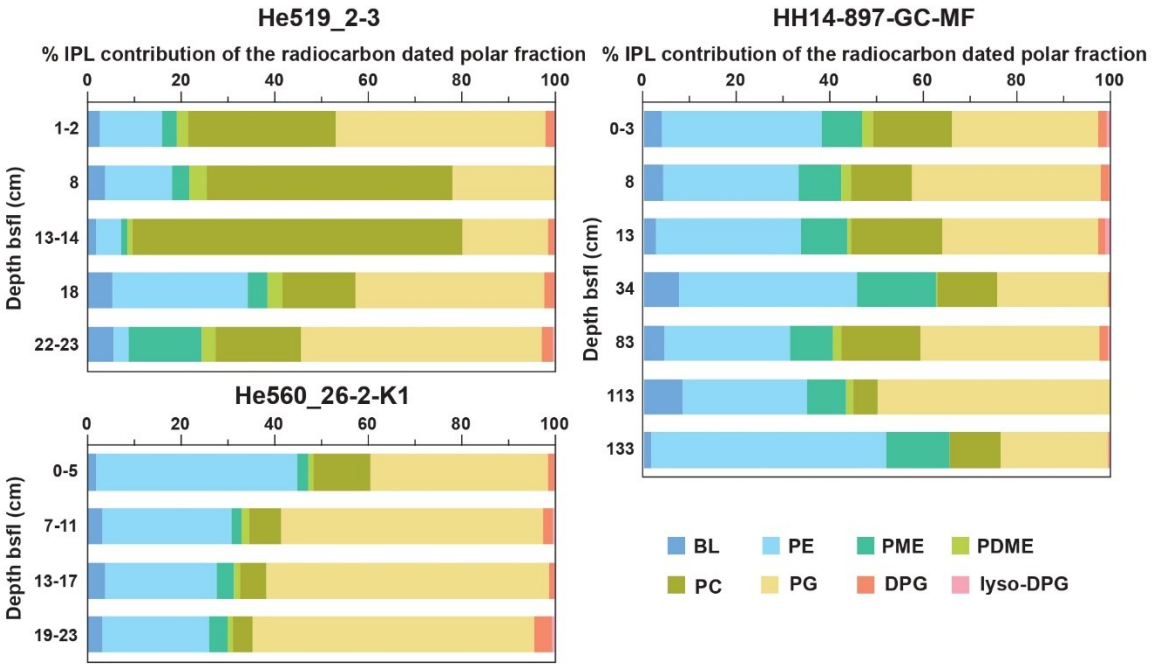

Figure S 1: Intact polar lipid distribution of the radiocarbon dated polar fraction with depth in the three analyzed cores. BL- betaine lipids, PE- phosphatidylethanolamine, PME- phosphatidyl-(N)-monomethylethanolamine, PDME- phosphatidyl-(N,N)-dimethylethanolamine (PDME), PC- phosphatidylcholine, PG- phosphatidylglycerol, DPG- diphosphatidylglycerol.

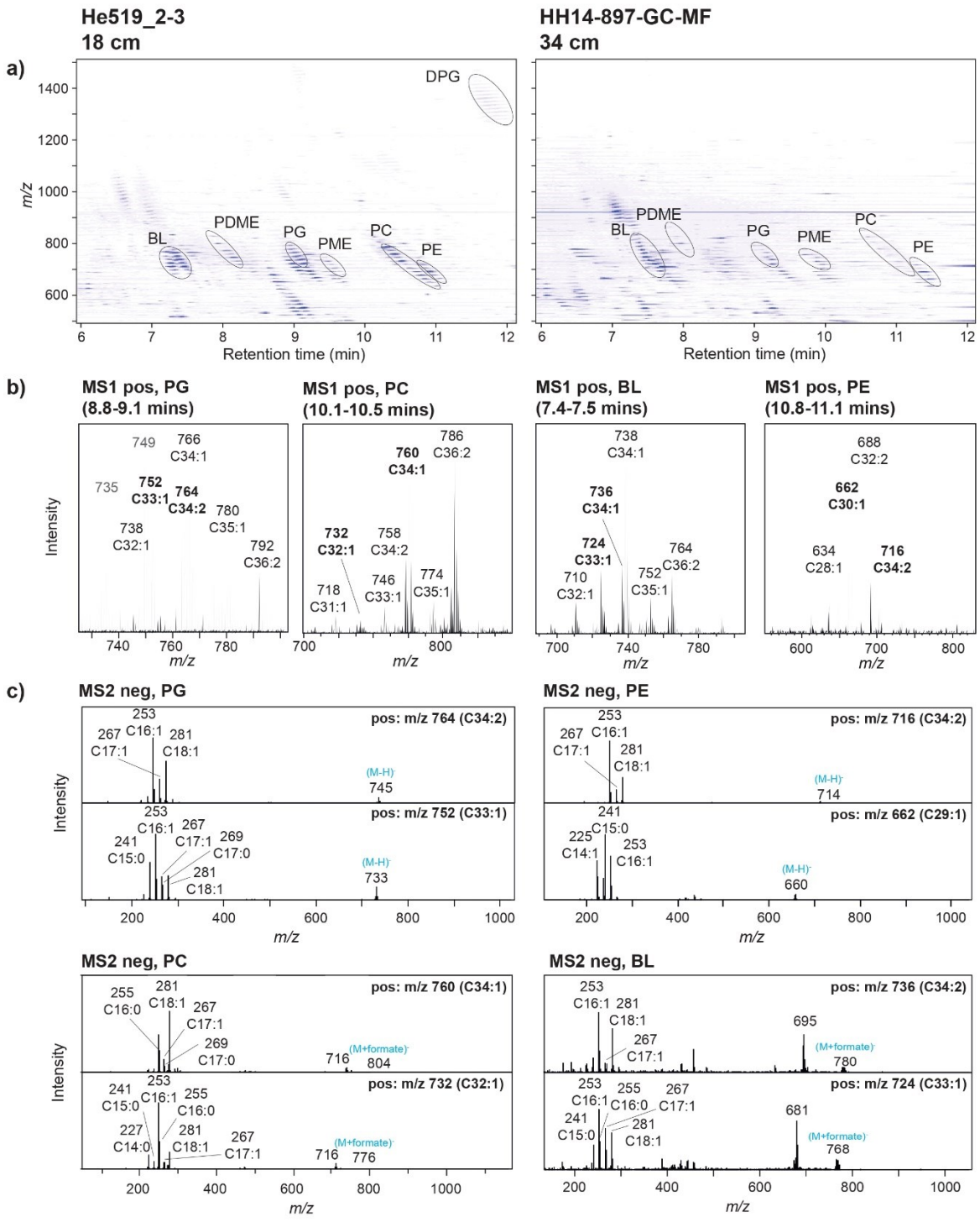

Figure S 2: a) Representative HPLC-MS chromatograms for the investigated sites depicted as heat maps showing the elution order of the detected phospholipids and amino lipids (zoom-in to retention time 6 to 12 min and m/z 550 to 1450) (for abbreviations see figure S 1). b) Distribution of molecular ions in the MS1 in positive mode with the corresponding combined fatty acid chain length for betaine lipids and the most abundant phospholipids. c) Representative negative mode MS2 fragmentation patterns of betaine lipids and phospholipids marked in bold in panel b) showing the presence of the radiocarbon dated $C_{16:1}$ and $C_{15:0}$ fatty acids in all of the polar lipids.

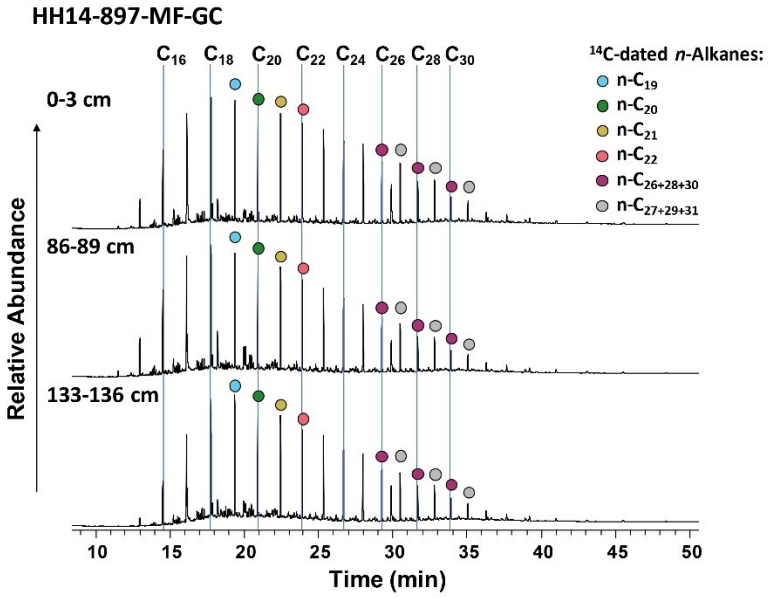

Figure S 3: Chromatograms for characteristic alkane distributions throughout the three cores displaying carbon preference index (CPI) values which indicate high (thermal) maturity (close to 1). The chromatograms shown here display the radiocarbon dated n-alkanes of the three depth intervals of sediment core HH14-897-GC-MF.

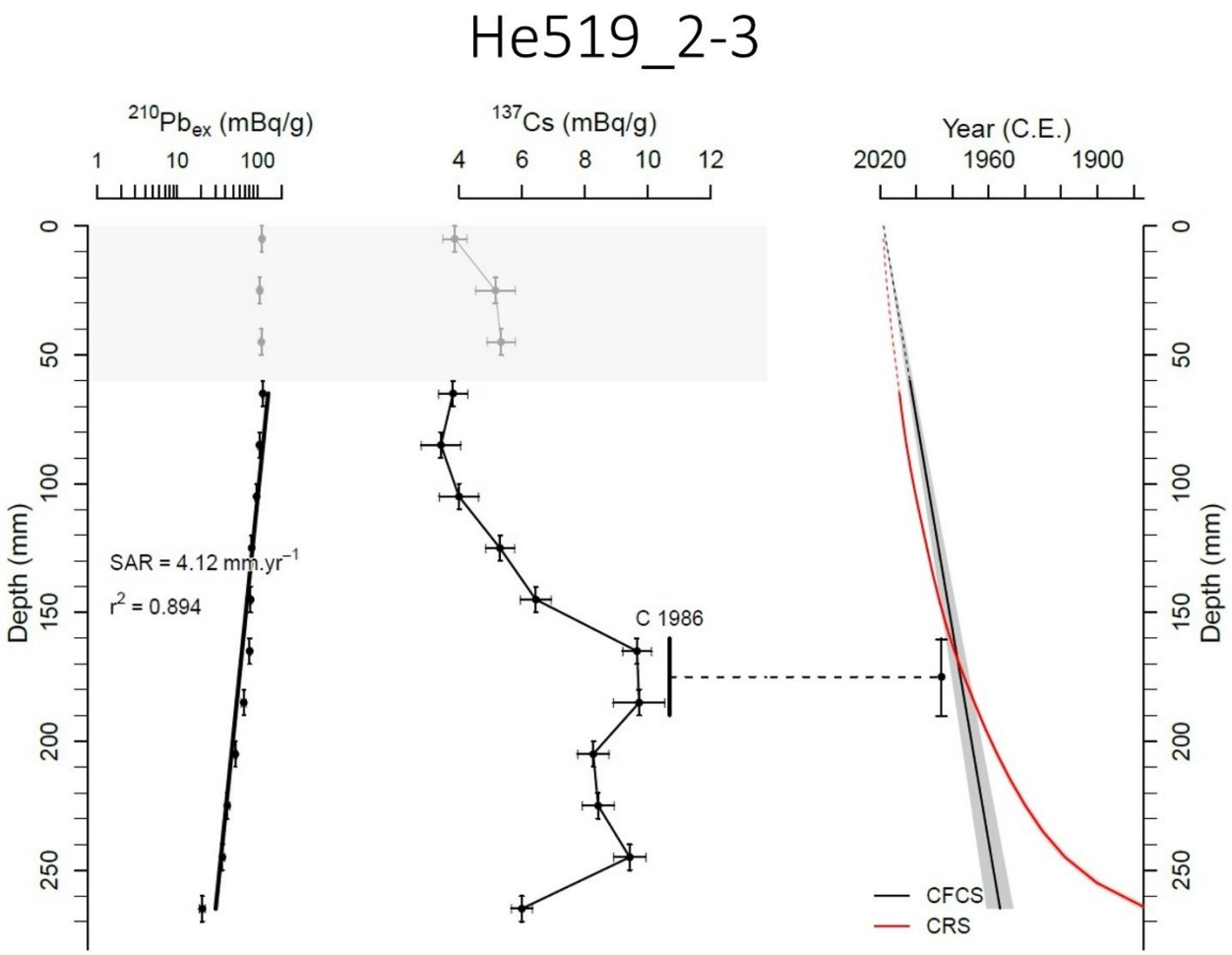

Figure S 4: Short-lived radionuclide measurements, and age depth model for He519_2-3 core. From left to right: $^{210}Pb_{ex}$ (semilogarithmic plot of excess ^{210}Pb), ^{137}Cs, the CFCS (constant flux constant sedimentation rate), and CRS (constant rate of supply) age models. SAR – sediment accumulation rate calculated with CFCS model, C 1986 – Chernobyl Nuclear Power Plant disaster in 1986. The surface mixed layer (SML) is in light gray (top 60 mm). Data are presented as mean values. The vertical error bars refer to analyzed sediment sample thickness, while the horizontal bars depict 1 SD uncertainties are based on decay counting statistics of individual samples (n=1) and include the error propagation from detector efficiency and background determinations. Uncertainties for the age model are calculated from the propagated 1 SD counting uncertainties of the individual samples. The uncertainty resulting from model assumptions is not considered by error bars, but by comparison of different age models. The figure was created in serac R package (Bruel & Sabatier, 2020).

HH14-897-GC-MF

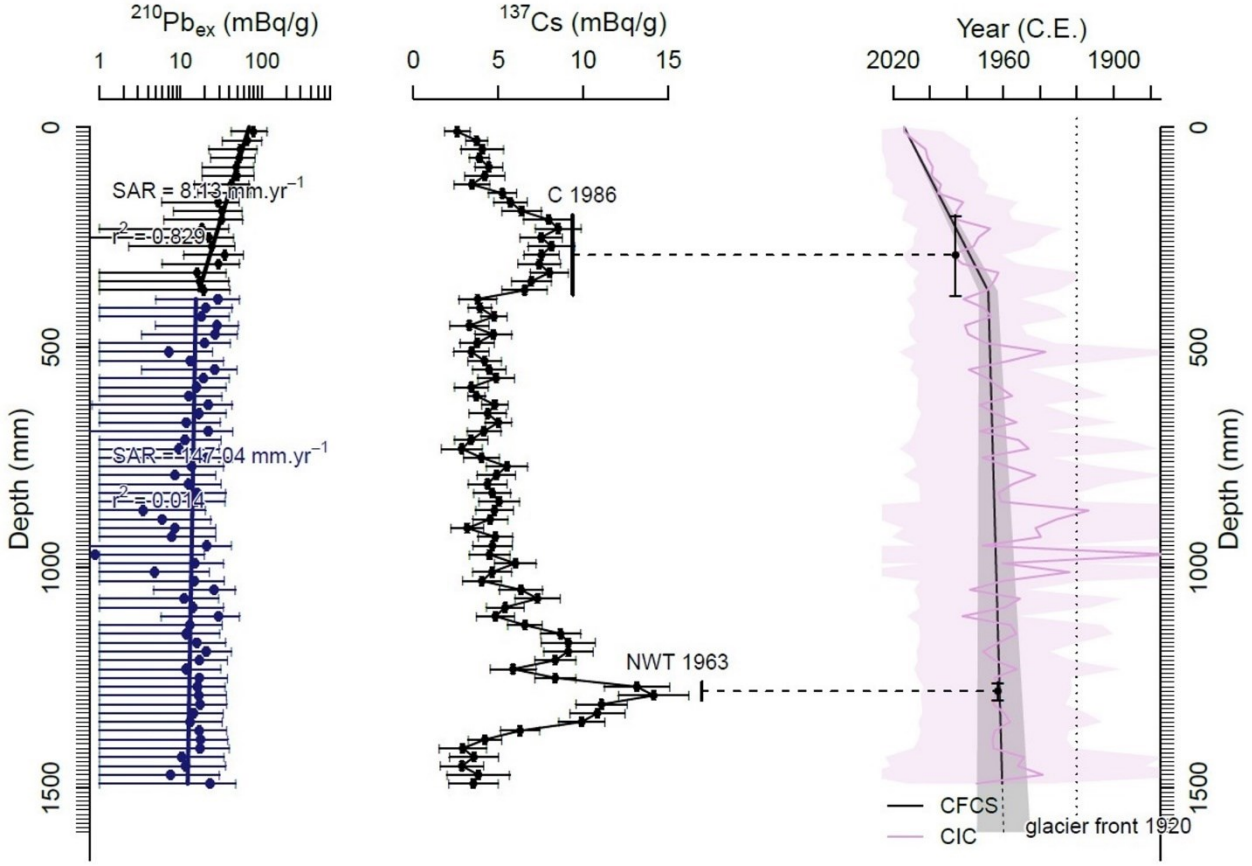

Figure S 5: Short-lived radionuclides measurements and age depth model for HH14-897-GC-MF core. From left to right: $^{210}Pb_{ex}$ (semilogarithmic plot of excess ^{210}Pb), ^{137}Cs, and the CFCS (constant flux constant sedimentation rate) with assumption of two periods of various accumulation rate, and CIC (constant initial concentration) age model. SAR – sediment accumulation rate calculated with CFCS model, C 1986 – Chernobyl Nuclear Power Plant disaster in 1986, NWT 1963 – Nuclear Weapon Tests fallout maximum in 1963. The coring site was deglaciated after 1920 (Błaszczyk et al., 2013)*. Data are presented as mean values. The vertical error bars refer to analyzed sediment sample thickness, while the horizontal bars depict 2 SD uncertainties are based on decay counting statistics of individual samples (n=1) and include the error propagation from detector efficiency and background determinations. Uncertainties for the age model are calculated from the propagated 2 SD counting uncertainties of the individual samples. The uncertainty resulting from model assumptions is not considered by error bars, but by comparison of different age models. The figure was created in serac R package* (Bruel & Sabatier, 2020)*.*

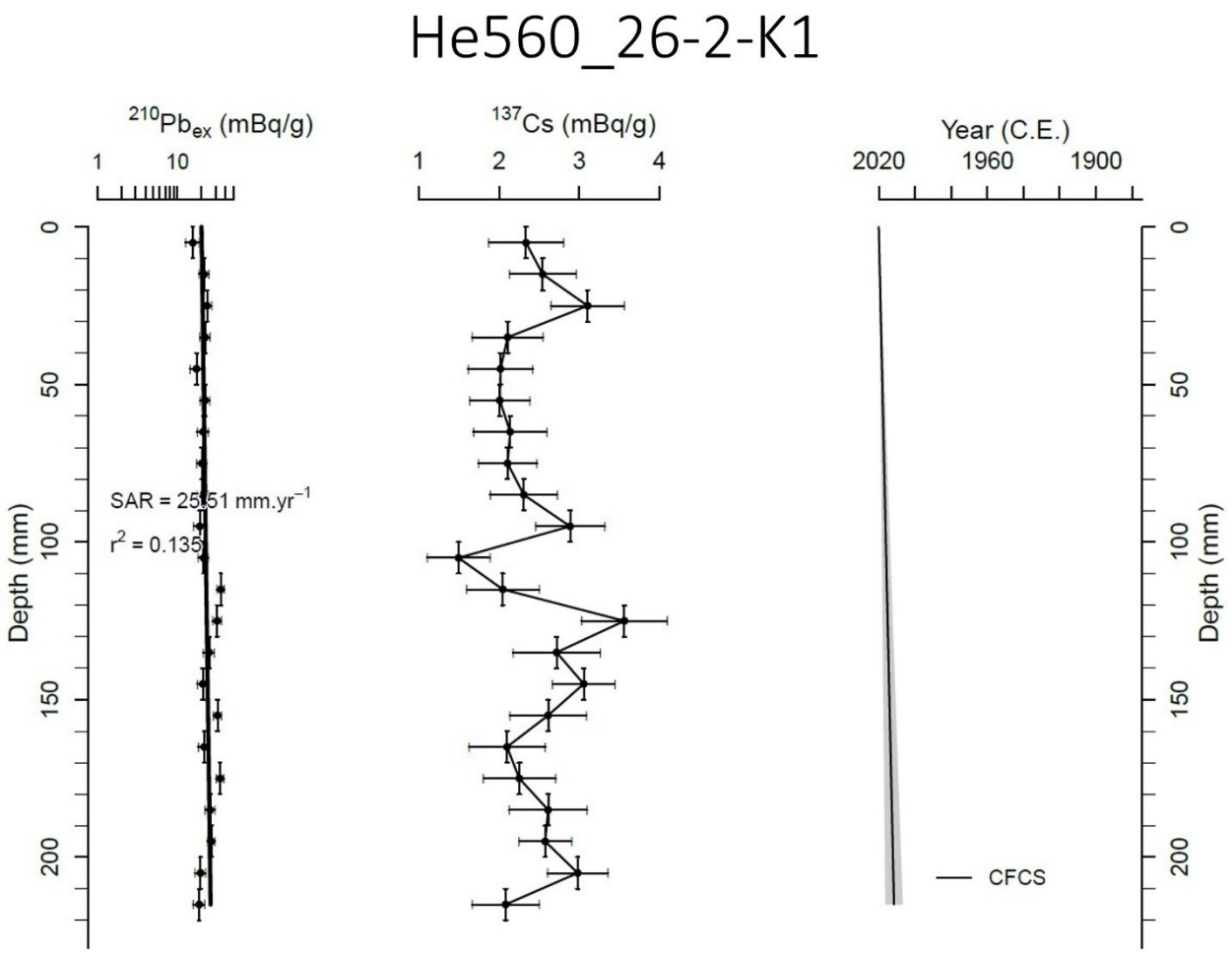

Figure S 6: Short-lived radionuclides measurements and age depth model for He560_26-2-K1 core. From left to right: $^{210}Pb_{ex}$ (semilogarithmic plot of excess ^{210}Pb), ^{137}Cs, and the CFCS (constant flux constant sedimentation rate) age model. SAR – sediment accumulation rate. Data are presented as mean values. The vertical error bars refer to analyzed sediment sample thickness, while the horizontal bars depict 1 SD uncertainties are based on decay counting statistics of individual samples (n=1) and include the error propagation from detector efficiency and background determinations. Uncertainties for the age model are calculated from the propagated 1 SD counting uncertainties of the individual samples. The uncertainty resulting from model assumptions is not considered by error bars, but by comparison of different age models. The figure was created in serac R package (Bruel & Sabatier, 2020).

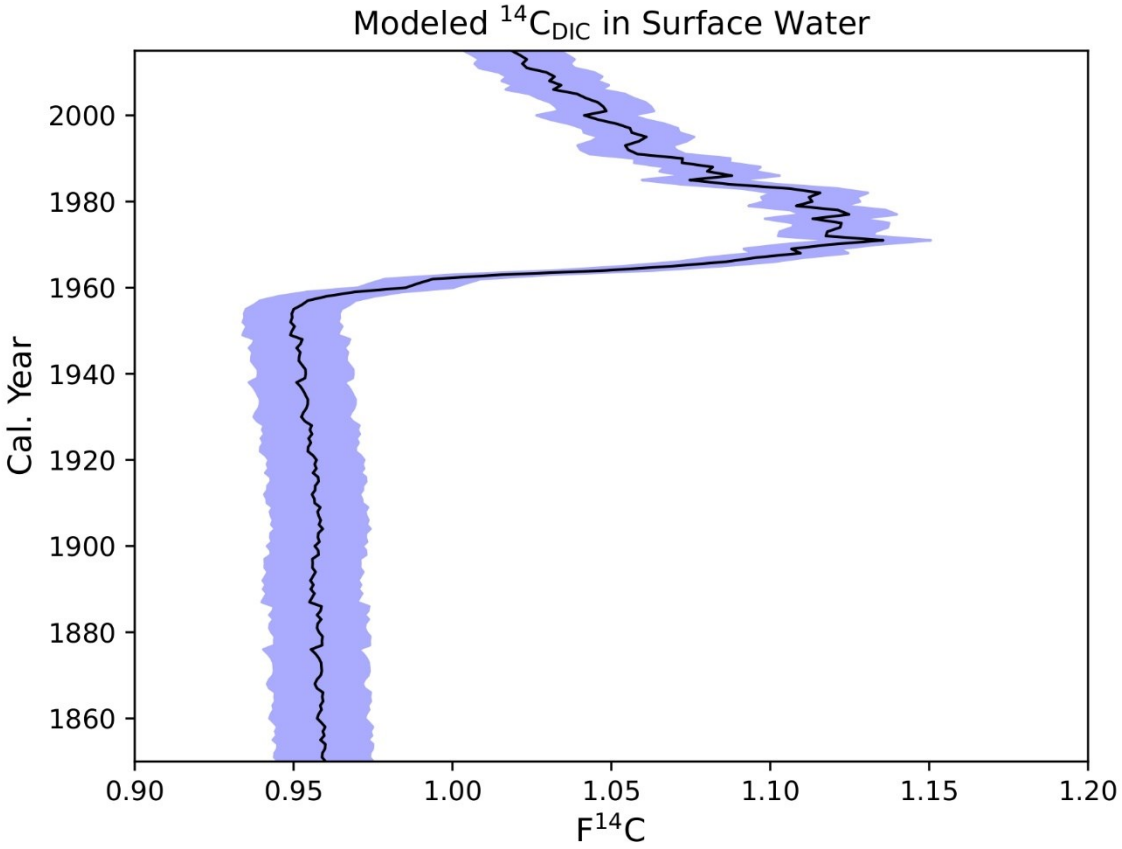

Figure S 7: History of dissolved inorganic radiocarbon ($F^{14}C$) near Hornsund according to a simulation with the FESOM2 model (see methods). Data are presented as mean values. Shading ($F^{14}C$ +-0.015) indicates the spatial variation of adjacent model results.

Manuscript 2

Release and microbial utilization of fossil carbon from eroding permafrost coastlines: fueling the short-term carbon cycle

Submitted: 7th July 2023 to Global Biogeochemical Cycles, AGU journal submission 2023GB007910

Authors

Manuel Ruben[1,2], Hannah Marchant[3,4], Matthias Wietz[1,4], Torben Gentz[1], Jens Strauss[5], Boris Koch[1,6], Gesine Mollenhauer[1,2,3]

Affiliation

[1] Alfred Wegener Institute Helmholtz Centre for Polar- and Marine Research, Am Handelshafen 12, 27570 Bremerhaven, Germany
[2] University of Bremen, Bibliothekstraße 1, 28359 Bremen, Germany
[3] MARUM - Center for Marine Environmental Sciences, University of Bremen, Leobener Straße 8, 28359 Bremen, Germany
[4] Max Planck Institute for Marine Microbiology, Celsiusstraße 1, 28359 Bremen, Germany
[5] Alfred Wegener Institute Helmholtz Centre for Polar- and Marine Research, Telegrafenberg A45, 14473 Potsdam, Germany
[6] University of Applied Sciences, An der Karlstadt 8, 27568 Bremerhaven, Germany

Abstract

The Arctic is experiencing rapid warming, causing increased erosion of coastal permafrost and the release of fossil organic carbon into the Arctic Ocean. This process likely not only contributes to climate change but also affects nutrient concentrations and the composition of microbial communities, highlighting the need to understand the fate of permafrost-derived carbon in this fragile ecosystem. During an incubation experiment lasting 85 days, 2.8±1.6% of organic carbon (OC) in sediments from coastal Yedoma permafrost was respired to CO_2. Radiocarbon analysis revealed that 88±15% of the released CO_2 had a fossil origin, indicating that degradation of permafrost OC reintroduces old carbon into the short-term carbon cycle. This suggests that permafrost climate feedback may be enhanced as coastal erosion accelerates in the coming decades. Additionally, 0.9±0.3% of Yedoma OC ended up as dissolved OC. In a natural setting, this dissolved OC will likely remain in the water column and be transported across the shelf, potentially undergoing further degradation. However, we also observed a net production of inorganic nitrogen during the incubation which could potentially provide a negative feedback by stimulating primary production. Bacterial community analysis indicated a succession of primary responders to labile substrates (e.g. *Psychrobacter* and *Colwellia*) followed by secondary consumers of semi-labile and semi-refractory substrates (e.g. *Maribacter* and *Pseudohongiella*), plus a potential

establishment of awakened permafrost-bacteria on particles. Overall, our data show that OC input from thawing permafrost boosts bacterial dynamics with expected effects on regional biogeochemical cycles and the Earth's climate.

Introduction

The Arctic is warming four times faster than the global average (Rantanen et al., 2022) due to a phenomenon known as Arctic amplification. Particularly since 2010, record high temperatures and sea-ice minima have been reported (Perovich et al., 2020). These changes have strongly impacted permafrost at the Arctic coastline as it is exposed to warmer air and soil temperatures as well as increased seawater temperature and wave erosion during the longer open water season (Lim et al., 2020). These processes accelerate the thaw of the stabilizing ground ice at coastal bluffs, maximizing erosion. Around 34% of the world's coastlines are Arctic permafrost coastlines (Lantuit et al., 2012), and of these 65% are unlithified coasts which have particularly high rates of erosion that are up to tens of meters annually (Fuchs et al., 2020; Irrgang et al., 2022; Martini & Wanless, 2014).

Coastal permafrost stores substantial amounts of organic matter, and Arctic coastal erosion is estimated to supply 15.4 TgC and 1.6 TgN annually to the Arctic Ocean (Terhaar et al., 2021). This could potentially increase by an order of magnitude in the coming decades (Wagner et al., 2011). Furthermore, the hydrological cycle is expected to continue intensifying well into the 21st century, mobilizing additional organic carbon (OC) from permafrost soils and peat (B M Jones et al., 2020; Mann et al., 2022) and increasing its transfer into the ocean. Much of this carbon is of fossil origin, such as the massive Pleistocene age Yedoma deposit that contains carbon fixed into organic matter >20 000 years ago (Strauss et al., 2017). While fossil OC in other environments is often extremely recalcitrant (as it has undergone and survived previous cycles of degradation), this is not the case for many permafrost soils, in which degradation is inhibited due to temperatures close to or below freezing (Guillemette et al., 2017). Therefore, upon reaching the near-shore Arctic Ocean, formerly freeze-locked OC has the potential to be degraded by microbial communities. In contrast to degradation of freshly synthesized OC, which has a quasi-net-zero effect on the carbon budget, the degradation of fossil OC adds additional carbon to the short-term carbon cycle (Guillemette et al., 2017; Lenton et al., 2019), enhancing permafrost carbon feedback and anthropogenic climate change (IPCC, 2019; Miner et al., 2022; Schuur et al., 2022). Furthermore, the erosion and thaw of coastal permafrost can affect nutrient concentrations, with 28-51% of the annual net primary production in the Arctic Ocean attributed to riverine input and coastal erosion. Therefore, increasing permafrost erosion in a warming climate will likely alter the local food web, as well

as impact global greenhouse gas (GHG) concentrations (Terhaar et al., 2021). It is thus critical to understand the fate of permafrost-derived OC after its release into the Arctic Ocean. The Yedoma domain covers 2,587,000 km^2 with approximately 500,000 km^2 Yedoma deposits at the surface (Strauss et al. 2021) containing around 130 gigatons of organic carbon and 20 gigatons of nitrogen which accumulated during the late Pleistocene (Strauss et al., 2022). Due to their high ice-content Yedoma is particularly vulnerable to thaw and erosion, which is particularly concerning as the organic matter froze shortly after deposition and is therefore well preserved and potentially highly labile (Kanevskiy et al., 2016). As Yedoma is a potential element towards a climatic tipping point (Lenton et al., 2019), it is essential to understand the mechanisms that contribute carbon release from this environment.

Incubation experiments with permafrost soil have been used to investigate terrestrial and freshwater carbon dynamics, assessing both the amount of GHGs produced (Knoblauch et al. 2013; Vonk et al. 2015) as well as the age of the respired OC (Dutta et al., 2006; Schuur et al., 2009). However, despite the high vulnerability of coastal permafrost soils, less attention has been given to the fate of permafrost soils reaching the Arctic Ocean via erosion. To our knowledge, only the studies of Tanski et al. (2019; 2021) have investigated permafrost soil degradation in the ocean, demonstrating a threefold higher CO_2 release from old compared to younger permafrost soils (Tanski et al., 2021). Microbial OC degradation can be carried out by both the ambient seawater community (Vonk et al. 2013) as well as by "awakened" permafrost microbes, both of which are coincident with rapid shifts in taxonomy, function and activity (Ernakovich et al., 2022; Hultman et al., 2015; Mackelprang et al., 2016, 2017; Scheel et al., 2022). A number of taxa have been suggested to respond to terrestrial and permafrost-derived OC, including *Colwellia* and *Polaribacter* (Sipler et al., 2017). However, few systematic linkages between biogeochemical and biological dynamics are yet established, especially considering OC age.

In this study we incubated Yedoma deposit in Arctic seawater for 85 days. Throughout the incubation experiment we quantified turnover of the carbon pool, and for the first time, determined the age of microbially respired material by radiocarbon age measurements, thereby assessing its potential as fossil carbon source in a warming climate. We gained further insights into the impact of Yedoma erosion by quantifying changes in nutrient availability in the seawater, and following the dynamics of marine- and permafrost-derived bacterial communities during organic matter degradation.

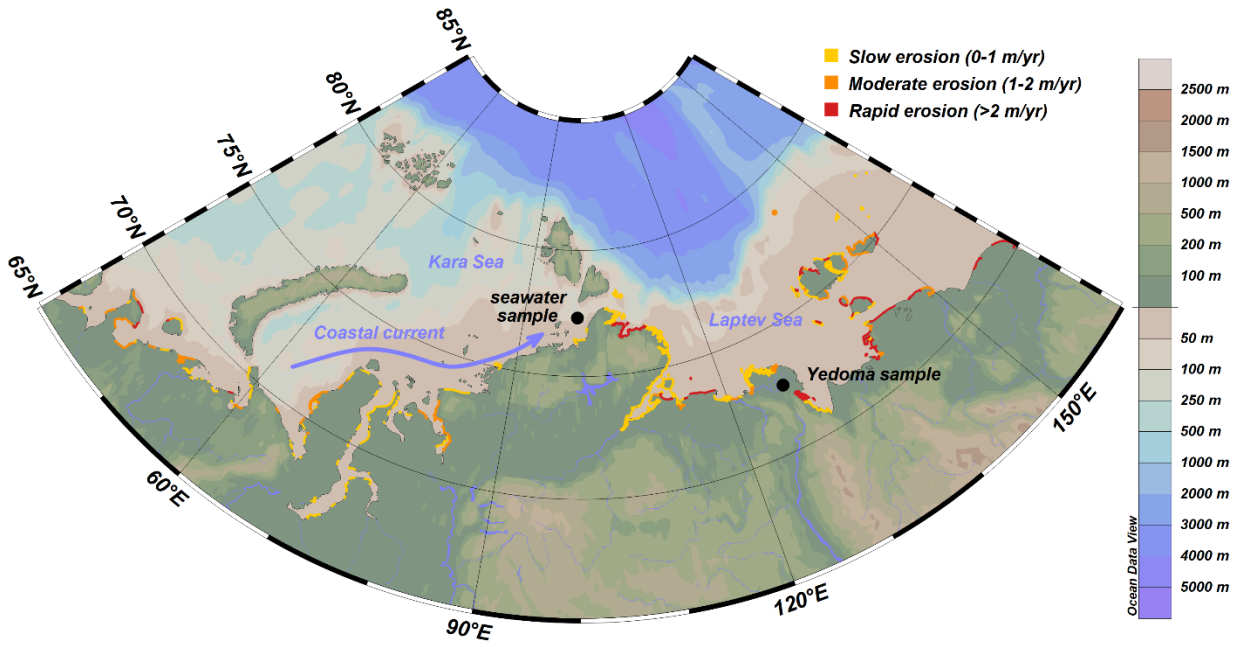

Figure 9: Sample locations of seawater and Yedoma permafrost. Erosion rates of permafrost underlain coastlines are indicated (based on Lantuit et al. 2020*).*

Methods

Experimental set-up

To simulate the effects of Arctic coastal permafrost soil erosion and subsequent supply of organic matter to the ocean in one summer season, Yedoma was incubated in Arctic Ocean water at 2°C for 85 days in the dark. The Yedoma was collected in the Lena Delta at a freshly dug vertical soil profile at Sobo Sise (Strauss et al. 2021; Fuchs et al. 2021; Latitude: 72.53743 N; Longitude: 128.28635 E; Figure 9) during the CACOON field campaign in 2019 (Fuchs et al., 2021). Samples were drilled at the bottom of the eroding river banks every 20 cm and kept frozen (Figure S 8; Fuchs et al. 2021). Four subsamples (13.75-14.35 m below coastal bluff surface) were thawed at 2°C immediately prior to the beginning of the experiment and homogenized using a glass stirrer to form a slurry. The homogenized slurry had a total organic carbon (TOC) content of 1.2±0.2 dry-wt% (n=6), with $\delta^{13}C$ of -25.4±0.3‰ (n=6), and $F^{14}C$ of 0.0071±0.0019 corresponding to 39,928±767 ^{14}C yrs (n=3). Total nitrogen (TN) was below detection limit of 0.1 dry wt% (n=6). As we did not have access to a location in the Laptev Sea adjacent to the Lena Delta, seawater was collected from the bottom layer in the south-eastern Kara Sea (Latitude: 77.18703 N; Longitude: 100.32823 E; Figure 9; 104m water depth) using a Niskin bottle attached to the CTC rosette on board the R/V Akademik Tryoshnikov during the Arctic Century Expedition in September 2021. The sampling location is considered to be appropriate, as Yedoma erosion rates near the sampling site are considerable, with up

to 2m of coast line lost annually (Aleksyutina et al., 2020; Lantuit et al., 2012). Hence, we expect ambient microbial communities to regularly encounter permafrost-derived substrates, allowing a realistic assessment of permafrost OC fate through microbial degradation. The water was transferred into an acid-cleaned (10% HCl) 10L HDPE jerry can and stored at 4°C in the dark until the start of the experiment. To account for possible microbial community shifts during seawater storage (62 days), samples for DNA analysis were taken on 31st of August 2021 immediately after sample collection and on 2nd of November 2021 (before starting the experiment).

For the experimental setup, 3 mL slurry and 90 mL of seawater each were transferred into 116 mL glass bottles, which were sealed with butyl stoppers. To prevent contamination, all glassware was combusted at 450°C for 3 hours. Butyl stoppers were sterilized and cleaned by boiling successively in Milli-Q water (Merk IQ 7000), 0.3 M oxalic acid, 0.1 M NaOH, and three more times in Milli-Q water.

The experiment consisted of three main treatments (Figure 10): 1) Yedoma slurry and unfiltered seawater (SW+YE; 20 vials), 2) Yedoma slurry and seawater filtered through a 0.2 µm PES filter (fSW+YE; 6 vials), and 3) control vials containing only filtered seawater (fSW; 6 vials). For each of these treatments further "monitoring" vials were set up, containing optode spots (PyroScience) to monitor *in situ* oxygen concentrations and pH. The latter vials were not used for radiocarbon analysis due to unknown carbon contamination introduced from the optode or the glue. After sealing the vials, the 23 mL headspace was ventilated with CO_2-free air to remove atmospheric CO_2, to prevent any unknown ^{14}C carryover from the atmosphere.

Vials were incubated at ~2°C in the dark. In order to simulate recurring cycles of deposition and remobilization by wave and tidal movements, as well as to prevent the formation of anoxic pockets in the sediment due to limited diffusion, vials were placed on a shaker table which was activated daily for 15 minutes at 100 rounds per minute. The thickness of slurry layers at the bottom of vials never exceeded 2 mm.

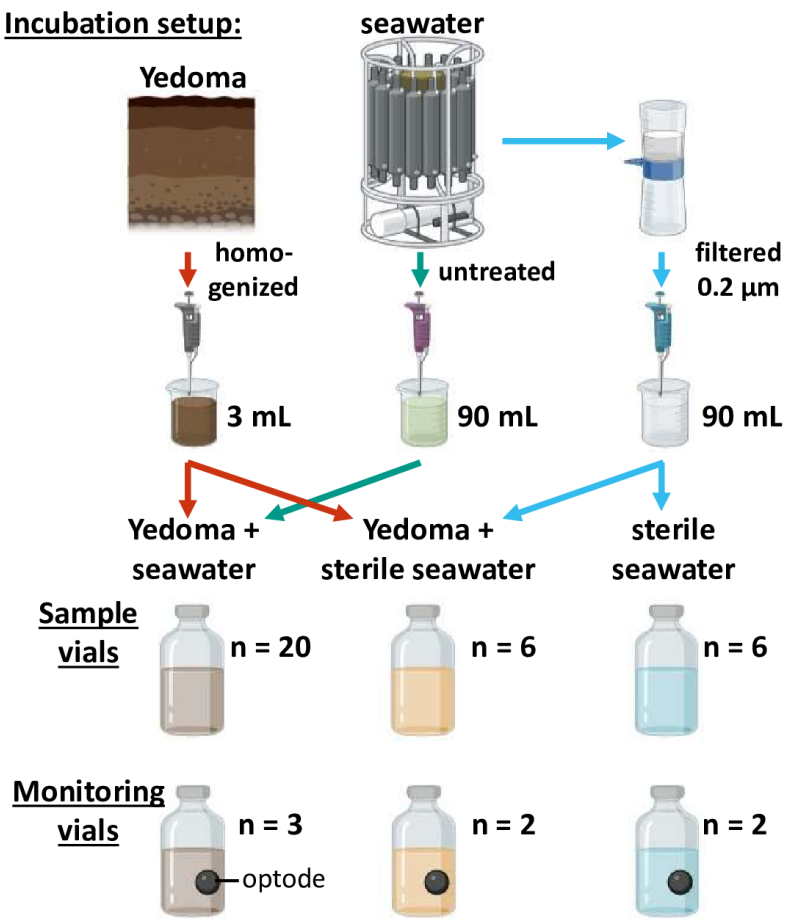

Figure 10: Experimental setup for both sample- and monitoring-vials, displaying quantities of Yedoma slurry, (filtered) seawater, and number of replicates. Monitoring vials include additional optodes for in-situ pH and O_2 measurements. Figure has been created using BioRender.com.

Sampling

All vials were sampled in the same manner over the 85-day long experiment. Sampling was carried out every two days over the first two weeks, every third day in week 3-4, once a week in week 5-8, and approximately every second week within the last month. This resulted in a total of 19 sampling event (day 0-85; Table 1).

At every sampling event, a 2 mL aliquot for analyses of dissolved inorganic carbon (DIC) concentration and radiocarbon content ($F^{14}C$) was taken from every incubation vial using a syringe and needle. Samples were transferred into 2 mL glass vials with Teflon septa and without headspaces, poisoned with 10 µL saturated $HgCl_2$ solution, and stored at 4°C in the dark. After sampling, the headspace of incubation vials was gently ventilated with CO_2-free synthetic air for 3 minutes. To ensure sufficient ventilation, at least one of every five simultaneously ventilated headspaces was checked for residual CO_2 by collecting the removed gas

during the last ~30 seconds of ventilation into a 110 mL syringe and subsequent measurement of CO_2 concentrations by cavity ring down spectroscopy in a Greenhouse Gas Analyzer (ABB - Los Gatos Research). All measurements were below 30 ppm and thus below or near detection limit. At all sampling events pH and O_2 concentrations were determined in the monitoring vials using the glued-in optodes. Further, temperature was measured in a reference vial.

Table 1: Sampling intervals and parameters measured per sampling event in seawater+Yedoma treatments.

time [days]	monitoring vials	all vials	water vol [mL]	head space vol [mL]	sacrificed bottles (quantity)
0	O_2+pH	1xDIC	93	23	DOC, TDN, nutrients, ions, DNA, solid phase (3x)
2	O_2+pH	1xDIC	91	25	---
4	O_2+pH	1xDIC	89	27	DOC, TDN, nutrients, ions, DNA, solid phase (1x)
6	O_2+pH	1xDIC	87	29	---
8	O_2+pH	1xDIC	85	31	DOC, TDN, nutrients, ions, DNA, solid phase (1x)
10	O_2+pH	1xDIC	83	33	---
12	O_2+pH	1xDIC	81	35	DOC, TDN, nutrients, ions, DNA, solid phase (3x)
14	O_2+pH	1xDIC	79	37	---
17	O_2+pH	1xDIC	77	39	DOC, TDN, nutrients, ions, DNA, solid phase (1x)
20	O_2+pH	1xDIC	75	41	---
23	O_2+pH	1xDIC	73	43	DOC, TDN, nutrients, ions, DNA, solid phase (1x)
26	O_2+pH	1xDIC	71	45	---
29	O_2+pH	1xDIC	69	47	DOC, TDN, nutrients, ions, DNA, solid phase (3x)
36	O_2+pH	1xDIC	67	49	---
43	O_2+pH	1xDIC	65	51	DOC, TDN, nutrients, ions, DNA, solid phase (1x)
50	O_2+pH	1xDIC	63	53	---
57	O_2+pH	1xDIC	61	55	DOC, TDN, nutrients, ions, DNA, solid phase (1x)
71	O_2+pH	2xDIC	59	57	DOC, TDN, nutrients, ions, DNA, solid phase (1x)
85	O_2+pH	2xDIC	55	61	DOC, TDN, nutrients, ions, DNA, solid phase (4x)

At every second sampling event, one to four SW+YE vials were sacrificed in order to measure dissolved organic carbon (DOC), total dissolved nitrogen (TDN), DNA, ions (SO_4^{2-} & Cl^-) and nutrients. The same was done for fSW+YE and fSW at every fourth sampling event.

For all sacrificed bottles the remaining water phase (ranging from 91 mL on day 0 to 51 mL on day 85) was pipetted out of the vials and filtered through Milli-Q rinsed (200mL) 0.2µm polycarbonate filters (Pall Corporation). DNA was extracted from filters using the PowerWater kit (QIAGEN, Germany) according to the manufacturer's instructions. The filtrate was subsampled in three fractions for quantifying ions (SO_4^{2+} and Cl^-), nutrients, and DOC plus TDN by transferring 2 mL, 8 mL, and the remaining fluid into separate vials, respectively. Of the remaining solid phase, about 0.5 g was transferred to PowerSoil tubes for DNA extraction using the PowerSoil Kit (QIAGEN, Germany) according to the manufacturer's instructions. The rest was transferred into separate glass vials for freeze-drying. All samples were frozen immediately after sampling at -20°C, with the exception of ion and DIC which were stored at 4°C.

Aqueous phase parameters

Concentrations of DIC, phosphate, ammonia, nitrite, and nitrate (virtual channel: NO_x-NO_2) were spectrophotometrically determined using a high performance microflow analyzer QuAAtro39 (SEAL analytics). All samples were measured in technical duplicates, quantified with a five-point calibration, and automatically drift-corrected. Analytical precision was determined for phosphate (>96%), ammonia (82%), nitrite (>96%), nitrate (>99%), and DIC (>99%) using reference materials.

The radiocarbon signature of the DIC fraction was obtained by direct CO_2 gas measurements. The 2 mL $HgCl_2$ poisoned samples were transferred with gas-tight syringes (flushed with N_2 gas) to 12 mL vials flushed with He (12 minutes at 80 mL/min), and CO_2 was transferred to the Gas Interface System (Wacker et al., 2013) coupled with the MICADAS accelerator mass spectrometer system (Synal et al., 2007) at Alfred Wegener Institute, which was used for radiocarbon measurements.

Sulfate and chloride concentrations were quantified by ion chromatography in a 1:100 dilution using a Metrohm 930 compact IC flex equipped with a pre-column (Metrosep A Supp 5-Guard/4.0) and an anion-column (Metrosep A Supp 5-150/4.0). Recovery rates for both sulfate and chloride exceeded >98%, with a precision of >99.5%.

DOM and TDN concentrations were determined by high temperature catalytic oxidation (HTCO) and subsequent nondispersive infrared spectroscopy and chemiluminescence detection (TOC-$L_{CPH/CPN}$ analyzer, Shimadzu). Samples were acidified (1 M HCl, Merck) and purged with O_2 for > 5 min to remove inorganic carbon. All measurements were performed as triplicates of 50 µL injected directly into the 680°C catalyst. If standard deviation exceeded 1%, two additional samples were analyzed and outliers excluded. The limit of detection was 7 µM for DOC and 11 µM for TDN, with a precision of ±5 %.

Solid phase parameters

Solid phase samples were freeze-dried and homogenized using spatula before analysis. The untreated Yedoma deposits were analyzed for bulk TOC following the protocols of Werner et al. (2001) and Brodie et al. (2011) using a continuous-flow elemental analyzer - isotope ratio mass spectrometer (Thermo Finnigan Flash EA 2000 coupled to a Delta V Plus isotope ratio mass spectrometer). TOC aliquots were decarbonated with 10% HCl prior to analysis. The incubated solid phase remains were analyzed for bulk TOC on a carbon-sulfur analyzer (CS-800, Eltra), using 0.1 g sediment after inorganic carbon removal with 500 µL 12 N HCl.

Radiocarbon measurements were performed by accelerator mass spectrometry using the MICADAS system. Solid phase samples were acidified 3 times with 6M HCl to remove inorganic carbon. Radiocarbon dating was performed on 1 mgC graphite targets. Sample treatment and blank determination was performed following the protocols by (Mollenhauer et al., 2021).

Carbon budget calculations

CO_2 headspace concentration and carbon budget calculations were performed under the assumption that CO_2 and DIC concentrations and their ^{14}C isotopic composition are in equilibrium within headspace and water, respectively (details in supplement).

In order to account for both the present DIC and the removed DIC and CO_2 (details in supplement), the cumulative concentration of DIC+CO_2 (ccDC) was calculated for each sampling event (t_n). For this purpose, the sum of removed CO_2 in the headspace ($c(CO_2)_{ventilation}$) via ventilation and DIC removed within the water samples taken ($c(DIC)_{sample\ taken}$) was added to the concentration of DIC ($c(DIC)_{tn}$) and CO_2 ($c(CO_2)_{tn}$; dissolved and in headspace) at the separate sampling event:

$$cc(DC)_{tn} = c(DIC)_{tn} + c(CO_2)_{tn} + \sum_{t0}^{tn-1} c(CO_2)_{ventilation} + c(DIC)_{sample\ taken}$$

Assuming that the seawater used for the incubation was in equilibrium with the atmosphere and therefore saturated in CO_2, we calculated the released CO_2 from the difference between cc(DC) on a t_n and on day 0:

$$c(CO_2)_{release} = cc(DC)_{increase} = cc(DC)_{tn} - cc(DC)_0$$

Subsequently, the mass of the released CO_2 ($gCO_{2\ release}$) was calculated by multiplying the atomic mass of CO_2 (~44 $g*mol^{-1}$) and the moles of CO_2 released:

$$gCO_{2\,release} = c(CO_2)_{release} * 44\frac{g}{mol}$$

To assess the percentage of TOC respired (%$TOC_{respired}$) during incubation, $cCO_{2\,release}$ multiplied by the atomic mass of carbon (12 g*mol^{-1}), was divided by the Yedoma OC added to the incubation vials, accounting for the mass of Yedoma dry weight added (m_{Yedoma}) and its TOC content (%TOC) determined:

$$\%\mathrm{TOC}_{\mathrm{respired}} = (cCO_{2\,release} * 12\frac{g}{mol})/(m_{Yedoma} * \%TOC)$$

In order to derive the radiocarbon signature of the produced DIC and CO_2, a similar approach was taken. The cumulative $F^{14}C$ signature ($cF^{14}C$) was calculated for the individual t_n, assuming DIC and CO_2 to be in equilibrium. In this case, it can be assumed that the removed CO_2 has the same $F^{14}C$ signature as measured in the DIC:

$$cF^{14}C(DC)_{tn} = [c(DIC)_{tn} * F^{14}C(DIC)_{tn} + \sum_{day\,0}^{tn-1}\{c(DIC)_{sample\,taken} * F^{14}C(CO_2)_{head\,space} + c(DIC)_{sample\,taken} * F^{14}C(DIC)_{sample\,taken}\}] \,/\, cc(DC)_{tn}$$

The $F^{14}C$ signature of the released DIC+CO_2 ($F^{14}C(DC)_{release}$) at a given t_n was determined using an isotope mass balance, using the values of the initial $c(DIC)_{day\,0}$ and its $F^{14}C_{day\,0}$ as well the $cc(DC)_{tn}$ and its $cF^{14}C(DC)_{tn}$:

$$cc(DC)_{tn} * cF^{14}C(DC)_{tn} = c(DIC)_{day\,0} * F^{14}C(DIC)_{day\,0} + c(DC)_{release} * F^{14}C(DC)_{release}$$

$$F^{14}C(DC)_{release} = \frac{cc(DC)_{tn} * cF^{14}C(DC)_{tn} - c(DIC)_{day\,0} * F^{14}C(DIC)_{day\,0}}{c(DC)_{release}}$$

Further, using a second isotope mass balance, the percentage of Yedoma carbon contributing to the released CO_2 (%$CO_{2\,Yedoma}$) was determined from the bulk radiocarbon signature of Yedoma ($F^{14}C_{Yedoma}$) and the initial $F^{14}C$ $DIC_{day\,0}$:

$$\%CO_{2\,Yedoma} = \frac{[F^{14}C(DC)_{release} - F^{14}C_{Yedoma}]}{[F^{14}C(DIC)_{day\,0} - F^{14}C_{Yedoma}]} * 100$$

Cumulative concentrations of nutrients, DOC, and TDN

During sampling, 2 mL subsamples of the liquid phase were repeatedly removed, thus the contents of DOC, TDN, nutrients, and ions in those subsamples (c_{tn}) had to be accounted to not overestimate production with decreasing water content of the incubation vials. Hence, cumulative concentrations (cc)

were calculated for the individual t_n, including the removed quantities of the previous sampling events at current concentrations:

$$cc = c_{tn} * V_{W\,tn} + \sum_{day\,0}^{tn-1} c_{tn} * 2\,mL$$

Uncertainty propagation

The uncertainties (σ) of the calculated values for cumulative DIC+CO_2 concentration, their respective $F^{14}C$ signatures, released gCO_2/gTOC, released CO_2 $F^{14}C$ signature, %TOC respired, and %fossil of released CO_2 were determined by propagation of the individual errors associated with DIC concentration, pH, salinity, TOC, and $F^{14}C$. The errors associated with temperature and pressure variations were assumed to be negligible (see supplement). Consistency between replicates was assessed via DIC concentrations and its $F^{14}C$ signature, as discussed in the supplement and Figure S 9.

Bacterial community analysis

Bacterial community composition was determined via 16S rRNA gene amplicon sequencing. Extracted DNA was quantified using Quantus (Promega, Madison, WI), followed by amplification of 16S rRNA gene fragments using primers 515F (GTGYCAGCMGCCGCGGTAA) and 926R (CCGYCAATTYMTTTRAGTTT) (Parada et al., 2016). Libraries were prepared and sequenced according to the 16S Metagenomic Sequencing Library Preparation protocol (Illumina, San Diego, CA) using MiSeq technology in 2x300bp paired-end runs. After primer removal using cutadapt (Magoč & Salzberg, 2011), reads were processed into amplicon sequence variants (ASVs) using DADA2 v1.18.1 (Callahan et al., 2016) with filtering settings truncLen = c(250, 180), maxN = 0, minQ = 2, maxEE = c(3,3), and truncQ = 0, followed by merging using minOverlap=15 and chimera removal. After singleton removal, we obtained on average 127,000 rRNA reads per sample that sufficiently covered community composition (Figure S 9). ASVs were taxonomically classified using the Silva v138.1 database (Quast et al., 2013). Data were processed and visualized using R packages tidyverse, phyloseq, ampvis2 and fishualize (Wickham et al. 2019; R Core Team 2013; Schiettekatte et al. 2019; Andersen et al. 2018). Read counts from negative PCR controls were subtracted from every sample to minimize false-positive results from potential contamination. Furthermore, we focus on patterns not occurring in the fSW to avoid potential bottle effects or other artifacts. For instance, SAR11 abundant in the original seawater was also detected in the fSW, indicating that some smaller cells evaded filtration. Since most other taxa showed markedly higher abundances in the actual treatments, observed patterns in those are likely linked to permafrost degradation.

Results

DIC, CO_2 and its radiocarbon signature

The cumulative concentrations of DIC+CO_2 were very similar in both SW+YE and fSW+YE, increasing from ~18.6 to ~26 µmol/L, corresponding to an increase of about 40% (Figure 12). In contrast, fSW showed a much lower increase from 18.82±0.82 µmol/L to 20.89 ±1.79 µmol/L, showing an increase of about 11%. In SW+YE the rapid release within the first 14 days accounted for 2.6±0.3 µmol DIC day^{-1} (a total 36.0±2.2 µmol DIC released) compared to 0.6±0.4 µmol DIC day^{-1} from day 14 to 85 (a total 44.4±5.0 µmol DIC released). Normalized to the gTOC added with the Yedoma slurry, the production accounts for 1047±30 µmol DIC * $gTOC^{-1}$ between day 0 and 14, and 2340±253 µmol DIC * $gTOC^{-1}$ during the entire 85 days (Figure 11).

While fSW showed an increase in the cumulative DIC+CO_2 budget over the 85 days of incubation, its radiocarbon signature remained stable, ranging from 1.027±0.057 to 1.067±0.132 with an average of 1.042±0.095. By contrast, both SW+YE and fSW+YE showed a negative offset in the $F^{14}C$ signature to fSW on day 0 of 0.069 and 0.056, respectively. In fSW+YE $F^{14}C$ values dropped rapidly within the first two weeks from 1.006±0.039 to 0.859±0.170, with a continuing but slower decrease to 0.838±0.291 on day 85. Similarly, SW+YE showed a slightly stronger decrease in $F^{14}C$ of DIC in the first two weeks from 0.993±0.037 to 0.831±0.106, followed by a slower decrease to 0.755±0.153 on day 85.

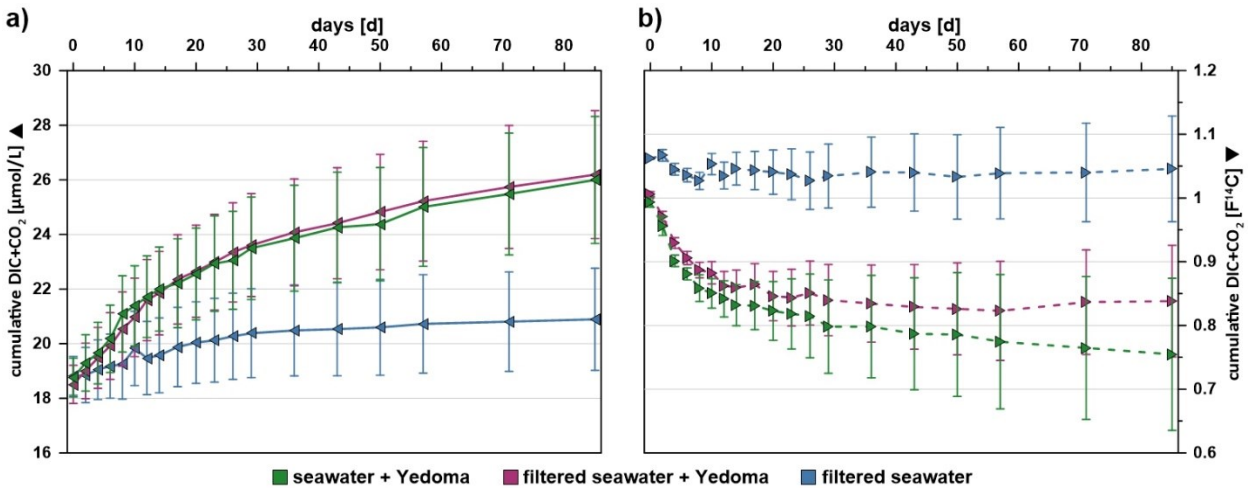

Figure 11: Cumulative concentrations of a) dissolved inorganic carbon plus carbon dioxide (DIC+CO_2) and b) corresponding $F^{14}C$ signatures (right). Propagated 1σ uncertainties are displayed in both panels (detail see supplement).

In both SW+YE and fSW+YE as well as the original Yedoma, the solid fraction was analyzed for TOC and bulk $F^{14}C$ (Figure S 13). The untreated Yedoma prior to incubation contained 1.2±0.2 dry wt% TOC (n=6)

with a $F^{14}C$ of 0.0071±0.0018 (n=3). During the incubation SW+YE contained on average 1.1±0.1 dry wt% TOC (n=20) with a $F^{14}C$ values of 0.0092±0.0011 (n=20), thus remained constant within measurement uncertainty and displayed values very similar to fSW+YE values for TOC of 1.1±0.0 wt% (n=6) and bulk $F^{14}C$ values of 0.0079±0.0009 (n=6).

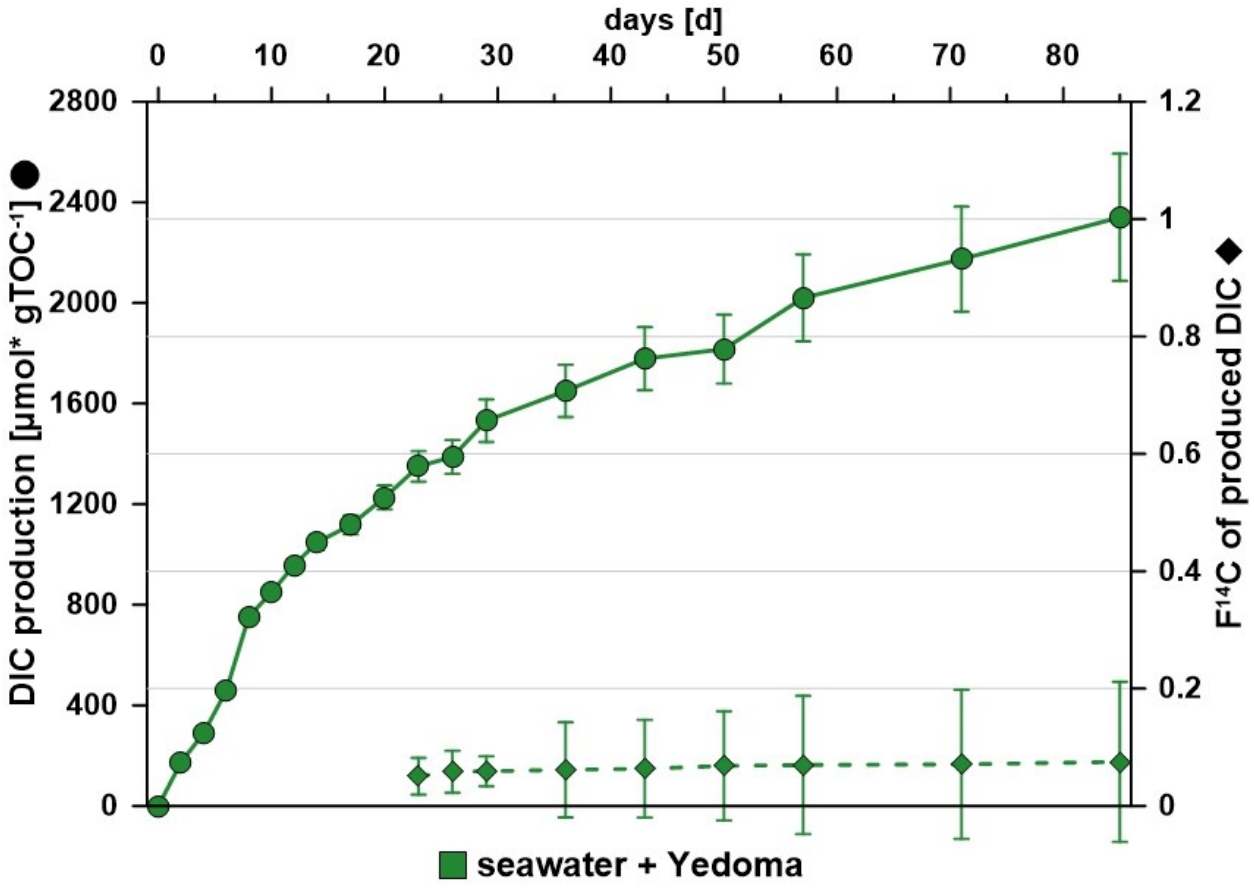

Figure 12: Dissolved inorganic carbon (DIC) production (left facing triangles with solid lines) and corresponding $F^{14}C$ signature (right facing triangles with dashed lines) in seawater + Yedoma (SW+YE) over 85 days. Error bars indicate propagated 1σ uncertainties for both datasets (for details see supplement).

Intra-treatment variability

The stability of salinity, pH-values, DIC concentrations, and DIC $F^{14}C$ signatures confirms low variability between vials of the same treatment (excluding SW+YE vial #8, details in supplement). However, the similarities in change are high between both SW+YE and fSW+YE and are in stark contrast to fSW; indicating that Yedoma addition had a profound impact at minimal "bottle effects" (Pernthaler & Amann, 2005) on key parameters like DIC concentration and $F^{14}C$ signature. Low variability between replicates was underlined by close clustering of replicates in bacterial community ordination (Figure S 9).

Dissolved nutrients and DOC

Overall, the three treatments had similar NO_2^-, NO_3^-, Cl^-, SO_4^{2-}, and O_2 concentrations (details in supplement; Figure S 10 to Figure S 12, Table S 3). SW+YE and fSW+YE showed similar trends for DOC, TDN, and PO_4^{3-}, although these three values differed from the fSW. The strongest difference between the individual treatments was observed in NH_4^+ concentrations.

DOC concentrations were fairly stable in fSW on average 88±2 µmol/L (n=5; Figure 13a), except 187±9 µmol/L on day 0 which probably reflects some minor contamination during sampling. In fSW+YE initial DOC concentrations were higher than in fSW, with 508±25 µmol/L, increased to 912±49 µmol/L on day 57 and thereafter decreased slightly to 875±45 µmol/L on day 85. Concentrations in SW+YE were similar to fSW+YE, with an initial DOC concentration of 570±146 µmol/L, which rapidly increased to 827±42 µmol/L on day 4 and then remained stable at an average of 825±44 µmol/L (n=15). TDN concentrations displayed similar trends, remaining constantly low at an average of 10.5±0.7 µmol/L (n=7) in fSW. Comparing the other treatments, in fSW+YE initial TDN concentrations were higher (46±2 µmol/L) on day 0 and peaked at 87±5 µmol/L on day 57, followed by a small decrease to 85±4 µmol/L on day 85. Concentrations in SW+YE were similar to fSW+YE, with initially 63±12 µmol/L subsequently increasing to 107±4 µmol/L on day 85.

PO_4^{3-} concentrations (Figure 13b) varied between treatments. fSW had fairly constant PO_4^{3-} values with an average of 0.555±0.027 µmol/L (n=6). In contrast, in fSW+YE PO_4^{3-} concentrations were initially 0.308±0.004 µmol/L, then dropped to a minimum of 0.110±0.006 µmol/L on day 2 before rising steadily to 0.205±0.001 µmol/L on day 85. Similarly, PO_4^{3-} concentrations in the SW+YE dropped from 0.285±0.002 µmol/L on day 0 to 0.102±0.020 µmol/L on day 8, increasing thereafter to 0.211±0.001 µmol/L at an average of 0.193±0.016 µmol/L (n=11).

NH_4^+ concentrations (Figure 13b) in fSW were stable between 1.94±0.16 µmol/L and 1.60±0.02 µmol/L. Initial NH_4^+ concentrations in fSW+YE were considerably higher with 35.32±2.27 µmol/L on day 0, decreasing to 26.40±0.17 µmol/L on day 17 before increasing to 29.87±0.03 µmol/L on day 85. Initial NH_4^+ concentrations were the highest in SW+YE with 38.66±0.52 µmol/L before decreasing until day 8 to 28.02±0.36 µmol/L, similar to fSW+YE. However, NH_4^+ concentrations in SW+YE thereafter increased substantially above initial concentrations, reaching to 46.79±2.21 µmol/L on day 85.

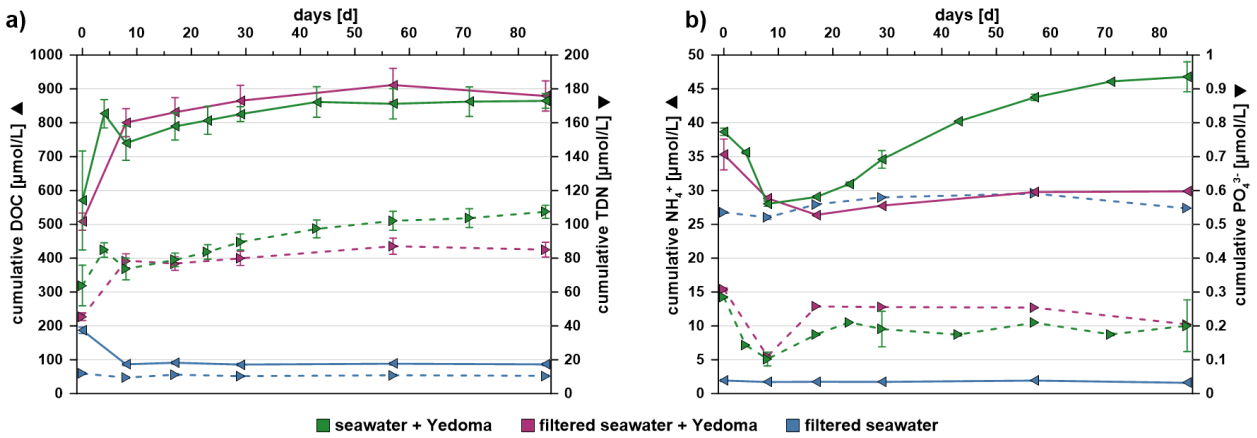

Figure 13: Cumulative concentrations of aqueous parameters. a) Dissolved organic carbon (DOC; left facing triangles with solid lines) and total dissolved nitrogen (TDN; right facing triangles with dashed lines); b) ammonium (NH_4^+ left facing triangles with solid lines) and phosphate (PO_4^{3-} right facing triangles with dashed lines). Propagated 1σ uncertainties are displayed in both panels (detail see supplement).

Bacterial community dynamics

16S rRNA gene amplicons illustrated bacterial community dynamics and possible responses to thawing permafrost, both regarding ambient permafrost and ambient seawater bacteria. We analyzed both the waterborne and attached community by extracting both aqueous and solid phase after centrifugation. Sample types clearly differed in community composition (Figure S 14a; PERMANOVA $R^2 = 0.45$, $p < 0.001$), with corresponding major differences on bacterial order level (Figure S 14b). The original seawater microbiome changed during transport, but still featured similar proportions of typical seawater groups like Flavobacteriales and SAR11 post-transport, hence being representative of the ambient Kara Sea community. The original permafrost community was dominated by Solirubrobacterales, Gaiellales, Micrococcales and Microtrichales (Actinobacteriota), Gitt-GS-136 and KD4-96 (Chloroflexi), as well as Rhizobiales (Alphaproteobacteria; Figure 14).

Overall, Yedoma thaw mostly stimulated taxa less abundant in the ambient seawater and permafrost (Figure 14). Alpha-diversity decreased during the experiment, whereas species richness remained high in permafrost incubations (Figure S 15). Most ambient permafrost taxa decreased in abundance over the first 17 days, only remaining detectable in the solid phase. Only 67-14 (Solirubrobacterales) retained considerable proportions throughout the experiment (Figure 14). Psychrobacter and Saccharospirillaceae dominated both solid and water phases of fSW+YE. In addition, Flavobacterium increased in abundance from day 17. The solid phase of SW+YE featured an initial predominance of Colwellia and Moritella, with subsequent establishment of flavobacteria (Maribacter, Aurantivirga and unclassified ASVs). The community change from day 57 onwards, as highlighted by ordination analyses (Figure 14), corresponded

to the appearance of Pseudohongiella. The water phases of fSW+YE and SW+YE showed mixed signals; featuring Polaribacter ASVs also detected in the original seawater, as well as lower and decreasing abundances of Colwellia. The different trajectories coincided with contrasting correlations between ASVs and physicochemical measurements, depending on whether ASVs originated from the ambient permafrost or seawater (Figure S 16). CO_2 release was mostly linked to Gammaproteobacteria, including *Psychrobacter* (permafrost-derived) as well as *Colwellia*, unclassified *Saccharospirillaceae* and *Moritella* (seawater-derived). From the flavobacteria, *Croceibacter* positively correlated with CO_2 production, but only represented ~0.5% relative abundance in the community.

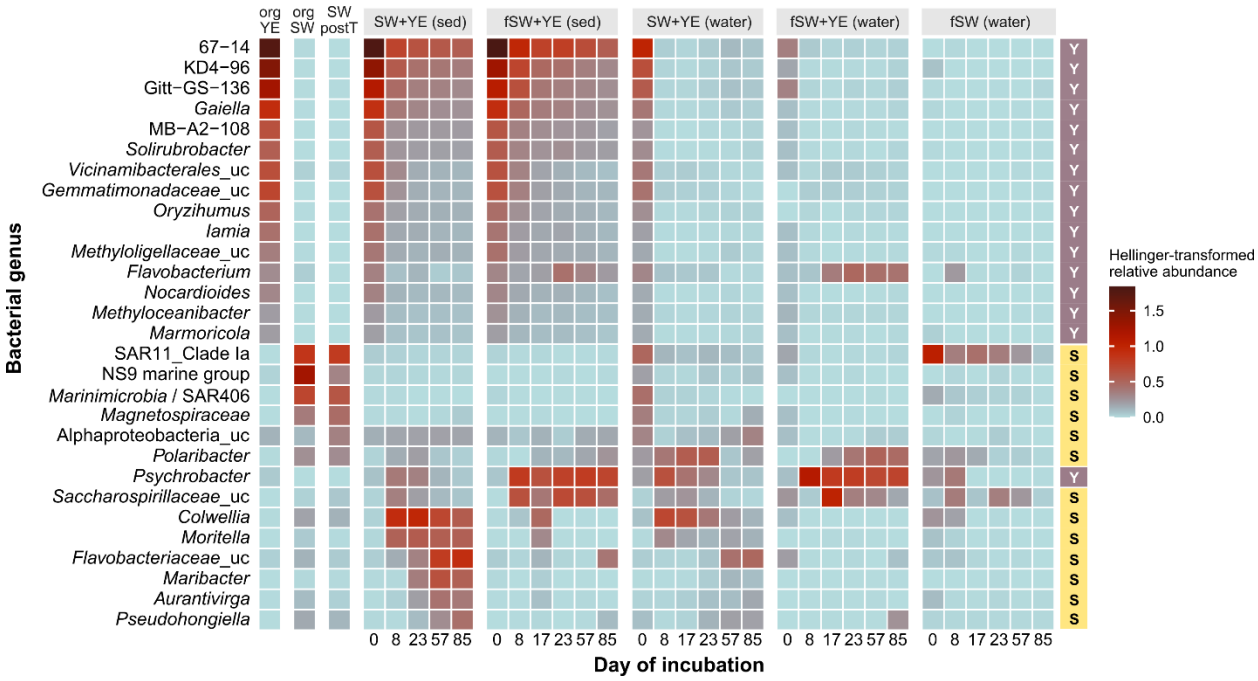

Figure 14: Heatmap of major bacterial genera per treatment and day of incubation, displayed as Hellinger-transformed relative abundances. orgYE: original Yedoma permafrost, orgSW: original seawater, SW.postT: original seawater after transport, SW+YE: seawater+Yedoma, fSW+YE: filtered seawater+Yedoma, fSW:filtered seawater, water: free-living fraction / aqueous phase, sed: particle-attached fraction. The right column illustrates whether genera had highest initial relative abundance in the ambient Yedoma (Y) or seawater (S), indicating their likely origin.

Discussion

Immediate microbial mineralization of organic carbon from fossil Yedoma permafrost

Thawing and coastal erosion are currently mobilizing substantial proportions of Pleistocene-age carbon from the Yedoma domain, entering the shelf areas of the Arctic Ocean. Previous observations from the Canadian Arctic have indicated that permafrost carbon has a high potential for remineralization once it reaches marine waters (Tanski et al., 2019), however, the bioavailability and fate of “old” OC from

permafrost remains unclear. Here, we show an immediate and rapid release of CO_2 from freshly thawed Yedoma soil when incubated in seawater containing a natural Arctic shelf microbial community (Figure 10). While CO_2 production indicates that OC was utilized by the microbial community, it does not necessarily imply that the carbon was derived from Yedoma. For example, CO_2 production also occurred (albeit to a much lower extent) in a parallel incubation only containing seawater and the small fraction of the microbial community that escaped 0.22 µm filtration (Nakai, 2020). Therefore, we carried out radiocarbon analysis of the released DIC, which revealed continuous "ageing" of the DIC pool when permafrost was present, confirming that fossil OC from Yedoma was being remineralized (rather than modern DOC in the seawater). By applying an isotope mass-balance and accounting for the bulk radiocarbon signature of the Yedoma deposit, we estimated that 88±15% (Figure 11) of the released DIC originated from a fossil source, i.e. almost all respired OC originated from thawing Yedoma.

The increase in cumulative DIC+CO_2 is equivalent to 2.8±1.6 % of the TOC originating from the Yedoma slurry. The rapid DIC release within the first 14 days accounts for ~1000 µmol DIC * $gTOC^{-1}$, with rates being considerably higher than between day 14 and 85 when an additional ~1300 µmol DIC * $gTOC^{-1}$ was produced (Figure 11). In total ~2300 µmol DIC * $gTOC^{-1}$ were released during the entire 85 days of incubation. Since CO_2 release rates did not plateau after 85 days, our data possibly underestimate the total CO_2 release compared to natural settings, where remineralization likely occurs over longer time periods than three months. Therefore, our data likely only represents the fast cycling fraction (<5%), with much of the OC still being available (20-90%) for many decades (Schädel et al., 2014). Overall, ~3% of the total permafrost TOC was hence respired to CO_2, consistent with previously reported Yedoma incubations (Dutta et al., 2006) and Canadian permafrost soil degradation in seawater (Tanski et al., 2019, 2021). This supports the suggestion that when permafrost thaws and enters the ocean a substantial amount of aged or fossil carbon will be reintroduced into the modern carbon cycle at accelerated rates, potentially aggravating the climate crisis (Irrgang et al., 2022).

The obtained $F^{14}C$-DIC data display a continuous "aging" of the DIC pool (lower $F^{14}C$ values; Figure 3) as the incubation progressed, providing evidence for the bioavailability of fossil CO_2. Applying an isotope mass-balance, we determined the radiocarbon signature of the released CO_2 to range from 0.025±0.125 to 0.136±0.155 between days 23-85 (uncertainties between day 0 and 20 were high and partly resulted in unrealistic and negative $F^{14}C$ values, thus no estimates are provided for first 20 days if the experiment). The mean $F^{14}C$ signature of the produced DIC was 0.136±0.122. By taking into consideration the bulk radiocarbon signature of the Yedoma deposit (0.0066±0.0002), we calculated that 88±15% of the released

DIC comes from a fossil source (Figure 11), meaning that virtually all of the respired organic material originates from Yedoma. Hence, the old permafrost organic matter is bioavailable, supporting previous observations of threefold higher CO_2 release from old (~14352 ^{14}C yr) in comparison to younger (~2365 ^{14}C yr) permafrost soils (Tanski et al., 2021). However, our findings are in contrast to the estimated (semi) modern GHGs emissions from Alaskan freshwater lakes system underlain by permafrost (Elder et al., 2018), or from thawing tundra permafrost in Alaska ($F^{14}C$ values >1; Schuur et al. 2009). Our direct assessment released carbon age is crucial as the mobilization of old carbon is one key tipping point in the global climate system (Lenton, 2012; Lenton et al., 2019; Lenton & Williams, 2013) and several authors recently encouraged studies assessing the respiration of old carbon (Miner et al., 2022; Schwab et al., 2020; Wild et al., 2019). Our data suggest that a positive feedback loop of increasing temperatures, coastal permafrost thaw, and release of microbially produced GHGs may establish. However, our data are in contrast to previously reported 66±16% of permafrost derived organic matter being remineralized upon release to the ocean (Vonk et al. 2012).

Additional to the production of DIC, we observed the immediate release of DOC from the permafrost slurry of ~500 µmol C per g sediment and a further release of ~250 µmol C per g sediment over the 85 days (Figure 12). In total this accounts for about 0.9±0.3% of the initially added Yedoma OC. Around two-thirds of this DOC was immediately released when permafrost was added to the seawater. This is indicative of leaching from the soil particles, as large amounts of DOC can be released from freshly thawed Yedoma deposits (Guo et al., 2007). The release was of a similar magnitude as in previous reports of DOC leaching from permafrost soils (Drake et al., 2015; Ewing et al., 2015; Mann et al., 2015; Wickland et al., 2018). Similar DOC is known to be highly bioavailable, with a rapid loss of >50% DOC over 8 to 28 days after release into aquatic systems (Drake et al., 2015; Rogers et al., 2021; Spencer et al., 2015). Therefore, part of the produced DIC in our incubations likely originated from respiration of the released DOC. However, the continued net accumulation of DOC over the course of the experiment indicates that additional particulate OC was utilized by the microbial community. Regardless of whether microorganisms respired OM from the particulate OC or DOC pool, DIC production persisted for the length of the experiment. However, the remineralization rate dropped by ~65% after ~15 days. This mirrored observations of Tanski et al. 2019 who incubated Canadian permafrost soil in seawater, as well as other permafrost incubation studies with plateauing CO_2-release after 1 to 3 months (Knoblauch et al., 2013; Lee et al., 2012; Schädel et al., 2014). The released DOC has the potential to be transported beyond the shelf (Mann et al., 2022; Polimene et al., 2022) and might therefore impact the entire Arctic Ocean.

Despite the high bio-availability of fossil Yedoma OC, our data also suggest that part of the CO_2 release might be counterbalanced by increased primary production driven by concurrent release of nitrogen compounds. Addition of the thawed permafrost to both the filtered and unfiltered seawater led to an immediate increase in ammonium concentrations, likely due to cation exchange with the ammonium rich permafrost (Mauclet et al., 2022). Despite the net decrease in ammonium during the first days of the incubation, SW+YE showed a net production of dissolved inorganic nitrogen from day 8 until day 85 (Figure 12). In fact, by the end of the incubation, there was a net accumulation of ~4 µmol L^{-1} of dissolved inorganic nitrogen in the form of ammonium (~1.4 µmol g-1 dry wt.) compared to day 1. Furthermore, by day 85 the ratio of produced C:N (i.e. CO_2:NH_4^+) was extremely low (<~1). No such N-accumulation was observed in fSW indicating that the ambient microbial community can convert substantial amounts of Yedoma organic nitrogen to inorganic nitrogen. Our data support a recent meta-analysis by Strauss et al. (2022) which showed that the stock of microbially available nitrogen in Yedoma deposits is larger than previously expected (about 49% of the permafrost N stock). Potentially, the inorganic nitrogen released during permafrost degradation could enhance primary production in the Arctic Ocean, capturing part of the released CO_2 (Strauss et al., 2022; Terhaar et al., 2021). However, the oxidation of ammonium is also a major source of the potent greenhouse gas nitrous oxide (Fiencke et al., 2022), and the implications of inorganic nitrogen release and associated feedback mechanisms remain poorly understood (Strauss et al., 2022).

Degradation of fossil organic matter is mediated by both modern-day Arctic seawater microbial communities and ambient permafrost communities

Amplicon sequencing provided a detailed picture of bacterial dynamics during permafrost thaw, identifying taxa that presumably contributed to OC degradation. Similar DIC production from permafrost incubated with unfiltered and filtered seawater indicates that both seawater and “awakened” permafrost bacteria participated in OC degradation. Overall, the ambient permafrost community comprised taxa commonly found in permafrost, soil and sediments, including *Chloroflexi* (*Solirubrobacterales* and KD4-96), *Actinobacteriota* (*Gaiellales*, *Micrococcales*, *Microtrichales*) as well as *Rhizobiales* (Costello & Schmidt, 2006; Gołębiewski et al., 2014; Goswami et al., 2023; Liu et al., 2022; B. Zhang et al., 2019). The ambient seawater microbiome was typical for pelagic marine waters, dominated by SAR11, *Flavobacteriales* and *Pseudomonadales* (e.g. SAR86, SAR92). Contrasting correlations depending on whether ASVs were originally more abundant in seawater or permafrost (Figure S 16) underlined different trajectories depending on their original habitat. These events were possibly amplified by the specific and diverse

adaptations of permafrost bacteria including dormancy (Johnson et al., 2007; Mackelprang et al., 2017), DNA repair (Hueffer et al., 2020; Johnson et al., 2007; Miner et al., 2021), stress response (Mackelprang et al., 2017), and membrane fluidity (Siliakus et al., 2017).

Decreasing abundances of most ambient permafrost bacteria during incubation indicated these were less competitive, and/or in dormant stages. Taxa that were detected throughout the incubation (mainly the uncultured 67-14 and KD4-96 clades) possibly constituted viable populations, whose potential metabolic activities are speculative. Their restriction to the solid phase suggests they can only persist in a soil/water matrix, but cannot establish in the pelagic microbiome. Distinct community changes within the first 8 to 17 days, observed in all treatments, provides further evidence that OC degradation started immediately. The strongest changes occurred within the solid phases, indicating that the water-soil slurry forms an ideal microenvironment for OC degradation. Our evidence supports Mann et al. (2015) who surmised that released OC is highly bioavailable and fuels a considerable part of the community and is in accordance with the approximately 1.5x higher CO_2 release when permafrost degraded in seawater rather than without seawater (Tanski et al., 2021). Higher species richness in permafrost soil incubations indicated that a diverse community established when seawater and permafrost deposits mix (Figure S 15), but at uneven ratios (i.e. a dominance of few taxa and long “tail” of rare taxa).

Of the permafrost-derived bacteria, *Psychrobacter* markedly increased in abundance and correlated with CO_2 production, indicating considerable metabolic activity upon thawing. The predominant *Psychrobacter* ASVs, constituting approximately 0.2% in the original Yedoma, are related to *Psychrobacter cryohalolentis* isolated from 40,000 year-old permafrost soil in Siberia (Bakermans et al., 2006). In addition, several seawater-derived Gammaproteobacteria presumably contributed to OC degradation and CO_2 production. The *Colwellia* population primarily consisted of *C. hornerae* and *C. psychrerythraea*, with known low-temperature activities including chemotaxis, indicating these actively colonized and utilized permafrost particles. *Psychrobacter*, *Colwellia* and *Moritella* synthesize polyunsaturated fatty acids via homologous gene clusters (Bowman, 2017), underlining their cold adaptation and similar dynamics. Some of their metabolic traits might be involved in degrading permafrost OC, e.g. related to C1 or aromatic compound metabolism as well as sulfate reduction (Methé et al., 2005; Mudge et al., 2021), but sulfate concentrations remained stable in our incubations. Furthermore, released extracellular enzymes from *C. psychrerythraea* that mediate the degradation of OC from melting sea-ice (Showalter & Deming, 2021) might be similarly active on permafrost OC.

The successional appearance of flavobacteria in the solid SW+YE phase potentially signify the presence of plant- or algae-derived substrates (Kappelmann et al., 2019), as flavobacteria are specialized in carbohydrate utilization. Flavobacterial ASVs almost all originated from seawater (approx. 100-fold higher abundances), indicating subsequent colonization of particles once more complex plant substrates, e.g. polysaccharides, became enriched during thaw. The appearance of *Pseudohongiella* after 57 days underlined altered substrate regimes over time, which stimulated so-far underrepresented ASVs. Overall, our evidence indicates successional, substrate-driven community dynamics with initial dominance of fast-responding Gammaproteobacteria, which quickly utilized the pool of labile substrates in line with their copiotrophic capacities (Pedler et al., 2014). This initial "bloom" was followed by secondary consumers of semi-labile and semi-refractory substrates. One relevant consideration is how our experimental dynamics translate to the field – i.e. to what extent the "inoculation" of permafrost bacteria might alter ambient seawater microbiomes, and to what extent this varies between permafrost types. Our evidence suggests that the input of permafrost OC is a strong major driver of microbiome structure, mainly stimulating seawater bacteria. Permafrost-awakened microbes might establish in the sediment after resettling; however, the potential ecological consequences are unclear. These aspects are further influenced by the extensive variation in taxonomic and functional genes among permafrost microbes depending on region and permafrost biochemistry (Waldrop et al., 2023).

Conclusion

Incubating Yedoma permafrost soil in seawater for 85 days revealed considerable utilization of permafrost OC, with around 3% of the incubated OC being respired into CO_2. According to DIC radiocarbon analysis, 88% of the released CO_2 had a fossil origin. Its release to the ocean can be regarded as an expanding source for "natural fossil" GHG emissions caused by anthropogenic climate change, reintroducing old OC, locked up since the last glacial, into the short-term carbon cycle. Our results therefore imply that permafrost carbon feedback will increase in response to the accelerating erosion of coastal permafrost deposits expected in the coming decades. The longer-term fate of the remaining 95% of the solid phase permafrost OC is less clear. However, a fraction will likely be degraded during sedimentation and resuspension cycles. Our results also suggest that permafrost erosion will have broader impacts on the Arctic Ocean, constituting an additional source of DOC likely remain in the water column and be transported across the shelf. Nonetheless, the immediate response of several bacterial taxa suggests that the DOC is highly bioavailable. Additionally, Yedoma appears to be a source of both organic and inorganic nitrogen, which could stimulate primary production. Successional dynamics among bacterial communities indicated that labile substrates were swiftly consumed, followed by establishment of secondary

consumers of semi-labile and semi-refractory substrates. Overall, our evidence illustrates a substantial impact of thawing permafrost on Arctic ecosystems, stimulating diverse bacterial taxa with expected consequences for local biogeochemical cycles and the global climate.

Acknowledgements

We are thankful for the AWI-institutional funding for MR in the INSPIRES framework. Many thanks to Lea Philips, Liz Bonk, Malte Höhn, Ingrid Stimac, Ingrid Dohrmann, Claudia Burau, and Jakob Barz, and Anja Batzke for their technical support. For the Yedoma field sampling we thank the German Federal Ministry of Education and Research (BMBF; project CACOON (#03F0806A) to JS and GM. We thank the AWI marine biogeoscience group for their support and the usage their facilities. For the seawater sample, we thank the Arctic Century Expedition, a joint initiative led by the Swiss Polar Institute (SPI), the Antarctic and Arctic Research Institute (AARI) and GEOMAR Helmholtz Centre for Ocean Research Kiel (GEOMAR) and funded by the Swiss Polar Foundation. We acknowledge funding by the Deutsche Forschungsgemeinschaft (DFG, German Science Foundation) under Germany's Excellence Strategy EXC 2077 390741603 supporting contributions from HM.

Data availability

Biogeochemical data are publicly available at the Pangaea Data Repository under https://issues.pangaea.de/browse/PDI-33090. Bacterial 16S rRNA reads have been deposited in the European Nucleotide Archive under accession number PRJEB59831 using the data brokerage service of the German Federation for Biological Data (GFBio) in compliance with MIxS standards. The amplicon analysis workflow, including metadata and accession numbers of fastq files, is available under https://github.com/matthiaswietz/yedoma-bacteria.

Supplementary Information

Details to carbon budget calculations

We determined the carbon balance on the basis of DIC concentrations and pH values. To assess the mineralization and release of carbon from Yedoma we made the following assumptions:

1) DIC concentrations and $F^{14}C$ values are in equilibrium between water and headspaces (Åberg & Wallin, 2014). Even though a fractionation of ^{13}C of 0.3‰ during gas-water CO_2 exchange was previously reported (J. Zhang et al., 1995), fractionation for ^{14}C values can be ignored, as $F^{14}C$ values are by definition corrected for fractionation (Reimer et al., 2004; Stuiver & Polach, 1977).

2) As conditions remained oxic throughout the experiment and sediments were resuspended, methane production can be neglected, as methanogenesis is absent in the presence of O_2 (Lyu et al., 2018). Further, even if CH_4 would have been produced, it would have likely been consumed by sulfate reducing bacteria (Jørgensen et al., 2001; Overduin et al., 2015). However, as SO_4^{2-} concentrations remained stable over the course of the experiment, CH_4 consumption and production are therefore excluded. Furthermore, even if small anaerobic pockets would have been present, the production of methane can be expected to be minimal as the establishment of methane producing communities was shown to take years (Knoblauch et al., 2013).

3) The pressure in the incubation vials remained stable at ambient pressure. Due to the ventilation at every sampling event, any long-term increase can be excluded. Further, as O_2 is assumed to be the primary electron acceptor, each mol of CO_2 released would roughly correspond to one mol of O_2 consumed. Hence, with CO_2 being the mainly emitted gaseous species, pressure can be expended to stay at ambient values.

To determine the carbon content and release in the individual vials per sampling event, several parameters had to be assessed. The water content of the Yedoma sample slurry ($\%_W$) was determined by the relationship of sample volume (V_S), water volume (V_W), water weight (wt_W), wet weight (wwt), and dry weight (dwt) under the assumption that wt_W equals V_W (n=5):

$$wwt - dwt = wt_W \approx V_W$$

$$\frac{V_W}{V_S} * 100 = \%_W$$

Organic carbon content of the added slurry (OC_{PF}) was determined by multiplying the %dwt:

$$100 - \%w = \%dwt$$

with the added mass of the slurry and the average total organic carbon (TOC) content (n=3):

$$\%dwt * wwt * TOC = OC_{PF}$$

Salinity (*S*) was based on chloride (Cl^-) concentration using the formula after (Grasshoff et al., 1999):

$$S\ ‰ = 1.80655 * Cl\ ‰$$

The partial pressure of CO_2 in the water (pCO_2) was calculated based on DIC concentrations and pH following Zeebe et al. (2001). With resulting pCO_2-values the CO_2 concentration in the headspace (xCO_2) was calculated assuming 100% humidity in the vial and ambient pressure (*p*), and taking temperature (*T*) and salinity (*S*) into account (Weiss & Price, 1980):

$$pCO_2 = xCO_2 * (p - pH_2O)$$

Accounting for water vapor saturation on the basis on measured temperature (*T*) and S (Weiss & Price, 1980):

$$\ln pH_2O = 24.4543 - \frac{6745.09}{T} - 4.8489 \ln \frac{T}{100} - 0.000544\, S$$

Both the amount of DIC present in the vials and CO_2 removed during headspace ventilation depended on the continuously changing volume (due DIC sampling) of both the water phase (V_{water}) and the headspace (V_{HS}) in the vials, respectively. With an average vial volume of 116.3 mL (slurry plus seawater = 93 mL, sterile seawater controls = 90 mL) and a DIC sample volume of 2 mL at every sampling event (*tn*; including t_0), the volume was determine as followed:

$$V_{water\ tn} = 93\ ml - (tn + 1) * 2\ mL$$

$$V_{HS\ tn} = 116.3\ mL - V_{water\ tn}$$

Further, the removed CO_2 during headspace ventilation was corrected for the T and xCO_2 at the individual t_n, assuming ambient p and the ideal gas constant R (0.08206; t_0 was not accounted for, as the ventilation was performed right after the experiment start and therefore flux from water to the headspace should be negligible):

$$nCO_2 = xCO_2 * pV_{HS}/RT$$

Uncertainty propagation

The uncertainties (σ) of cumulative DIC+CO_2 concentrations (cc(DC)), their respective $F^{14}C$ signatures, released $gCO_2/gTOC$, released CO_2 $F^{14}C$ signature, %TOC respired, and %fossil of released CO_2 was determined by propagation of the individual analytical errors associated with DIC concentration, pH, salinity, TOC and $F^{14}C$:

- σDIC; determined by the average (day 0-85; n=19) standard deviation of measured vials at a single sampling event (n=2-4; Figure S 2)
- σpH; = determined by the average (day 0-85; n=19) standard deviation of measured monitoring vials at a single sampling event (n=3; Figure S 4), in absolute H^+ concentrations.
- σS; determined by the standard deviation between the analyzed vials (n=19).
- σTOC; standard deviation of the TOC measurements (n=3)
- $\sigma F^{14}C$; measurement uncertainties at the individual time points.

Further assumptions:

- Temperature uncertainty (σT) of the measurements is <0.01 °C and negligible between the vials
- Pressure is constant and uncertainty between the vials is negligible.

CO_2 concentration uncertainty (σCO_2) in the headspace was determined for each sampling event as follows:

$$\sigma {CO_2}^2 = \left(\frac{\partial CO_2}{\partial DIC} * \sigma DIC\right)^2 + \left(\frac{\partial CO_2}{\partial pH} * \sigma pH\right)^2 + \left(\frac{\partial CO_2}{\partial T} * \sigma T\right)^2 + \left(\frac{\partial CO_2}{\partial S} * \sigma S\right)^2$$

Individual partial derivatives were calculated numerically using analytical uncertainties afore mentioned:

$$\frac{\partial CO_2}{\partial DIC} \approx \frac{f(\overline{DIC} + \sigma DIC, \overline{pH}, \bar{T}, \bar{S}) - f(\overline{DIC} - \sigma DIC, \overline{pH}, \bar{T}, \bar{S})}{2\sigma DIC}$$

$$\frac{\partial CO_2}{\partial pH} \approx \frac{f(\overline{DIC}, \overline{pH} + \sigma pH, \bar{T}, \bar{S}) - f(\overline{DIC}, \overline{pH} - \sigma pH, \bar{T}, \bar{S})}{2\sigma pH}$$

$$\frac{\partial CO_2}{\partial T} \approx \frac{f(\overline{DIC}, \overline{pH}, \bar{T} + \sigma T, \bar{S}) - f(\overline{DIC}, \overline{pH}, \bar{T} - \sigma T, \bar{S})}{2\sigma T}$$

$$\frac{\partial CO_2}{\partial S} \approx \frac{f(\overline{DIC}, \overline{pH}, \bar{T}, \bar{S} + \sigma S) - f(\overline{DIC}, \overline{pH}, \bar{T}, \bar{S} - \sigma S)}{2\sigma S}$$

The uncertainties of the ccDC concentrations were determined in in 3 steps:

1) uncertainties of the removed DIC ($\sigma DIC_{removed}$) at a given sampling event were performed by propagating the uncertainties in the sampled 2mL water samples of the previous sampling events:

$$\sigma \mathrm{DIC}_{removed}{}^2 = (\sigma \mathrm{DIC}_{t0} * 2mL)^2 + (\sigma \mathrm{DIC}_{t1} * 2mL)^2 + \cdots (\sigma \mathrm{DIC}_{tn} * 2mL)^2$$

2) Due to the ventilation of the headspace at all sampling events, the uncertainties of the removed CO_2 ($\sigma CO_{2\ removed}$) at a given sampling event was determined by propagating the σCO_2 of the previous sampling events, accounting for the increase of V_{HS}:

$$\sigma \mathrm{CO}_{2\ removed}{}^2 = (\sigma \mathrm{CO}_{2\ t0} * V_{HS\ t0})^2 + (\sigma \mathrm{CO}_{2\ t1} * V_{HS\ t1})^2 + \cdots (\sigma \mathrm{CO}_{2\ tn} * V_{HS\ tn})^2$$

3) Due to the cumulative nature of the cc(DC), its uncertainty (σcc(DC)) was calculated by propagating the uncertainties of DIC, $DIC_{removed}$, and $CO_{2\ removed}$ at a given tn, as followed:

$$\sigma \mathrm{cc(DC)}_{tn}{}^2 = \sigma \mathrm{DIC}_{tn}{}^2 + \sigma \mathrm{CO}_{2\ tn}{}^2 + \sigma \mathrm{DIC}_{removed}{}^2 + \sigma \mathrm{CO}_{2\ removed}{}^2$$

Further, the uncertainties of the removed ccDC ($ccDC_{removed}$) were determined as follows:

$$\sigma ccDC_{removed}{}^2 = \sigma DIC_{removed\ t0}{}^2 + \sigma CO_{2\ removed\ t0}{}^2 + \sigma DIC_{removed\ t1}{}^2 + \sigma CO_{2\ removed\ t1}{}^2 + \cdots + \sigma DIC_{removed\ tn}{}^2 + \sigma CO_{2\ removed\ tn}{}^2$$

The uncertainty of the released gCO_2 per gTOC (σgCO_2) was determined by propagating mass of $\sigma cc(DC)_{tn}$ and σTOC:

$$\sigma \mathrm{gCO}_2{}^2 = \sigma \mathrm{cc(DC)}_{tn}{}^2 + \sigma \mathrm{TOC}^2$$

The same uncertainty values were used for error range of the percentage of TOC released, as the mathematic operations did only include a change of units.

Similar to carbon species concentrations, the uncertainty of the $F^{14}C$ signatures was determined. This was performed in multiple steps:

1) the uncertainty of the removed DIC and CO_2 ($\sigma F^{14}C_{removed}$) at a given sampling event was determined by propagating the measurement uncertainties from AMS of the previous sampling events:

$$\sigma F^{14}C_{removed}{}^2 = \sigma F^{14}C^2_{AMS\ t0} + \sigma F^{14}C^2_{AMS\ t1} + \cdots + \sigma F^{14}C^2_{AMS\ tn}$$

2) The $F^{14}C$ uncertainties of cc(DC) ($\sigma F^{14}C_{ccDC}$) were determined accounting for the weighted (W) carbon pool sizes of the water phase and headspace:

$$ccDC_{tn} = ccDC_{removed} + cDC_{tn}$$

In percent:

$$W_{cDC\ tn} = 1 - \frac{ccDC_{removed}}{ccDC_{tn}}$$

at the current sampling event (AMS measurement at the particular time point) and the previously removed ($\sigma F^{14}C_{removed}$):

$$\sigma F^{14}C_{ccDC\ tn}{}^{2} = (\sigma F^{14}C_{DIC\ tn} * W_{cDC\ tn} + F^{14}C_{DIC\ tn} * \sigma W_{cDC\ tn})^2 + (\sigma F^{14}C_{removed} * (1 - W_{cDC\ tn}) + F^{14}C_{removed} * \sigma W_{cDC\ tn})^2$$

assuming σW to be equally to the percentile uncertainties of $ccDC_{tn}$ and $ccDC_{removed\ tn}$:

$$\sigma F^{14}C_{ccDC\ tn}{}^{2} = (\sigma F^{14}C_{DIC\ tn} * W_{cDC\ tn} + F^{14}C_{DIC\ tn} * \sigma W_{cDC\ tn})^2 + (\sigma F^{14}C_{removed} * (1 - W_{cDC\ tn}) + F^{14}C_{removed} * \sigma W_{ccDC\ removed\ tn})^2$$

3) The uncertainty in the calculated Yedoma-derived C ($\sigma\%_{Yedoma}$) contributing to the released CO_2 was determined by propagating $\sigma F^{14}C_{removed}$ at t20, the uncertainty of the Yedoma bulk $F^{14}C$ ($\sigma F^{14}C_{Yedoma}$), and the uncertainty of the initial, untreated seawater DIC concentration ($\sigma F^{14}C_{DIC\ fSW\ t0}$):

$$\sigma\%\text{Yedoma} = 100 * \sqrt{\sigma F^{14}C^2_{removed\ t20} + \sigma F^{14}C^2_{Yedoma} + \sigma F^{14}C^2_{DIC\ SW\ t0}}$$

Data consistency

To ensure data quality and assess potential bottle effects, we compared DIC concentrations and $F^{14}C$ signatures between treatments. For SW+YE, we continuously analyzed DIC and $F^{14}C$ from day 0 to 85 in two vials each, as well as in randomly picked samples from the remaining vials at every time point (in total measuring 17 vials for both parameters). Both DIC concentrations (n=56) and $F^{14}C$ values (n=57) in the continuously measured vials agreed well with one another, and with the randomly picked vials (Figure S 2). To assess the carbon budget, pH was an important parameter as pH, DIC concentrations, and CO_2 headspace concentrations are interdependent. In order to attribute the pH measurements from

monitoring vials (slightly different setup due to glued optodes in vials) to the sample vials, the DIC concentration in one of the monitoring vials of SW+YE (day 0-85) was determined. The values closely aligned to DIC concentrations in vials without optodes. Thus, we are confident that pH of monitoring vials represents the pH in sample vials.

A similar approach was taken for fSW and fSW+YE, with one vial each measured continuously for DIC concentration and $F^{14}C$. Likewise, out of the remaining vials additional samples were taken, which align similarly well with the continuous measurements (Figure S 9).

Throughout the 85 days of incubation, temperature remained stable between 2.15 to 2.90°C. As the in-situ measurements of pH and oxygen concentrations are salinity-dependent, we assessed the salinity for each vial by measuring chloride concentrations (Figure S 10), finding no significant shift in chloride over the 85 days with stable values of 481±8 mmol/L. This translates to an average salinity of S=30.8±0.3 (n=31). Similarly, sulfate concentrations were consistent at 24.8±0.4 mmol/L (n=31). Oxygen concentrations measured at every sampling event confirmed that vials were always replete in oxygen, with lowest values at day 2 of 289±11 µmol/L (Figure S 11). pH changed within all three treatments. The pH in fSW increased between day 0 and 2 from 7.41±0.03 to 7.61±0.01 and rose steadily thereafter to 7.95±0.02 at 85 days. In contrast, pH in both SW+YE and fSW+YE dropped between day 0 and 2 from 7.65±0.03 to 7.50±0.03 and from 7.58±0.01 to 7.28±0.01, respectively. Afterwards, pH in both treatments increased similarly until day 14 to 7.55±0.03 and 7.33±0.01, and then remained relatively stable. All three treatments showed only minor variations in NO_3^- concentrations, and NO_2^- concentrations were continuously below the detection limit of <0.25 µmol/L (Figure S 12).

Figure S 8: Coastal bluff soil profile CAC19-Y1 at Sobo Sise (Lena Delta, Russia) where Yedoma was sampled.

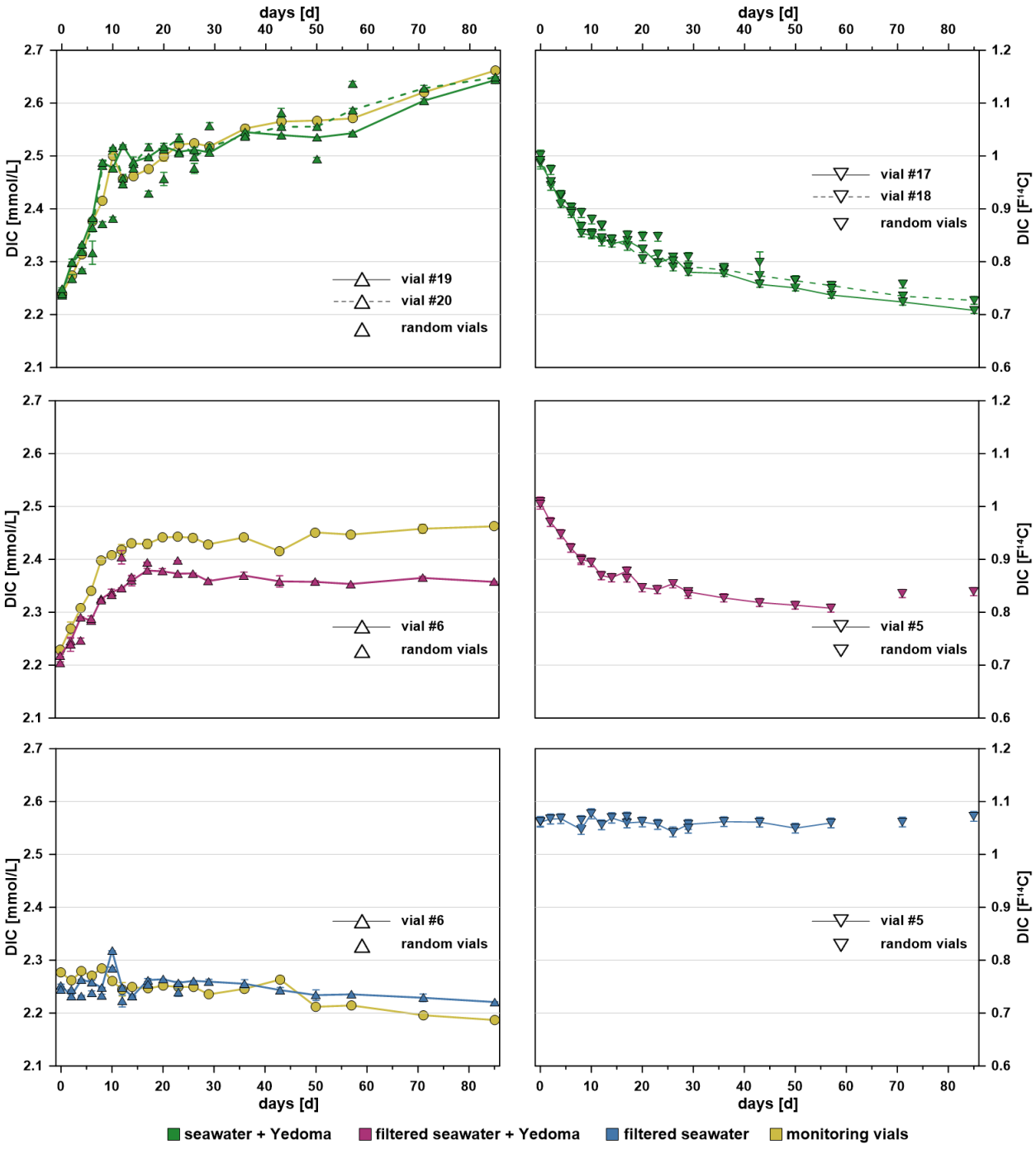

Figure S 9: Raw DIC (left) and DI^{14}C (right) in continuous vials (connected by lines) and random vials of the same category (scatter). Error bars display measurement uncertainties (SW+YE in green; fSW+YE in magenta; fSW in blue; monitoring vials of the associated treatment in yellow). 1σ measurement uncertainties are displayed for all datasets.

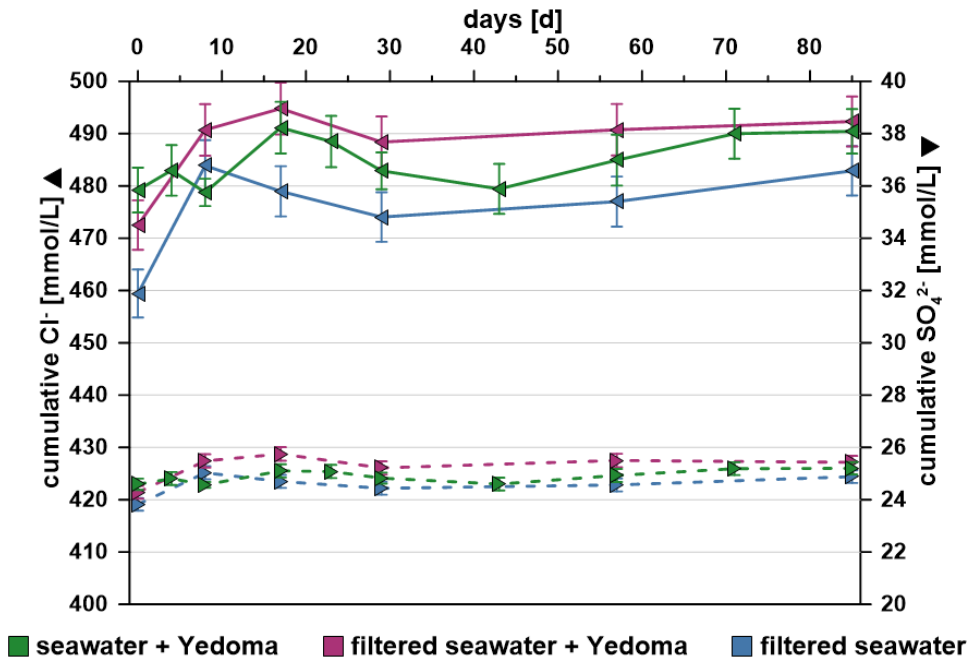

Figure S 10: Concentrations of chloride Cl^- (left facing triangles with solid lines) and sulfate SO_4^{2-} (right facing triangles with dashed lines) in SW+YE (green), fSW+YE (magenta) and fSW (blue). 1σ measurement uncertainties are displayed for all datasets. SW+YE uncertainties at day 0, 8, 29, and 85 are determined by standard deviation of all vials measured per timepoint.

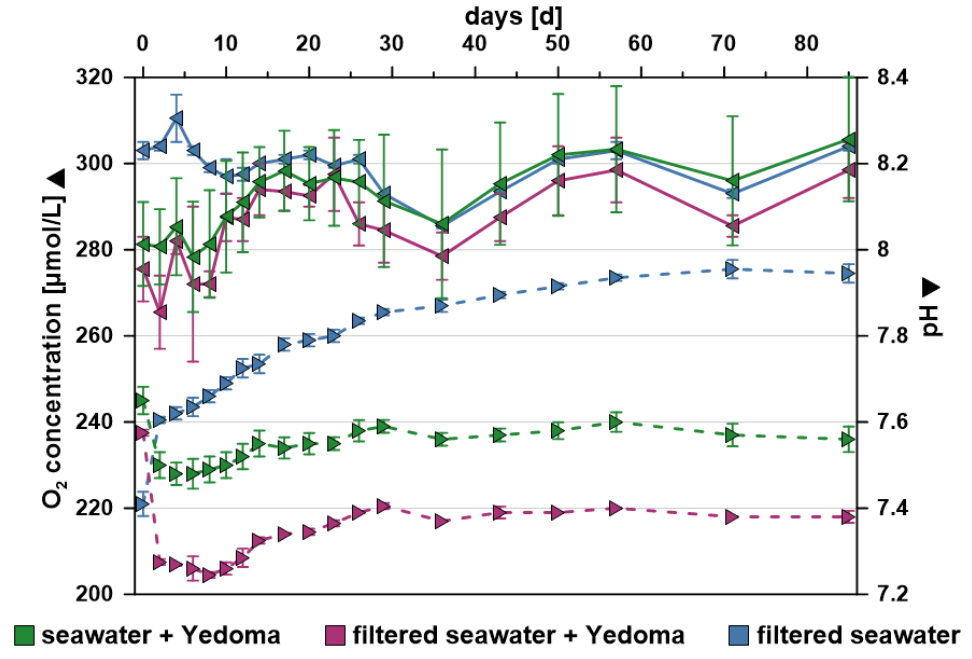

Figure S 11: Optode measurements in monitoring vials. O_2 concentrations (left facing triangles with solid lines) and pH (right facing triangles with dashed lines) for SW+YE (green); fSW+YE (magenta); and fSW (blue) over 85 days at an average salinity of 30.8 ± 0.8 (n=31). Error bars indicate 1σ uncertainty in SW+YE, and range of measurements in fSW+YE and fSW (may be smaller than the symbols).

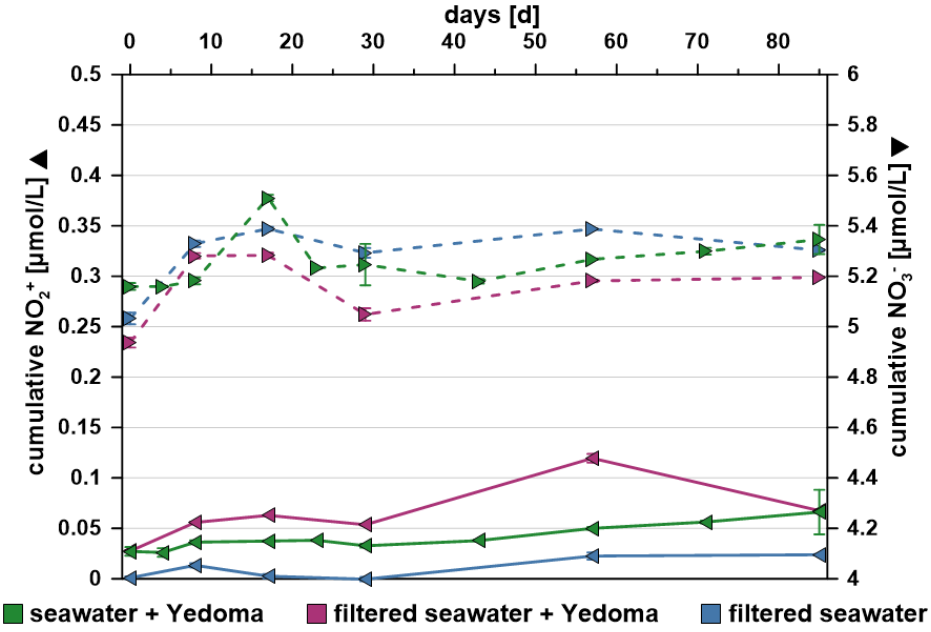

Figure S 12: Concentrations of nitrite NO_2^- (left facing triangles with solid lines) and nitrate NO_3^- (right facing triangles with dashed lines) in SW+YE (green), fSW+YE (magenta), and fSW (blue). 1σ measurement uncertainties are displayed for all datasets. SW+YE uncertainties at day 0, 8, 29, and 85 are determined by standard deviation of all vials measured per timepoint.

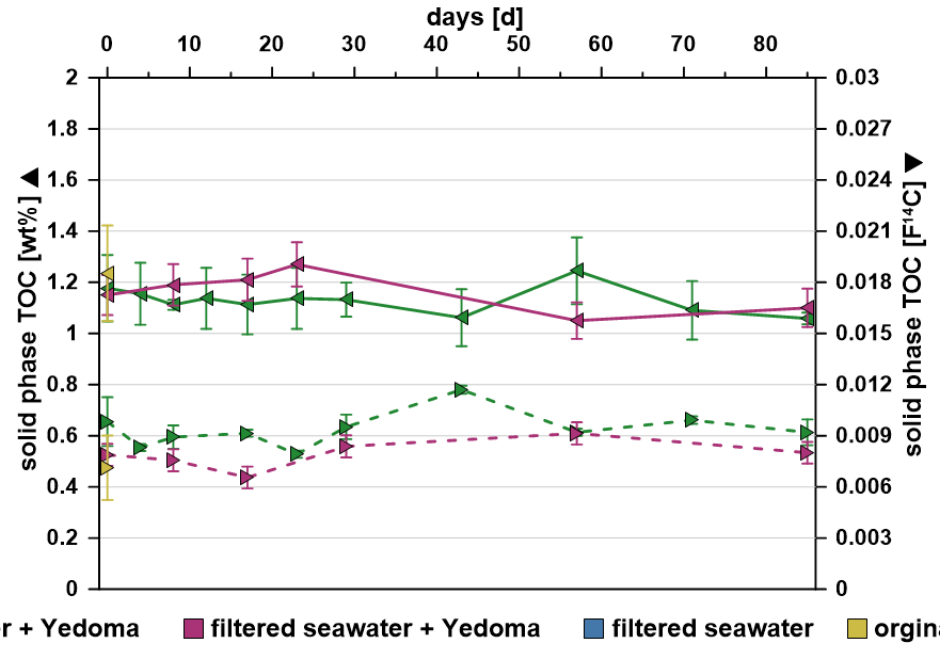

Figure S 13: Total organic carbon (TOC; left facing triangles with solid lines) content in wt% of the residual particulate matter at days 0 to 85 and corresponding $F^{14}C$ values (right facing triangles with dashed lines) in SW+YE (green) and fSW+YE

(magenta). 1σ measurement uncertainties are displayed for both datasets. SW+YE uncertainties at day 0, 8, 29, and 85 are determined by standard deviation of all vials measured per timepoint.

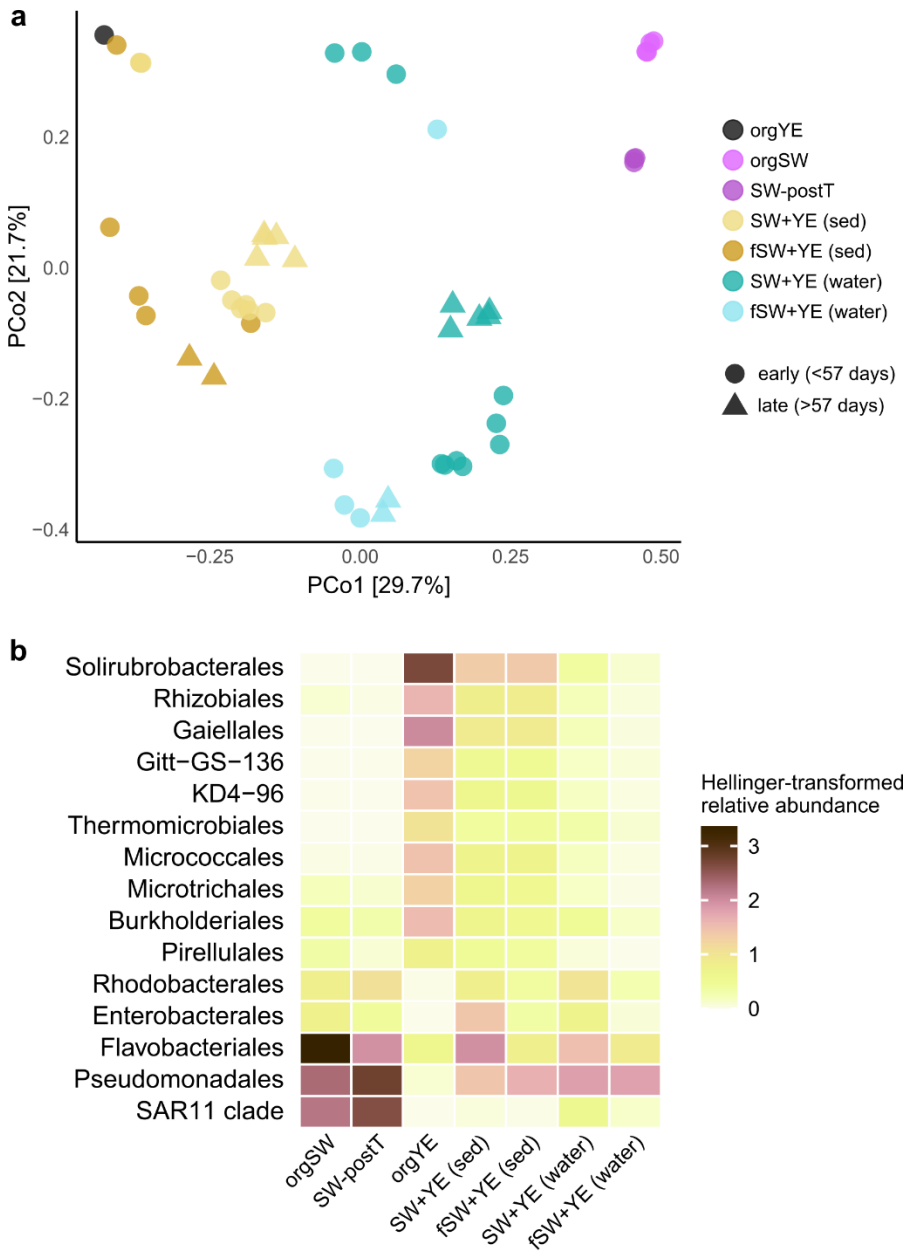

Figure S 14: Overview of bacterial community structure. A: Principal Coordinates Analysis showing distinct differences between treatments, with some separation between early vs. late incubation stages. B: Heatmap of most abundant bacterial orders, displayed as Hellinger-transformed relative abundances. *orgSW: original seawater, SW-postT: original seawater after transport, orgYE: original Yedoma permafrost, SW+YE: seawater+Yedoma, fSW+YE: filtered seawater+Yedoma, fSW: filtered seawater, water: free-living fraction / aqueous phase, sed: particle-attached fraction.*

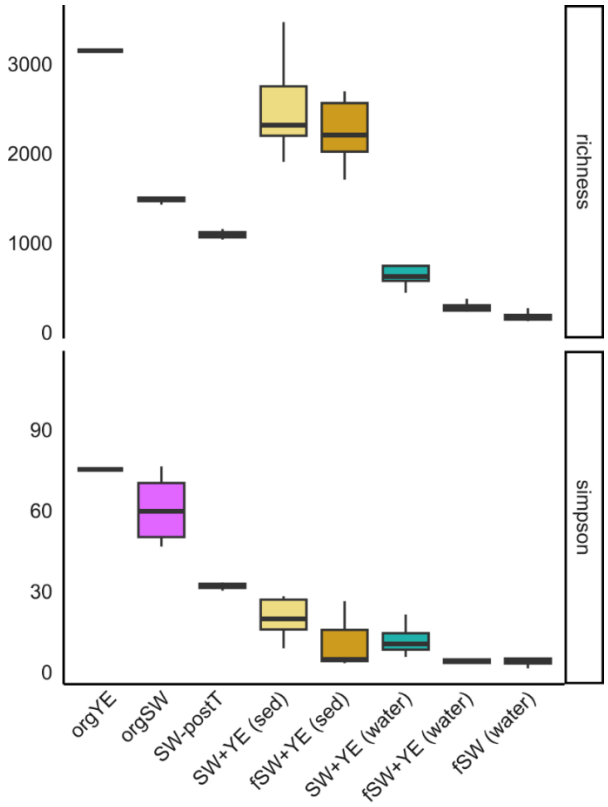

Figure S 15: Bacterial alpha-diversity, displayed as species richness (top) and inverse Simpson index (bottom). orgSW: original seawater, SW-postT: original seawater after transport, orgYE: original Yedoma permafrost, SW+YE: seawater+Yedoma, fSW+YE: filtered seawater+Yedoma, fSW: filtered seawater, water: free-living fraction / aqueous phase, sed: particle-attached fraction.

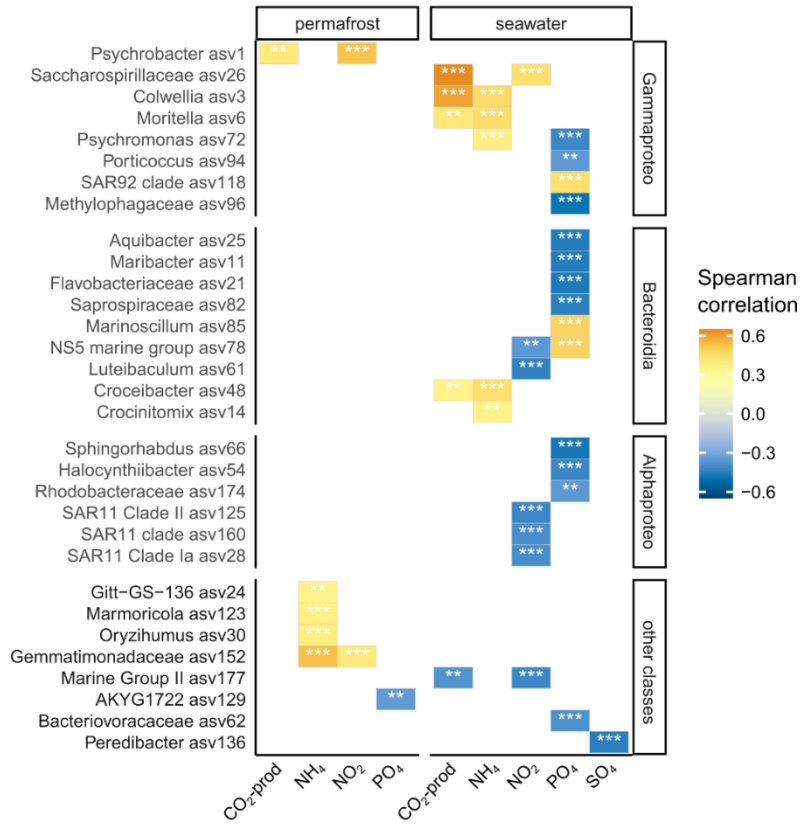

Figure S 16: Correlations of bacterial ASVs with physicochemical parameters. ASVs were assigned to originating from either permafrost or seawater based on their maximum relative abundance.

Table S 3: Oxygen concentrations [µmol/L] in monitoring vials of SW+YE (green), fSW+YE (magenta), and fSW (blue).

time point	time [days]	SW+YE M1	SW+YE M2	SW+YE M3	fSW+YE M1	fSW+YE M2	fSW M1	fSW M2
t0	0	-	-	-	-	-	-	-
t1	2	274	275	293	257	274	305	303
t2	4	280	275.0	301.0	285.0	279.0	316.0	305.0
t3	6	273	266.0	296.0	254.0	290.0	304.0	302.0
t4	8	273	272.0	299.0	269.0	275.0	300.0	298.0
t5	10	278	279.0	306.0	282.0	293.0	301.0	293.0
t6	12	286	280.0	307.0	282.0	292.0	299.0	296.0
t7	14	292	288.0	307.0	288.0	300.0	300.0	300.0
t8	17	295	289.0	311.0	289.0	298.0	302.0	300.0
t9	20	292	287.0	307.0	290.0	295.0	303.0	301.0
t10	23	292	286.0	312.0	289.0	306.0	299.0	300.0
t11	26	295	284.0	308.0	281.0	291.0	300.0	302.0
t12	29	282	279.0	313.0	277.0	292.0	293.0	293.0
t13	36	278	270.0	310.0	273.0	284.0	285.0	286.0
t14	43	289	282.0	315.0	282.0	293.0	294.0	293.0
t15	50	292	292.0	322.0	288.0	304.0	302.0	300.0
t16	57	294	292.0	324.0	291.0	306.0	305.0	301.0
t17								
t18	71	288	283.0	317.0	283.0	288.0	294.0	292.0
t19								
t20	85	297	294.0	326.0	305.0	292.0	305.0	303.0

Manuscript 3

^{14}C age distribution in organic matter fractions separated by Ramped Pyrolysis-Oxidation from permafrost soils incubated in seawater

In preparation for Geophysical Research Letters

Authors

Manuel Ruben[1,2], Hannah Marchant[3,4], Torben Gentz[1], Valier Galy[5], Gesine Mollenhauer[1,2,3]

Affiliation

[1] Alfred Wegener Institute Helmholtz Centre for Polar- and Marine Research, Am Handelshafen 12, 27570 Bremerhaven, Germany
[2] University of Bremen, Bibliothekstraße 1, 28359 Bremen, Germany
[3] MARUM - Center for Marine Environmental Sciences, University of Bremen, Leobener Straße 8, 28359 Bremen, Germany
[4] Max Planck Institute for Marine Microbiology, Celsiusstraße 1, 28359 Bremen, Germany
[5] Woods Hole Oceanographic Institution, 86 Water St, Falmouth, MA 02543, United States of America

Abstract

Along the Arctic coastlines, rapid warming results in the release of significant amounts of previously frozen permafrost organic carbon (OC) into the coastal ocean. This has the potential to amplify the permafrost carbon feedback through rapid microbial respiration. Despite the global importance of this process, the long-term destiny of permafrost OC upon deposition on the seabed remains largely unknown. The specific traits of the organic matter that could be the source of carbon emissions are uncertain. It is hypothesized that a labile subfraction within the permafrost soils, rather than millennia-old organic carbon, is more likely to be remineralized. To evaluate this hypothesis, we subjected samples to ramped pyrolysis-oxidation coupled with ^{14}C analysis of emitted gases. The samples are the remains of an incubation experiment where Yedoma permafrost soils were incubated in seawater for 85 days. Based on the analysis of produced gas, there was no preference for utilizing a younger subfraction of Yedoma deposits during incubation. This suggests that emissions from microbially utilized permafrost soils reintroduce fossil carbon back into the active carbon cycle. Furthermore, the analysis of the thermograms produced during pyrolysis suggests that the current state of ramped pyrolysis-oxidation may not be sensitive enough to investigate OC cycling in sediments during an incubation experiment with homogeneous substrate subfractions.

Introduction

Organic carbon in sediments is ENTRAINED located in particle mesopores, bound to particle surfaces, or remains unprotected in pore space (Blattmann et al., 2019; Mayer et al., 2004), influencing OC reactivity (Cui et al., 2022) and thus its susceptibility to biotic and abiotic decomposition (Hemingway et al., 2017a; Leifeld & von Lützow, 2014; Plante et al., 2009). Quantifying OC susceptibility and decomposition is crucial for a total estimate of the carbon-climate feedback as it counteracts OC sequestration by the production and release of greenhouse gases (Galy et al., 2015; Hilton & West, 2020; Kölling et al., 2019). However, the assessment of OC degradability in sediments is challenging. Using specific compounds (biomarkers) as indicators for OC degradability allows for an estimation of certain subfractions (e.g. pigment degradation using chlorins), but biomarkers account for <1 % of the total OC in sediments (Alkhatib et al., 2012). On the contrary, using bulk parameters provides information on mean characteristics of often complex OC mixtures in sediments (Hedges, 1992), thus oversimplifying or masking processes.

An intermediate technique involves the thermal degradation of OC through the use of ramped pyrolysis-oxidation (RPO) paired with isotopic analysis of the emitted gases, such as the performance of radiocarbon (^{14}C) analysis (Rosenheim et al., 2008). The underlying concept behind RPO is the correlation between molecular thermal stability and susceptibility to biological degradation of OC. By quantifying CO_2 emissions from the combustion of pyrolysis products produced in a temperature ramp, the proportions of labile (low-temperature pyrolysis) to refractory (high-temperature pyrolysis) organic matter can be determined. The thermal resistance of OC to pyrolysis has been suggested as a proxy for OC lability and is thus indicative of, but not equivalent to, bioavailability (Leifeld & von Lützow, 2014). This method has become widespread in the analysis of soil or sediment samples (Plante et al., 2013; Rosenheim et al., 2008; Zhang et al., 2017). Its use in conjunction with ^{14}C analysis enables the determination of residence times or turnover rates of specific fractions within the sedimentary OC pool and across environmental gradients (Cui et al., 2022; Hemingway et al., 2018). Furthermore, in a recent study the OC dynamics in a short term incubation experiment were investigated, making it possible to estimate OC degradation rates related to the age of dissolved permafrost OC (Rogers et al., 2021). This discovery paves the way for a novel application approach for PRO-^{14}C analysis.

The release and remineralization of permafrost OC in the Arctic is commonly seen as a strong feedback mechanism, which results from global warming (Schuur et al., 2022). However, there is limited knowledge regarding the destiny of permafrost OC in the marine ecosystem, even though there are considerable erosion rates along Arctic coastlines (Irrgang et al., 2022). This knowledge gap is exemplified by the

significant variation in anticipated permafrost OC utilization after entering the Arctic Ocean, which ranges from approximately 3% (Tanski et al., 2019) to roughly 66% (Vonk et al., 2012) to 85% (Bröder et al., 2018). Incubating Yedoma permafrost soil in Arctic seawater for 85 days, Ruben et al. (submitted; manuscript 2) estimated that ~3 % of the Yedoma OC was released of which ~88 % originated from a fossil source (likely within the Yedoma). However, they further reported that changes in bulk sedimentary composition are below detection limit. Both the total OC (TOC) content and its respective radiocarbon signatures ($F^{14}C$) did not show significant changes throughout the incubation experiment. The sizes of samples used in this incubation experiment are too small to apply methods like e.g. compound specific radiocarbon analysis (Ruben et al., 2023). To resolve this issue we investigated the residual sedimentary OC mixture using temperature ramped pyrolysis, coupled with both subsequent oxidation (RPO) and carbon isotopic analysis of evolved CO_2 gases (Hemingway et al., 2017a). CO_2 splits were collected in the range between 50-300 kJ mol^{-1}, covering low (<150 kJ mol^{-1} or <350°C), medium (150-185 kJ mol^{-1} or ~350-500°C), and high (>185 kJ mol^{-1} or >500°C) activation energy intervals defined and used in previous studies (Hemingway et al. 2018; Cui et al. 2022; Venturelli et al. 2020). By quantifying continuously the evolved CO_2 with RPO during a controlled temperature ramp (Hemingway et al., 2017b) and subsequent estimation of modeled Arrhenius activation energy (E) via the inverse method of Hemingway et al. (2017a), we were able to investigate changes in E distribution over time and to link E to $F^{14}C$ values of the respective fractions. This allows for an estimation of the source and age of the different fractions. This approach has previously been shown to be an effective tool to investigate soil and permafrost soil dynamics, in both spatial (Hemingway et al., 2018; X. Zhang et al., 2017) and temporal (Rogers et al., 2021; Sanderman & Grandy, 2020) resolution.

Methods

Experimental setup and previous data

The samples analyzed in this experiment were obtained during the experiment described in Ruben et al. (submitted; manuscript 2), who incubated Yedoma permafrost from the Lena delta in near shore sea water from the eastern Kara Sea in the dark at ~2°C. The analysis of the dissolved carbon pools over the course of the experiment in the previous study showed that of the initially incubated organic carbon (OC), 2.9 ± 0.3% and 0.9 ± 0.3 % were released into the dissolved inorganic carbon (DIC) and dissolved organic carbon (DOC) pools, respectively. While 89 ± 6% of the incubated OC remained particle-bound in the sediment phase, total organic carbon (TOC) measurements of the residue were not precise enough to quantify changes in the sediments. Samples of the sediment residue were therefore selected for RPO from

7 time points throughout the 85-day long experiment (Table 2) and thus represent different states of decomposition.

In addition to the samples produced by the incubation experiment, two samples were prepared to assess the effects of DOC leaching from Yedoma. For this purpose, 90 mL of MQ-water were added to 3 mL of a Yedoma slurry (same setup as in the incubation experiment) and homogenized by shaking. Both samples were centrifuged at 1000 rpm for 5 minutes and the supernatant water-phase was pipetted off – equivalent to the treatment of the incubated samples.

Bulk TOC content and bulk radiocarbon analysis were performed and reported in Ruben et al. (submitted; manuscript 2). Within the scope of our study, a total of 19 RPO measurements were performed on 16 samples to investigate changes in the sediments over time. The samples comprised 2 original Yedoma permafrost samples (org.YE) without any treatment, 2 Yedoma permafrost samples rinsed with MQ (YE+MQ; to remove DOC factions), and 12 sediment residue samples of Yedoma after incubation in seawater (SW+YE), spanning from day 0 until day 85 (Table 3, no DOC present - due to sample treatment, see above). Additionally, sub-fractions of 9 samples were collected for more detailed analysis using radiocarbon (Table 3). Sediment samples were freeze-dried, homogenized, and decarbonated by fumigation with HCl at 60°C for 72 hours following the protocol of Whiteside et al. (2011), prior to RPO.

Ramped pyrolysis-oxidation

The RPO setup of the National Ocean Sciences Accelerator Mass Spectrometry (NOSAMS, Woods Hole, USA) facility was used for sample pyrolysis-oxidation and subsequent collection of produced CO_2 gas for $F^{14}C$ measurements (Hemingway et al., 2017b; Rosenheim et al., 2008). The setup consists of a two-stage oven, where samples are steadily pyrolyzed in the first oven (ramped temperature) under a constant O_2 and He flow. The emitted volatile OC compounds were subsequently fully oxidized into CO_2 in the combustion oven. The temperature ramp in the sample oven was set to 5°C min^{-1} and temperature was increased to a maximum of 920°C, while the combustion oven temperature was kept constant at 800°C. CO_2 production was quantified using a Stable Systems CA-10a CO_2 analyzer. The recoded thermograms were converted into Arrhenius activation energy using the code of Hemingway et al. (2017a), setting the correction factor λ uniformly at 0.3 for better sample comparison. Even though the model parameters do not cover the wide range of enzymatic reactions possible, it was used to estimate OC lability (Cui et al., 2022). Splits for $F^{14}C$ were frozen out in liquid nitrogen and separated right at the vacuum line. To assess thermogram precision the temperature fluctuations between oven and temperature logger were determined by three runs each of a sucrose and a potassium hydrogen phthalate (KPH) standard. Between

Table 3: Performed RPO runs of individual treatments, days incubated, related number of thermograms and radiocarbon samples.

treatment	days incubated	Subsamples analyzed [#]	Themograms [#]	Radiocarbon samples [5 fractions]
org. YE	N/A	2	2	1
YE+MQ	N/A	2	2	1
SW+YE	0	3	4	1
SW+YE	4	1	1	1
SW+YE	8	2	2	1
SW+YE	17	1	1	1
SW+YE	29	2	2	1
SW+YE	57	1	1	1
SW+YE	85	2	4	1

the two standard materials, the maximum temperature shifts of a total of three peak maxima were determined, displaying shifts in temperature of 10°C (sucrose ~265°C), 35°C (sucrose ~500°C), and 21°C (KPH ~290°C). In energy space this correlates to about 2-9 kJ mol^{-1}, accounting for an average standard deviation of 10°C (4-16°C; n=3) or 2.5 kJ mol^{-1} (0.5-4 kJ mol^{-1}; n=3).

Radiocarbon analysis

Five splits were taken per analyzed sample at about the same temperature intervals of F1 ~125-270°C (~90-125 kJ mol^{-1}), F2 ~270-320°C (~125-137 kJ mol^{-1}), F3 ~320-370°C (~137-150 kJ mol^{-1}), F4 ~370-450°C (~150-170 kJ mol^{-1}), and F5 ~450-920°C (~170-290kJ mol^{-1}). CO_2 gas splits were cryogenically trapped, dried and flame-sealed in glass tubes containing copper oxide and sliver for subsequent re-combustion at 550°C for 4 hours to remove any leftover sulfur and phosphorus impurities prior to measurements. Radiocarbon analysis were performed at the MICADAS facility at the Alfred-Wegener-Institute, Bremerhaven, Germany. Sealed glass ampules were cracked open under a constant He flow (80 mL sec^{-1}) and transferred for 60 seconds onto a CO_2 adsorbing zeolite trap. Subsequent CO_2 radiocarbon analysis was performed as described in Mollenhauer et al. (2021). $F^{14}C$ values of the RPO trapped gases were blank corrected using the blank determined by Hanke et al. (2023), assuming a constant blank for all samples of 13.8 ngC $°C^{-1}$ and a $F^{14}C = 0.268 \pm 0.054$.

Results and Discussion*Thermograms*

In this sample set, the first maximum of CO_2 yield is observed in the low activation energy interval <150 kJ mol^{-1} and the second in the medium activation energy interval between 150-185 kJ mol^{-1}. In the high activation energy interval >185 kJ mol^{-1}, the majority of CO_2 is emitted under E of below 200 kJ mol^{-1} followed by uniform tailing (Figure 15). The strongest variance in the thermograms between the samples can be observed in the medium activation energy range between 150-185 kJ mol^{-1}. However, sample heterogeneities of the individual sampling events were bigger than trends over time. In all samples but one (SW+YE #19) the E maximum was found in the in medium activation energy interval at 169±4 kJ mol^{-1} (n=18), while for SW+YE #19, the E maximum was at 139 kJ mol^{-1} (n=1). The E maximum of the incubated and MQ washed samples is at 166±8 kJ mol^{-1} (n=15; Figure 16) and is therefore slightly lower in comparison to 172±5 kJ mol^{-1} (n=2) of the original Yedoma. The incubated samples showed a slightly higher p(0;E) maximum of 0.028±0.006 and a lower E mean distribution of 154±2 kJ mol^{-1} (n=15; Figure 17) in comparison to the original Yedoma with a p(0;E) maximum of 0.023±0.001 and E mean of 159±2 kJ mol^{-1} (n=2). Collectively E_std is uniformly distributed between all samples (incl. org.YE) with 25.9±0.9 kJ mol^{-1} (n=18). However, none of these values show a significant shift, with all but E_std (p = 0.07 and stabile values) displaying p > 0.35. Distribution of activation energy (E) of the analyzed samples yielded fairly consistent bimodal values throughout the spectrum of measured samples (Figure 15), indicating the presence of both labile and more stable molecular compounds (X. Zhang et al., 2017). Previous RPO work of Zhang et al. (2017) displays a less pronounced bimodal distribution in their analyzed Yedoma samples. Comparing our thermograms with their selection of permafrost soils and downstream sediments, our incubated Yedoma sample resembles more the organic rich top soil samples, even though our samples have a Pleistocene age (Fuchs et al., 2020). On the contrary, by comparing thermograms to the Hemingway et al. (2018) selection of mountainous soils and downstream sediments, the high relative percentage of mid to high activation energy interval of our samples resembles more sedimentary characteristics.

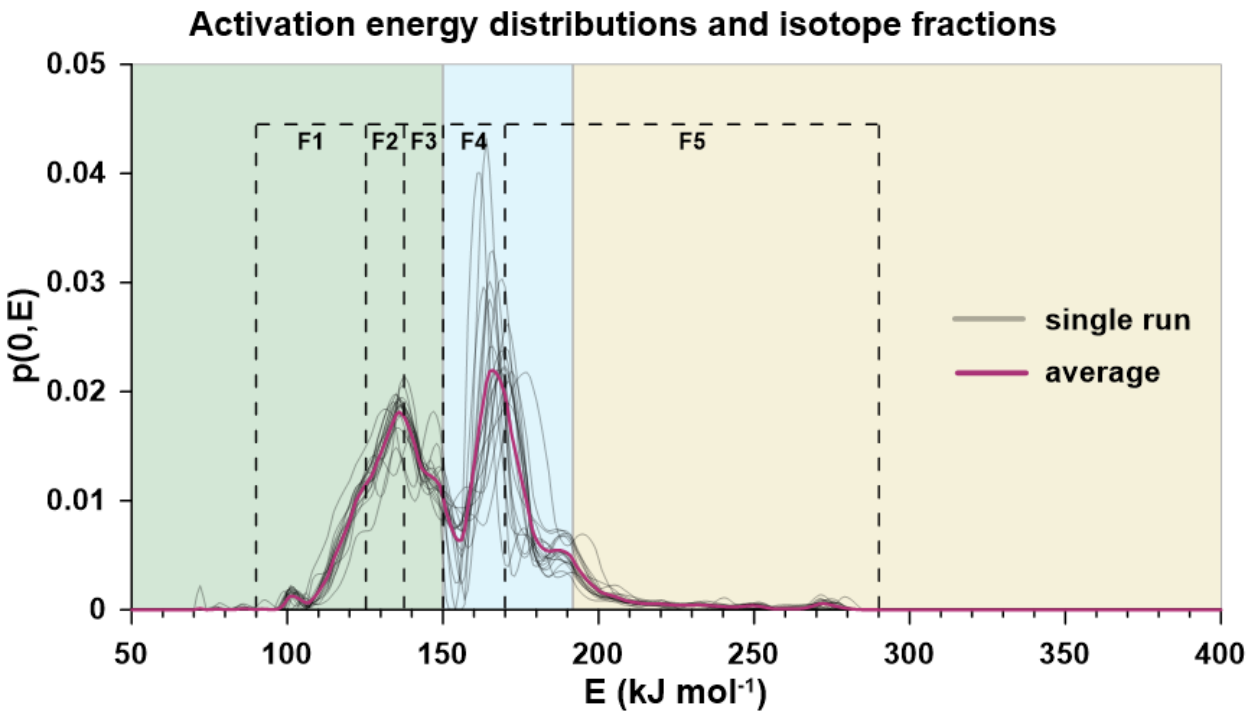

Figure 15: Thermograms of all samples run on the RPO in gray and the average in magenta, displayed in relative contributions of p(0,E) per calculated energy bin (E). Low, medium, and high activation energy intervals are indicated in the green, blue, and light brown boxes, respectively. Splits (F1-5) of for ^{14}C splits are indicated in dashed lines.

The weighted distribution of emitted CO_2 with activation energy located in three intervals (different OC thermal lability) showed more nuanced differences. However, statistically significant changes are only observed in the medium activation energy interval. By comparing the three activation energy intervals of original Yedoma with 45 ± 2 % (low), 44 ± 1 % (medium), and 11 ± 3 % (high; n=2) to the mean of day 85 of 48 ± 1 % (low), 42 ± 1 % (medium), and 10 ± 0 % (high; n=4), a relative increase of low activation energy interval is apparent with a loss in the medium range. Thus, four likely scenarios are apparent:

1. A loss of particle bound OC in the medium and high activation energy interval.
2. Accumulation of low activation energy OC onto sedimentary particles by sorption.
3. Microbial breakdown of more complex OC (with higher activation energy), resulting in enrichment of less complex OC (smaller molecules, lower activation energy) during the incubation.
4. A combination of the above.

Furthermore, it was hypothesized that the molecular components of the high activation energy interval are stabilized OC due to mineral association, which shield OC in the pore space from microorganisms and their extracellular enzymes (Plante et al., 2009). This suggests that sorption of labile OC to particles may cause mineral which may prevent microbial breakdown of the high activation energy interval during incubation. Nevertheless, the observed temperature discrepancy between standard materials may be caused by offsets in the oven and the temperature logger and thus may have a noteworthy influence on the above-mentioned quantification (in particular considering possible matrix effects that have not been quantified). While the thermograms of the incubated Yedoma resemble those of typical soils, the changes to the sedimentary OC pool during the incubation were too subtle for the resolution of the RPO method alone in its current state.

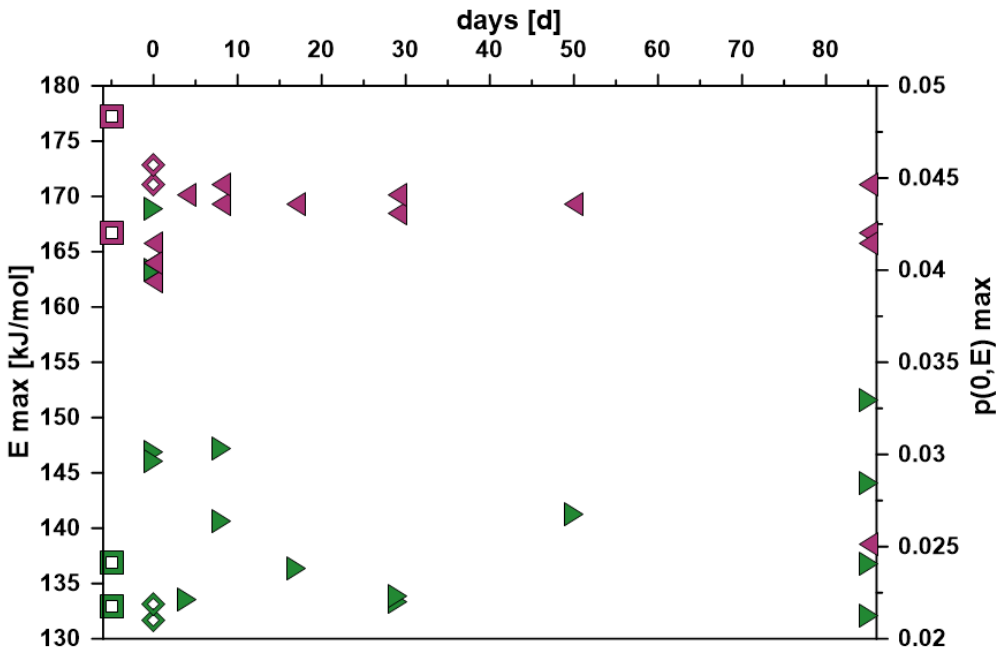

Figure 16: Individual sample run parameters of E maxiumim of both E bin (kJ mol-1) and maximum relative intensity in p(0,E) are displayed in magenta and green, respectivly. Trangels show indubated time points, stratching from day 0 to 85. Diamonds indicated MilliQ rinsed samples at day 0. Squares display original Yedoma samples (not incubated).

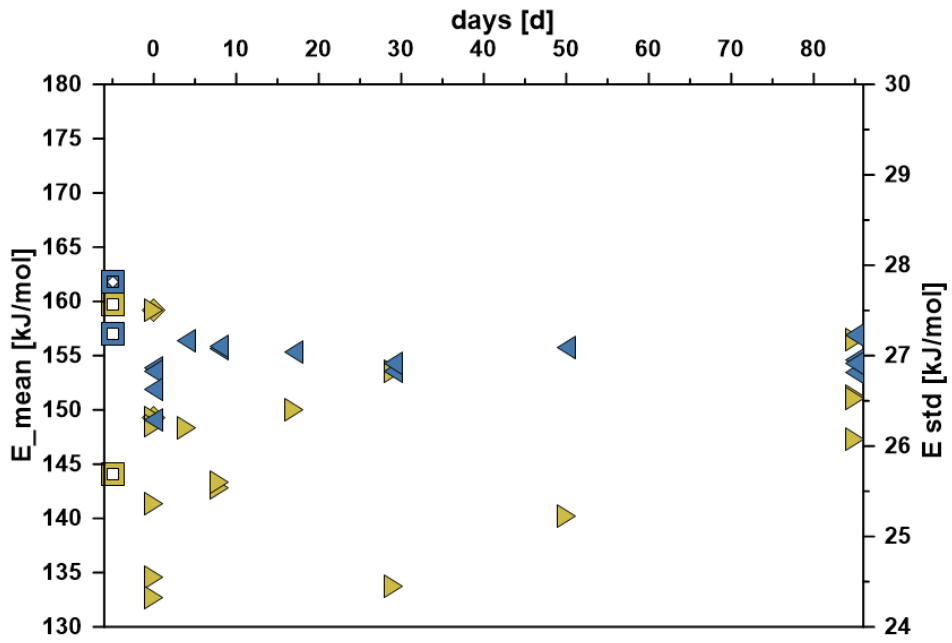

Figure 17: Individual sample run papameters of E mean and its standard diviation are displayed in blue and yellow, respectivly. Trangels show indubated time points, stretching from day 0 to 85. Squares display original Yedoma samples (not incubated).

Radiocarbon analysis

The emitted CO_2 gas from RPO combustion was trapped and measured for radiocarbon content in 5 temperature/activation energy intervals, here forth "^{14}C-splits" (Table 4). The total ^{14}C-splits measured collected within the temperature range of 125-920°C (90-290 kJ mol^{-1}) show F^{14}C values ranging between 0.0041±0.0017 and 0.0178±0.020 with an average F^{14}C signature of 0.0084±0.0035 which corresponds to an age of 38417±2772 ^{14}C years (n=37). Data from the incubated Yedoma samples do not show a systematic shift over time when all ^{14}C-splits are combined. Overall, radiocarbon data are fairly homogeneous when considered as a total, while the individual ^{14}C-splits by themselves show a more nuanced picture. Our data thus suggest that the Yedoma sample studied here contained organic matter of rather uniform age, which could be expected considering the proposed formation process for Yedoma deposits (Schirrmeister et al., 2013). Our observations, however, are in contrast with results from Zhang et al. (2017), who analyzed Yedoma using similar methods. These authors reported distinctively younger ages in the low activation energy interval (~20000 ^{14}C yrs) in comparison to the high activation energy interval (~35000 ^{14}C yrs), despite the overall younger bulk TOC age of 25202 ^{14}C years, indicating a more heterogeneous composition of their sample.

The radiocarbon signatures of the ^{14}C-splits of both the non-incubated original and the leached Yedoma lay within their 2-sigma uncertainty ranges in F2-3 (Figure 18), and a slightly lower value in the leached Yedoma in F5 is observed. ^{14}C-splits 1 of the leached Yedoma was lost due to sample preparation issues (tubes broke in cracker before chamber was sealed).

To investigate the changes in more detail in the different ^{14}C-splits, we applied a linear fit to the data. However, with the exception of F4 R^2 values are <0.5 (Table 4; Figure 18) and changes in $F^{14}C$ values are minor. Only the ^{14}C-split 4 shows a statistically significant change over the incubation period with a P = 0.025. Of the 5 temperature ^{14}C-splits, changes in the $F^{14}C$ signature over the time of incubation showed an increase in $F^{14}C$ in F1-4 and a slight decrease in F5. Overall, F3 displays the lowest change at a range of $F^{14}C$ values from 0.0071±0.0017 to 0.0136±0.0019 with an average of 0.0083±0.0030. (n=8). In F3 the linear fit suggests that on average the $F^{14}C$ values increased between day 0 to 85 by 0.0012 (R^2=0.034; n=6). F1 and F2 show the biggest change over the 85 days of incubation, with linear fits suggesting an $F^{14}C$ increase of 0.0045 (R^2=0.142; n=6) and 0.0044 (R^2=0.121; n=7), respectively. Of these two, F1 is younger with average $F^{14}C$ of 0.0109±0.0027 (n=7) in comparison to $F^{14}C$ of 0.0093±0.0044 of F2 (n=9), which displays the biggest scatter in all of the 5 fractions. While F4 was collected in the range of medium

*Table 4: Data compilation of ^{14}C-splits (temperature and activation energy) for $F^{14}C$ signature and ^{14}C age, as well as changes over the incubation period (*based on linear regression).*

^{14}C-splits	Temp. [°C]	Activation energy [kJ mol-1]	Average $F^{14}C$	Average ^{14}C age	n	Average change of $F^{14}C$ day 0-85*	R^2	n
F1	125-270	90-125	0.0109 ±0.0027	36320 ±1780	7	0.0048	0.143	6
F2	270-320	125-137	0.0093 ±0.0044	37567 ±3105	9	0.0047	0.121	7
F3	320-375	137-150	0.0083 ±0.0030	38452 ±2496	8	0.0012	0.034	6
F4	375-450	150-170	0.0052 ±0.0006	41911 ±1460	6	0.0029	0.950	4
F5	450-920	170-290	0.0075 ±0.0017	39355 ±1694	7	-0.0029	0.447	5
All	125-920	90-290	0.0084 ±0.0035	38418 ±2772	37	0.0015	0.024	28

activation energy and thus can be considered to be semi-labile, $F^{14}C$ data suggest likewise little alterations during the incubation processes of this fraction. Average $F^{14}C$ values are at 0.0056±0.0006 (n=6) with the lowest scatter of all fractions, ranging from 0.0043±0.0018 to 0.0063±0.0019. Using the linear regression to estimate an average increase of $F^{14}C$ over the 85-day period, F4 $F^{14}C$ values increase by 0.0029 (n=4) displaying by far the best fit with R^2=0.950. The $F^{14}C$ data of the collected F5 is in contrast to F1-4, as the linear regression indicates a decrease of -0.0028 (R^2=0.447; n=5) over the course of the experiment. Values range from 0.0051±0.0018 to 0.0102±0.0018 with an average of 0.0075±0.0017 (n=7). F5 was collected between ~170-290 kJ mol^{-1} in the high-E interval. However, >75 % of the F5 CO_2 collected for ^{14}C analysis was obtained in the mid-E interval between 170-185 kJ mol^{-1}, therefore, the F5 can be considered a mixture of presumably semi-labile and refractory material.

Overall, the ^{14}C data show only very subtle changes in $F^{14}C$ over the course of the experiment, which are only possible to observe due to improvements in radiocarbon analysis in the recent decades. The increase in $F^{14}C$ in F1-4 could indicate:

1. The loss of a particularly old subfraction of the particulate OC (in comparison with the bulk) within the low to mid E interval, due to e.g. microbial utilization or dissolution.
2. Accumulation of younger particulate OC (in comparison with the bulk) or due to sorption onto the particles, e.g. of OC from the water column still introduced with the seawater.
3. A mixture of the two above.

In comparison the decrease in F5 indicates the inverse effects of F1-4, thus either a loss of younger OC, the accumulation of older OC, or both. However, with the "petrogenic tail" above 200 kJ mol^{-1} (likely being radiocarbon free) it seems plausible that F5 becomes increasingly dominated by the petrogenic subfraction in the sample. Nevertheless, it is an interesting observation in itself that the three low and mid activation energy ^{14}C-splits (F1-F4) were collected within the range with highest expected changes during the incubation experiment, due to the lowest molecular bond strength (Leifeld & von Lützow, 2014). However, despite the low activation energy, the F14C data indicates no discernible changes in this range. This suggests that no significantly younger OC subfraction was utilized during the incubation, potentially because it was not present initially. Therefore, it has to be expected that the carbon emissions measured by Ruben et al. (submitted; manuscript 2) may in part have originated from the particulate OC, releasing millennia-old previously locked carbon back to the active carbon cycle.

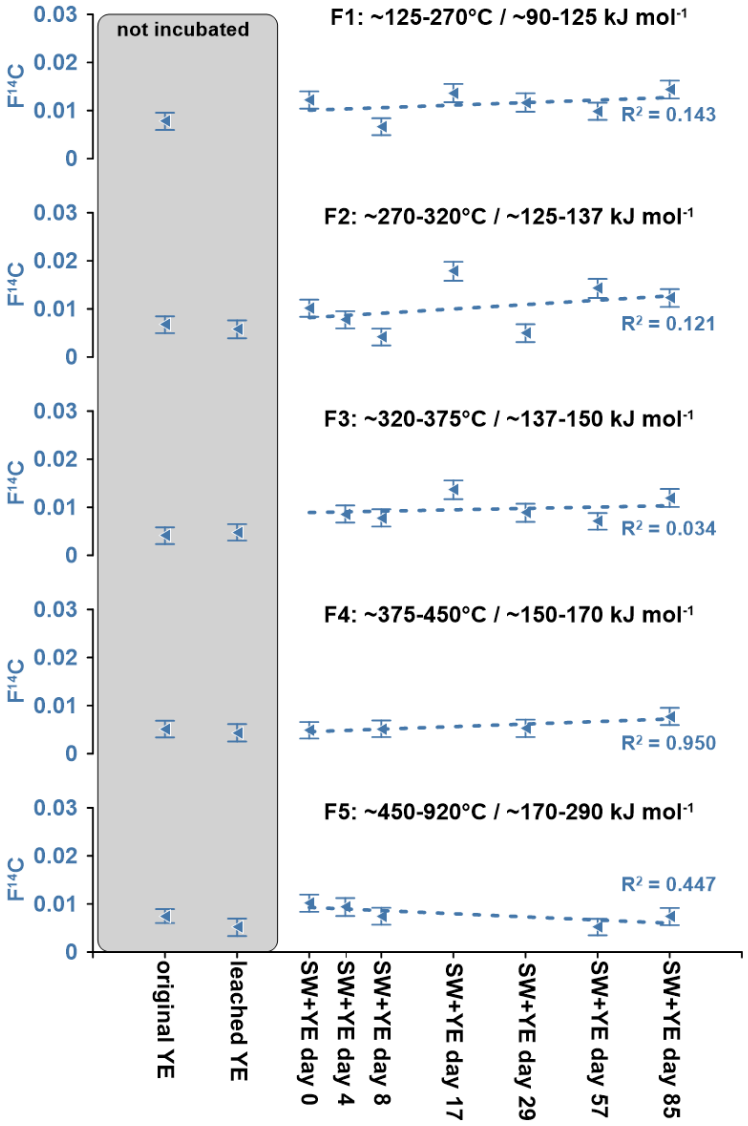

Figure 18: Radiocarbon data of the different ^{14}C-splits (F1-5) of the individual Yedoma (YE) treatments for both not incubated (original and milliQ rinsed) and in seawater (SW) incubated samples at 7 time points. Including the linear fit over the time of incubation and the related R^2 values.

OC remineralization or sorption

Both the thermograms and the ^{14}C data indicated mechanisms related to either OC utilization and dissolution or sorption. When comparing the original Yedoma with the sediments after 85 days of incubation we were able to observe a relative mass gain of the low E interval. Under the assumption that due to the experimental setup, i.e., leaching during the experiment, shaking, and removal of the water phase during sampling, only particulate and mineral associated OC should remain in the samples used for the RPO analysis, sorption of OC onto the particles with low bond strength is the more likely process. Considering the shift of $F^{14}C$ signatures of these fractions (although statistically insignificant) further

supports the sorption of relatively younger material to accumulate on particles. However, the analysis of the dissolved phase parameters by Ruben et al. (submitted; manuscript 2) stands in stark contrast to this hypothesis. Their analysis indicates that ~2.9 ± 0.3 % the incubated OC is released to the DIC pool with 88 ± 12 % of it coming from a fossil (radiocarbon free) source, and an additional 0.9 ± 0.3 % of the initial OC being leached and becoming part of the DOC pool in the water phase. This implies that the observed effects in RPO radiocarbon analysis might rather be attributed to microbial break-down of older OC in the mid and high E intervals. The high variance of the thermograms in the mid E interval supports this hypothesis and aligns with findings of Rogers et al. (2021) who reported the most pronounced shifts in the the mid E interval when incubating permafrost derived DOC for 28 days.

Environmental implications

A long-lasting debate concerning the bio-availability of permafrost organic carbon after thaw concerns the question whether or not the emerging CO_2 and CH_4 originates from the old material which was frozen for millennia or if it simply comes from a younger more labile subfraction within the permafrost complex (Mueller et al., 2015). The radiocarbon analysis of F1-5 of the original Yedoma display an average $F^{14}C$ of 0.0084±0.0035 (n=5) with values ranging from 0.0041±0.0017 to 0.0078±0.0018. There is no statistically significant difference between the 5-temperature based ^{14}C fractions of the original Yedoma used for ^{14}C analysis. Thus, there is no evidence for the presence of a significantly younger subfraction, indicating that not just a younger subfraction within permafrost OC is readily utilized, but that the millennia old organic carbon is bio-available. This is supported by the findings of Ruben et al. (submitted; manuscript 2) reporting that to 88 ± 12 % of the released DIC during the incubation originated from a fossil source. Thus, we suggest that old carbon is released when permafrost soil enters the ocean. This indicates that in fact ancient previously locked up OC is reintroduced in today's carbon cycle when Yedoma is thawed and microbially degraded in marine settings. The rapid release of DOC (Drake et al., 2015; Ewing et al., 2015; Mann et al., 2015; Wickland et al., 2018) and its remineralization (Drake et al., 2015; Rogers et al., 2021; Spencer et al., 2015) has been reported to contribute to an increase of the carbon permafrost feedback (Schuur et al., 2022), but to what extent the carbon emissions from the particle-bound OC will contribute to overall carbon emissions when entering the water column remains to be quantified. Likewise, we cannot estimate how much of the released carbon derives from DOC or the mineral associated OC on the basis of our data. We thus conclude that our approach of using RPO on the sedimentary residue of the incubated sediments is not a suitable method to assess lability changes in the particulate phase of this sample set. However, in settings where a heterogeneous sample is incubated, RPO might reveal preferential degradation of a certain reactivity fraction.

Due to the experimental design of Ruben et al. (submitted; manuscript 2), our data can only be taken as indication towards processes happening in the water column, but enzymatic pathways may very well differ in the sediments after redeposition (Arnosti, 2008, 2011). Therefore, other subfractions of the sedimented Yedoma OC may be available to today's microbes in the sediments and thus may contribute in a different manner to the permafrost carbon feedback. Interestingly, our data suggests, that most of the changes in the particulate OC pool do occur in the medium activation energy range and thus may indicate microbial reworking of larger organic molecules which may be similar in a sedimentary setting.

Conclusion

The analysis of the incubated sediments displayed little change both in the thermograms and their associated $F^{14}C$ signatures. The thermograms show intra-sample variability in the sediments to be bigger than changes over time, even though other parameters (TOC, DIC, or DOC) show strong homogeneity. Thus, RPO does not appear to be suitable for this sample set, despite its much higher sensitivity compared with other methods like simple TOC quantification and bulk radiocarbon analysis. Radiocarbon signatures of the analyzed subfractions are largely uniform and show no significant shift during the incubation period. While this does prevent a quantitative assessment of the carbon released over time, it allows the conclusion that microorganisms do not utilize a particularly young subfraction from the Yedoma, as otherwise a shift towards older ^{14}C ages would have to be visible. Rather the contrary can be concluded: that the microorganisms are able to utilize the Yedoma OC despite its old age and that Yedoma contains old but bioavailable material. Our results therefore support the conclusions of Ruben et al. (submitted; manuscript 2) who report that Yedoma entering the costal ocean will enhance the permafrost carbon feedback with increasing coastal erosion in a warming climate.

Acknowledgements

We are thankful to POLMAR for funding the short-term research stay of M.R. at WHOI and the AWI INSPIRES program for funding the thesis framework. High amount gratitude goes out to the staff of NOSAMS, WHOI, and the MICADAS facility, special thanks to Mary Gaylord and Lea Phillips.

Data availability

All obtained data is publicly available at the PANGAEA data repository at https://issues.pangaea.de/browse/PDI-35860.

Manuscript 4

Release and remineralization of permafrost organic carbon after redeposition on the ocean floor

In preparation for Nature Geoscience

Authors

Manuel Ruben[1,2], Jens Hefter[1], Torben Gentz[1], Florence Schubotz[2,3], Bingbing Wei[1], Bo Liu[1], Michael Fritz[4], Anna Irrgang[4], Anabel von Jackowski[5], Walter Geibert[1], Gesine Mollenhauer[1,2,3]

Affiliation

[1] Alfred Wegener Institute Helmholtz Centre for Polar- and Marine Research, Am Handelshafen 12, 27570 Bremerhaven, Germany
[2] University of Bremen, Bibliothekstraße 1, 28359 Bremen, Germany
[3] MARUM - Center for Marine Environmental Sciences, University of Bremen, Leobener Straße 8, 28359 Bremen, Germany
[4] Alfred Wegener Institute Helmholtz Centre for Polar- and Marine Research, Telegrafenberg, 14473 Potsdam, Germany
[5] CNRS/Sorbonne Université, UMR7621 Laboratoire d'Océanographie Microbienne, Banyuls-sur-Mer, France

Abstract

The Arctic permafrost has been identified as a critical global tipping element in a warming climate. Coastal permafrost erosion releases between 5 and 14 Tg of organic carbon (OC) annually into the Arctic Ocean. Once discharged into the ocean and redeposited on the ocean floor, the fate of permafrost organic matter remains largely unclear. Despite its significant potential to release previously stored carbon back into the atmosphere, the process is accelerated by anthropogenic climate change. By quantifying fluxes of dissolved inorganic carbon (DIC) and analyzing the isotopic composition of nearshore sediments off Herschel Island in the Canadian Beaufort Sea, we identified a release of 0.217 mmo/m²/d DIC with an average signature of $\delta^{13}C$ = -22.44 ± 72 ‰ and $F^{14}C$ = 0.548 ± 0.007. Using a dual carbon isotope endmember model, we estimate that up to 38 ± 10% of the released DIC is derived from subsurface degradation of redeposited permafrost OC, and an additional 15 ± 12% from redeposited active layer OC. This study represents the first direct quantitative assessment of permafrost OC's release into the active carbon cycle after its redeposition on the ocean floor, to the best of our knowledge. By utilizing dual-carbon isotope endmember analysis of bacterial membrane lipids from live sedimentary bacteria, it was

estimated that bacterial communities in shallow subsurface sediment (<25 cm) utilize on average 73 ± 10% of OC from recent marine primary production, 11 ± 6% from permafrost OC, and 16 ± 11% active layer OC. Our data indicate that redeposited permafrost OC can be readily utilized in the subsurface. Considering the tremendous size of the eroding coastal permafrost reservoir even the conservative ~27% contribution may have a long-lasting effect on the global climate, increasing the climate crisis.

Coastal Permafrost

A globally significant reservoir of organic matter resides in the soils and sediments of the northern permafrost zone. In terrestrial ecosystems of the permafrost zone, around 1500 Gt of organic carbon (OC) is estimated to be in the soil and an additional 400 Gt OC in areas with substantial sediment cover and Arctic deltas (Hugelius et al., 2014; Mishra et al., 2021; Schuur et al., 2022; Strauss et al., 2021). Climate change is warming Arctic regions four times faster than the global average (Rantanen et al., 2022). The rate of warming in e.g. Siberia has been unparalleled compared to the previous seven millennia (Hantemirov et al., 2022) and has led to widespread permafrost thaw and collapse (Biskaborn et al., 2019; Turetsky et al., 2020). The thawing of permafrost exposes frozen organic matter (OM) to microbial processes which has been dormant for a long time. Until 2300 this process is expected to lead to a potential loss of 341 Gt (20 %) of the now-frozen OM under climate change scenario RCP8.5 (McGuire et al., 2018). Coastal permafrost contains a considerable quantity of OM. Arctic coastal erosion is estimated to export up to 15.4 TgC and 1.6 TgN into the Arctic Ocean each year (Wegner et al., 2015; Terhaar et al., 2021). This input might increase by 70 to 150 % until 2100 (Nielsen et al., 2022). Additionally, it is anticipated that the hydrological cycle will become more intense during the 21st century, which will increase the amount of OC that is transported to the ocean stemming from erosion of peat and permafrost soils (Jones et al., 2020; Mann et al., 2022). In the coastal regions, extensive Pleistocene-age Yedoma deposits, typically rich in OM, can be found (Strauss et al., 2017). Of the total area of 2,587,000 km^2 which is occupied by permafrost, the Yedoma domain comprises around 500,000 km^2 of surface permafrost (Strauss et al., 2017), which contain about 20 gigatons of nitrogen and 130 gigatons of OC (Strauss et al., 2022), presently locked up as organic matter since its biosynthesis over 20,000 years ago. Thus, Yedoma stores substantial amounts of old OC, and it is particularly susceptible to thaw and erosion due to its high ice content (Strauss et al., 2017). Given that the OM froze quickly after deposition without undergoing much degradation, it is potentially extremely reactive (Kanevskiy et al., 2016) and may be highly bioavailable for present microbes. Understanding the mechanisms causing the carbon release from OC-rich permafrost is essential to estimate the occurrence of the permafrost related climatic tipping event (Lenton et al., 2019).

The majority OC in permafrost deposits has not been not part of the active carbon cycle since at least the last glacial maxiumum (Schirrmeister et al., 2013) and we thus consider it as “fossil” carbon. Due to the elevated age of permafrost deposit OC, it is generally considered to be resistant to degradation in settings where prevailing temperatures below freezing prevent OC decomposition, resulting in the preservation of largely undegraded OM (Guillemette et al., 2017). However, as soon as this previously freeze-locked OM reaches the nearshore zone of the Arctic Ocean, it is accessible to microbial degradation. The microbial utilization of fossil permafrost OM adds additional carbon emissions to the short-term carbon cycle (Guillemette et al., 2017; Lenton et al., 2019), intensifying the permafrost carbon feedback and climate warming (IPCC, 2019; Miner et al., 2022; Schuur et al., 2022). This stands in contrast to the degradation of freshly synthesized OM, which has a limited influence on the global carbon budget (Guillemette et al., 2017). Furthermore, the influx of eroded coastal permafrost into the nearshore zone has the potential to affect nutrient levels, with riverine input and coastal erosion accounting for 28 - 51 % of the Arctic Ocean's yearly net primary production. Accordingly, intensifying permafrost degradation under a warmer climate is expected to offset the regional food chain and impact global greenhouse gas (GHG) concentrations (Terhaar et al., 2021). Therefore, it is critical to comprehend what happens to permafrost-derived OC after it is released into the Arctic Ocean.

Despite its importance on a global scale, little is known about the bioavailability of permafrost OM entering the ocean. This results in tremendous differences between estimates of the proportion of permafrost OC being reintroduced into the active carbon cycle upon entering the ocean ranging from ~3 % in one summer season (Tanski et al., 2019; Ruben et al., submitted - manuscript 2) to 66 ± 12 % on the long run (Vonk et al., 2012). While a few studies have investigated the release of carbon and nutrients by incubating permafrost-derived material in seawater (Tanski et al., 2019, 2021; Ruben et al., submitted - manuscript 2), very little is known about the degradation processes that occur after deposition. While incubation experiments support estimates of approximately 3 % of the (TOC) being released in one summer season within the water column (Tanski et al., 2019; Ruben et al., submitted - manuscript 2), we expect that the bulk of the particles will be deposited quickly in the nearshore zone (Grotheer et al., 2020; Jong et al., 2020). However, microbial degradation likely differs substantially between the water column and the sediments due to the presence of different microbial communities and environmental conditions (Arnosti, 2008, 2011). To fully incorporate the impacts of permafrost erosion in earth system models, it is crucial to understand the long-term fate of permafrost OC after redeposition (Irrgang et al., 2022).

The study focuses on the nearshore zone along the Yukon coast that can be subjected to intensive coastal erosion (Obu et al., 2017), of Yedoma like OC and ice-rich permafrost deposits (Bristol et al., 2021). Following the approach of Dumoulin et al. (2022), we have analyzed the concentrations of dissolved inorganic carbon (DIC) and isotopic compositions ($\delta^{13}C$ and $F^{14}C$) of DIC in porewaters from two sediment cores retrieved from the nearshore zone, that have been affected by intensive coastal permafrost erosion and redeposition on the ocean floor. We hypothesize that heterotrophic microbes (here archaea and bacteria) use the sedimentary OM as the substrate for both their anabolic and catabolic pathways to produce lipids and CO_2/DIC (Carlson et al., 2007). The data we have obtained enables us to determine microbially mitigated permafrost OC contributions to DIC released from the sediment into the water column, along with the rates of release. We additionally performed compound specific isotope analysis ($\delta^{13}C$ and $F^{14}C$) of intact polar lipid fatty acids, as markers for live microbiota, to measure in-*situ* utilization of permafrost OC. Combining the biogeochemical indicators with benthic microbial community analysis will allow for a comprehensive insight into permafrost OC lability and utilization after redeposition on the sea floor.

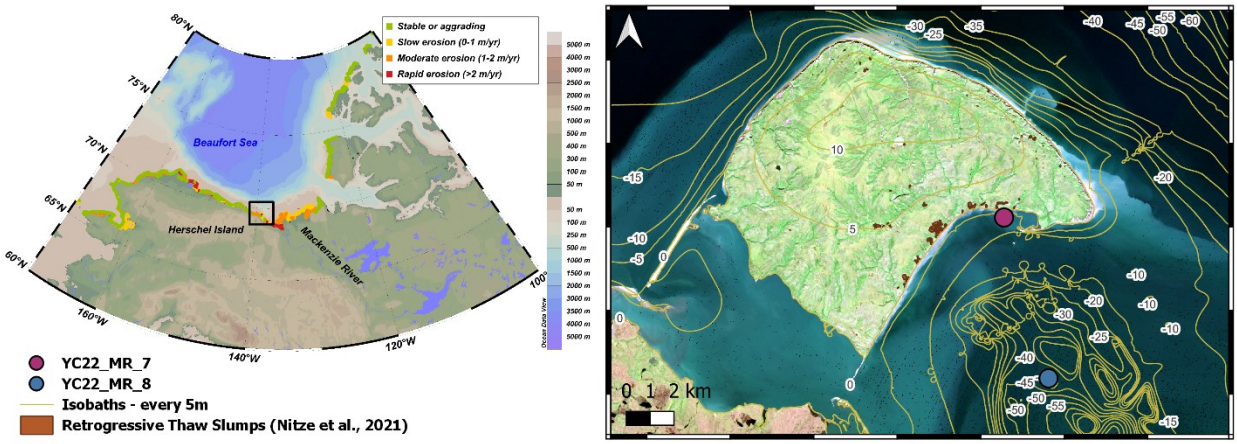

Figure 19: Left panel displays coastal erosion rates (Lantuit et al., 2012) along the Beaufort Sea, the black square indicates the outcrop of the right panel. First describe what you show here and then provide details about the data The right panel is based on a Landsat image (https://earthexplorer.usgs.gov/), with isobaths representing a compilation of three different datasets (details in methods). Sediment core locations are displayed as magenta and blue dots. Local retrogressive thaw slumps are indicated in brown (Nitze et al., 2021).

Sediment Cores

We analyzed parallel cores from two locations close to Herschel Island, Canada (Figure 19). The island was formed by the advance of the Laurentide Ice Sheet during the late Wisconsinan and is underlain by ice-rich permafrost (Fritz et al., 2012). Accelerating permafrost decay causes substantial amounts of permafrost OM to be mobilized from the eroding coast (Couture et al., 2018) and large retrogressive thaw

slumps (Lantuit & Pollard, 2008). Four parallel cores were retrieved from site YC22_MR_7 (hereinafter coastal) located about 220 m from the shoreline at a water depth of 6 m, penetrating the sediment up to 26 cm deep. According to the $^{210}Pb_{xs}$ and ^{137}Cs age model (details in methods), the sediments were continuously deposited within approximately 50 years (details in SI; Figure S 21). Bulk and biomarker analyses were conducted to identify sources of OC contributing to the sediments, displaying very homogeneous sediments that are dominated by the deposition of mobilized permafrost soils (details in SI; Figure S 17). At site YC22_MR_8 (hereinafter basin), two 35 cm deep parallel cores were collected about 3.2 km off the shoreline in a water depth of 45 m. Similarly to the coastal site, previous work in the Herschel Basin suggests a strong dominance of permafrost deposits contributing to the sediments (Grotheer et al., 2020). At both sites, porewater was extracted using rhizone samplers (Rhizosphere) at 3 cm intervals. Porewater samples from one core were analyzed for DIC concentrations and isotopic composition ($\delta^{13}C$ and $F^{14}C$; details in methods). Additionally, at YC22_MR_7 porewaters of the second parallel core were analyzed for nutrient, anion, and cation concentrations (details in methods and SI; Figure S 18).

DIC concentrations and flux

DIC concentrations were measured with a QuAAtro39 high-performance microflow analyzer (SEAL analytics; details in methods). The concentration of DIC in bottom water (above sediment) was found to be almost the same at both study locations, with 2.11±0.07 mmol/L at the coastal and 2.07±0.07 mmol/L at the basin site (Figure 20). Both cores showed a gradual increase in DIC concentration with sediment depth, reaching a maximum of 6.85±0.24 mmol/L in the coastal and 9.74±0.34 mmol/L in the basin core. In the basin core, a local maximum was observed directly below the sediment-water interface at 1 cm. This can be explained by increased oxygen flux to the sediment and consequently high local OC remineralization rates (Rassmann et al., 2020). The otherwise linear increase in concentration with depth at both sites indicates that the majority of DIC diffuses from greater depths upwards towards the sediment surface.

At both site locations, the respective DIC concentrations were used to determine the DIC flux at the sediment-water interface, using the PROFILE software by Berg et al. (1998; details in methods), allowing to determined the flux of carbon from OC degradation in the sediments into the water column and thus quantifying its impact on the active carbon cycle. At the coastal site, DIC is released at a rate of 0.217 mmol/m²/d, which is slightly lower than the rates in the basin with 0.251 mmol/m²/d. The observed rates are similar to modeled anaerobic DIC fluxes reported by Brüchert et al. (2018) of about ~0.2 mmol/m²/d,

based on whole core incubation of shelf sediments from the Laptev Sea. Both core sites receive sediment input from eroded ancient permafrost (Grotheer et al., 2020) and are influenced by high rates of coastal erosion (Obu et al., 2017).

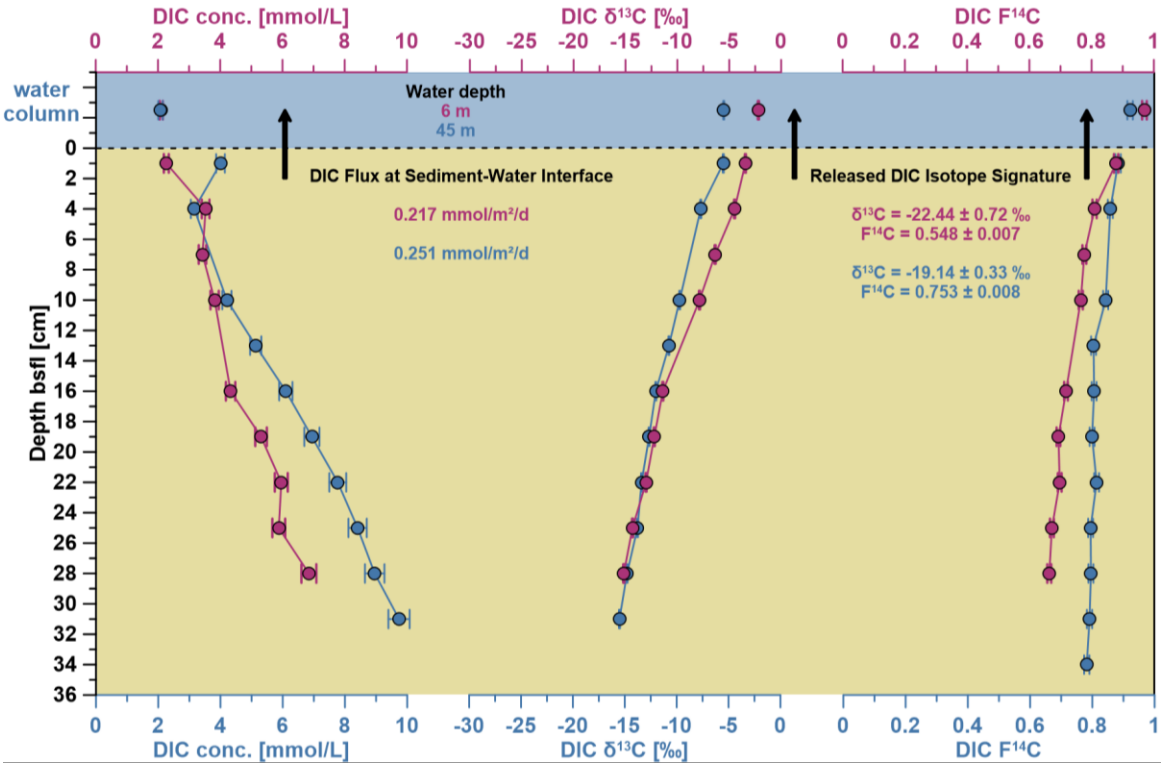

Figure 20: Dissolved inorganic carbon (DIC) data of cores YC22_MR_7 in magenta and YC22_MR_8 in blue, displaying concentrations, its stable- ($\delta^{13}C$) and radiocarbon-isotopic ($F^{14}C$) values plotted against depth (in cm below sea floor). DIC flux at the sediment surface and released DIC isotope signature were calculated based on displayed DIC concentrations and isotopic values (details in methods).

DIC isotopic signature

In addition to DIC concentrations, its isotopic signatures were determined for both $\delta^{13}C$ and $F^{14}C$. Similar to the DIC concentration, their trends in the sediment were almost linear. Above the sediment, bottom water signatures showed lower values for the basin location with $\delta^{13}C$ = -5.46±0.05 ‰ and $F^{14}C$ = 0.921±0.009 compared to $\delta^{13}C$ = -2.19±0.05 ‰ and $F^{14}C$ = 0.970±0.007 at the coastal site. At both sites, the $\delta^{13}C$ values decrease in the sediments with increasing depth. On the contrary, $F^{14}C$ values at 1 cm sediment depth are almost identical at both sites with 0.879±0.007 and 0.883±0.009 at the basin and coastal site, respectively. Although there is a decline in the $F^{14}C$ values at both locations as sediment depth increases, the decrease is notably more pronounced in the coastal core, dropping to as low as 0.664±0.006, while the lowest value in the basin core is 0.782±0.008.

Using a so-called Miller-Tans plot (modified Keeling-Plot), we were able to determine the isotopic signature of the DIC produced in the sediments (Miller & Tans, 2003). This can be assumed to reflect the isotopic signature of OC which is microbially utilized in the sediments (Dumoulin et al., 2022). While the $\delta^{13}C$ signature can be used to distinguish between terrestrial and marine primary production, $F^{14}C$ allows the determination of the age of the utilized OC (Dumoulin et al., 2022). By combining both isotopes, we are therefore able to determine to what extent permafrost soil OC is utilized in the subsurface after redeposition in this environmental setting. The local soils have a distinctive low $\delta^{13}C$ and $F^{14}C$ (old) signatures (Grotheer et al., 2020), while marine OM has higher $\delta^{13}C$ and $F^{14}C$ (younger) signatures (Tesi et al., 2016). The isotopic signature of the produced DIC at the coastal site was estimated to have $\delta^{13}C$ = -22.4±0.7 ‰ and $F^{14}C$ = 0.548±0.007, while in the basin estimates are at $\delta^{13}C$ = -19.1±0.3 ‰ and $F^{14}C$ = 0.753±0.008 (Figure 21). Comparing these values to the isotopic signature of the eroding permafrost soils on Herschel Island (the main source of OM contributing to the sediments) with $\delta^{13}C$ = -26.3±0.3 ‰ and $F^{14}C$ = 0.056±0.041 (Grotheer et al., 2020), a significant difference can be observed. At both sites, the produced DIC $\delta^{13}C$ is more similar to the isotopic signature typical for marine phytoplankton of about -19 to -21 ‰ (Harmelin-Vivien et al., 2010) rather than to the deposited permafrost soil OC. Similarly, the $F^{14}C$ signatures of the produced DIC suggest that the utilized OC is on average much younger in both, the coastal (~4.8±0.1 $k^{14}C$ years) and the basin site (~2.3±0.1 $k^{14}C$ years), than the permafrost soil OC (~25±6 $k^{14}C$ years; Grotheer et al., 2020). Thus, this indicates that younger marine OC in the sedimentary subsurface is preferentially utilized by sedimentary microbial communties.

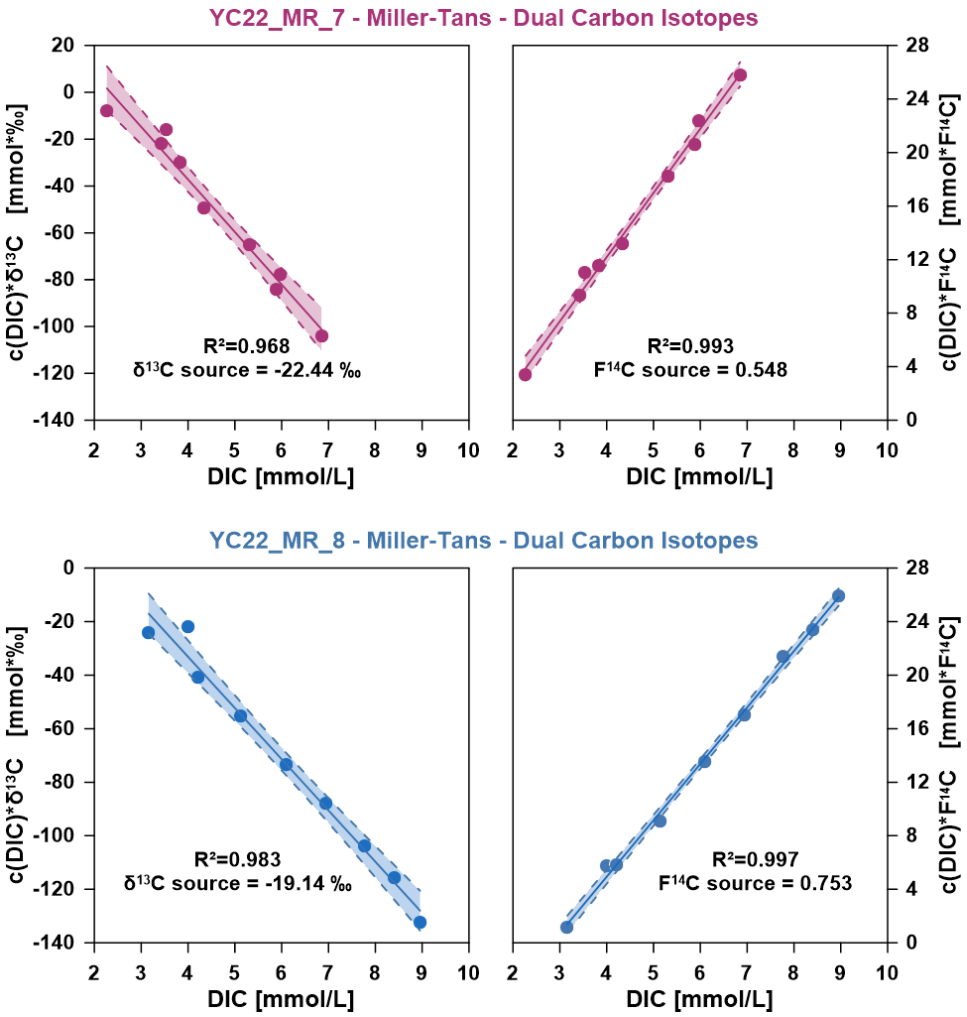

Figure 21: Miller-Tans plots of DIC data from both core sites, used to calculate the isotopic signature of the DIC released in the sediments.

IPL-FA analysis

The isotopic signature of a substrate is incorporated into the biomass during heterotrophic microbial utilization. Thus, determining the isotopic composition of microbial lipids allows us to make inferences based on their isotopic signature regarding the mean composition of the carbon source utilized in their metabolic pathways (Petsch et al., 2001). Following the approach by Ruben et al. (2023), we extracted and purified phosphate-bearing intact polar lipids (IPL) down core from four depth intervals at the coastal site and obtained the isotopic signature of their fatty acid (FA) side chains. Phospholipids decay between days to weeks after cell lysis, allowing interpretations about the in-*situ* microbial substrate preference of live bacteria (Logemann et al., 2011). The depth intervals were chosen based on the sedimentary biogeochemical zonation (details in SI) to obtain data from the “quasi-oxic” (1-3 cm), suboxic (5-7 cm), and anoxic (15-18 cm and 21-24 cm) zones (details in SI). Additionally, the precursor lipids of the analyzed

FAs were determined by high-pressure liquid chromatography coupled to mass spectrometry (HPLC–MS) to ensure bacterial origin (details in methods and SI). The $C_{br\text{-}15:0}$ and $C_{16:1}$ FAs chosen for compound-specific isotope analyses were derived overwhelmingly from (lyso-) diphosphatidylglycerol and phosphatidylglycerol lipids, which both are commonly assigned to sulfate-reducing (Seidel et al., 2013) and other marine sedimentary bacteria (Schubotz et al., 2011) in sediments. In the 1-3 cm interval $C_{16:1}$ FA was found in high abundance in betaine lipids, thus indicating a potential carry-over from algae at this depth (Cañavate et al., 2016). We excluded this data point from further analysis.

With the exception of the 1-3 cm $C_{16:1}$ FA, the analyzed $C_{br\text{-}15:0}$ and $C_{16:1}$ FAs show a uniform distribution in their $\delta^{13}C$ and $F^{14}C$ signature (Figure 22) with an average of -24.68±0.97 ‰ and 0.856±0.043, respectively (n=7). Comparing the FA isotopic signature to the bulk sedimentary OC, a strong offset can be observed towards higher values in both $\delta^{13}C$ and $F^{14}C$. Part of the $\delta^{13}C$ difference between sedimentary OC and FAs is due to isotopic fractionation during FA biosynthesis, which can be assumed to result in offsets of about -4 to -2 ‰ (Hayes, 2001). This correction is not necessary for $F^{14}C$, as the values are by definition corrected for fractionation (Reimer et al., 2004; Stuiver & Polach, 1977). Taking the ~3‰ offset into account, the IPL-FA isotopic signature suggests a similar $\delta^{13}C$ value of the carbon source as has been estimated from the DIC data (see above). However, $F^{14}C$ values of IPL-FA are substantially higher than the released DIC. Considering the upward flux of DIC from the deeper sediments (deposited since the last glacial maximum) and the time-dependent decay of ^{14}C, an at least partial overprint of shallowly produced young DIC by old upward diffusing DIC is plausible.

Isotope endmember model

We used a dual carbon isotope endmember model to quantitavely estimate the relative contribution of individual OC substrates to the released DIC (Wei et al., 2023). The three endmembers contributing OC to the sediments were defined as OM derived from marine primary production (*fM*; $\delta^{13}C$ = -21.0±2.6 ‰ and $F^{14}C$ = 1.043±0.050), deep permafrost soil (*fP*; $\delta^{13}C$ = -26.8±0.33 ‰ and $F^{14}C$ = 0.007±0.005), and a Holocene carbon pool from active layer and soils including recent terrestrial primary production, e.g. plant litter (*fAL*; $\delta^{13}C$ = -28.0±0.9 ‰ and $F^{14}C$ = 0.480±0.205; details in methods and SI).

The sediments at the coastal site comprise to 4 ± 4 % of *fM*, 41 ± 22 % of *fP*, and 55 ± 22 % of *fAL* (n=12), which corroborates results from biomarker analyses (see above), indicating a minor presence of OC from marine primary production and a strong dominance of the adjacent soils. However, the model estimates the released DIC to contain 48 ± 5 % C from *fM*, 38 ± 10 % C from *fP*, and 15 ± 12 % C from *fAL*. This discrepancy between the estimates for the bulk sediment and DIC suggests that about half of the released

OC originates from recent marine primary production and about one-third from old permafrost soils. At the basin site, the released DIC was estimated to be even more strongly dominated by utilization of marine OC, contributing to 69 ± 5 %, while *fP* contributed 20 ± 7 % and *fAL* accounted for 11 ± 9 %. However, due to the diffusion of DIC from deeper and thus older parts of the sediments upwards into the analyzed depth intervals, the model may overestimate the ancient permafrost components contributing to the DIC release. Therefore, our estimate of old permafrost contribution to the released DIC has to be considered an upper limit. Nevertheless, our estimate is in broad agreement with the reported 32 – 36 % of terrestrial OC contribution to produced DIC in Siberian shelf sediments as reported by Brüchert et al. (2018).

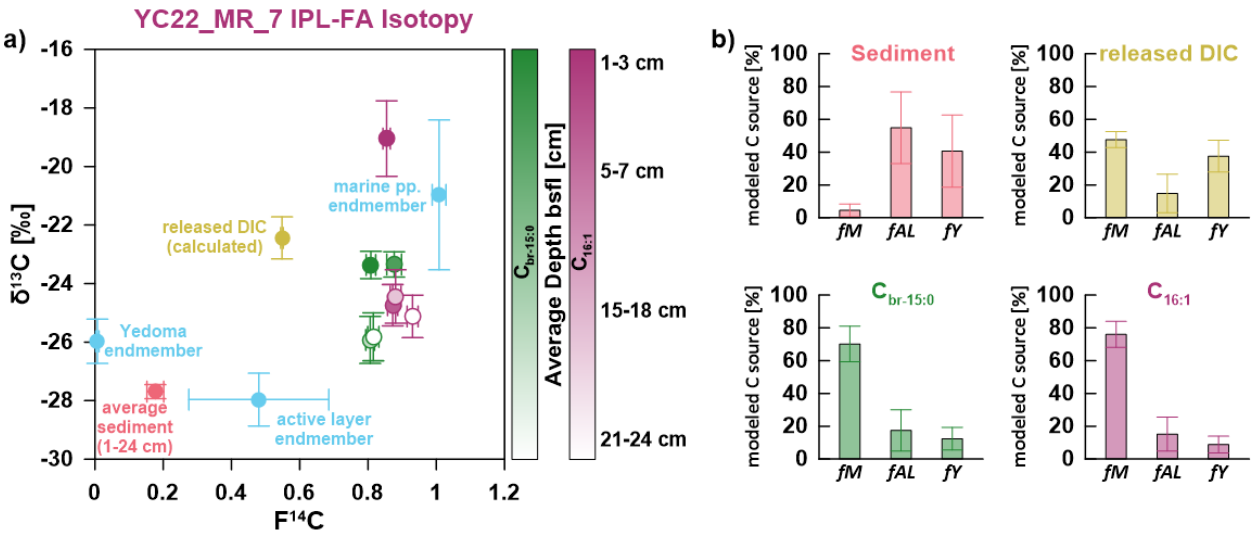

Figure 22: Carbon isotope data of core YC22_MR_7. Panel a) Isotopic compositions of different fractions of the coastal core site (YC22_MR_7), including average sediment TOC (red), calculated released DIC (yellow), IPL-FA $C_{br-15:0}$ (green) and $C_{16:1}$ (purple). Isotopic signatures of endmembers are shown in cyan for ancient permafrost, active layer, and marine primary production. Panel b) estimated percentages of endmembers (in a) contributing to the average sediment (n=12), released DIC (n=9), $C_{br-15:0}$ (n=4), and $C_{16:1}$ (n=3).

The isotopic values of the IPL-FA should not be influenced by the upward flux of DIC. Indeed, values of the IPL-FA show on average a much higher contribution of *fM* with 73 ± 10 % to the bacterial membrane lipids, while *fP* and *fAL* decrease to 11 ± 6 % and 16 ± 11 % (n=7), respectively. The $C_{br-15:0}$ indicates a slightly higher contribution of both *fAL* (17 ± 11 %) and *fP (12* ± 7 %) compared with the $C_{16:1}$ *fAL* (15 ± 10 %) and *fP* (9 ± 5 %). These results are in line with a recent study on glacial meltwater-fed sediments at the Hornsund Fjord in Svalbard where a similar pattern was observed. The authors report marine OC contributions of ~5% in the sediments, of which microbes use ~70% for their lipid synthesis (Ruben et al., 2023). Our dataset also supports their hypothesis that the presence or absence of recently produced biomass prevents or promotes the utilization of old OC.

Overall, the endmember model indicates that 11 ± 6 % of the bacterially utilized OC in the sediments and a maximum of 38 ± 10 % of the DIC released into the sediment-water interface are derived from old permafrost stored since at least the last glacial (Schirrmeister et al., 2013). The escaping DIC will contribute to the permafrost carbon feedback, even though the permafrost OC contributes 41 ± 22 % to the sedimentary OC pool with an additional 55 ± 22 % supplied by the active layer. Additonally, microbes utilize to 16 ± 4 % OM for their biosynthesis derived from the active layer which contributes another 15 ± 12 % to the released DIC. While active layer OM is on average younger than the permafrost deposits with about 5.9±3.7 ka ^{14}C years (Bristol et al., 2021), the release of its OC still reintroduces C stored for the last ~2-10 ka years. Due to the high sediment accumulation rates (~0.5 cm/a; detail in SI) it has to be assumed that the relative contribution of freshly synthesized marine OC is lower than the site of the coastal core, compared to more distal sediments. Our estimates from both core sites agree well with previous estiamtes of porewater DIC being derived to 32 to 47 % from terrestrial OM mineralization in Laptev and East Sibirian sea shelf sediments (Brüchert et al., 2018). The decrease in permafrost OC utilization at the basin site, compared to the coastal site, suggests that as the distance from the shore increases (resulting in a relative decrease in permafrost soil OC contribution to the sediment OC pool, relative to OC from marine production), the microbial communities (see below) in the subsurface rely less on the permafrost OC and rather feed on marine detritus. Similar observations were made in the proximity of glaciers exporting old OC to the sediments, where microbes only in the absence of freshly synthesized marine OC utilized the old substrate as the primary energy source (Ruben et al., 2023). The offshore decrease in old carbon utilization also suggests that only a fraction of the permafrost OC is utilized in the sedimentary subsurface after redeposition.

Microbial community patterns in the sediment

Similar to the biogeochemical parameters, the microbial community composition also varied with depth. Alpha-diversity measures such as richness peaked in 10-11 cm and 20-21 cm (*Spearman's* rank r=-0.31, p=0.56), while measures of evenness, including Shannon-Wiener and Inverse Simpson diversity, peaked in 10-11 cm and generally increased with depth (*Spearman's* rank r=-0.49, p=0.36). The variability in the microbial community was also illustrated in the non-metric multidimensional scaling (NMDS; Figure S 22) that significantly differed by depth (ANOVA $F_{(1,4)}$=3.0; p<0.01).

Cyanobacteria, Bacteroidia, Nitrososphaeria, and Gammaproteobacteria dominated the upper few centimeters of the sediment, while other microbial classes increased below 10 cm. The four major classes represented 88.5% of the community in the 0-1 cm and 68.4% relative abundance at 5-6 cm depth,

whereas the relative dominance shifted to approximately 60% of other microbial classes at 10-26 cm depth (Figure 23a). Notably, Cyanobacteria dominated the community by 58.2% in the 0-1 cm, 12.3% in 5-6 cm, and decreased to below <1% at 10-26 cm (Figure 23a), suggesting that cyanobacteria were either sedimented planktonic taxa (Belevich et al., 2019; Sivarajah et al., 2021) or rather benthic cyanobacterial mats that are suited to the extreme environmental fluctuations (Lionard et al., 2012). The microbial community composition results are supported by the IPL analysis, which indicates a potential phytoplankton carryover into the $C_{16:1}$ fraction at the 1-3 cm interval, which led us to exclude the C16:1 compound-specific isotope data at this depth from further analysis. Similarly, to cyanobacteria, Bacteroidia decreased with depth from ~11% relative abundance at 0-1 cm and 5-6 cm depth to ~4% relative abundance at 25-26 cm depth. Additionally, we observed a shift at the genus level from *Flavobacterium* in 0-1 cm to *Aquibacter* and *Lutibacter* in 5-6 cm (Figure 23b). *Flavobacterium* has been isolated from streams or tidal sediments and, like many Bacteroidia, is characterized by the capacity to metabolize mono- and polysaccharides (Kolton et al., 2013) in the presence of cyanobacterial biomass (Rosselló-Mora et al., 1999). The shift from the potential cyanobacterial mat to increasing refractory organic carbon resulted in a decreasing Bacteroidia abundance and a shift to taxa like *Aquibacter* that have been considered to be a potential new hadal-adapted species (Peoples et al., 2019) alongside *Lutibacter* in the suboxic conditions of 5-6 cm depth. Additional major players in the suboxic conditions were Nitrososphaeria and Gammaproteobacteria. Nitrososphaeria consisted exclusively of one amplicon sequence variant (ASV) that was classified as the *Candidatus* Nitrosopumilus and peaked at 20.8% relative abundance in 5-6 cm depth. Gammaproteobacteria peaked in the suboxic conditions in 5-6 cm depth and anoxic conditions in 10-11 cm at ~24% relative abundance (Figure 23a). Further specifying the genus level showed that *Woeseia* increased from ~4% relative abundance in most depths to ~10% suboxic and anoxic zone (Figure 23b), supporting their ubiquitous abundance in marine sediments (Hoffmann et al., 2020) while also suggesting a potential for sulfur oxidation (Mußmann et al., 2017) at Herschel Island.

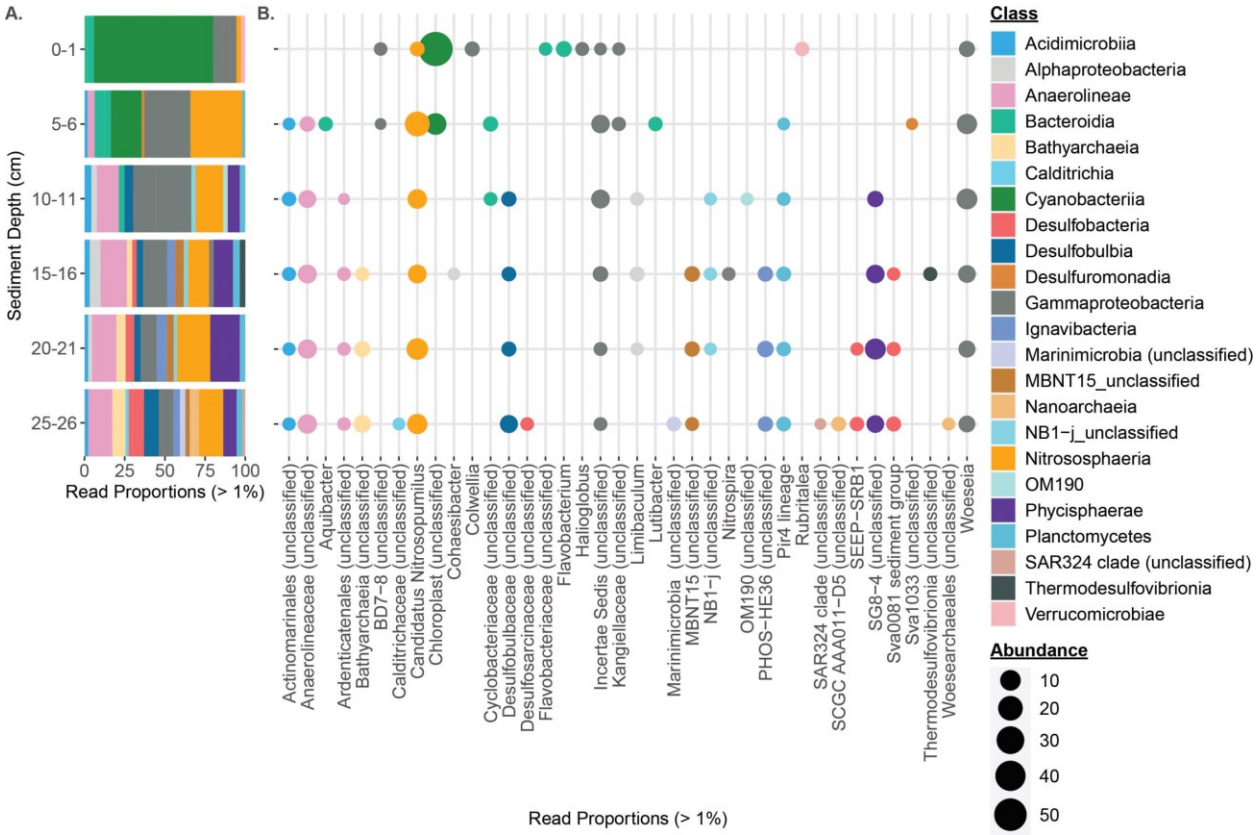

Figure 23: Relative abundance of microbial community on (A) class level and (B) genus level. The colors correspond to the class level and increasing circle area represents a higher genus-level abundance. The cut-off is greater than 1% relative genus abundance.

Environmental Implications

Our results indicate that the majority of the utilized OC and released DIC in the nearshore subsurface of the permafrost thaw affected Arctic Ocean comes from marine primary production. However, the quantity, remineralization potential, and bioavailability of the coastal permafrost OM stocks is still considerable ranging from approxamtly 25 to 50 %, yet poorly constrained to date (Lantuit et al., 20212; Wegner et al., 2015; Irrgang et al., 2022). Comparable proportions have been reported from the Eurasian shelf (Brüchert et al., 2018). However, even though sedimentary microbes use a limited amount of permafrost OC for biosynthesis, with only 11 ± 3% being utilized, and a maximum of up to 38 ± 11% of the released DIC coming from permafrost OM degradation, this still indicates that the eroding coastal permafrost is a substantial carbon source, and with the expected increase in coastal erosion in the coming decades, it may continue to increase (Irrgang et al., 2022). The subsequent intensifying changes in the Arctic shelf carbonate systems are of global concern as the outgasing of CO_2 from the water columns to the atmosphere (Semiletov et al., 2016) could potentially transform parts of the Arctic Ocean from a sink to a source of carbon.

The reported flux estimates pertain solely to the processes within sediments after settling of permafrost particles eroded from the sea floor. Incubating permafrost OC in seawater revealed that roughly ~3% of TOC will re-enter the active carbon cycle in approximately one summer season (Tanski et al., 2019; Ruben et al., submitted - manuscript 2). However, it is presently unknown to what degree these emissions relate to particulate or dissolved OC. It is anticipated that significant quantities of OC will leach from eroded particles and enter the ocean as dissolved OC. Prior research indicates that dissolved OC exhibits high reactivity upon release from thawing permafrost (Drake et al., 2015; Rogers et al., 2021; Spencer et al., 2015). Given that this fraction does not settle at the sea floor, it must be included in the proportion contributing to the PCF. Nevertheless, both estimates of PFC in the water column and sediments rely on a robust export rate of permafrost organic matter to the ocean, as recently presented by Martens et al. (2022).

Processes such as the release of nutrients from riverine and coastal erosion can offset some of the carbon emissions by boosting net primary production on the Arctic shelves (Terhaar et al., 2021). A remarkable 57% increase in net primary production between 1998 and 2018 provides optimism that some of the PCF can be counteracted by marine production (Lewis et al., 2020). However, due to rapid cycling, only approximately 3% of the terrestrially stimulated net primary production OM will be resequestered in ocean sediments, while the same amount is exported as dissolved OC off the shelf (Terhaar et al., 2021). Additionally, increased allochthonous inputs from permafrost thaw and erosion substantially increases sediment and carbon concentrations in coastal waters, leading to an increase in turbidity (browning). The anticipated browning will likely inhibit phytoplankton productivity, whereas the introduction of extra carbon will serve as a direct energy source for bacteria, increasing bacterial production and altering the ratio between basal autotrophic and heterotrophic production (Juma et al. in prep). Consequently, a comprehensive interdisciplinary strategy is necessary to comprehend and anticipate the impending shifts along the Arctic coasts and their influence on local and global scales.

Data availability

All biogeochemical data are publicly available in the Pangaea data repository (PDI-36258). Raw fastq sequence files have been deposited at the European Nucleotide Archive (ENA) and the complete amplicon workflow is available at https://github.com/anabelvonjackowski/Publications.

Authors contributions

All authors contributed extensively to the work presented in this paper. MR and GM designed the study; MF led the fieldwork campaign and assisted MR in sample acquisition in 2022; MR, JH, FS, and TG

performed lab experiments and performed measurements; AvJ prepared the samples for sequencing, processed, analyzed and interpreted the sequence data; BW performed endmember modeling; MR and BL calculated DIC fluxes. WG was responsible for the sedimentary age model; MR was lead author but all co-authors contributed to the discussion and writing of the manuscript.

Competing interests

The authors declare no competing interests.

Acknowledgments

We express our thanks to the Hunters and Trappers Committee of Aklavik, the Yukon Territorial Government and the Yukon Parks (Herschel Island – Qiqiktaruk Territorial Park), including the much appreciated help from the Park Rangers. The authors acknowledge the logistical support of the Aurora Research Institute (ARI, Inuvik). Financial support for this project has been provided by the European Research and Innovation programme Horizon 2020 to the Nunataryuk project (grant no. 773421). We are very grateful to Malte Höhn, Jens Hammes, Jan Gerdes, Lea Phillips, Elizabeth Bonk, Ingrid Dohrmann, Ingrid Stimac, Jenny Wendt, and Heidi Taubner for their support in the Lab. We thank Boris Radosavljevic for his work on the bathymetry data set. AWI-institutional funding for MR in the INSPIRES framework is acknowledged.

Methods

Sampling Location

The sediment cores were obtained off the coast of Herschel Island in July 2022, within the framework of an expedition managed by Alfred-Wegener-Institute and the Nunataryuk project. Two sampling sites were chosen, where four parallel cores were taken at each location, using two for pore-water extraction and two for sedimentary analysis. The first core, YC22_MR_7, was retrieved at the southern shore about 250m off the coast at a creek outlet (69°34'23.53"N, 138°56'37.66"W), draining the area of the two retrogressive thaw slums B-C in the area (Figure 19) Fast-ice coverage in 2022 extended way into summer and lasted right until the day of sampling. Thus, the water column displayed a strong stratification with a ~1.5 m thick freshwater lense at the surface, underlain by about 1 m mixing layer and brackish conditions below (determined using a SonTek CastAway-CTD). At site YC22_MR_7, cores were collected at a water depth of ~5.8 m and penetrated the sea floor about ~30 cm deep. At site YC22_MR_8, cores were taken in Herschel Basin (69°30'22.75''N, 138°53'21.69''W) at 45 m water depth, penetrating about 35 cm into the sea floor.

The water column was not stratified, however, a gradual mixing occurred in the top most ~17.2m between the brackish surface layer and the marine arctic bottom water.

Bathymetry

The isobaths (Figure 19) represent a compilation of three different datasets. The majority of information stems from a georeferenced scanned image of the Canadian Hydrographic Service map #7661 from Demarcation Bay to Phillips Bay (Canadian Hydrographic Service, 1986). Soundings and isobaths were digitized. Own single-point sonar soundings obtained with the GPS and sonar system (Garmin) onboard a Zodiac in 2013 were added to the dataset. Lastly, a coastline was digitized based on a Geoeye satellite image at 1:1000 scale to provide the 0 m contour (Radosavljevic et al., 2016). The data (i.e. points and contours) were gridded using the "topo to raster" tool in ArcMap. No corrections for sea level elevation were carried out.

Porewater and Sediment Sampling

Porewater extractions were performed right after the coring. The porewater was extracted from two parallel cores in intervals of 3 cm downcore using rhizomes (Rhizosphere) with a pore size of 0.15 µm. Aliquots were taken for DIC- (2 per depth interval), nutrient-, anion-, and cation-analysis. Further, the pH of extracted porewater was determined using a pH-probe on a 1 mL aliquot. Both of the DIC aliquots were poisoned with 10 µL $HgCl_2$, tightly sealed, and stored in a 2mL vial without a headspace at 4°C. Nutrient aliquots were stored frozen at -20°C right after collection. The anion aliquots were stored at 4°C without any treatment. Cation aliquots of 1 mL were acidified with 60 µL of supra-pure HCl and stored at 4°C. The procedure was followed as described in Oni et al. (2015). In addition, the bottom water right above the sediment interface was sampled in the same manner.

The two parallel sediment cores were sliced in 1 cm intervals, stored in pre-combusted glass Petri dishes (450°C for 3 hours), and frozen at -20°C. All sediment slices were subsequently weighed, freeze-dried, weighed again, and homogenized in an agate mortar. Sedimentary porosity was determined by water loss during drying.

Pore water analysis

Sulfate and Chloride

Anion concentrations (SO_4^{2-} and Cl^-) were determined using a Metrohm 930 compact IC flex equipped with a pre-column (Metrosep A Supp 5-Guard/4.0) and an anion-column (Metrosep A Supp 5-150/4.0).

Measurements were conducted in 1:100 dilution and verified using Iapso standard material. The precision and accuracy for SO_4^{2-} were >99% and >99%, and for Cl^- >99% and 98.7%, respectively.

Dissolved Iron and Manganese

The acidified aliquots were quantified for cation concentrations using inductively coupled plasma optical emission spectroscopy (ICP-OES). Detection limits of dissolved Fe and Mn were at 0.13 mg/L and 0.14 mg/L, respectively. The precision and accuracy were determined using Iapso standard material, accounting for Fe to >99.9% and >106.8%, and for Mn of >99.9% and 113.0%, respectively.

Nutrients and Dissolved Inorganic Carbon quantification

Nutrient and DIC concentrations were determined on a high-performance microflow analyzer QuAAtro39 (SEAL analytics). Samples were measured as technical duplicates and quantified using a five-point calibration. Analytical precision for phosphate (>96%), silicate (>99%) ammonia (82%), nitrite (>96%), nitrate (>99%), and DIC (>96%) were determined using standard material, with an accuracy of 105% for phosphate, 100% for silicate, 121% for nitrite, 76% for nitrate, and 96% for DIC.

Dissolved Inorganic Carbon Isotopy

The carbon isotopic composition of DIC was determined for both $\delta^{13}C$ and $F^{14}C$. Stable carbon isotope analysis was performed on the residual of the aliquots used for DIC quantification. The residuals (1 mL) were transferred immediately after the quantification into CO_2-free 12 mL vials (flushed with synthetic air) containing 100 µL of phosphoric acid using a needle and syringe. Transferred samples were kept at room temperature overnight to ensure complete CO_2 outgassing. Emitted CO_2 in the headspace was measured according to the method described in Torres et al. (2005), using a delta ray isotope ratio infrared spectrometer coupled to a universal reference interface (Thermo Fischer Scientific), at MARUM, Bremen. Measurement accuracy was determined with 180 individual measurements per sample over 3 minutes and calculated against VDP using a reference gas and verified with an internal Na_2CO_3 standard (with a standard deviation of <0.05 ‰ for 180 values). Radiocarbon signatures of the DIC were determined on the second aliquots of the same depths by transferring DIC into the gas phase with a similar method. The entire aliquot (~2 mL) was transferred into pre He-flushed 12 mL Exetainer® vials (5 minutes at 80 mL*min-1) and 200 µL of ortho-phosphoric acid (puriss. P.a.) was added to the sealed vials at 60°C which reacted for >1 hour. The emerging CO_2 gas was subsequently measured with the MICADAS accelerator mass spectrometer at the Alfred-Wegener-Institute, Bremerhaven (Mollenhauer et al., 2021), using a gas interface system for transfer (Wacker et al., 2013). DIC source isotope values for both $\delta^{13}C$ and F14C in the analyzed pore waters were determined using Miller-Tans equations (Miller & Tans, 2003). The background was defined by the bottom water for DIC concentration, $F^{14}C$, and $\delta^{13}C$.

Dissolved Inorganic Carbon flux and production calculation

DIC fluxes were calculated using the PROFILE software by Berg et al. (1998). Porosity (0.65) was chosen based on the mass loss during freeze-drying for different depth intervals and steady-state conditions were assumed during the short time period represented by the record according to the age model (detail below). Constant boundary conditions for DIC were chosen at the top and bottom according to DIC concentrations in seawater and the deepest porewater sample. DIC diffusion coefficients were calculated based on the input parameters temperature, salinity, and pressure (Table 5) using the online application of R. Luff (http://visumod.freeshell.org/thermo/difcoef.html), based on the work of Boudreau (1997). The three input parameters were taken from the bottom water reading of the CTD at the sampling locations.

Table 5: Input parameter used for DIC flux calculation.

Core ID	Temperature [°C]	Pressure [atm]	Salinity	Coefficient [cm²/s]
YC22_MR_7	0.3	1.6	28	$4.9484*10^{-6}$
YC22_MR_8	0	4.5	31	$4.8543*10^{-6}$

Sediment Analysis

Age model

The age model for YC22_MR_7 was established using the short-lived isotopes ^{210}Pb and ^{137}Cs. Measurements for the sediment core YC22_MR_7 were performed in a 1 cm resolution. $^{210}Pb_{ex}$ was analysed with a low background Ametek well-type HPGe gamma detector (GWL-150-15-LB-AWT-S) with a nominal volume of 150 cm^3 and a well diameter of 15 mm. After drying and homogenizing, the weighed samples of approximately 5 g mass were sealed in polyethylene tubes and stored until ^{222}Rn and its daughter nuclides had grown into equilibrium from ^{226}Ra. The emission lines at 295 keV, 351 keV and 609 keV were then measured to determine ^{226}Ra via ^{214}Bi and ^{214}Pb. Total ^{210}Pb was measured at 46 keV. $^{210}Pb_{ex}$ was then calculated as the difference between total ^{210}Pb and supported ^{210}Pb (as ^{226}Ra). Errors were calculated from counting statistics, taking the uncertainty of the calibration and of the background spectrum into account, including error propagation. The spectra evaluation and the subsequent data processing and error calculation was performed with the software package “ScientissiMe”. We chose a constant rate of supply (CRS) model (Appleby, 2001) here, due to the non-exponential profile. Due to the close proximity of the sediment cores YC22_MR_8 to PG2303 (both located in the Heschel basin), similar sediment accumulation rates of ~ 0.3 cm per year are assumed (Grotheer et al., 2020).

Total Organic Carbon Concentrations and Isotopy

Bulk organic carbon parameters were determined on freeze-dried and homogenized material. For total organic carbon (TOC) content, 0.1g of sediment was decarbonated with 500 µL of 12 N hydrochloric acid and C was quantified using a carbon-sulfur analyzer (CS-800, Eltra) with a precision of ±0.04%, following the protocol described in Lamping et al. (2021). Bulk radiocarbon values of sediments were measured on graphite targets containing 1 mg C using accelerator mass spectrometry. Sediments were pre-treated with three times 6M HCl to remove inorganic carbon, following the procedures described in Mollenhauer et al. (2021). Stable carbon isotope concentrations were determined using a Thermo Finnigan Flash EA 2000 coupled to a Delta V Plus isotope ratio mass spectrometer following the approach of Werner et al. (2001) and Brodie et al. (2011). Samples were pre-treated with three times 10% HCl and neutralized with deionized water.

Biomarker Quantification

Lipid biomarkers were extracted from ~3 g sediment with DCM:MeOH in a ratio 9:1 (*v:v*) following the protocol of Mollenhauer & Eglinton (2007). Quantifications were made relative to compound class-specific internal standards added to the sediment prior to extraction. Lipid sub-classes of alkanes, ketones, alcohols, and fatty acids were separated using wet chemical preparations and quantified using gas chromatography-flame ionization detection (GC-FID) following the protocol of Wei et al. (2020). Glycerol dialkyl glycerol tetraethers (GDGTs) contained in the alcohol fraction were measured using high-performance liquid chromatography-mass spectrometry (HPLC-MS) following the approach from Hopmans et al. (2016). Hopanes and sterols were quantified on a GC-MS as described in Meyer et al. (2019) and Dauner et al. (2022), respectively.

Intact Polar Lipid-Fatty Acid Extraction and Quantification

Intact polar lipids (IPLs) were extracted using a Bligh & Dyer (1959) approach modified by Slater et al. (2006). Of the initial IPL extract a subfraction containing primarily phospholipids (PL) was separated using Silica gel column chromatography separating lipids into neutral, glycol lipid, and targeted polar lipids (Akondi et al., 2017; Slater et al., 2006; Wakeham et al., 2006). After separation fatty acid side chains were transformed into methyl ester (FAME) and subsequently purified into single compound fractions using gas chromatography coupled to a preperative fraction collector, as described in Ruben et al. (2023). Aliquots of 1 % of the initial IPL extract and the PL subfraction were analyzed by ultra-high-pressure liquid chromatography-mass spectrometry using a Bruker maXis Plus ultra-high-resolution quadrupole time-of-flight mass spectrometer (Q-TOF) with an electrospray ionization source, applying the method described

in Wörmer et al. (2013). Procedural blanks were analyzed for the initial IPL extract, separated PL, and FAME to ensure no contamination was being introduced during preparative work.

Compound-Specific Radiocarbon Analysis

PL-derived FAME were further purified into single compound fractions using a gas chromatography setup coupled to a preparative fraction collector (GC-PFC), following the approach from Ruben et al. (2023). The radiocarbon signature of the purified single compounds was determined by AMS of CO_2 gas emitted by compound combustion, following the protocol of Mollenhauer et al. (2021). To account for possible $F^{14}C$ contaminations during the wet chemical preparation, single compound separation, and AMS measurements, the isotopic singnature of the FAME were corrected according to blanks reported by Ruben et al. (2023), following the approach of Sun et al. (2020) and Winterfeld et al. (2018).

Isotope endmember model

Following the approach of Wei et al. (2023), a three-end-member mixing model based on a Markov chain Monte Carlo Bayesian approach was used to apportion the relative OC contributions of the active layer including recent plant littler (*fAL*), Yedoma-like permafrost deposits (*fP*), and marine primary production (*fM*). A detailed description of the mixing model, end-member values, calculated uncertainties, and model run is provided in the supplementary information.

DNA extraction and sequencing

The sediment was sliced into five layers: 0-1 cm, 5-6 cm, 10-11 cm, 15-16 cm, 20-21 cm, and 25-26 cm. From each layer, 0.5 g of homogenized sediment was transferred into a matrix tube and extracted using the MoBio FastDNA™ Spin kit (MP Biomedicals, USA) according to the manufacturer's instructions. The concentration and purity of the extracts were quantified using the Quantus™ Fluorometer (Promega, Germany). The v4-v5 region of 16S rRNA genes was amplified using primers 515R (GTGYCAGCMGCCGCGGTAA) and 926R (CCGYCAATTYMTTTRAGTTT), providing high coverage of both archaea and bacteria (Parada et al., 2016). Amplicon libraries were prepared following the standard instructions of the 16S Metagenomic Sequencing Library Preparation protocol (Illumina, CA) and sequenced using MiSeq technology in 2×300 bp paired-end runs at Biosearch Technologies LGC, Berlin, Germany.

For Amplicon analysis, 16S rRNA reads were processed into amplicon sequence variants (ASVs) using DADA2 (v1.26.0; Callahan et al., 2016). Filtering settings were truncLen=c(230,195), maxN=0, minQ=2, maxEE=c(3,3) and truncQ=0, followed by merging using minOverlap=10 and chimera removal. After singleton removal, we obtained an average of 28,208 reads per sample that sufficiently covered

community composition (Figure S 23). ASVs were taxonomically classified using the Silva v138 database, which resulted in 2318 ASVs (McLaren & Callahan, 2021). Subsequently, we only considered ASVs with >3 counts in >3 samples, which resulted in 2206 ASVs.

Statistical analysis for ASV data were analyzed and visualized using R packages ampvis2 (v. 2.8.3), and ggplot2 (v. 3.4.3) with aesthetic modifications of figures using Adobe Illustrator. Alpha-diversity indices including richness, Shannon-Wiener, and Inverse Simpson diversity (Figure S 24) were calculated using iNEXT (v3.0.0; Chao et al., 2014). Non-metric multidimensional scaling (NMDS) was applied using central-log transformation based on Euclidean distances followed by an Analysis of Variance (ANOVA) on the clr transformed dissimilarity matrix and Euclidean distances.

Supplementary Information

Sediment bulk parameter

TOC concentrations in YC22_MR_7 remained constant (Figure S 17) throughout the core at an average of 1.10±0.05 wt% (n=24), with a single outlier of 0.93±0.4 wt% at the depth interval of 3-4 cm. Bulk $F^{14}C$ values ranged in the core from 0.146±0.002 to 0.220±0.002, with an average of 0.177±0.025 (n=12). This translates to apparent ^{14}C ages ranging from 12134±86 to 15619±88 ^{14}C years B.P., with an average of 13907±1126 ^{14}C yrs. $F^{14}C$ values of the lower part of the core (>13cm) are considerably higher than above with 0.192±0.022 and 0.162±0.017, respectively. From the core top downwards, the TOC becomes slowly older, reaching its maximum age at 11 cm. Right below this depth, the TOC age is the youngest at 13 cm. Stable carbon isotope values are relatively constant throughout the core ranging from -27.1±0.3 ‰ to -28.0±0.1 ‰, with an average of -27.7±0.2 ‰. Thus, bulk sedimentary isotopic values have a strong resemblance to local permafrost soils (Bristol et al., 2021).

Biomarker Analysis

Biomarker indices in YC22_MR_7 indicate a relatively homogeneous distribution throughout the core (Figure S 17). The CPI of *n*-alkanes is at an average of 5.73±0.44 (n=27) with two minor excursions to 4.45 at 3.5 cm and 4.44 at 22.5 cm, indicating a low maturity of the sedimentary OC (Bray & Evans, 1961). GDGT-derived values of the BIT-Index are even more uniform, ranging from 0.72 to 0.76 with an average of 0.74±0.02 (n=27), representing a strong dominance of soil OC input to the sediment (Hopmans et al., 2004). Similarly uniform are hopanoid *ƒßß*-indices ranging from 0.43 to 0.46 with an average of 0.44±0.01 (n=25), thus pointing towards a constant contribution of petrogenic OC in the sediments (Meyer et al., 2019). Dinosterol contents were continuously low with an average of 1.6 ± 0.4 ng/g (n=22), thus indicating marine primary production only contributes a minor fraction to the sedimentary OC pool (Fahl & Stein, 1999).

Porewater Data of YC22_MR_7

Cl^- concentrations in the bottom water were 407±2 mmol/L (Figure S 18). Throughout the sediment core, the Cl^- concentrations were fairly stable at 418±15 mmol/L (n=10) with one negative excursion at 13 cm at 380±1 mmol/L. Sulfate concentration changes follow the Cl^- pattern closely until 19 cm at an average of 20.8±1.1 mmol/L, including the negative excursion at 13 cm with 18.9±0.1 mmol/L. Below this depth, the SO_4^{2-} pattern are lower from the Cl^- pattern.

Concentrations of both PO_4^{3-} and NH_4^+ are below the detection limit in the bottom water (Figure S 18). Within the sediment, PO_4^{3-} concentrations remain below the detection limit from the surface until 7 cm, thereafter steadily increasing to 33.0±1.2 µmol/L at 19 cm, where concentrations plateau until the bottom of the core at 32.9±0.4 µmol/L.

Nitrate concentrations increase slightly from the water column concentration of 0.37±0.01 µmol/L to 0.53±0.08 µmol/L at 1 cm sediment depth and decrease thereafter to 0.13±0.03 µmo/L at 7 cm (Figure S 18). Below 10 cm concentrations are below the detection limit.

Silicate concentrations are lowest in the bottom water at 6.6±0.1 µmol/L and sharply increase within the sediment to 63.7±0.1 µmol/L at 1 cm bsfl (Figure S 18). Concentrations peak at 10 cm with 131.6±1.5 µmol/L and decrease downcore thereafter.

Both dissolved iron and manganese are below the detection limit in the bottom water and at 1 cm sediment depth (Figure S 18). Manganese concentrations increase rapidly to 2.18±0.01 mg/L at 4 cm and stay stable below at an average of 1.75±0.20 µmol/L (n=8). Iron concentrations increase more steadily than manganese concentrations to a maximum of 37.97±0.05 mg/L at 22 cm, with a slight decrease thereafter to 35.66±0.11 mg/L at 28 cm.

Intact Polar Lipid-Fatty Acid Analysis

The quantification of IPL of the PL extract showed five main contributing lipid classes in all four extracted sediment intervals. Within these, phosphate-bearing IPLs were dominating with DPG, Lyso-DPG, PE, PME, PC, and PG being the main contributors. Concentrations of DPG, Lyso-DPG, and PME increased with increasing sediment depth, while PG decreased. The emerging pattern of PC is less clear. In addition, minor contributions (<5%) of the amino-lipids class of BL were relatively constantly present in all four sediment intervals. Purified IPL-FA sources for isotope analysis were identified to be DPG and Lyso-DPG for $C_{15:0\text{-}br}$ FAME and PE, PME, PC, and PG for $C_{16:1}$ FAME.

The performed radiocarbon analysis on purified bacterial IPL-FAs of $C_{15\text{-}br}$ and $C_{16:1}$ revealed relatively uniform $F^{14}C$ values ranging from 0.8063±0.0128 to 0.9305±0.0160, with an average of 0.8556±0.0407 (n=8). $C_{15\text{-}br}$ displays slightly lower average $F^{14}C$ values in comparison to $C_{16:1}$ of 0.8267±0.0290 and 0.8845±0.0282, respectively. Using an isotope mass balance with a defined $F^{14}C$ endmember for the Herschel Island permafrost soil organic carbon (0.056±0.041; Grotheer et al., 2020) and marine phytoplankton (0.872±0.011 ; Vonk et al., 2014) indicates that between 90±2 to 100±2 % of the carbon taken up into the bacterial membrane lipids originates from a modern source.

Mixing model and end-member values

The relative fractional contribution of OC from the active layer including recent plant littler (*fAL*), permafrost deposits (*fP*), and marine primary production (*fM*) were assessed by the following equations:

$$f_{AL} * F^{14}C_{AL} + f_P F^{14}C_P + f_M F^{14}C_M = F^{14}C_{OC}$$

$$f_{AL} * \delta^{13}C_{AL} + f_P \delta^{13}C_P + f_M \delta^{13}C_M = \delta^{13}C_{OC}$$

$$f_{AL} + f_P + f_M = 1$$

A previous study on permafrost coastal erosion along the Beaufort Sea coast has provided valuable insights into terrestrial end-member values (Bristol et al., 2021). It involved the collection of permafrost cores spanning from the tundra surface to below sea level in three dominant geomorphic terrain units near the Beaufort Sea coast. These units include i) the active layer which remained unaltered by thermokarst lake formation and drainage, ii) ancient and iii) young drained thermokarst lake basins. Down-core patterns reveal distinctions between the upper and lower sections of the cores (Bristol et al., 2021; Figure S 20). The upper soil and lacustrine sediments exhibit exceptionally high organic carbon (OC) content (12.1 wt.%), C/N ratio (18.3), and $F^{14}C$ (0.480±0.205) values but low $\delta^{13}C$ (−28.0±0.9‰) values, indicating the active layer and upper permafrost layer formed during the Holocene. In contrast, the lower ice-rich old permafrost deposits feature low OC content (1.2 wt.%), C/N ratio (12), and $F^{14}C$ (0.007±0.005) values but high $\delta^{13}C$ (−26.0±0.8‰) values. These characteristics are indicative of Late Pleistocene permafrost depostis (Bristol et al., 2021), and are also referred to as “Pleistocene Ice Complex Deposits” (e.g., Martens et al., 2020; Tesi et al., 2016). Therefore, $F^{14}C$ and $\delta^{13}C$ values for the active layer (*fAL*) are defined as 0.480±0.205 and −28.0±0.9‰, respectively, which includes the contribution of fresh terrestrial production. $F^{14}C$ and $\delta^{13}C$ values for permafrost deposits (*fP*) are defined as 0.007±0.005 and −26.0±0.8‰, respectively. $\delta^{13}C$ values for marine OC (*fM*) are defined as −21.0±2.6‰ based on measurements of marine phytoplankton (Tesi et al., 2016), with ±2.6‰ uncertainty accounting for seasonal and annual changes in $\delta^{13}C_M$ over the last 50 years. Due to the lack of a ^{14}C time series of regional seawater dissolved inorganic carbon (DIC), a direct ^{14}C measurement of DIC in the Beaufort Sea was used to define a $F^{14}C$ value (1.008±0.020) for marine OC in the 2010s (Druffel et al., 2017). $F^{14}C$ values of DIC before the 2000s are taken from a ^{14}C time series of cod otoliths in the Barents Sea (Kalish et al., 2001). Note that while the $F^{14}C$ value of seawater DIC exhibits spatial differences in the Arctic Ocean, these variations have minor effects on calculated results. Minor decay corrections have been applied to all reported $F^{14}C$ values following the equation:

$$F^{14}C_y = F^{14}C * e^{(1950-y)/8267}$$

where y is the time of deposition (Reimer et al., 2004), based on the sediment age model. Regarding $\delta^{13}C$ values of bacterial PLFA, a ^{13}C fractionation ($\delta^{13}C_{biomass}$–$\delta^{13}C_{PLFA}$) factor of 2–4‰ is considered relative to the $\delta^{13}C$ value of bulk biomass (Hayes, 2001). In addition, Arctic rivers produce substantial particulate OC through primary production (Behnke et al., 2023), however, burial of OC from riverine primary production is negligible in the coastal sediments due to its rapid degradation in river mouth (Wei et al., 2020; Ogneva et al., 2023).

End-member contributions were determined using Bayesian Markov chain Monte Carlo simulations, applying arbitrary assignments of end-member values to minimize errors (Andersson et al., 2015). 1,000,000 out of 100,000,000 random samples were taken from the normal distribution of each end member within the given mean and standard deviations to fulfill the given system in simulations. The mean relative contributions and the standard deviation of different OC sources were then estimated.

Age model constrains

The artificial radioisotope ^{137}Cs was detected throughout the 25 cm long core, with the exception of the top 3 cm, where it was below detection limit. In the absence of intense mixing or vertical mobility, this indicates an age of the entire core younger than year 1954, when global fallout is assumed to first have occurred (Appleby, 2001). The shape of the profile would indicate that the peak of ^{137}Cs in 1963, and possibly that of 1986, if potentially present in this area, is below the sampling depth of the core.

There is a small, but clearly detectable fraction of ^{210}Pb in excess of its parent isotope ($^{210}Pb_{ex}$). This fraction shows a decrease throughout the core to almost nil, but does not fully reach background levels, which prevents the application of a $^{210}Pb_{ex}$ constant rate of supply model (CRS). Therefore, tentative ages are constrained by the constant initial concentration (CIC)-approach and a constant flux, constant supply model (CFCS). Both models agree fairly well and indicate an age of 47.9 +- 7.6 years (CFCS) or 42 +- 28 years (CIC) respectively at a midpoint depth of 20.5 cm, which corresponds to year 1975 (CFCS). The clear trend in the ^{210}Pb profile limits the extent of possible mixing that could affect the ^{137}Cs profile (Figure S 21).

^{241}Am, another artificial radioisotope which is less prone to vertical relocation, was below the detection limit at all depths.

In summary, the radiometric constraints all point towards a sedimentation rate around 0.5 cm/year and clearly demonstrate that the sediment has been recently deposited.

Supplementary Figures

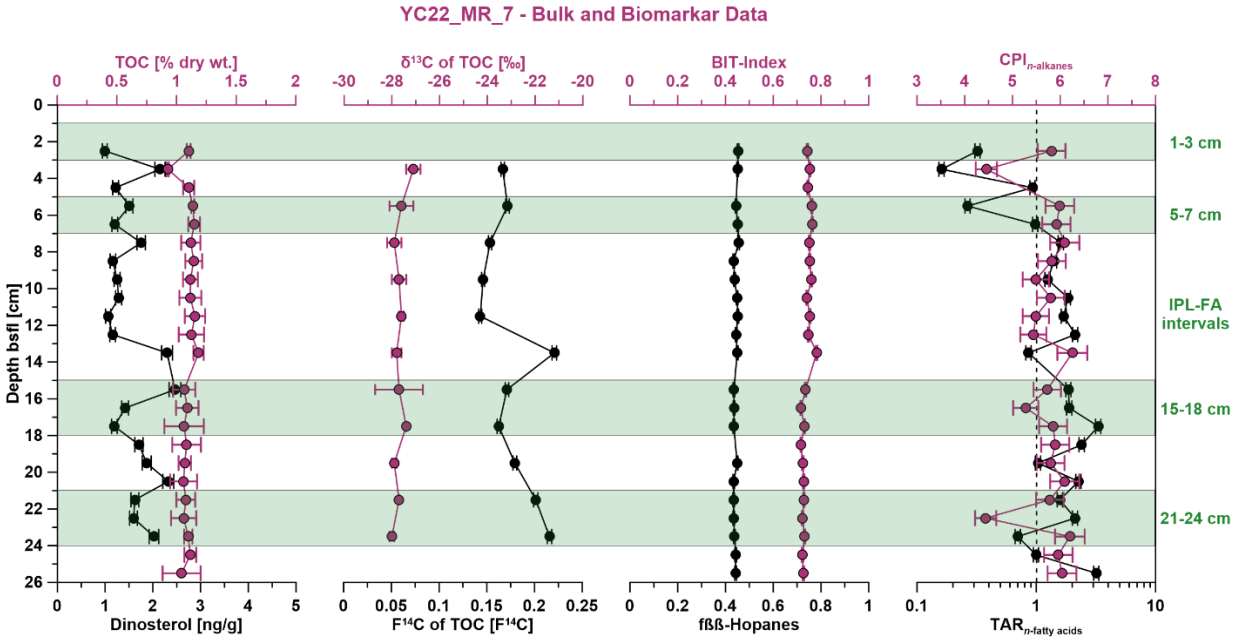

Figure S 17: Bulk and biomarker data of the coastal core site (YC22_MR_7).

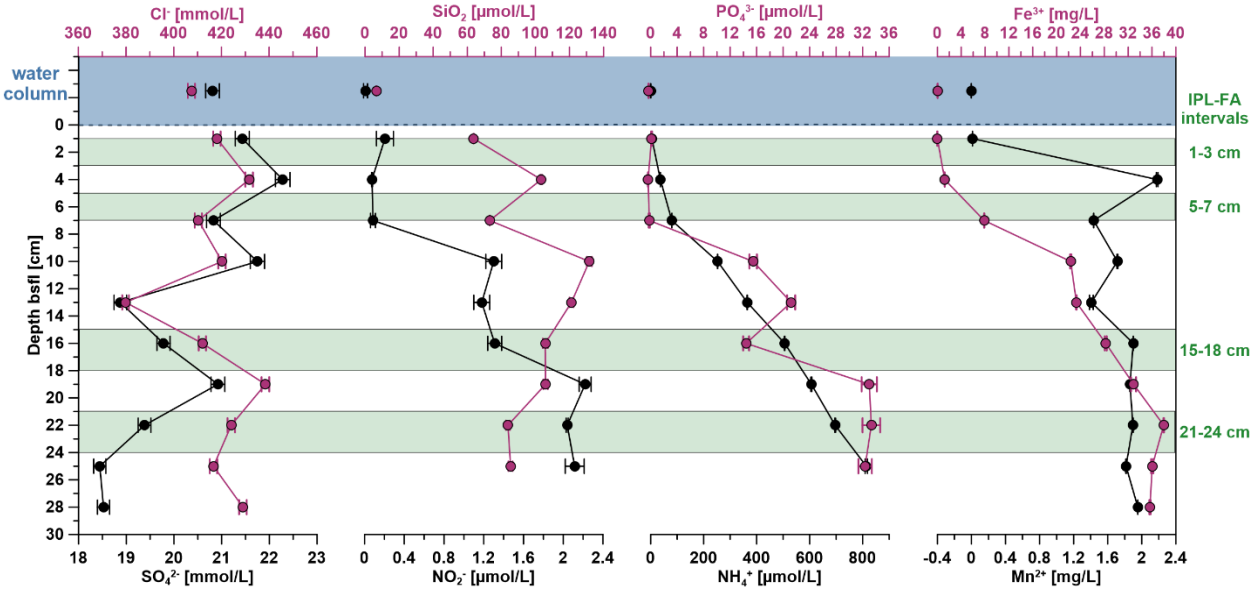

Figure S 18: Pore water data of the coastal core site (YC22_MR_7).

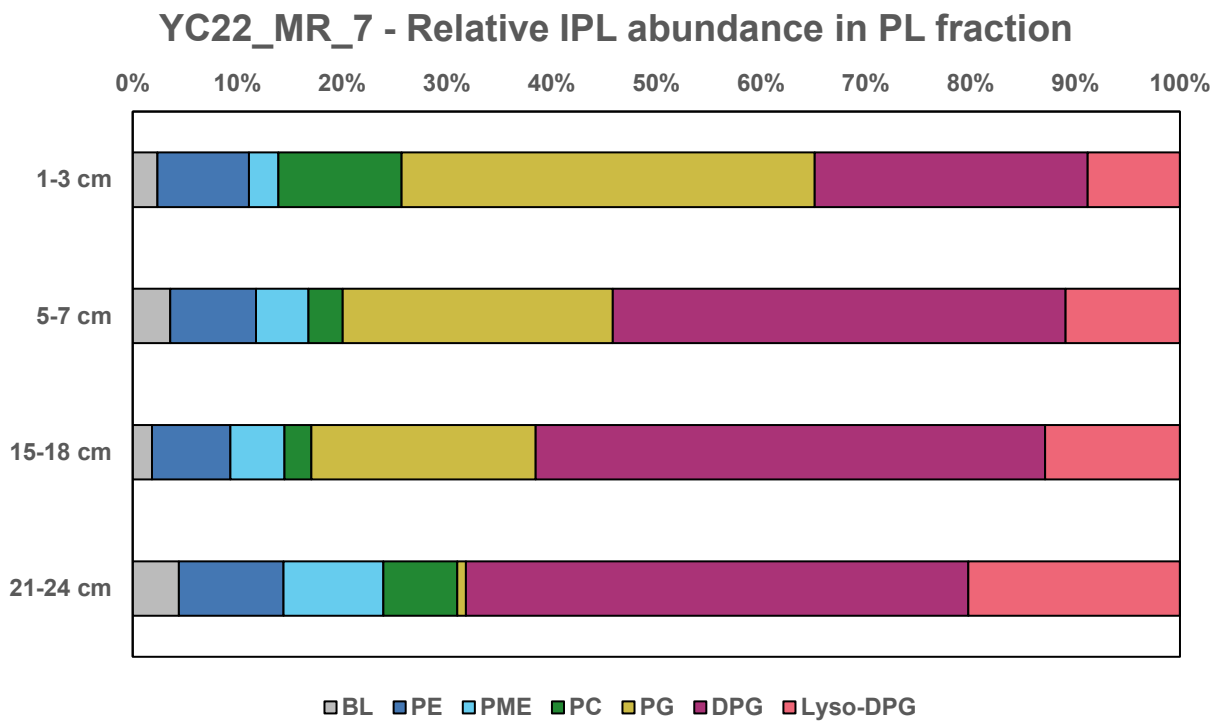

Figure S 19: Abundances of IPL in the extracted polar lipids fraction, representing the precursor lipids of the purification IPL-FA used for compound-specific isotope analysis.

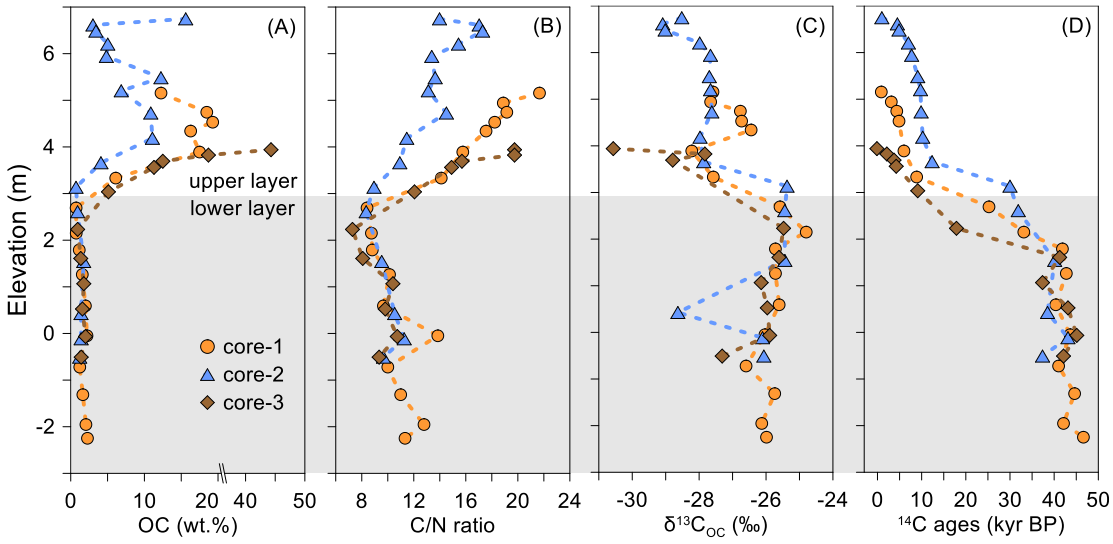

*Figure S 20: **Profiles of (A) OC content, (B) C/N ratio, (C) $\delta^{13}C$, and (D)** $F^{14}C$ values of OC in three permafrost cores (data from Bristol et al., 2021).*

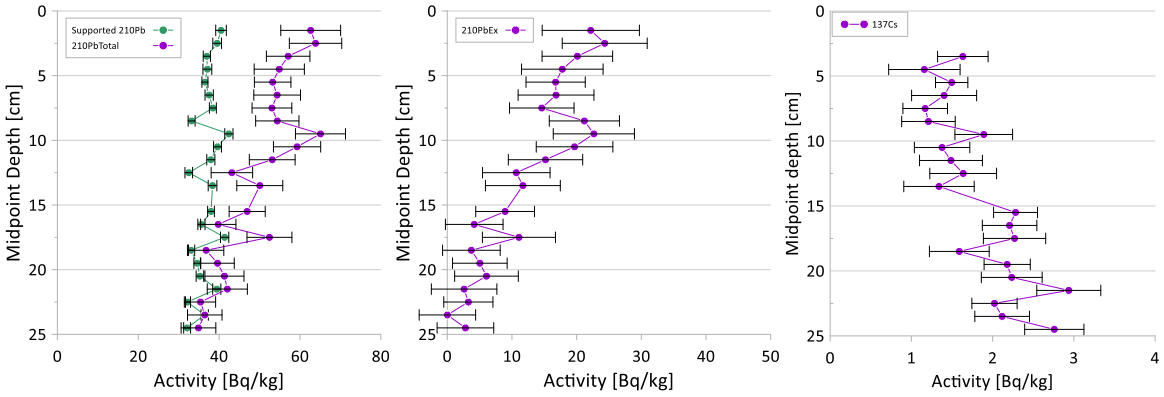

Figure S 21: Compilation of ^{210}Pb and ^{137}Cs data used for the sedimentary age model produced for sediment core YC22_MR_7.

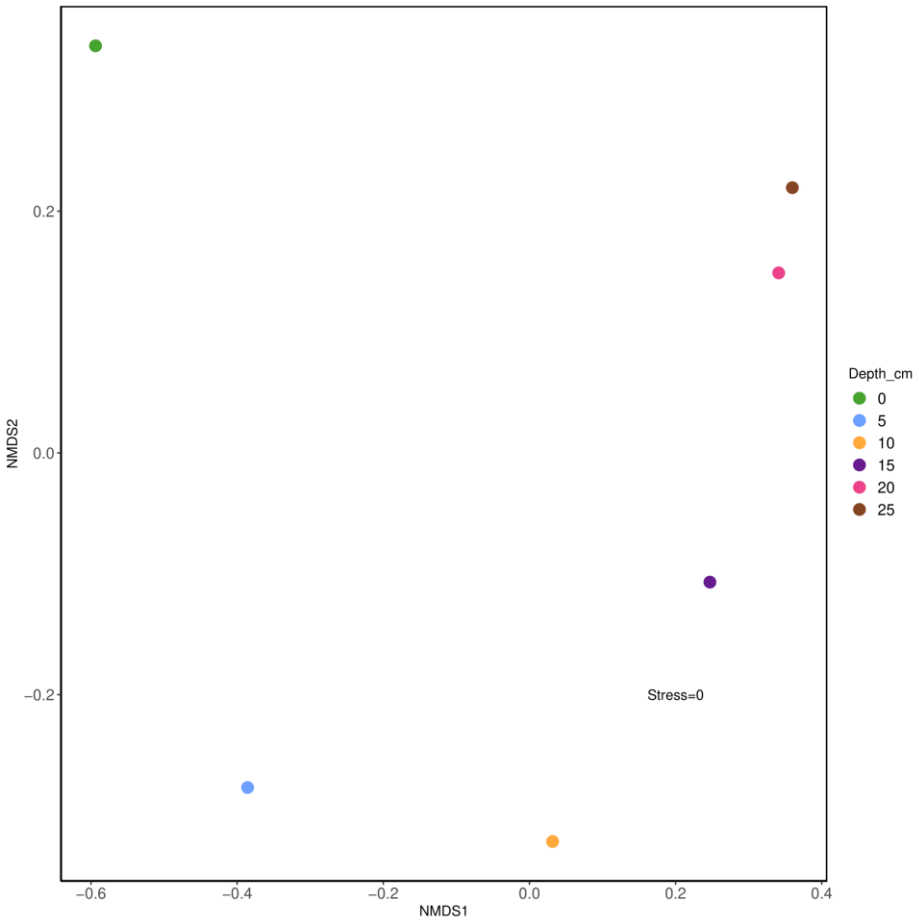

Figure S 22: Microbial structure by depth illustrated through non-metric multidimensional scaling (NMDS) based on central-log transformation and euclidean distances.

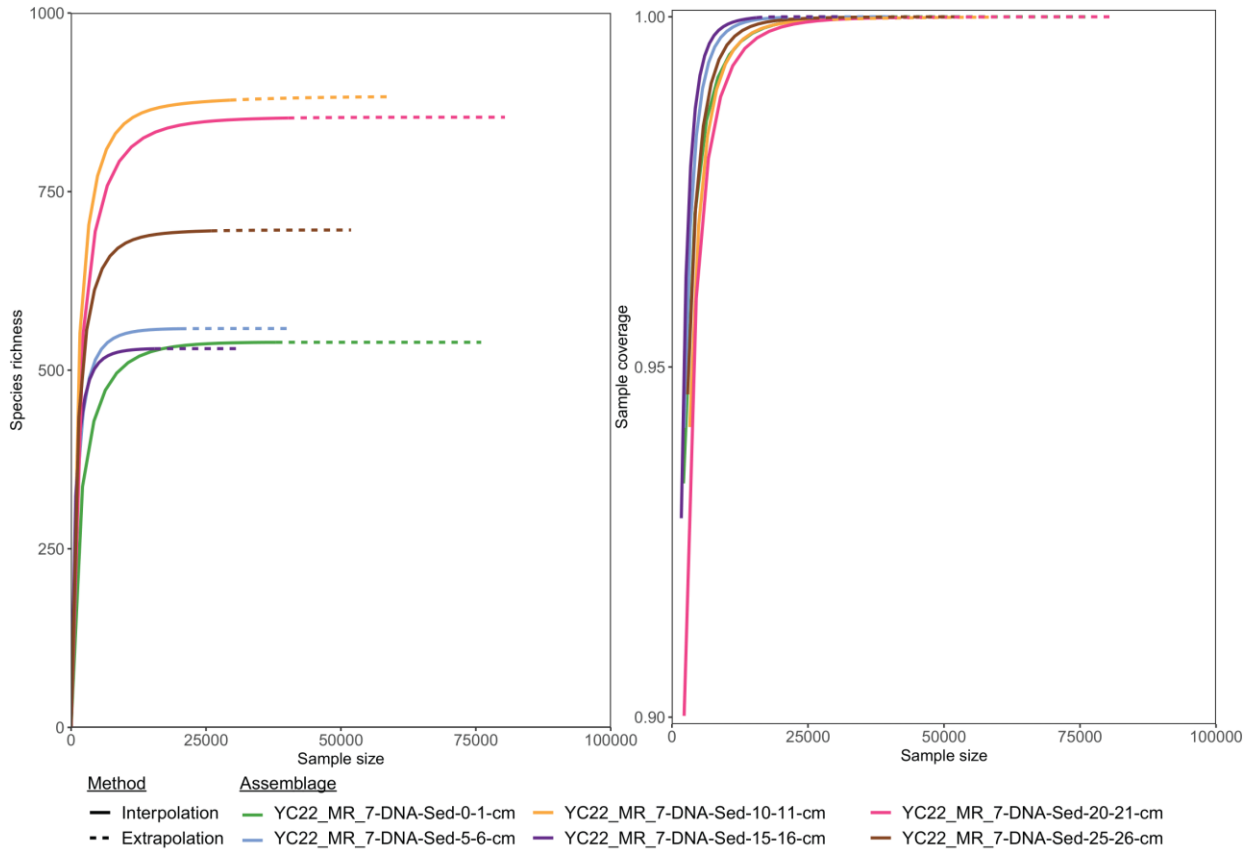

Figure S 23: Rarefaction (left) and coverage (right) analysis of amplicon sequence variants showing that the microbial community composition was sufficiently covered. Each colored line corresponds to an individual sample.

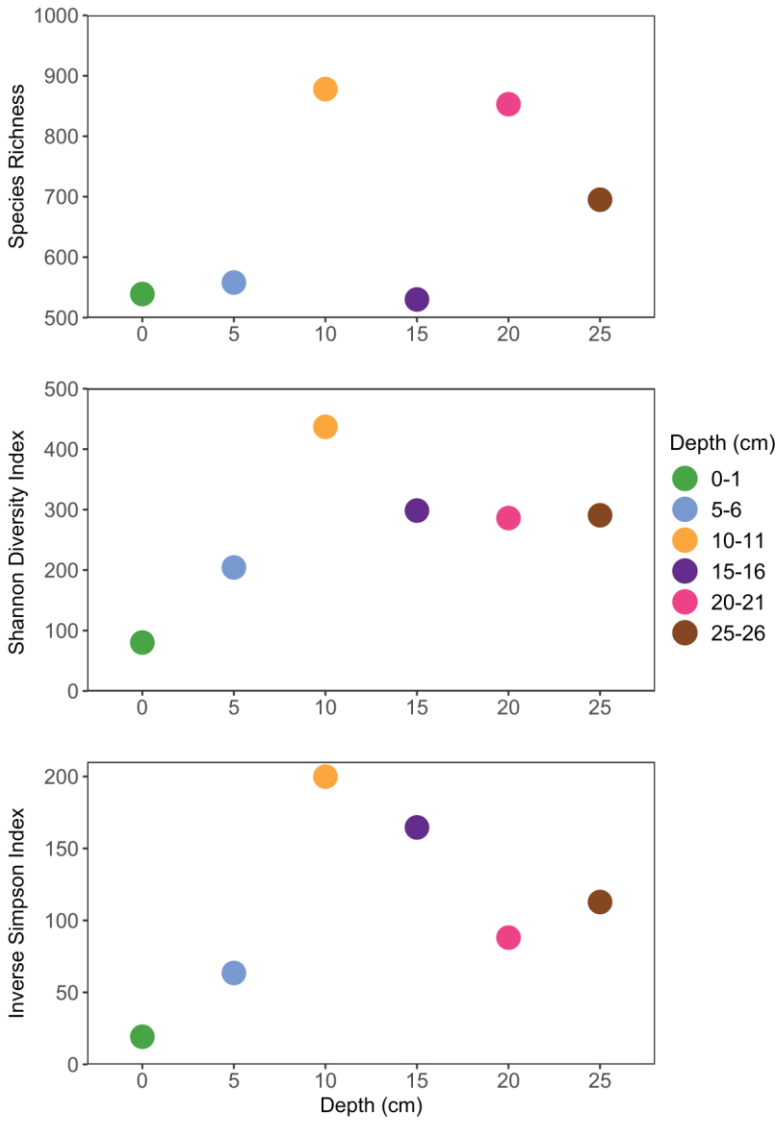

Figure S 24: Species richness, Shannon Diversity Index, and Inverse Simpson index by depth.

Summary and Outlook

In the first manuscript, we show that Arctic benthic microbial communities are able to utilize up to 56% of supposedly non-bioavailable ancient carbon from glacially remobilized kerogen for the biosynthesis of their biomass. However, ancient carbon utilization is negatively correlated with the presence of fresh modern carbon from recent primary production, suggesting that ancient carbon utilization may be limited to the most proximal areas in the fjords, directly at the glacier front. Nevertheless, these locations represent the depocenters for the majority of glacially derived sediments (Szczuciński & Zajączkowski, 2012), so this process could very well have implications on a global scale. As our study was the first of its kind, further studies are needed to investigate whether this phenomenon occurs in other locations, such as Greenland, Antarctica, Alaska, Franz-Joseph-Land, or Sewernaja Semlja. This is of particular interest as sediment export rates are expected to increase in the coming decades (Delaney & Adhikari, 2020). A combination of DIC quantification and isotope analysis of DIC and IPL-FA allow an appropriate approach to investigate the actual flux of ancient carbon from these glacial ecosystems (similar to the approach in manuscript 4). By determining the rates of remineralization of glacially derived OC_{petro}, it will be possible to assess over what time scales these processes are significant and thus indicate whether there is a positive feedback mechanism between anthropogenic climate change and OC_{petro}-derived greenhouse gas fluxes.

Manuscripts 2-4 addressed the fate of ancient carbon from permafrost soils. Taken together, the studies we have conducted provide a diverse picture of the bioavailability of ancient permafrost carbon. While the analysis of our data revealed a less dramatic view than that of, for example, Vonk et al. (2012), who suggested that 66 ± 16 % of the OC_{PS} escapes back to the atmosphere upon entering the Arctic Ocean, our estimate of ~3% escaping back to the active carbon cycle (within about a summer season) is of considerable concern given the sheer size of the OC stored in it and the vulnerability of the permafrost domain (Schuur et al., 2022). Regarding the contribution of OC_{PS} to the permafrost carbon feedback upon entry into the sea, a prominent feature to be explored in the future will be the spatial variability. In particular, the conflicting data from the incubation experiment (almost exclusive release of ancient permafrost OC) and the near shore down core study (release and remineralization of predominantly modern marine and/or terrestrial OC) suggest an environmental mechanism that limits or enables the use of OC_{PS}. An important compound class to explore is DOC, which has been shown to be highly bioavailable during permafrost thaw (Drake et al., 2015; Rogers et al., 2021; Spencer et al., 2015). During the incubation experiment, DOC was introduced into the experimental vials with the permafrost slurry and

thus likely contributed as a source to the release of DIC. On the contrary, it is likely that only a small fraction of the DOC from thawing permafrost soils will end up in the seafloor sediments, as the majority of the DOC can be expected to remain in the water column and not settle to the seafloor like the POC. Thus, this may well be one of the major differences between the ancient carbon utilization of the incubation experiment and the down-core study. This hypothesis is supported by the work of Ogneva et al. (2023), who report a similar phenomenon in the Lena River, where particulate OC is extremely old, while DOC in the river system barley shows any contribution of old DOC contributing to the pool. This raises the question of its fate and whether it contributes to GHG emissions. The study of Rogers et al. (2021) suggests a rapid utilization of DOC when entering river systems. However, whether this is also the case when DOC enters the ocean has not yet been investigated, even though it seems likely. To investigate this question, new analytical approaches need to be explored, which I tried in manuscript 3 using RPO, but with little success. Thus, other types of experiments such as separate incubation of DOC-leached soils versus DOC-bearing soils seem worth exploring in the future.

Another recurring issue in all the studies conducted is the influence of freshly produced labile OC on the bioavailability of ancient OC. In this context, the "priming" of ancient or labile OC by the introduction of small amounts of freshly synthesized OC (Bianchi, 2011) may need to be considered more closely. Most striking is the difference in the Hornsund Fjord sediment cores, where ancient carbon utilization correlates well with the presence of recently produced OC from marine primary production. Similarly, the microbial community of the incubation experiment was starved of freshly produced OC during the two-month transport, indicating that labile OC was absent from the experiment. However, this is in contrast to the presence of freshly produced OC from both the water column and terrestrial land plants in the Herschel down-core study. This raises the question of to what extent or at what threshold the presence of more labile OC "prevents" or enables the microbial degradation of ancient OC, and how environmental changes in the coming decades to centuries may alter their relative abundances and thus bioavailability. The methods used in this thesis may be appropriate to aid in the discussion of the “priming topic”, as it would allow a quantitative assessment of refractory carbon utilization using ^{14}C as an inverse tracer, similar to the incubation experiment. In addition to these different climatic conditions, processes such as photodegradation of ancient carbon in the water column may be more important than currently recognized (Ward et al., 2017), which was not considered in the experiments conducted for this thesis.

Other ecosystems may also be worth exploring. A prominent example is the current formation of 253 thermokarst lagoon systems, some of which are large and complex, as a result of sea level rise and

increased coastal erosion along the Arctic coastline (Angelopoulos et al., 2020). This will lead to the emergence of yet another permafrost ecosystem with similarly poorly constrained carbon (Jenrich et al., 2021) and potentially nitrogen dynamics. In the context of the conflicting evidence presented in manuscripts 2 and 4, the evolution of the lagoon systems may once again indicate another unique circumstance in which ancient carbon use may differ from other previously studied ecosystems. Overall, the implications of this thesis reveal circumstantial evidence for the availability of ancient carbon, rather than simply stating whether or not it is bioavailable upon entry into the ocean. This highlights the need for a more nuanced analysis of many ecosystem types, at least on a pan-Arctic scale, but perhaps even on a global scale, as well as the need to study these ecosystems independently rather than using a "one size fits all" strategy. The statement by Irrgang et al. (2022) provides a very nice summary: "…*environmental impacts can vary from one coastal location to another, adding to the level of complexity, and highlighting the need to understand individual coastal environments (for example, river deltas, marshes and the nearshore) within the context of the entire coastal ecosystem. Only when the burial, export and turnover processes for each of these environments can be clearly separated will reliable sediment and organic matter budgets along Arctic coasts be possible. These will help to better predict how coastal- erosion-derived nutrient and organic matter fluxes lead to changes in marine ecosystems through changes of light and nutrient availability, and are an important step towards integrating carbon and nutrient loadings from Arctic land loss into Earth system models (ESMs)*". Their statement is aimed at Arctic permafrost coastal erosion, but it could very well be applied to, for example, Antarctic glacial erosion and subsequent ancient carbon utilization in the Southern Ocean, even though the ecosystems are located in opposite parts of the world and have quite different climatic conditions. As a result, I would like to draw attention to the lack of knowledge about ancient carbon utilization across the globe and urge further research in this area, especially since it has been shown that even small regional and environmental variations have a significant impact on bioavailability, making it extremely difficult to incorporate them into Earth system models that guide global policy makers and thus our path to the future as a global society.

Acknowledgements

First of all, I would like to thank my doctor mother Gesine Mollenhauer for her excellent support over the last years, not just limited to scientific advice but for the entire experience. A personal note: “you are a role model of an adviser and boss!”

Furthermore, I’d like to thank Florence Schubotz, Hannah Marchant, and Valier Galy for their support during the individual projects. The experience to work with all of you was very rewarding and taught me a lot in both a professional and personal way.

A special thanks goes to Jens Hefter and Torben Gentz, who helped out tremendously with their expertise in the labs and with structuring the manual work of the thesis. In the same context I want to send out my ad most gratitude to Ingrid Dohrmann, Liz Bonk, Lea Phillips, Malte Höhn, Ingrid Stimac, Mary Gaylord, Heidi Taubner, and Jenny Wendt without their help none of the projects would have been possible. Their work is the foundation, not just of my thesis, but of much of the scientific work done in the sections.

A personal thanks goes out on all the people who helped out on expedition, a few of them I’d like to mention personally here like: Vasily Povazhny, Thomas Opel, Anabel von Jackowski, Hanno Meier, Micha Fritz, Maarten Boersma, Cédric Meunier, Justus Gimsa, and many others. Likewise, I’d like to express my gratitude to all the people of the “Lunch Groupe” of the last several years (Lukas, Olga, Sarah, Spela, Mica, Ayla, Julia, Agathe, Josefa, Cami, Cote, Eduardo, Lea, and all the others) – you made lunch an amazing experience of community, friendship, laughter, and international communication. Special thanks go to Olga and Ayra Ogneva for the many walk and talks during COVID and beyond.

Besides the scientific environment, I’d like to thank my friends (and somewhat family) in Bremen to have kept me sane during the PhD with COVID, the Russian lead war in the Ukraine, and the resulting difficulties and drawbacks within the last years. Special mentions are: Lars Grütjen, Julia Kaufmann, Marlien Ettien, Andreas Türke, Onur Krakus, Sebastian Geißer, Olvier Helten, Frederik Lange, Sebastian Gfellner, Florian Krauss, and all the people from the former *Irgendwo-Crew Bremen (2019-2022)*.

Last but not least, I’d like to thank my parents. My dad, who gave me the confidence and resilience to get through life. My mom, who got me through school and who made sure that - even a super dyslexic kid like me - gets a chance to prove himself and who refused listening nor accept teachers telling them that it is not worth a try.

Tanks to all of you!

References

Åberg, J., & Wallin, M. B. (2014). Evaluating a fast headspace method for measuring DIC and subsequent calculation of pCO2 in freshwater systems. *Inland Waters*, *4*(2), 157–166. https://doi.org/10.5268/IW-4.2.694

Adams, R. M., Hurd, B. H., Lenhart, S., & Leary, N. (1998). Effects of global climate change on world agriculture: an interpretive review. *Climate Research*, *11*(1), 19–30. https://doi.org/10.3354/cr011019

Adhikari, S., & Marshall, S. J. (2013). Influence of high-order mechanics on simulation of glacier response to climate change: Insights from Haig Glacier, Canadian Rocky Mountains. *Cryosphere*, *7*(5), 1527–1541. https://doi.org/10.5194/TC-7-1527-2013

Akondi, R. N., Trexler, R. V, Pfiffner, S. M., Mouser, P. J., & Sharma, S. (2017). Modified lipid extraction methods for deep subsurface shale. *Front Microbiol*, *8*, 1408. https://doi.org/10.3389/fmicb.2017.01408

Aleksyutina, D., Ogorodov, S., & Shilova, O. (2020). Simulation of Coastal Dynamics at the Kara Sea. *Journal of Coastal Research*, *95*(SI), 330–335. https://doi.org/10.2112/SI95-064.1

Alkhatib, M., Schubert, C. J., Del Giorgio, P. A., Gelinas, Y., & Lehmann, M. F. (2012). Organic matter reactivity indicators in sediments of the St. Lawrence Estuary. *Estuarine, Coastal and Shelf Science*, *102–103*, 36–47. https://doi.org/10.1016/J.ECSS.2012.03.002

Andersen, K. S., Kirkegaard, R. H., Karst, S. M., & Albertsen, M. (2018). ampvis2: an R package to analyse and visualise 16S rRNA amplicon data. *BioRxiv*, 299537.

Andersson, A., Deng, J., Du, K., Zheng, M., Yan, C., Sköld, M., & Gustafsson, O. (2015). Regionally-varying combustion sources of the January 2013 severe haze events over eastern China. *Environmental Science & Technology*, *49*(4), 2038–2043.

Angelopoulos, M., Overduin, P. P., Westermann, S., Tronicke, J., Strauss, J., Schirrmeister, L., Biskaborn, B. K., Liebner, S., Maksimov, G., & Grigoriev, M. N. (2020). Thermokarst lake to lagoon transitions in eastern Siberia: do submerged taliks refreeze? *Journal of Geophysical Research: Earth Surface*, *125*(10), e2019JF005424.

Appleby, P. G. (2001). Chronostratigraphic techniques in recent sediments. *Tracking Environmental Change Using Lake Sediments: Basin Analysis, Coring, and Chronological Techniques*, 171–203.

Arnosti, C. (2008). Functional differences between Arctic seawater and sedimentary microbial communities: contrasts in microbial hydrolysis of complex substrates. *FEMS Microbiol Ecol*, *66*(2), 343–351. https://doi.org/10.1111/j.1574-6941.2008.00587.x

Arnosti, C. (2011). Microbial extracellular enzymes and the marine carbon cycle. *Ann Rev Mar Sci*, *3*(1), 401–425. https://doi.org/10.1146/annurev-marine-120709-142731

Bakermans, C., Ayala-del-Río, H. L., Ponder, M. A., Vishnivetskaya, T., Gilichinsky, D., Thomashow, M. F., & Tiedje, J. M. (2006). Psychrobacter cryohalolentis sp. nov. and Psychrobacter arcticus sp. nov., isolated from Siberian permafrost. *International Journal of Systematic and Evolutionary Microbiology*, *56*(6), 1285–1291. https://doi.org/10.1099/IJS.0.64043-0/CITE/ENDNOTE

Bamber, J. L., Westaway, R. M., Marzeion, B., & Wouters, B. (2018). The land ice contribution to sea level

during the satellite era. *Environmental Research Letters*, *13*(6), 063008. https://doi.org/10.1088/1748-9326/AAC2F0

Bardgett, R. D., Richter, A., Bol, R., Garnett, M. H., Baumler, R., Xu, X., Lopez-Capel, E., Manning, D. A., Hobbs, P. J., Hartley, I. R., & Wanek, W. (2007). Heterotrophic microbial communities use ancient carbon following glacial retreat. *Biol Lett*, *3*(5), 487–490. https://doi.org/10.1098/rsbl.2007.0242

Barry, R. G., & Gan, T. Y. (2011). *The global cryosphere: past, present, and future*. Cambridge University Press.

Behnke, M. I., Tank, S. E., McClelland, J. W., Holmes, R. M., Haghipour, N., Eglinton, T. I., Raymond, P. A., Suslova, A., Zhulidov, A. V, & Gurtovaya, T. (2023). Aquatic biomass is a major source to particulate organic matter export in large Arctic rivers. *Proceedings of the National Academy of Sciences*, *120*(12), e2209883120.

Belevich, T. A., Il'yash, L. V, Chul'tsova, A. L., & Flint, M. V. (2019). The spatial distribution of plankton picocyanobacteria on the shelf of the Kara, Laptev, and East Siberian seas. *Moscow University Biological Sciences Bulletin*, *74*(4), 194–199.

Bendixen, M., Lønsmann Iversen, L., Anker Bjørk, A., Elberling, B., Westergaard-Nielsen, A., Overeem, I., Barnhart, K. R., Abbas Khan, S., Box, J. E., Abermann, J., Langley, K., & Kroon, A. (2017). Delta progradation in Greenland driven by increasing glacial mass loss. *Nature*, *550*(7674), 101–104. https://doi.org/10.1038/nature23873

Bennett, M. M., & Glasser, N. F. (2011). *Glacial geology: ice sheets and landforms*. John Wiley & Sons.

Berg, P., Risgaard-Petersen, N., & Rysgaard, S. (1998). Interpretation of measured concentration profiles in sediment pore water. *Limnology and Oceanography*, *43*(7), 1500–1510.

Berner, R. A., & Caldeira, K. (1997). The need for mass balance and feedback in the geochemical carbon cycle. *Geology*, *25*(10), 955–956.

Bhatia, M. P., Das, S. B., Xu, L., Charette, M. A., Wadham, J. L., & Kujawinski, E. B. (2013). Organic carbon export from the Greenland ice sheet. *Geochimica et Cosmochimica Acta*, *109*, 329–344. https://doi.org/10.1016/j.gca.2013.02.006

Bhatia, M. P., Kujawinski, E. B., Das, S. B., Breier, C. F., Henderson, P. B., & Charette, M. A. (2013). Greenland meltwater as a significant and potentially bioavailable source of iron to the ocean. *Nature Geoscience*, *6*(4), 274–278.

Bianchi, T. S. (2011). The role of terrestrially derived organic carbon in the coastal ocean: A changing paradigm and the priming effect. *Proceedings of the National Academy of Sciences*, *108*(49), 19473–19481. https://doi.org/10.1073/pnas.1017982108

Bianchi, T. S., & Canuel, E. A. (2011). *Chemical biomarkers in aquatic ecosystems*. Princeton University Press.

Bianchi, T. S., Cui, X., Blair, N. E., Burdige, D. J., Eglinton, T. I., & Galy, V. (2018). Centers of organic carbon burial and oxidation at the land-ocean interface. *Organic Geochemistry*, *115*, 138–155. https://doi.org/10.1016/j.orggeochem.2017.09.008

Bird, M., Santrùcková, H., Lloyd, J., & Veenendaal, E. (2001). Global soil organic carbon pool. In *Global biogeochemical cycles in the climate system* (pp. 185–199). Elsevier.

Birkenmajer, K. (1990). Geology of the Hornsund area, Spitsbergen. *Katowice, Poland*, *1*(75,000), 1–42.

Biskaborn, B. K., Smith, S. L., Noetzli, J., Matthes, H., Vieira, G., Streletskiy, D. A., Schoeneich, P., Romanovsky, V. E., Lewkowicz, A. G., & Abramov, A. (2019). Permafrost is warming at a global scale. *Nature Communications*, *10*(1), 264. https://doi.org/https://doi.org/10.1038/s41467-018-08240-4

Błaszczyk, M., Jania, J. A., & Kolondra, L. (2013). Fluctuations of tidewater glaciers in Hornsund Fjord (Southern Svalbard) since the beginning of the 20th century. *Polish Polar Research*, *34*(4), 327–352. https://doi.org/10.2478/popore-2013-0024

Blattmann, T. M., Liu, Z., Zhang, Y., Zhao, Y., Haghipour, N., Montluçon, D. B., Plötze, M., & Eglinton, T. I. (2019). Mineralogical control on the fate of continentally derived organic matter in the ocean. *Science*, *366*(6466), 742–745. https://doi.org/https://doi.org/10.1126/science.aax5345

Blattmann, Thomas M. (2022). Ideas and perspectives: Emerging contours of a dynamic exogenous kerogen cycle. *Biogeosciences*, *19*(2), 359–373.

Bligh, E. G., & Dyer, W. J. (1959). A rapid method of total lipid extraction and purification. *Can J Biochem Physiol*, *37*(8), 911–917. https://doi.org/10.1139/o59-099

Boetius, A., & Damm, E. (1998). Benthic oxygen uptake, hydrolytic potentials and microbial biomass at the Arctic continental slope. *Deep Sea Research Part I: Oceanographic Research Papers*, *45*(2–3), 239–275. https://doi.org/10.1016/s0967-0637(97)00052-6

Bogard, M. J., Kuhn, C. D., Johnston, S. E., Striegl, R. G., Holtgrieve, G. W., Dornblaser, M. M., Spencer, R. G. M., Wickland, K. P., & Butman, D. E. (2019). Negligible cycling of terrestrial carbon in many lakes of the arid circumpolar landscape. *Nature Geoscience*, *12*(3), 180–185. https://doi.org/10.1038/s41561-019-0299-5

Bojesen-Koefoed, J. A., Kalkreuth, W., Petersen, H. I., & Piasecki, S. (2012). A remote coal deposit revisited: Middle Jurassic coals at Kulhøj, western Germania Land, northeast Greenland. *International Journal of Coal Geology*, *98*, 50–61.

Boudreau, B. P. (1997). *Diagenetic models and their implementation* (Vol. 505). Springer Berlin.

Boulton, G. S. (1979). Processes of Glacier Erosion on Different Substrata. *Journal of Glaciology*, *23*(89), 15–38. https://doi.org/10.3189/S0022143000029713

Bourgeois, S., Kerhervé, P., Calleja, M. L., Many, G., & Morata, N. (2016). Glacier inputs influence organic matter composition and prokaryotic distribution in a high Arctic fjord (Kongsfjorden, Svalbard). *Journal of Marine Systems*, *164*, 112–127. https://doi.org/10.1016/j.jmarsys.2016.08.009

Bowman, J. P. (2017). Genomics of psychrophilic bacteria and archaea. *Psychrophiles: From Biodiversity to Biotechnology*, 345–387. https://doi.org/10.1007/978-3-319-57057-0_15/TABLES/3

Box, J. E., Hubbard, A., Bahr, D. B., Colgan, W. T., Fettweis, X., Mankoff, K. D., Wehrlé, A., Noël, B., van den Broeke, M. R., Wouters, B., Bjørk, A. A., & Fausto, R. S. (2022). Greenland ice sheet climate disequilibrium and committed sea-level rise. *Nature Climate Change 2022 12:9*, *12*(9), 808–813. https://doi.org/10.1038/s41558-022-01441-2

Brander, K. (2010). Impacts of climate change on fisheries. *Journal of Marine Systems*, *79*(3–4), 389–402. https://doi.org/10.1016/j.jmarsys.2008.12.015

Bray, E. E., & Evans, E. D. (1961). Distribution of n-paraffins as a clue to recognition of source beds.

Geochimica et Cosmochimica Acta, *22*(1), 2–15. https://doi.org/10.1016/0016-7037(61)90069-2

Bristol, E. M., Connolly, C. T., Lorenson, T. D., Richmond, B. M., Ilgen, A. G., Choens, R. C., Bull, D. L., Kanevskiy, M., Iwahana, G., & Jones, B. M. (2021). Geochemistry of coastal permafrost and erosion-driven organic matter fluxes to the Beaufort Sea near Drew Point, Alaska. *Frontiers in Earth Science*, *8*, 598933.

Bröder, L., Tesi, T., Andersson, A., Semiletov, I., Gustafsson, Ö., & Gustafsson, O. (2018). Bounding cross-shelf transport time and degradation in Siberian-Arctic land-ocean carbon transfer. *Nature Communications*, *9*(1), 806. https://doi.org/10.1038/s41467-018-03192-1

Brodie, C. R., Leng, M. J., Casford, J. S. L., Kendrick, C. P., Lloyd, J. M., Yongqiang, Z., & Bird, M. I. (2011). Evidence for bias in C and N concentrations and δ13C composition of terrestrial and aquatic organic materials due to pre-analysis acid preparation methods. *Chemical Geology*, *282*(3–4), 67–83. https://doi.org/10.1016/J.CHEMGEO.2011.01.007

Brüchert, V., Bröder, L., Sawicka, J. E., Tesi, T., Joye, S. P., Sun, X., Semiletov, I. P., & Samarkin, V. A. (2018). Carbon mineralization in Laptev and East Siberian sea shelf and slope sediment. *Biogeosciences*, *15*(2), 471–490. https://doi.org/10.5194/bg-15-471-2018

Bruel, R., & Sabatier, P. (2020). serac: an R package for ShortlivEd RAdionuclide chronology of recent sediment cores. *Journal of Environmental Radioactivity*, *225*, 106449. https://doi.org/10.1016/J.JENVRAD.2020.106449

Burrows, K., & Kinney, P. L. (2016). Exploring the Climate Change, Migration and Conflict Nexus. *Int J Environ Res Public Health*, *13*(4), 443. https://doi.org/10.3390/ijerph13040443

Butzin, M., Sidorenko, D., & Köhler, P. (2021). *A multi-resolution ocean simulation of the anthropogenic radiocarbon transient* (EGU General Assembly Conference Abstracts (ed.); pp. EGU21-3118). https://doi.org/10.5194/EGUSPHERE-EGU21-3118

Callahan, B. J., McMurdie, P. J., Rosen, M. J., Han, A. W., Johnson, A. J. A., & Holmes, S. P. (2016). DADA2: High-resolution sample inference from Illumina amplicon data. *Nature Methods*, *13*(7), 581–583.

Calleja, M. L., Kerhervé, P., Bourgeois, S., Kędra, M., Leynaert, A., Devred, E., Babin, M., & Morata, N. (2017). Effects of increase glacier discharge on phytoplankton bloom dynamics and pelagic geochemistry in a high Arctic fjord. *Progress in Oceanography*, *159*, 195–210. https://doi.org/10.1016/j.pocean.2017.07.005

Canadian Hydrographic Service. (1986). *Nautical Chart 7661: Demarcation Bay to/à Phillips Bay. 1:150,000.*

Cañavate, J. P., Armada, I., Ríos, J. L., & Hachero-Cruzado, I. (2016). Exploring occurrence and molecular diversity of betaine lipids across taxonomy of marine microalgae. *Phytochemistry*, *124*, 68–78.

Carlson, C. A., Del Giorgio, P. A., & Herndl, G. J. (2007). Microbes and the dissipation of energy and respiration: from cells to ecosystems. *Oceanography*, *20*(2), 89–100.

Chadburn, S. E., Burke, E. J., Cox, P. M., Friedlingstein, P., Hugelius, G., & Westermann, S. (2017). An observation-based constraint on permafrost loss as a function of global warming. *Nature Climate Change*, *7*(5), 340–344.

Chao, A., Gotelli, N. J., Hsieh, T. C., Sander, E. L., Ma, K. H., Colwell, R. K., & Ellison, A. M. (2014). Rarefaction

and extrapolation with Hill numbers: a framework for sampling and estimation in species diversity studies. *Ecological Monographs*, *84*(1), 45–67.

Ćmiel, S. R., & Fabiańska, M. J. (2004). Geochemical and petrographic properties of some Spitsbergen coals and dispersed organic matter. *International Journal of Coal Geology*, *57*(2), 77–97. https://doi.org/10.1016/j.coal.2003.09.002

Costello, E. K., & Schmidt, S. K. (2006). Microbial diversity in alpine tundra wet meadow soil: novel Chloroflexi from a cold, water-saturated environment. *Environmental Microbiology*, *8*(8), 1471–1486. https://doi.org/10.1111/J.1462-2920.2006.01041.X

Couture, N. J., Irrgang, A., Pollard, W., Lantuit, H., & Fritz, M. (2018). Coastal erosion of permafrost soils along the Yukon Coastal Plain and fluxes of organic carbon to the Canadian Beaufort Sea. *Journal of Geophysical Research: Biogeosciences*, *123*(2), 406–422.

Cowton, T., Nienow, P., Bartholomew, I., Sole, A., & Mair, D. (2012). Rapid erosion beneath the Greenland ice sheet. *Geology*, *40*(4), 343–346. https://doi.org/10.1130/G32687.1

Cuffey, K. M., Conway, H., Gades, A. M., Hallet, B., Lorrain, R., Severinghaus, J. P., Steig, E. J., Vaughn, B., & White, J. W. C. (2000). Entrainment at cold glacier beds. *Geology*, *28*(4), 351–354.

Cui, X., Bianchi, T. S., Jaeger, J. M., & Smith, R. W. (2016). Biospheric and petrogenic organic carbon flux along southeast Alaska. *Earth and Planetary Science Letters*, *452*, 238–246. https://doi.org/10.1016/j.epsl.2016.08.002

Cui, X., Bianchi, T. S., & Savage, C. (2017). Erosion of modern terrestrial organic matter as a major component of sediments in fjords. *Geophysical Research Letters*, *44*(3), 1457–1465. https://doi.org/10.1002/2016gl072260

Cui, X., Bianchi, T. S., Savage, C., & Smith, R. W. (2016). Organic carbon burial in fjords: Terrestrial versus marine inputs. *Earth and Planetary Science Letters*, *451*, 41–50. https://doi.org/10.1016/j.epsl.2016.07.003

Cui, X., Mucci, A., Bianchi, T. S., He, D., Vaughn, D., Williams, E. K., Wang, C., Smeaton, C., Koziorowska-Makuch, K., Faust, J. C., Plante, A. F., & Rosenheim, B. E. (2022). Global fjords as transitory reservoirs of labile organic carbon modulated by organo-mineral interactions. *Science Advances*, *8*(46), 0610. https://doi.org/10.1126/SCIADV.ADD0610

da Silva, V. de P. R. (2004). On climate variability in Northeast of Brazil. *Journal of Arid Environments*, *58*(4), 575–596. https://doi.org/10.1016/j.jaridenv.2003.12.002

Danilov, S., Sidorenko, D., Wang, Q., & Jung, T. (2017). The finite-volume sea ice-Ocean model (FESOM2). *Geoscientific Model Development*, *10*(2), 765–789. https://doi.org/10.5194/GMD-10-765-2017

Dauner, A. L. L., Mollenhauer, G., Hefter, J., Bicego, M. C., de Mahiques, M. M., & Martins, C. de C. (2022). Late Pleistocene to Holocene variations in marine productivity and terrestrial material delivery to the western South Atlantic. *Frontiers in Marine Science*, *9*, 924556.

Delaney, I., & Adhikari, S. (2020). Increased Subglacial Sediment Discharge in a Warming Climate: Consideration of Ice Dynamics, Glacial Erosion, and Fluvial Sediment Transport. *Geophysical Research Letters*, *47*(7). https://doi.org/10.1029/2019GL085672

Dembitsky, V. M. (1996). Betaine ether-linked glycerolipids: Chemistry and biology. *Progress in Lipid*

Research, *35*(1), 1–51. https://doi.org/10.1016/0163-7827(95)00009-7

Dibner, V. D., Bro, E. G., Preobrazhenskaya, E. N., Pchelina, T. M., Shkola, I. V, Solheim, A., Musatov, E., & Heinz, N. (1992). *The geology of Franz Josef Land Archipelago, Russian Federation*.

Dowdeswell, J. A., Hagen, J. O., Björnsson, H., Glazovsky, A. F., Harrison, W. D., Holmlund, P., Jania, J., Koerner, R. M., Lefauconnier, B., Ommanney, C. S. L., & Thomas, R. H. (1997). The Mass Balance of Circum-Arctic Glaciers and Recent Climate Change. *Quaternary Research*, *48*(1), 1–14. https://doi.org/10.1006/QRES.1997.1900

Drake, T. W., Wickland, K. P., Spencer, R. G. M., McKnight, D. M., & Striegl, R. G. (2015). Ancient low–molecular-weight organic acids in permafrost fuel rapid carbon dioxide production upon thaw. *Proceedings of the National Academy of Sciences*, *112*(45), 13946–13951.

Drenzek, N. J., Montluçon, D. B., Yunker, M. B., Macdonald, R. W., & Eglinton, T. I. (2007). Constraints on the origin of sedimentary organic carbon in the Beaufort Sea from coupled molecular 13C and 14C measurements. *Marine Chemistry*, *103*(1–2), 146–162.

Druffel, E. R. M., Griffin, S., Glynn, C. S., Benner, R., & Walker, B. D. (2017). Radiocarbon in dissolved organic and inorganic carbon of the Arctic Ocean. *Geophysical Research Letters*, *44*(5), 2369–2376.

Dumoulin, J. P., Rabouille, C., Pourtout, S., Bombled, B., Lansard, B., Caffy, I., Hain, S., Perron, M., Sieudat, M., & Thellier, B. (2022). IDENTIFICATION IN PORE WATERS OF RECYCLED SEDIMENT ORGANIC MATTER USING THE DUAL ISOTOPIC COMPOSITION OF CARBON (δ 13C AND Δ14C): NEW DATA FROM THE CONTINENTAL SHELF INFLUENCED BY THE RHÔNE RIVER. *Radiocarbon*, *64*(6), 1617–1627.

Dutta, K., Schuur, E. A. G., Neff, J. C., & Zimov, S. A. (2006). Potential carbon release from permafrost soils of Northeastern Siberia. *Global Change Biology*, *12*(12), 2336–2351.

Eglinton, T. I., Aluwihare, L. I., Bauer, J. E., Druffel, E. R. M., & McNichol, A. P. (1996). Gas chromatographic isolation of individual compounds from complex matrices for radiocarbon dating. *Analytical Chemistry*, *68*(5), 904–912.

Eglinton, T. I., Benitez-Nelson, B. C., Pearson, A., McNichol, A. P., Bauer, J. E., & Druffel, E. R. M. (1997). Variability in radiocarbon ages of individual organic compounds from marine sediments. *Science*, *277*(5327), 796–799.

Elder, C. D., Xu, X., Walker, J., Schnell, J. L., Hinkel, K. M., Townsend-Small, A., Arp, C. D., Pohlman, J. W., Gaglioti, B. V., & Czimczik, C. I. (2018). Greenhouse gas emissions from diverse Arctic Alaskan lakes are dominated by young carbon. *Nature Climate Change 2018 8:2*, *8*(2), 166–171. https://doi.org/10.1038/s41558-017-0066-9

Elliot, D. H., Fanning, C. M., & Hulett, S. R. W. W. (2015). Age provinces in the Antarctic craton: Evidence from detrital zircons in Permian strata from the Beardmore Glacier region, Antarctica. *Gondwana Research*, *28*(1), 152–164. https://doi.org/10.1016/J.GR.2014.03.013

Ernakovich, J. G., Barbato, R. A., Rich, V. I., Schädel, C., Hewitt, R. E., Doherty, S. J., Whalen, E. D., Abbott, B. W., Barta, J., Biasi, C., Chabot, C. L., Hultman, J., Knoblauch, C., Vetter, M. C. Y. L., Leewis, M. C., Liebner, S., Mackelprang, R., Onstott, T. C., Richter, A., … Winkel, M. (2022). Microbiome assembly in thawing permafrost and its feedbacks to climate. *Global Change Biology*, *28*(17), 5007–5026. https://doi.org/10.1111/GCB.16231

Ewing, S. A., O'Donnell, J. A., Aiken, G. R., Butler, K., Butman, D., Windham-Myers, L., & Kanevskiy, M. Z.

(2015). Long-term anoxia and release of ancient, labile carbon upon thaw of Pleistocene permafrost. *Geophysical Research Letters*, *42*(24), 10–730. https://doi.org/https://doi.org/10.1002/2015GL066296

Fahey, T. J., Woodbury, P. B., Battles, J. J., Goodale, C. L., Hamburg, S. P., Ollinger, S. V, & Woodall, C. W. (2010). Forest carbon storage: ecology, management, and policy. *Frontiers in Ecology and the Environment*, *8*(5), 245–252.

Fahl, K., & Stein, R. (1999). Biomarkers as organic-carbon-source and environmental indicators in the Late Quaternary Arctic Ocean: problems and perspectives. *Marine Chemistry*, *63*(3–4), 293–309.

Farquharson, L. M., Romanovsky, V. E., Cable, W. L., Walker, D. A., Kokelj, S. V, & Nicolsky, D. (2019). Climate change drives widespread and rapid thermokarst development in very cold permafrost in the Canadian High Arctic. *Geophysical Research Letters*, *46*(12), 6681–6689.

Feng, X., Vonk, J. E., van Dongen, B. E., Gustafsson, O., Semiletov, I. P., Dudarev, O. V, Wang, Z., Montlucon, D. B., Wacker, L., & Eglinton, T. I. (2013). Differential mobilization of terrestrial carbon pools in Eurasian Arctic river basins. *Proc Natl Acad Sci U S A*, *110*(35), 14168–14173. https://doi.org/10.1073/pnas.1307031110

Fiadeiro, M. E. (1982). Three-dimensional modeling of tracers in the deep Pacific Ocean II. Radiocarbon and the circulation. *Journal of Marine Research*, *40*(2), 537–550.

Fiencke, C., Marushchak, M. E., Sanders, T., Wegner, R., & Beer, C. (2022). Microbiogeochemical Traits to Identify Nitrogen Hotspots in Permafrost Regions. *Nitrogen*, *3*(3), 458–501.

Forwick, M., Szczuciński, W., & Jernas, P. E. (2014). *Cruise report: Marine-geological cruise to Hornsund, Svalbard*.

France-Lanord, C., & Derry, L. A. (1997). Organic carbon burial forcing of the carbon cycle from Himalayan erosion. *Nature*, *390*(6655), 65–67.

Fritz, M., Opel, T., Tanski, G., Herzschuh, U., Meyer, H., Eulenburg, A., & Lantuit, H. (2015). Dissolved organic carbon (DOC) in Arctic ground ice. *The Cryosphere*, *9*(2), 737–752.

Fritz, M., Vonk, J. E., & Lantuit, H. (2017). Collapsing arctic coastlines. *Nature Climate Change*, *7*(1), 6–7. https://doi.org/10.1038/nclimate3188

Fritz, M., Wetterich, S., Schirrmeister, L., Meyer, H., Lantuit, H., Preusser, F., & Pollard, W. H. (2012). Eastern Beringia and beyond: late Wisconsinan and Holocene landscape dynamics along the Yukon Coastal Plain, Canada. *Palaeogeography, Palaeoclimatology, Palaeoecology*, *319*, 28–45.

Fuchs, M., Bolshiyanov, D., Grigoriev, M., Morgenstern, A., Pesttryakova, L., Tsibizov, L., & Dill, A. (2021). *Russian-German Cooperation: Expeditions to Siberia in 2019*. https://doi.org/10.48433/BzPM_0749_2021

Fuchs, M., Nitze, I., Strauss, J., Günther, F., Wetterich, S., Kizyakov, A., Fritz, M., Opel, T., Grigoriev, M. N., & Maksimov, G. T. (2020). Rapid Fluvio-Thermal Erosion of a Yedoma Permafrost Cliff in the Lena River Delta. *Frontiers in Earth Science*, *8*(336).

Galy, V., Beyssac, O., France-Lanord, C., & Eglinton, T. (2008). Recycling of graphite during Himalayan erosion: a geological stabilization of carbon in the crust. *Science*, *322*(5903), 943–945. https://doi.org/10.1126/science.1161408

Galy, V., Peucker-Ehrenbrink, B., & Eglinton, T. (2015). Global carbon export from the terrestrial biosphere controlled by erosion. *Nature*, *521*(7551), 204–207. https://doi.org/10.1038/nature14400

Gołębiewski, M., Deja-Sikora, E., Cichosz, M., Tretyn, A., & Wróbel, B. (2014). 16S rDNA pyrosequencing analysis of bacterial community in heavy metals polluted soils. *Microbial Ecology*, *67*(3), 635–647.

Goodwin, B. P., Mosley-Thompson, E., Wilson, A. B., Porter, S. E., & Roxana Sierra-Hernandez, M. (2016). Accumulation Variability in the Antarctic Peninsula: The Role of Large-Scale Atmospheric Oscillations and Their Interactions. *Journal of Climate*, *29*(7), 2579–2596. https://doi.org/10.1175/JCLI-D-15-0354.1

Goswami, A., Adkins-Jablonsky, S. J., Barreto Filho, M., Schilling, M., Dawson, A., Heiser, S., O'Connor, A., Walker, M., Roberts, Q., & Morris, J. J. (2023). Heavy metal pollution impacts soil bacterial community structure and antimicrobial resistance at the Birmingham 35th Avenue Superfund Site. *BioRxiv*, *11*(2), e02426-22.

Grasshoff, K., Kremling, K., & Ehrhardt, M. (1999). *Methods of seawater analysis*. John Wiley & Sons.

Graven, H., Allison, C. E., Etheridge, D. M., Hammer, S., Keeling, R. F., Levin, I., Meijer, H. A. J. J., Rubino, M., Tans, P. P., Trudinger, C. M., Vaughn, B. H., & White, J. W. C. (2017). Compiled records of carbon isotopes in atmospheric CO 2 for historical simulations in CMIP6. *Geoscientific Model Development*, *10*(12), 4405–4417. https://doi.org/10.5194/GMD-10-4405-2017

Grotheer, H., Meyer, V., Riedel, T., Pfalz, G., Mathieu, L., Hefter, J., Gentz, T., Lantuit, H., Mollenhauer, G., & Fritz, M. (2020). Burial and Origin of Permafrost-Derived Carbon in the Nearshore Zone of the Southern Canadian Beaufort Sea. *Geophysical Research Letters*, *47*(3), e2019GL085897.

Guillemette, F., Bianchi, T. S., & Spencer, R. G. M. (2017). Old before your time: Ancient carbon incorporation in contemporary aquatic foodwebs. *Limnology and Oceanography*, *62*(4), 1682–1700. https://doi.org/10.1002/lno.10525

Günther, F., Overduin, P. P., Sandakov, A. V, Grosse, G., & Grigoriev, M. N. (2013). Short-and long-term thermo-erosion of ice-rich permafrost coasts in the Laptev Sea region. *Biogeosciences*, *10*(6), 4297–4318. https://doi.org/10.5194/bg-10-4297-2013

Guo, L., Ping, C.-L. L., & Macdonald, R. W. (2007). Mobilization pathways of organic carbon from permafrost to arctic rivers in a changing climate. *Geophysical Research Letters*, *34*(13), n/a-n/a. https://doi.org/10.1029/2007gl030689

Gutiérrez, M. H., Galand, P. E., Moffat, C., & Pantoja, S. (2015). Melting glacier impacts community structure of Bacteria, Archaea and Fungi in a Chilean Patagonia fjord. *Environmental Microbiology*, *17*(10), 3882–3897. https://doi.org/10.1111/1462-2920.12872/SUPPINFO

Haddeland, I., Heinke, J., Biemans, H., Eisner, S., Florke, M., Hanasaki, N., Konzmann, M., Ludwig, F., Masaki, Y., Schewe, J., Stacke, T., Tessler, Z. D., Wada, Y., & Wisser, D. (2014). Global water resources affected by human interventions and climate change. *Proc Natl Acad Sci U S A*, *111*(9), 3251–3256. https://doi.org/10.1073/pnas.1222475110

Hanke, U. M., Gagnon, A. R., Reddy, C. M., Gaylord, M. C. L., Cruz, A. J., Galy, V., Hansman, R. L., & Kurz, M. D. (2023). Sequential Thermal Analysis of Complex Organic Mixtures: Procedural Standards and Improved CO2 Purification Capacity. *Radiocarbon*, *65*(2), 389–409.

Hantemirov, R. M., Corona, C., Guillet, S., Shiyatov, S. G., Stoffel, M., Osborn, T. J., Melvin, T. M.,

Gorlanova, L. A., Kukarskih, V. V, & Surkov, A. Y. (2022). Current Siberian heating is unprecedented during the past seven millennia. *Nature Communications*, *13*(1), 4968. https://doi.org/https://doi.org/10.1038/s41467-022-32629-x

Harland, W. B. (1997). Chapter 20 Paleogene history. *Geological Society, London, Memoirs. Geological Society, London*.

Harmelin-Vivien, M., Dierking, J., Bănaru, D., Fontaine, M. F., & Arlhac, D. (2010). Seasonal variation in stable C and N isotope ratios of the Rhone River inputs to the Mediterranean Sea (2004–2005). *Biogeochemistry*, *100*, 139–150.

Harvey, H. R., Fallon, R. D., & Patton, J. S. (1986). The effect of organic matter and oxygen on the degradation of bacterial membrane lipids in marine sediments. *Geochimica et Cosmochimica Acta*, *50*(5), 795–804. https://doi.org/10.1016/0016-7037(86)90355-8

Hawkings, J. R., Wadham, J. L., Benning, L. G., Hendry, K. R., Tranter, M., Tedstone, A., Nienow, P., & Raiswell, R. (2017). Ice sheets as a missing source of silica to the polar oceans. *Nature Communications 2017 8:1*, *8*(1), 1–10. https://doi.org/10.1038/ncomms14198

Hayes, J. M. (2001). Fractionation of the isotopes of carbon and hydrogen in biosynthetic processes, pp. 225Ð277. *Stable Isotope Geochemistry*, *43*.

Hedges, J. I. (1992). Global biogeochemical cycles: progress and problems. *Marine Chemistry*, *39*(1–3), 67–93. https://doi.org/10.1016/0304-4203(92)90096-S

Hemingway, J. D., Galy, V. V., Gagnon, A. R., Grant, K. E., Rosengard, S. Z., Soulet, G., Zigah, P. K., & McNichol, A. P. (2017). Assessing the Blank Carbon Contribution, Isotope Mass Balance, and Kinetic Isotope Fractionation of the Ramped Pyrolysis/Oxidation Instrument at NOSAMS. *Radiocarbon*, *59*(1), 179–193. https://doi.org/10.1017/RDC.2017.3

Hemingway, J. D., Hilton, R. G., Hovius, N., Eglinton, T. I., Haghipour, N., Wacker, L., Chen, M.-C., & Galy, V. V. (2018). Microbial oxidation of lithospheric organic carbon in rapidly eroding tropical mountain soils. *Science*, *360*(6385), 209–212. https://doi.org/https://doi.org/10.1126/science.aao6463

Hemingway, J. D., Rothman, D. H., Grant, K. E., Rosengard, S. Z., Eglinton, T. I., Derry, L. A., & Galy, V. V. (2019). Mineral protection regulates long-term global preservation of natural organic carbon. *Nature*, *570*(7760), 228–231. https://doi.org/10.1038/s41586-019-1280-6

Hemingway, J. D., Rothman, D. H., Rosengard, S. Z., & Galy, V. V. (2017). An inverse method to relate organic carbon reactivity to isotope composition from serial oxidation. *Biogeosciences*, *14*(22), 5099–5114. https://doi.org/10.5194/BG-14-5099-2017

Herman, F., Beyssac, O., Brughelli, M., Lane, S. N., Leprince, S., Adatte, T., Lin, J. Y. Y., Avouac, J. P., & Cox, S. C. (2015). Erosion by an Alpine glacier. *Science*, *350*(6257), 193–195. https://doi.org/10.1126/SCIENCE.AAB2386/SUPPL_FILE/AAB2386S2.MOV

Herman, F., De Doncker, F., Delaney, I., Prasicek, G., & Koppes, M. (2021). The impact of glaciers on mountain erosion. *Nature Reviews Earth & Environment 2021 2:6*, *2*(6), 422–435. https://doi.org/10.1038/s43017-021-00165-9

Herraiz-Borreguero, L., Lannuzel, D., van der Merwe, P., Treverrow, A., & Pedro, J. B. (2016). Large flux of iron from the Amery Ice Shelf marine ice to Prydz Bay, East Antarctica. *Journal of Geophysical Research: Oceans*, *121*(8), 6009–6020. https://doi.org/10.1002/2016JC011687

Hilton, R. G., Gaillardet, J., Calmels, D., & Birck, J.-L. (2014). Geological respiration of a mountain belt revealed by the trace element rhenium. *Earth and Planetary Science Letters*, *403*, 27–36.

Hilton, R. G., & West, A. J. (2020). Mountains, erosion and the carbon cycle. *Nature Reviews Earth & Environment 2020 1:6*, *1*(6), 284–299. https://doi.org/10.1038/s43017-020-0058-6

Hinkel, K. M., & Nelson, F. E. (2003). Spatial and temporal patterns of active layer thickness at Circumpolar Active Layer Monitoring (CALM) sites in northern Alaska, 1995–2000. *Journal of Geophysical Research: Atmospheres*, *108*(D2).

Hinojosa, J. L., Moy, C. M., Stirling, C. H., Wilson, G. S., & Eglinton, T. I. (2014). Carbon cycling and burial in New Zealand's fjords. *Geochemistry, Geophysics, Geosystems*, *15*(10), 4047–4063. https://doi.org/10.1002/2014GC005433

Hodson, A., Nowak, A., Sabacka, M., Jungblut, A., Navarro, F., Pearce, D., Ávila-Jiménez, M. L., Convey, P., & Vieira, G. (2017). Climatically sensitive transfer of iron to maritime Antarctic ecosystems by surface runoff. *Nature Communications 2017 8:1*, *8*(1), 1–7. https://doi.org/10.1038/ncomms14499

Hoffmann, K., Bienhold, C., Buttigieg, P. L., Knittel, K., Laso-Pérez, R., Rapp, J. Z., Boetius, A., & Offre, P. (2020). Diversity and metabolism of Woeseiales bacteria, global members of marine sediment communities. *The ISME Journal*, *14*(4), 1042–1056.

Hood, E., Battin, T. J., Fellman, J., O'Neel, S., & Spencer, R. G. M. (2015). Storage and release of organic carbon from glaciers and ice sheets. *Nature Geoscience*, *8*(2), 91–96. https://doi.org/10.1038/ngeo2331

Hood, E., Fellman, J., Spencer, R. G. M., Hernes, P. J., Edwards, R., D'Amore, D., & Scott, D. (2009). Glaciers as a source of ancient and labile organic matter to the marine environment. *Nature*, *462*(7276), 1044–1047. https://doi.org/10.1038/nature08580

Hopmans, E. C., Schouten, S., & Sinninghe Damsté, J. S. (2016). The effect of improved chromatography on GDGT-based palaeoproxies. *Organic Geochemistry*, *93*, 1–6. https://doi.org/10.1016/j.orggeochem.2015.12.006

Hopmans, E. C., Weijers, J. W. H., Schefuß, E., Herfort, L., Sinninghe Damsté, J. S., & Schouten, S. (2004). A novel proxy for terrestrial organic matter in sediments based on branched and isoprenoid tetraether lipids. *Earth and Planetary Science Letters*, *224*(1–2), 107–116. https://doi.org/10.1016/j.epsl.2004.05.012

Horan, K., Hilton, R. G., Selby, D., Ottley, C. J., Gröcke, D. R., Hicks, M., & Burton, K. W. (2017). Mountain glaciation drives rapid oxidation of rock-bound organic carbon. *Science Advances*, *3*(10), e1701107.

Hueffer, K., Drown, D., Romanovsky, V., & Hennessy, T. (2020). Factors Contributing to Anthrax Outbreaks in the Circumpolar North. *EcoHealth 2020 17:1*, *17*(1), 174–180. https://doi.org/10.1007/S10393-020-01474-Z

Hugelius, G., Strauss, J., Zubrzycki, S., Harden, J. W., Schuur, E. A. G., Ping, C.-L., Schirrmeister, L., Grosse, G., Michaelson, G. J., & Koven, C. D. (2014). Estimated stocks of circumpolar permafrost carbon with quantified uncertainty ranges and identified data gaps. *Biogeosciences*, *11*(23), 6573–6593.

Hultman, J., Waldrop, M. P., Mackelprang, R., David, M. M., McFarland, J., Blazewicz, S. J., Harden, J., Turetsky, M. R., McGuire, A. D., Shah, M. B., VerBerkmoes, N. C., Lee, L. H., Mavrommatis, K., & Jansson, J. K. (2015). Multi-omics of permafrost, active layer and thermokarst bog soil microbiomes.

Nature 2015 521:7551, *521*(7551), 208–212. https://doi.org/10.1038/nature14238

Hunt, A., & Watkiss, P. (2010). Climate change impacts and adaptation in cities: a review of the literature. *Climatic Change*, *104*(1), 13–49. https://doi.org/10.1007/s10584-010-9975-6

IPCC. (2007). The physical science basis. *Contribution of Working Group I to the Fourth Assessment Report of the Intergovernmental Panel on Climate Change*, *996*.

IPCC. (2019). IPCC Special Report on the Ocean and Cryosphere in a Changing Climate. *Intergovernmental Panel on Climate Change*, *1*(3), undefined. https://www.ipcc.ch/srocc/chapter/summary-for-policymakers/

Irrgang, A. M., Bendixen, M., Farquharson, L. M., Baranskaya, A. V., Erikson, L. H., Gibbs, A. E., Ogorodov, S. A., Overduin, P. P., Lantuit, H., Grigoriev, M. N., & Jones, B. M. (2022). Drivers, dynamics and impacts of changing Arctic coasts. *Nature Reviews Earth & Environment 2022 3:1*, *3*(1), 39–54. https://doi.org/10.1038/s43017-021-00232-1

Jenrich, M., Angelopoulos, M., Grosse, G., Overduin, P. P., Schirrmeister, L., Nitze, I., Biskaborn, B. K., Liebner, S., Grigoriev, M., & Murray, A. (2021). Thermokarst Lagoons: a core-based assessment of depositional characteristics and an estimate of carbon pools on the Bykovsky Peninsula. *Frontiers in Earth Science*, *9*, 637899.

Johnson, S. S., Hebsgaard, M. B., Christensen, T. R., Mastepanov, M., Nielsen, R., Munch, K., Brand, T., Gilbert, M. T. P., Zuber, M. T., Bunce, M., Rønn, R., Gilichinsky, D., Froese, D., & Willerslev, E. (2007). Ancient bacteria show evidence of DNA repair. *Proceedings of the National Academy of Sciences*, *104*(36), 14401–14405. https://doi.org/10.1073/PNAS.0706787104

Jones, B M, Irrgang, A. M., Farquharson, L. M., Lantuit, H., Whalen, D., Ogorodov, S., Grigoriev, M., Tweedie, C., Gibbs, A. E., & Strzelecki, M. C. (2020). *Arctic Report Card 2020: coastal permafrost erosion*. https://doi.org/https://doi.org/10.25923/e47w-dw52

Jones, Benjamin M, Grosse, G., Arp, C. D., Jones, M. C., Walter Anthony, K. M., & Romanovsky, V. E. (2011). Modern thermokarst lake dynamics in the continuous permafrost zone, northern Seward Peninsula, Alaska. *Journal of Geophysical Research: Biogeosciences*, *116*(G2).

Jong, D., Bröder, L., Tanski, G., Fritz, M., Lantuit, H., Tesi, T., Haghipour, N., Eglinton, T. I., & Vonk, J. E. (2020). Nearshore zone dynamics determine pathway of organic carbon from eroding permafrost coasts. *Geophysical Research Letters*, *47*(15). https://doi.org/https://doi.org/10.1029/2020GL088561

Jørgensen, B. B., Weber, A., & Zopfi, J. (2001). Sulfate reduction and anaerobic methane oxidation in Black Sea sediments. *Deep Sea Research Part I: Oceanographic Research Papers*, *48*(9), 2097–2120. https://doi.org/10.1016/S0967-0637(01)00007-3

Kalish, J. M., Nydal, R., Nedreaas, K. H., Burr, G. S., & Eine, G. L. (2001). A time history of pre-and post-bomb radiocarbon in the Barents Sea derived from Arcto-Norwegian cod otoliths. *Radiocarbon*, *43*(2B), 843–855.

Kanevskiy, M., Shur, Y., Strauss, J., Jorgenson, T., Fortier, D., Stephani, E., & Vasiliev, A. (2016). Patterns and rates of riverbank erosion involving ice-rich permafrost (yedoma) in northern Alaska. *Geomorphology*, *253*, 370–384. https://doi.org/https://doi.org/10.1016/j.geomorph.2015.10.023

Kappelmann, L., Krüger, K., Hehemann, J.-H., Harder, J., Markert, S., Unfried, F., Becher, D., Shapiro, N.,

Schweder, T., & Amann, R. I. (2019). Polysaccharide utilization loci of North Sea Flavobacteriia as basis for using SusC/D-protein expression for predicting major phytoplankton glycans. *The ISME Journal*, *13*(1), 76–91.

Key, R. M., Kozyr, A., Sabine, C. L., Lee, K., Wanninkhof, R., Bullister, J. L., Feely, R. A., Millero, F. J., Mordy, C., & Peng, T. H. (2004). A global ocean carbon climatology: Results from Global Data Analysis Project (GLODAP). *Global Biogeochemical Cycles*, *18*(4), 1–23. https://doi.org/10.1029/2004GB002247

Kim, J.-H., Peterse, F., Willmott, V., Klitgaard Kristensen, D., Baas, M., Schouten, S., & Sinninghe Damsté, J. S. (2011). Large ancient organic matter contributions to Arctic marine sediments (Svalbard). *Limnology and Oceanography*, *56*(4), 1463–1474. https://doi.org/10.4319/lo.2011.56.4.1463

Kjeldsen, K. K., Korsgaard, N. J., Bjørk, A. A., Khan, S. A., Box, J. E., Funder, S., Larsen, N. K., Bamber, J. L., Colgan, W., Van Den Broeke, M., Siggaard-Andersen, M. L., Nuth, C., Schomacker, A., Andresen, C. S., Willerslev, E., & Kjær, K. H. (2015). Spatial and temporal distribution of mass loss from the Greenland Ice Sheet since AD 1900. *Nature 2015 528:7582*, *528*(7582), 396–400. https://doi.org/10.1038/nature16183

Knoblauch, C., Beer, C., Sosnin, A., Wagner, D., & Pfeiffer, E. (2013). Predicting long-term carbon mineralization and trace gas production from thawing permafrost of Northeast Siberia. *Global Change Biology*, *19*(4), 1160–1172.

Kohler, T. J., Vinšová, P., Falteisek, L., Žárský, J. D., Yde, J. C., Hatton, J. E., Hawkings, J. R., Lamarche-Gagnon, G., Hood, E., Cameron, K. A., & Stibal, M. (2020). Patterns in microbial assemblages exported from the meltwater of Arctic and Sub-Arctic glaciers. *Frontiers in Microbiology*, *11*(669), 669. https://doi.org/10.3389/fmicb.2020.00669

Kölling, M., Bouimetarhan, I., Bowles, M. W., Felis, T., Goldhammer, T., Hinrichs, K. U., Schulz, M., & Zabel, M. (2019). Consistent CO2 release by pyrite oxidation on continental shelves prior to glacial terminations. *Nature Geoscience 2019 12:11*, *12*(11), 929–934. https://doi.org/10.1038/s41561-019-0465-9

Kolton, M., Sela, N., Elad, Y., & Cytryn, E. (2013). Comparative genomic analysis indicates that niche adaptation of terrestrial Flavobacteria is strongly linked to plant glycan metabolism. *PloS One*, *8*(9), e76704.

Koppes, M., & Hallet, B. (2006). Erosion rates during rapid deglaciation in Icy Bay, Alaska. *Journal of Geophysical Research: Earth Surface*, *111*(F2), 2023. https://doi.org/10.1029/2005JF000349

Koppes, M., Hallet, B., & Anderson, J. (2009). Synchronous acceleration of ice loss and glacial erosion, Glaciar Marinelli, Chilean Tierra del Fuego. *Journal of Glaciology*, *55*(190), 207–220. https://doi.org/10.3189/002214309788608796

Koppes, M., Sylwester, R., Rivera, A., & Hallet, B. (2010). Variations in Sediment yield Over the Advance and Retreat of a Calving Glacier, Laguna San Rafael, North Patagonian Icefield. *Quaternary Research*, *73*(1), 84–95. https://doi.org/10.1016/J.YQRES.2009.07.006

Kurylyk, B. L., Hayashi, M., Quinton, W. L., McKenzie, J. M., & Voss, C. I. (2016). Influence of vertical and lateral heat transfer on permafrost thaw, peatland landscape transition, and groundwater flow. *Water Resources Research*, *52*(2), 1286–1305.

Kusch, S., Rethemeyer, J., Schefuß, E., & Mollenhauer, G. (2010). Controls on the age of vascular plant biomarkers in Black Sea sediments. *Geochimica et Cosmochimica Acta*, *74*(24), 7031–7047.

https://doi.org/10.1016/j.gca.2010.09.005

Lammers, R. B., Shiklomanov, A. I., Vörösmarty, C. J., Fekete, B. M., & Peterson, B. J. (2001). Assessment of contemporary Arctic river runoff based on observational discharge records. *Journal of Geophysical Research: Atmospheres*, *106*(D4), 3321–3334. https://doi.org/10.1029/2000jd900444

Lamping, N., Müller, J., Hefter, J., Mollenhauer, G., Haas, C., Shi, X., Vorrath, M.-E., Lohmann, G., & Hillenbrand, C.-D. (2021). Evaluation of lipid biomarkers as proxies for sea ice and ocean temperatures along the Antarctic continental margin. *Climate of the Past*, *17*(5), 2305–2326.

Lantuit, H., Overduin, P. P., Couture, N., Wetterich, S., Are, F., Atkinson, D., Brown, J., Cherkashov, G. A., Drozdov, D. S., Forbes, D. L., Graves-Gaylord, A., Grigoriev, M. N., Hubberten, H.-W., Jordan, J., Jorgenson, M. T., Ødegård, R. S., Ogorodov, S., Pollard, W. H., Rachold, V., … Vasiliev, A. (2020). *The ACD Classification of Arctic Coasts*. PANGAEA. https://doi.org/10.1594/PANGAEA.919573

Lantuit, H., Overduin, P. P., Couture, N., Wetterich, S., Aré, F., Atkinson, D., Brown, J., Cherkashov, G., Drozdov, D., Forbes, D. L., Graves-Gaylord, A., Grigoriev, M., Hubberten, H.-W., Jordan, J., Jorgenson, T., Ødegård, R. S., Ogorodov, S., Pollard, W. H., Rachold, V., … Vasiliev, A. (2012). The Arctic Coastal Dynamics Database: A New Classification Scheme and Statistics on Arctic Permafrost Coastlines. *Estuaries and Coasts*, *35*(2), 383–400. https://doi.org/10.1007/s12237-010-9362-6

Lantuit, H., & Pollard, W. H. (2008). Fifty years of coastal erosion and retrogressive thaw slump activity on Herschel Island, southern Beaufort Sea, Yukon Territory, Canada. *Geomorphology*, *95*(1–2), 84–102.

Large, W. G., & Yeager, S. G. (2009). The global climatology of an interannually varying air - Sea flux data set. *Climate Dynamics*, *33*(2–3), 341–364. https://doi.org/10.1007/S00382-008-0441-3/FIGURES/15

Lee, H., Schuur, E. A. G., Inglett, K. S., Lavoie, M., & Chanton, J. P. (2012). The rate of permafrost carbon release under aerobic and anaerobic conditions and its potential effects on climate. *Global Change Biology*, *18*(2), 515–527.

Leifeld, J., & von Lützow, M. (2014). Chemical and microbial activation energies of soil organic matter decomposition. *Biology and Fertility of Soils*, *50*(1), 147–153. https://doi.org/10.1007/S00374-013-0822-6/

Lenton, T. M. (2012). Arctic Climate Tipping Points. *AMBIO 2012 41:1*, *41*(1), 10–22. https://doi.org/10.1007/S13280-011-0221-X

Lenton, T. M., Rockström, J., Gaffney, O., Rahmstorf, S., Richardson, K., Steffen, W., & Schellnhuber, H. J. (2019). Climate tipping points — too risky to bet against. *Nature 2021 575:7784*, *575*(7784), 592–595. https://doi.org/10.1038/d41586-019-03595-0

Lenton, T. M., & Williams, H. T. P. (2013). On the origin of planetary-scale tipping points. *Trends in Ecology & Evolution*, *28*(7), 380–382. https://doi.org/10.1016/J.TREE.2013.06.001

Lewińska-Preis, L., Fabiańska, M. J., Ćmiel, S., & Kita, A. (2009). Geochemical distribution of trace elements in Kaffioyra and Longyearbyen coals, Spitsbergen, Norway. *International Journal of Coal Geology*, *80*(3–4), 211–223. https://doi.org/10.1016/j.coal.2009.09.007

Lewis, K. M., Van Dijken, G. L., & Arrigo, K. R. (2020). Changes in phytoplankton concentration now drive increased Arctic Ocean primary production. *Science*, *369*(6500), 198–202.

Liljedahl, A. K., Gädeke, A., O'Neel, S., Gatesman, T. A., & Douglas, T. A. (2017). Glacierized headwater

streams as aquifer recharge corridors, subarctic Alaska. *Geophysical Research Letters*, *44*(13), 6876–6885. https://doi.org/10.1002/2017GL073834

Lim, M., Whalen, D., Martin, J., Mann, P. J., Hayes, S., Fraser, P., Berry, H. B., & Ouellette, D. (2020). Massive Ice Control on Permafrost Coast Erosion and Sensitivity. *Geophysical Research Letters*, *47*(17), e2020GL087917. https://doi.org/10.1029/2020GL087917

Lionard, M., Péquin, B., Lovejoy, C., & Vincent, W. F. (2012). Benthic cyanobacterial mats in the high arctic: multi-layer structure and fluorescence responses to osmotic stress. *Frontiers in Microbiology*, *3*, 140.

Lipp, J. S., & Hinrichs, K. U. (2009). Structural diversity and fate of intact polar lipids in marine sediments. *Geochimica et Cosmochimica Acta*, *73*(22), 6816–6833. https://doi.org/10.1016/J.GCA.2009.08.003

Liu, J., Xue, C.-X., Wang, J., Crombie, A. T., Carrión, O., Johnston, A. W. B., Murrell, J. C., Liu, J., Zheng, Y., & Zhang, X.-H. (2022). Oceanospirillales containing the DMSP lyase DddD are key utilisers of carbon from DMSP in coastal seawater. *Microbiome*, *10*(1), 1–21.

Logemann, J., Graue, J., Köster, J., Engelen, B., Rullkötter, J., & Cypionka, H. (2011). A laboratory experiment of intact polar lipid degradation in sandy sediments. *Biogeosciences*, *8*(9), 2547–2560. https://doi.org/10.5194/BG-8-2547-2011

Lohmann, G., Butzin, M., Eissner, N., Shi, X., & Stepanek, C. (2020). Abrupt Climate and Weather Changes Across Time Scales. *Paleoceanography and Paleoclimatology*, *35*(9). https://doi.org/10.1029/2019PA003782

Lyu, Z., Shao, N., Akinyemi, T., & Whitman, W. B. (2018). Methanogenesis. *Current Biology*, *28*(13), R727–R732. https://doi.org/10.1016/J.CUB.2018.05.021

Macdonald, R. W., Kuzyk, Z. Z. A., & Johannessen, S. C. (2015). The vulnerability of Arctic shelf sediments to climate change. *Environmental Reviews*, *23*(4), 461–479. https://doi.org/10.1139/er-2015-0040

Mackelprang, R., Burkert, A., Haw, M., Mahendrarajah, T., Conaway, C. H., Douglas, T. A., & Waldrop, M. P. (2017). Microbial survival strategies in ancient permafrost: insights from metagenomics. *The ISME Journal 2017 11:10*, *11*(10), 2305–2318. https://doi.org/10.1038/ismej.2017.93

Mackelprang, R., Saleska, S. R., Jacobsen, C. S., Jansson, J. K., & Taş, N. (2016). Permafrost Meta-Omics and Climate Change. *Https://Doi.Org/10.1146/Annurev-Earth-060614-105126*, *44*, 439–462. https://doi.org/10.1146/ANNUREV-EARTH-060614-105126

Magoč, T., & Salzberg, S. L. (2011). FLASH: fast length adjustment of short reads to improve genome assemblies. *Bioinformatics*, *27*(21), 2957–2963. https://doi.org/10.1093/BIOINFORMATICS/BTR507

Mann, P. J., Eglinton, T. I., McIntyre, C. P., Zimov, N., Davydova, A., Vonk, J. E., Holmes, R. M., & Spencer, R. G. M. (2015). Utilization of ancient permafrost carbon in headwaters of Arctic fluvial networks. *Nature Communications*, *6*(1), 7856. https://doi.org/https://doi.org/10.1038/ncomms8856

Mann, P. J., Strauss, J., Palmtag, J., Dowdy, K., Ogneva, O., Fuchs, M., Bedington, M., Torres, R., Polimene, L., & Overduin, P. (2022). Degrading permafrost river catchments and their impact on Arctic Ocean nearshore processes. *Ambio*, *51*(2), 439–455. https://doi.org/https://doi.org/10.1007/s13280-021-01666-z

Marín-Spiotta, E., Gruley, K. E., Crawford, J., Atkinson, E. E., Miesel, J. R., Greene, S., Cardona-Correa, C., & Spencer, R. G. M. (2014). Paradigm shifts in soil organic matter research affect interpretations of

aquatic carbon cycling: transcending disciplinary and ecosystem boundaries. *Biogeochemistry*, *117*(2–3), 279–297.

Mark, F. C. (2020). *HEINCKE-Berichte: Influence of climate change on interactions and biodiversity in Arctic ecosystems. Cruise No. HE 560*.

Mark, F. C., Gentz, T., & Rokitta, S. (2018). *Cruise Report RV Heincke HE519*.

Marshall, C., Uguna, J., Large, D. J., Meredith, W., Jochmann, M., Friis, B., Vane, C., Spiro, B. F., Snape, C. E., & Orheim, A. (2015). Geochemistry and petrology of palaeocene coals from Spitzbergen — Part 2: Maturity variations and implications for local and regional burial models. *International Journal of Coal Geology*, *143*, 1–10. https://doi.org/10.1016/j.coal.2015.03.013

Martens, J., Wild, B., Muschitiello, F., O'Regan, M., Jakobsson, M., Semiletov, I., Dudarev, O. V, & Gustafsson, Ö. (2020). Remobilization of dormant carbon from Siberian-Arctic permafrost during three past warming events. *Science Advances*, *6*(42), eabb6546.

Martens, J., Wild, B., Semiletov, I., Dudarev, O. V, & Gustafsson, Ö. (2022). Circum-Arctic release of terrestrial carbon varies between regions and sources. *Nature Communications*, *13*(1), 5858.

Martín-Español, A., Zammit-Mangion, A., Clarke, P. J., Flament, T., Helm, V., King, M. A., Luthcke, S. B., Petrie, E., Rémy, F., Schön, N., Wouters, B., & Bamber, J. L. (2016). Spatial and temporal Antarctic Ice Sheet mass trends, glacio-isostatic adjustment, and surface processes from a joint inversion of satellite altimeter, gravity, and GPS data. *Journal of Geophysical Research: Earth Surface*, *121*(2), 182–200. https://doi.org/10.1002/2015JF003550

Martini, I. P., & Wanless, H. R. (2014). *Sedimentary coastal zones from high to low latitudes: Similarities and differences*.

Matthews, E., Johnson, M. S., Genovese, V., Du, J., & Bastviken, D. (2020). Methane emission from high latitude lakes: methane-centric lake classification and satellite-driven annual cycle of emissions. *Scientific Reports*, *10*(1), 1–9.

Mauclet, E., Villani, M., Monhonval, A., Hirst, C., Schuur, E. A. G., & Opfergelt, S. (2022). Quantifying stocks in exchangeable base cations in permafrost: a reserve of nutrients about to thaw. *Earth System Science Data Discussions*, 1–28.

Mayer, L. M., Schick, L. L., Hardy, K. R., Wagai, R., & McCarthy, J. (2004). Organic matter in small mesopores in sediments and soils. *Geochimica et Cosmochimica Acta*, *68*(19), 3863–3872. https://doi.org/10.1016/J.GCA.2004.03.019

McCallister, S L, & del Giorgio, P. A. (2012). Evidence for the respiration of ancient terrestrial organic C in northern temperate lakes and streams. *Proc Natl Acad Sci U S A*, *109*(42), 16963–16968. https://doi.org/10.1073/pnas.1207305109

McCallister, S Leigh, Bauer, J. E., Cherrier, J. E., & Ducklow, H. W. (2004). Assessing sources and ages of organic matter supporting river and estuarine bacterial production: A multiple-isotope (Δ14C, 曖 C, and δ15N) approach. *Limnology and Oceanography*, *49*(5), 1687–1702.

McGuire, A. D., Lawrence, D. M., Koven, C., Clein, J. S., Burke, E., Chen, G., Jafarov, E., MacDougall, A. H., Marchenko, S., & Nicolsky, D. (2018). Dependence of the evolution of carbon dynamics in the northern permafrost region on the trajectory of climate change. *Proceedings of the National Academy of Sciences*, *115*(15), 3882–3887.

https://doi.org/https://doi.org/10.1073/pnas.1719903115

McLaren, M. R., & Callahan, B. J. (2021). Silva 138.1 prokaryotic SSU taxonomic training data formatted for DADA2 [Data set]. *Zenodo, Geneva, Switzerland*.

Meinshausen, M., Vogel, E., Nauels, A., Lorbacher, K., Meinshausen, N., Etheridge, D. M., Fraser, P. J., Montzka, S. A., Rayner, P. J., Trudinger, C. M., Krummel, P. B., Beyerle, U., Canadell, J. G., Daniel, J. S., Enting, I. G., Law, R. M., Lunder, C. R., O'Doherty, S., Prinn, R. G., … Weiss, R. (2017). Historical greenhouse gas concentrations for climate modelling (CMIP6). *Geoscientific Model Development*, *10*(5), 2057–2116. https://doi.org/10.5194/GMD-10-2057-2017

Meire, L., Mortensen, J., Meire, P., Juul-Pedersen, T., Sejr, M. K., Rysgaard, S., Nygaard, R., Huybrechts, P., & Meysman, F. J. R. (2017). Marine-terminating glaciers sustain high productivity in Greenland fjords. *Global Change Biology*, *23*(12), 5344–5357.

Methé, B. A., Nelson, K. E., Deming, J. W., Momen, B., Melamud, E., Zhang, X., Moult, J., Madupu, R., Nelson, W. C., Dodson, R. J., Brinkac, L. M., Daugherty, S. C., Durkin, A. S., DeBoy, R. T., Kolonay, J. F., Sullivan, S. A., Zhou, L., Davidsen, T. M., Wu, M., … Fraser, C. M. (2005). The psychrophilic lifestyle as revealed by the genome sequence of Colwellia psychrerythraea 34H through genomic and proteomic analyses. *Proceedings of the National Academy of Sciences*, *102*(31), 10913–10918. https://doi.org/10.1073/PNAS.0504766102/SUPPL_FILE/04766FIG2.PDF

Meyer, V. D., Hefter, J., Köhler, P., Tiedemann, R., Gersonde, R., Wacker, L., & Mollenhauer, G. (2019). Permafrost-carbon mobilization in Beringia caused by deglacial meltwater runoff, sea-level rise and warming. *Environmental Research Letters*, *14*(8), 85003. https://doi.org/10.1088/1748-9326/ab2653

Meyers, P. A. (1997). Organic geochemical proxies of paleoceanographic, paleolimnologic, and paleoclimatic processes. *Organic Geochemistry*, *27*(5–6), 213–250. https://doi.org/10.1016/s0146-6380(97)00049-1

Miller, J. B., & Tans, P. P. (2003). Calculating isotopic fractionation from atmospheric measurements at various scales. *Tellus B: Chemical and Physical Meteorology*, *55*(2), 207–214.

Miner, K. R., D'Andrilli, J., Mackelprang, R., Edwards, A., Malaska, M. J., Waldrop, M. P., & Miller, C. E. (2021). Emergent biogeochemical risks from Arctic permafrost degradation. *Nature Climate Change*, *11*(10), 809–819. https://doi.org/10.1038/s41558-021-01162-y

Miner, K. R., Turetsky, M. R., Malina, E., Bartsch, A., Tamminen, J., McGuire, A. D., Fix, A., Sweeney, C., Elder, C. D., & Miller, C. E. (2022). Permafrost carbon emissions in a changing Arctic. *Nature Reviews Earth & Environment 2022 3:1*, *3*(1), 55–67. https://doi.org/10.1038/s43017-021-00230-3

Mishra, U., Hugelius, G., Shelef, E., Yang, Y., Strauss, J., Lupachev, A., Harden, J. W., Jastrow, J. D., Ping, C.-L., & Riley, W. J. (2021). Spatial heterogeneity and environmental predictors of permafrost region soil organic carbon stocks. *Science Advances*, *7*(9). https://doi.org/https://doi.org/10.1126/sciadv.aaz523

Mollenhauer, G., & Eglinton, T. I. (2007). Diagenetic and sedimentological controls on the composition of organic matter preserved in California Borderland Basin sediments. *Limnology and Oceanography*, *52*(2), 558–576. https://doi.org/10.4319/lo.2007.52.2.0558

Mollenhauer, G., Grotheer, H., Gentz, T., Bonk, E., & Hefter, J. (2021). Standard operation procedures and performance of the MICADAS radiocarbon laboratory at Alfred Wegener Institute (AWI), Germany.

Nuclear Instruments and Methods in Physics Research Section B: Beam Interactions with Materials and Atoms, *496*, 45–51. https://doi.org/10.1016/J.NIMB.2021.03.016

Mudge, M. C., Nunn, B. L., Firth, E., Ewert, M., Hales, K., Fondrie, W. E., Noble, W. S., Toner, J., Light, B., & Junge, K. A. (2021). Subzero, saline incubations of Colwellia psychrerythraea reveal strategies and biomarkers for sustained life in extreme icy environments. *Environmental Microbiology*, *23*(7), 3840–3866. https://doi.org/10.1111/1462-2920.15485

Mueller, C. W., Rethemeyer, J., Kao-Kniffin, J., Löppmann, S., Hinkel, K. M., & G. Bockheim, J. (2015). Large amounts of labile organic carbon in permafrost soils of northern A laska. *Global Change Biology*, *21*(7), 2804–2817. https://doi.org/https://doi.org/10.1111/gcb.12876

Mußmann, M., Pjevac, P., Krüger, K., & Dyksma, S. (2017). Genomic repertoire of the Woeseiaceae/JTB255, cosmopolitan and abundant core members of microbial communities in marine sediments. *The ISME Journal*, *11*(5), 1276–1281.

Nakai, R. (2020). Size matters: ultra-small and filterable microorganisms in the environment. *Microbes and Environments*, *35*(2), ME20025.

Nauta, A. L., Heijmans, M. M. P. D., Blok, D., Limpens, J., Elberling, B., Gallagher, A., Li, B., Petrov, R. E., Maximov, T. C., & Van Huissteden, J. (2015). Permafrost collapse after shrub removal shifts tundra ecosystem to a methane source. *Nature Climate Change*, *5*(1), 67–70.

Nielsen, D. M., Pieper, P., Barkhordarian, A., Overduin, P., Ilyina, T., Brovkin, V., Baehr, J., & Dobrynin, M. (2022). Increase in Arctic coastal erosion and its sensitivity to warming in the twenty-first century. *Nature Climate Change*, *12*(3), 263–270.

Nitze, I., Heidler, K., Barth, S., & Grosse, G. (2021). Developing and testing a deep learning approach for mapping retrogressive thaw slumps. *Remote Sensing*, *13*(21), 4294.

Obu, J., Lantuit, H., Grosse, G., Günther, F., Sachs, T., Helm, V., & Fritz, M. (2017). Coastal erosion and mass wasting along the Canadian Beaufort Sea based on annual airborne LiDAR elevation data. *Geomorphology*, *293*, 331–346.

Ogneva, O., Mollenhauer, G., Juhls, B., Sanders, T., Palmtag, J., Fuchs, M., Grotheer, H., Mann, P. J., & Strauss, J. (2023). Particulate organic matter in the Lena River and its delta: from the permafrost catchment to the Arctic Ocean. *Biogeosciences*, *20*(7), 1423–1441. https://doi.org/https://doi.org/10.5194/bg-20-1423-2023

Olefeldt, D., Goswami, S., Grosse, G., Hayes, D., Hugelius, G., Kuhry, P., Mcguire, A. D., Romanovsky, V. E., Sannel, A. B. K., Schuur, E. A. G., & Turetsky, M. R. (2016). Circumpolar distribution and carbon storage of thermokarst landscapes. *Nature Communications 2016 7:1*, *7*(1), 1–11. https://doi.org/10.1038/ncomms13043

Oni, O., Miyatake, T., Kasten, S., Richter-Heitmann, T., Fischer, D., Wagenknecht, L., Kulkarni, A., Blumers, M., Shylin, S. I., Ksenofontov, V., Costa, B. F., Klingelhofer, G., & Friedrich, M. W. (2015). Distinct microbial populations are tightly linked to the profile of dissolved iron in the methanic sediments of the Helgoland mud area, North Sea. *Front Microbiol*, *6*, 365. https://doi.org/10.3389/fmicb.2015.00365

Overduin, P. P., Liebner, S., Knoblauch, C., Günther, F., Wetterich, S., Schirrmeister, L., Hubberten, H., & Grigoriev, M. N. (2015). Methane oxidation following submarine permafrost degradation: Measurements from a central Laptev Sea shelf borehole. *Journal of Geophysical Research:*

Biogeosciences, *120*(5), 965–978.

Overeem, I., Hudson, B. D., Syvitski, J. P. M., Mikkelsen, A. B., Hasholt, B., Van Den Broeke, M. R., Noel, B. P. Y., & Morlighem, M. (2017). Substantial export of suspended sediment to the global oceans from glacial erosion in Greenland. *Nature Geoscience 2017 10:11*, *10*(11), 859–863. https://doi.org/10.1038/ngeo3046

Pachauri, R. K., Allen, M. R., Barros, V. R., Broome, J., Cramer, W., Christ, R., Church, J. A., Clarke, L., Dahe, Q., & Dasgupta, P. (2014). *Climate change 2014: synthesis report. Contribution of Working Groups I, II and III to the fifth assessment report of the Intergovernmental Panel on Climate Change*. Ipcc.

Page, D. S., Boehm, P. D., Douglas, G. S., Bence, A. E., Burns, W. A., & Mankiewicz, P. J. (1996). The natural petroleum hydrocarbon background in subtidal sediments of Prince William Sound, Alaska, USA. *Environmental Toxicology and Chemistry: An International Journal*, *15*(8), 1266–1281.

Parada, A. E., Needham, D. M., & Fuhrman, J. A. (2016). Every base matters: Assessing small subunit rRNA primers for marine microbiomes with mock communities, time series and global field samples. *Environmental Microbiology*, *18*(5), 1403–1414. https://doi.org/10.1111/1462-2920.13023/SUPPINFO

Parmentier, F.-J. W., Christensen, T. R., Sørensen, L. L., Rysgaard, S., McGuire, A. D., Miller, P. A., & Walker, D. A. (2013). The impact of lower sea-ice extent on Arctic greenhouse-gas exchange. *Nature Climate Change*, *3*(3), 195–202. https://doi.org/10.1038/nclimate1784

Pattyn, F. (2010). Antarctic subglacial conditions inferred from a hybrid ice sheet/ice stream model. *Earth and Planetary Science Letters*, *295*(3–4), 451–461. https://doi.org/10.1016/J.EPSL.2010.04.025

Paulsen, M. L., Nielsen, S. E. B., Müller, O., Møller, E. F., Stedmon, C. A., Juul-Pedersen, T., Markager, S., Sejr, M. K., Delgado Huertas, A., & Larsen, A. (2017). Carbon bioavailability in a high arctic fjord influenced by glacial meltwater, NE Greenland. *Frontiers in Marine Science*, *4*, 176.

Pedler, B. E., Aluwihare, L. I., & Azam, F. (2014). Single bacterial strain capable of significant contribution to carbon cycling in the surface ocean. *Proceedings of the National Academy of Sciences*, *111*(20), 7202–7207.

Peoples, L. M., Grammatopoulou, E., Pombrol, M., Xu, X., Osuntokun, O., Blanton, J., Allen, E. E., Nunnally, C. C., Drazen, J. C., & Mayor, D. J. (2019). Microbial community diversity within sediments from two geographically separated hadal trenches. *Frontiers in Microbiology*, *10*, 347.

Pernthaler, J., & Amann, R. (2005). Fate of heterotrophic microbes in pelagic habitats: focus on populations. *Microbiology and Molecular Biology Reviews*, *69*(3), 440–461.

Perovich, D., Meier, W., Tschudi, M., Hendricks, S., Petty, A. A., Divine, D., Farrell, S., Gerland, S., Haas, C., & Kaleschke, L. (2020). *Arctic report card 2020: Sea ice*.

Petsch, S. T. (2014). Weathering of organic carbon. In *Treatise on Geochemistry, v. 12,* (pp. 217–238). Elsevier.

Petsch, S. T., Edwards, K. J., & Eglinton, T. I. (2003). Abundance, distribution and δ13C analysis of microbial phospholipid-derived fatty acids in a black shale weathering profile. *Organic Geochemistry*, *34*(6), 731–743.

Petsch, S. T., Eglington, T. I., Edwards, K. J., Eglinton, T. I., & Edwards, K. J. (2001). 14C-dead living biomass:

evidence for microbial assimilation of ancient organic carbon during shale weathering. *Science*, *292*(5519), 1127–1131. https://doi.org/10.1126/science.1058332

Piwosz, K., Walkusz, W., Hapter, R., Wieczorek, P., Hop, H., & Wiktor, J. (2009). Comparison of productivity and phytoplankton in a warm (Kongsfjorden) and a cold (Hornsund) Spitsbergen fjord in mid-summer 2002. *Polar Biology*, *32*(4), 549–559. https://doi.org/10.1007/s00300-008-0549-2

Plante, A. F., Beaupré, S. R., Roberts, M. L., & Baisden, T. (2013). Distribution of radiocarbon ages in soil organic matter by thermal fractionation. *Radiocarbon*, *55*(2), 1077–1083. https://doi.org/https://doi.org/10.1017/S0033822200058215

Plante, A. F., Fernández, J. M., & Leifeld, J. (2009). Application of thermal analysis techniques in soil science. *Geoderma*, *153*(1–2), 1–10. https://doi.org/10.1016/J.GEODERMA.2009.08.016

Polimene, L., Torres, R., Powley, H. R., Bedington, M., Juhls, B., Palmtag, J., Strauss, J., & Mann, P. J. (2022). Biological lability of terrestrial DOM increases CO2 outgassing across Arctic shelves. *Biogeochemistry*, *160*(3), 289–300.

Quast, C., Pruesse, E., Yilmaz, P., Gerken, J., Schweer, T., Yarza, P., & Peplies, J. (2013). an d FO Glöckner. 2013. *The SILVA Ribosomal RNA Gene Database Project: Improved Data Processing and Web-Based Tools. Nucleic Acids Res*, *41*, D590–D596.

Radosavljevic, B., Lantuit, H., Pollard, W., Overduin, P., Couture, N., Sachs, T., Helm, V., & Fritz, M. (2016). Erosion and flooding—threats to coastal infrastructure in the Arctic: a case study from Herschel Island, Yukon Territory, Canada. *Estuaries and Coasts*, *39*, 900–915.

Raiswell, R., Hawkings, J. R., Benning, L. G., Baker, A. R., Death, R., Albani, S., Mahowald, N., Krom, M. D., Poulton, S. W., Wadham, J., & Tranter, M. (2016). Potentially bioavailable iron delivery by iceberg-hosted sediments and atmospheric dust to the polar oceans. *Biogeosciences*, *13*(13), 3887–3900. https://doi.org/10.5194/BG-13-3887-2016

Rantanen, M., Karpechko, A. Y., Lipponen, A., Nordling, K., Hyvärinen, O., Ruosteenoja, K., Vihma, T., & Laaksonen, A. (2022). The Arctic has warmed nearly four times faster than the globe since 1979. *Communications Earth & Environment*, *3*(1), 1–10. https://doi.org/10.1038/s43247-022-00498-3

Rassmann, J., Eitel, E. M., Lansard, B., Cathalot, C., Brandily, C., Taillefert, M., & Rabouille, C. (2020). Benthic alkalinity and dissolved inorganic carbon fluxes in the Rhône River prodelta generated by decoupled aerobic and anaerobic processes. *Biogeosciences*, *17*(1), 13–33.

Reimer, P. J., Brown, T. A., & Reimer, R. W. (2004). Discussion: reporting and calibration of post-bomb 14C data. *Radiocarbon*, *46*(3), 1299–1304.

Rieley, G., Collier, R. J., Jones, D. M., Eglinton, G., Eakin, P. A., & Fallick, A. E. (1991). Sources of sedimentary lipids deduced from stable carbon-isotope analyses of individual compounds. *Nature*, *352*(6334), 425–427. https://doi.org/10.1038/352425a0

Rogers, J. A., Galy, V., Kellerman, A. M., Chanton, J. P., Zimov, N., & Spencer, R. G. M. (2021). Limited Presence of Permafrost Dissolved Organic Matter in the Kolyma River, Siberia Revealed by Ramped Oxidation. *Journal of Geophysical Research: Biogeosciences*, *126*(7). https://doi.org/10.1029/2020JG005977

Rosenheim, B. E., Day, M. B., Domack, E., Schrum, H., Benthien, A., & Hayes, J. M. (2008). Antarctic sediment chronology by programmed-temperature pyrolysis: Methodology and data treatment.

Geochemistry, Geophysics, Geosystems, *9*(4). https://doi.org/https://doi.org/10.1029/2007GC001816

Rosselló-Mora, R., Thamdrup, B., Schäfer, H., Weller, R., & Amann, R. (1999). The response of the microbial community of marine sediments to organic carbon input under anaerobic conditions. *Systematic and Applied Microbiology*, *22*(2), 237–248.

Ruben, M., Hefter, J., Schubotz, F., Geibert, W., Butzin, M., Gentz, T., Grotheer, H., Forwick, M., Szczuciński, W., & Mollenhauer, G. (2023). Fossil organic carbon utilization in marine Arctic fjord sediments by subsurface micro-organisms. *Nature Geoscience*, *16*, 1–6. https://doi.org/https://doi.org/10.1038/s41561-023-01198-z

Sabine, C. L., & Tanhua, T. (2010). Estimation of anthropogenic CO2 inventories in the ocean. *Annual Review of Marine Science*, *2*, 175–198.

Sanderman, J., & Grandy, A. S. (2020). Ramped thermal analysis for isolating biologically meaningful soil organic matter fractions with distinct residence times. *Soil*, *6*(1), 131–144. https://doi.org/https://doi.org/10.5194/soil-6-131-2020

Sarmiento, J. L. (2013). Ocean biogeochemical dynamics. In *Ocean Biogeochemical Dynamics*. Princeton University Press. https://doi.org/10.1515/9781400849079/HTML

Schädel, C., Schuur, E. A. G., Bracho, R., Elberling, B., Knoblauch, C., Lee, H., Luo, Y., Shaver, G. R., Turetsky, M. R., Schädel, C., Schuur, E. A. G., Bracho, R., Elberling, B., Knoblauch, C., Lee, H., Luo, Y., Shaver, G. R., & Turetsky, M. R. (2014). Circumpolar assessment of permafrost C quality and its vulnerability over time using long-term incubation data. *Glob Chang Biol*, *20*(2), 641–652. https://doi.org/10.1111/gcb.12417

Scheel, M., Zervas, A., Jacobsen, C. S., & Christensen, T. R. (2022). Microbial Community Changes in 26,500-Year-Old Thawing Permafrost. *Frontiers in Microbiology*, *13*, 571. https://doi.org/10.3389/FMICB.2022.787146/BIBTEX

Schiettekatte, N. M. D., Brandl, S. J., & Casey, J. M. (2019). fishualize: Color palettes based on fish species. *CRAN Version 0.2. 0*.

Schirrmeister, L., Froese, D., Tumskoy, V., Grosse, G., & Wetterich, S. (2013). Yedoma: Late Pleistocene ice-rich syngenetic permafrost of Beringia. *Encyclopedia of Quaternary Science. 2nd Edition*, 542–552.

Schubotz, F., Lipp, J. S., Elvert, M., Kasten, S., Mollar, X. P., Zabel, M., Bohrmann, G., & Hinrichs, K.-U. U. (2011). Petroleum degradation and associated microbial signatures at the Chapopote asphalt volcano, Southern Gulf of Mexico. *Geochimica et Cosmochimica Acta*, *75*(16), 4377–4398. https://doi.org/10.1016/j.gca.2011.05.025

Schuur, E. A. G., Abbott, B. W., Commane, R., Ernakovich, J., Euskirchen, E., Hugelius, G., Grosse, G., Jones, M., Koven, C., & Leshyk, V. (2022). Permafrost and climate change: carbon cycle feedbacks from the warming Arctic. *Annual Review of Environment and Resources*, *47*, 343–371. https://doi.org/https://doi.org/10.1146/annurev-environ-012220-011847

Schuur, E. A. G., McGuire, A. D., Schädel, C., Grosse, G., Harden, J. W., Hayes, D. J., Hugelius, G., Koven, C. D., Kuhry, P., Lawrence, D. M., Natali, S. M., Olefeldt, D., Romanovsky, V. E., Schaefer, K., Turetsky, M. R., Treat, C. C., & Vonk, J. E. (2015). Climate change and the permafrost carbon feedback. *Nature*, *520*(7546), 171–179. https://doi.org/10.1038/nature14338

Schuur, E. A. G., Vogel, J. G., Crummer, K. G., Lee, H., Sickman, J. O., & Osterkamp, T. E. (2009). The effect of permafrost thaw on old carbon release and net carbon exchange from tundra. *Nature 2009 459:7246*, *459*(7246), 556–559. https://doi.org/10.1038/nature08031

Schwab, M. S., Hilton, R. G., Raymond, P. A., Haghipour, N., Amos, E., Tank, S. E., Holmes, R. M., Tipper, E. T., & Eglinton, T. I. (2020). An Abrupt Aging of Dissolved Organic Carbon in Large Arctic Rivers. *Geophysical Research Letters*, *47*(23), e2020GL088823. https://doi.org/10.1029/2020GL088823

Seidel, M., Rütters, H., Rullkötter, J., & Sass, H. (2013). Phosphate-free ornithine lipid contents in Desulfovibrio spp. respond to growth temperature. *Organic Geochemistry*, *59*, 133–142. https://doi.org/10.1016/J.ORGGEOCHEM.2013.04.004

Semiletov, I. P., Pipko, I. I., Shakhova, N. E., Dudarev, O. V, Pugach, S. P., Charkin, A. N., McRoy, C. P., Kosmach, D., & Gustafsson, Ö. (2011). Carbon transport by the Lena River from its headwaters to the Arctic Ocean, with emphasis on fluvial input of terrestrial particulate organic carbon vs. carbon transport by coastal erosion. *Biogeosciences*, *8*(9), 2407–2426. https://doi.org/10.5194/bg-8-2407-2011

Semiletov, I., Pipko, I., Gustafsson, Ö., Anderson, L. G., Sergienko, V., Pugach, S., Dudarev, O., Charkin, A., Gukov, A., & Bröder, L. (2016). Acidification of East Siberian Arctic Shelf waters through addition of freshwater and terrestrial carbon. *Nature Geoscience*, *9*(5), 361–365.

Shadwick, E. H., Rintoul, S. R., Tilbrook, B., Williams, G. D., Young, N., Fraser, A. D., Marchant, H., Smith, J., & Tamura, T. (2013). Glacier tongue calving reduced dense water formation and enhanced carbon uptake. *Geophysical Research Letters*, *40*(5), 904–909. https://doi.org/10.1002/GRL.50178

Shah, S. R., Mollenhauer, G., Ohkouchi, N., Eglinton, T. I., & Pearson, A. (2008). Origins of archaeal tetraether lipids in sediments: Insights from radiocarbon analysis. *Geochimica et Cosmochimica Acta*, *72*(18), 4577–4594. https://doi.org/10.1016/j.gca.2008.06.021

Showalter, G. M., & Deming, J. W. (2021). Extracellular enzyme activity of model cold-adapted bacteria and Arctic sea-ice microbial communities under subzero hypersaline conditions. *Aquatic Microbial Ecology*, *87*, 99–111. https://doi.org/10.3354/AME01974

Siegert, M. J., Kulessa, B., Bougamont, M., Christoffersen, P., Key, K., Andersen, K. R., Booth, A. D., & Smith, A. M. (2018). Antarctic subglacial groundwater: A concept paper on its measurement and potential influence on ice flow. *Geological Society Special Publication*, *461*(1), 197–213. https://doi.org/10.1144/SP461.8/ASSET/FC44E89E-98A2-46DF-80D6-DF7BE37EF81D/ASSETS/GRAPHIC/SP461-1948F08.JPEG

Siliakus, M. F., van der Oost, J., & Kengen, S. W. M. (2017). Adaptations of archaeal and bacterial membranes to variations in temperature, pH and pressure. *Extremophiles 2017 21:4*, *21*(4), 651–670. https://doi.org/10.1007/S00792-017-0939-X

Sipler, R. E., Kellogg, C. T. E., Connelly, T. L., Roberts, Q. N., Yager, P. L., & Bronk, D. A. (2017). Microbial community response to terrestrially derived dissolved organic matter in the coastal Arctic. *Frontiers in Microbiology*, *8*(JUN), 1018. https://doi.org/10.3389/FMICB.2017.01018/BIBTEX

Sivarajah, B., Simmatis, B., Favot, E. J., Palmer, M. J., & Smol, J. P. (2021). Eutrophication and climatic changes lead to unprecedented cyanobacterial blooms in a Canadian sub-Arctic landscape. *Harmful Algae*, *105*, 102036.

Skei, J. (1983). Why sedimentologists are interested in Fjords. *Sedimentary Geology*, *36*(2–4), 75–80.

https://doi.org/10.1016/0037-0738(83)90002-7

Slater, G. F., Nelson, R. K., Kile, B. M., & Reddy, C. M. (2006). Intrinsic bacterial biodegradation of petroleum contamination demonstrated in situ using natural abundance, molecular-level 14C analysis. *Organic Geochemistry*, *37*(9), 981–989. https://doi.org/10.1016/j.orggeochem.2006.06.014

Smith, R. W., Bianchi, T. S., Allison, M., Savage, C., & Galy, V. (2015). High rates of organic carbon burial in fjord sediments globally. *Nature Geoscience*, *8*(6), 450–453. https://doi.org/10.1038/ngeo2421

Smoła, Z. T., Tatarek, A., Wiktor, J. M., Wiktor, J. M. W., Kubiszyn, A., & Węsławski, J. M. (2017). Primary producers and production in Hornsund and Kongsfjorden – comparison of two fjord systems. *Polish Polar Research*, *38*(3), 351–373. https://doi.org/10.1515/popore-2017-0013

Sohlenkamp, C., & Geiger, O. (2016). Bacterial membrane lipids: diversity in structures and pathways. *FEMS Microbiol Rev*, *40*(1), 133–159. https://doi.org/10.1093/femsre/fuv008

Sohlenkamp, C., López-Lara, I. M., & Geiger, O. (2003). Biosynthesis of phosphatidylcholine in bacteria. *Progress in Lipid Research*, *42*(2), 115–162. https://doi.org/10.1016/S0163-7827(02)00050-4

Soulet, G., Hilton, R. G., Garnett, M. H., Roylands, T., Klotz, S., Croissant, T., Dellinger, M., & Le Bouteiller, C. (2021). Temperature control on CO2 emissions from the weathering of sedimentary rocks. *Nature Geoscience*, *14*(9), 665–671.

Spencer, R. G. M., Mann, P. J., Dittmar, T., Eglinton, T. I., McIntyre, C., Holmes, R. M., Zimov, N., & Stubbins, A. (2015). Detecting the signature of permafrost thaw in Arctic rivers. *Geophysical Research Letters*, *42*(8), 2830–2835. https://doi.org/https://doi.org/10.1002/2015GL063498

St. Pierre, K. A., St. Louis, V. L., Lehnherr, I., Schiff, S. L., Muir, D. C. G., Poulain, A. J., Smol, J. P., Talbot, C., Ma, M., Findlay, D. L., Findlay, W. J., Arnott, S. E., & Gardner, A. S. (2019). Contemporary limnology of the rapidly changing glacierized watershed of the world's largest High Arctic lake. *Scientific Reports 2019 9:1*, *9*(1), 1–15. https://doi.org/10.1038/s41598-019-39918-4

Stein, R., Macdonald, R. W., Stein, R., & MacDonald, R. W. (2004). *The organic carbon cycle in the Arctic Ocean*.

Strauss, J., Biasi, C., Sanders, T., Abbott, B. W., von Deimling, T. S., Voigt, C., Winkel, M., Marushchak, M. E., Kou, D., Fuchs, M., Horn, M. A., Jongejans, L. L., Liebner, S., Nitzbon, J., Schirrmeister, L., Walter Anthony, K., Yang, Y., Zubrzycki, S., Laboor, S., … Grosse, G. (2022). A globally relevant stock of soil nitrogen in the Yedoma permafrost domain. *Nature Communications 2022 13:1*, *13*(1), 1–9. https://doi.org/10.1038/s41467-022-33794-9

Strauss, J., Laboor, S., Schirrmeister, L., Fedorov, A. N., Fortier, D., Froese, D., Fuchs, M., Günther, F., Grigoriev, M., & Harden, J. (2021). Circum-Arctic Map of the Yedoma permafrost domain. *Frontiers in Earth Science*, 1001. https://doi.org/https://doi.org/10.3389/feart.2021.758360

Strauss, J., Ogneva, O., Palmtag, J., & Fuchs, M. (2021). CACOON Ice: Spring campaign NERC-BMBF project 'Changing Arctic Carbon Cycle in the Coastal Ocean Near-Shore (CACOON)(chapter 2.1). In *Reports on Polar and Marine Research-Russian-German Cooperation: Expeditions to Siberia in 2019* (pp. 14–24). Alfred Wegener Institute.

Strauss, J., Schirrmeister, L., Grosse, G., Fortier, D., Hugelius, G., Knoblauch, C., Romanovsky, V., Schädel, C., Schneider von Deimling, T., Schuur, E. A. G., Shmelev, D., Ulrich, M., & Veremeeva, A. (2017).

Deep Yedoma permafrost: A synthesis of depositional characteristics and carbon vulnerability. *Earth-Science Reviews*, *172*, 75–86. https://doi.org/10.1016/J.EARSCIREV.2017.07.007

Strauss, J., Schirrmeister, L., Grosse, G., Wetterich, S., Ulrich, M., Herzschuh, U., & Hubberten, H. W. (2013). The deep permafrost carbon pool of the Yedoma region in Siberia and Alaska. *Geophysical Research Letters*, *40*(23), 6165–6170. https://doi.org/10.1002/2013GL058088

Stuiver, M., & Polach, H. A. (1977). Discussion reporting of 14C data. *Radiocarbon*, *19*(3), 355–363.

Sun, S., Meyer, V. D., Dolman, A. M., Winterfeld, M., Hefter, J., Dummann, W., McIntyre, C., Montluçon, D. B., Haghipour, N., Wacker, L., Gentz, T., Van Der Voort, T. S., Eglinton, T. I., & Mollenhauer, G. (2020). 14C Blank Assessment in Small-Scale Compound-Specific Radiocarbon Analysis of Lipid Biomarkers and Lignin Phenols. *Radiocarbon*, *62*(1), 207–218. https://doi.org/10.1017/RDC.2019.108

Sundquist, E. T., & Visser, K. (2005). The Geologic History of. *Biogeochemistry*, *8*, 425.

Synal, H.-A., Stocker, M., & Suter, M. (2007). MICADAS: A new compact radiocarbon AMS system. *Nuclear Instruments and Methods in Physics Research Section B: Beam Interactions with Materials and Atoms*, *259*(1), 7–13.

Szczuciński, Witold, Dominiczak, A., Apolinarska, K., Forwick, M., Goslar, T., Moskalik, M., Strzelecki, M. C., & Woszczyk, M. (2017). Climate-driven variations in source-to-sink fluxes of sediment and carbon in High Arctic fjord (Hornsund, Svalbard). *33rd International Meeting of Sedimentology and 16ème Congrés Français Sédimen-Tologie, Toulouse*, 10–12.

Szczuciński, WITOLD, & Zajączkowski, M. (2012). Factors controlling downward fluxes of particulate matter in glacier-contact and non-glacier contact settings in a subpolar fjord (Billefjorden, Svalbard). *Sediments, Morphology and Sedimentary Processes on Continental Shelves*, *44*, 369–386.

Szczuciński, Witold, Zajączkowski, M., & Scholten, J. (2009). Sediment accumulation rates in subpolar fjords – Impact of post-Little Ice Age glaciers retreat, Billefjorden, Svalbard. *Estuarine, Coastal and Shelf Science*, *85*(3), 345–356. https://doi.org/10.1016/j.ecss.2009.08.021

Tanski, G., Bröder, L., Wagner, D., Knoblauch, C., Lantuit, H., Beer, C., Sachs, T., Fritz, M., Tesi, T., & Koch, B. P. (2021). Permafrost carbon and CO2 pathways differ at contrasting coastal erosion sites in the Canadian Arctic. *Frontiers in Earth Science*, *9*, 207. https://doi.org/https://doi.org/10.3389/feart.2021.630493

Tanski, G., Couture, N., Lantuit, H., Eulenburg, A., & Fritz, M. (2016). Eroding permafrost coasts release low amounts of dissolved organic carbon (DOC) from ground ice into the nearshore zone of the Arctic Ocean. *Global Biogeochemical Cycles*, *30*(7), 1054–1068. https://doi.org/10.1002/2015gb005337

Tanski, G., Wagner, D., Knoblauch, C., Fritz, M., Sachs, T., & Lantuit, H. (2019). Rapid CO2 release from eroding permafrost in seawater. *Geophysical Research Letters*, *46*(20), 11244–11252. https://doi.org/https://doi.org/10.1029/2019GL084303

Tao, S., Eglinton, T. I., Montluçon, D. B., McIntyre, C., & Zhao, M. (2015). Pre-aged soil organic carbon as a major component of the Yellow River suspended load: Regional significance and global relevance. *Earth and Planetary Science Letters*, *414*, 77–86. https://doi.org/10.1016/j.epsl.2015.01.004

Tarnocai, C., Canadell, J. G., Schuur, E. A. G., Kuhry, P., Mazhitova, G., & Zimov, S. (2009). Soil organic carbon pools in the northern circumpolar permafrost region. *Global Biogeochemical Cycles*, *23*(2),

n/a-n/a. https://doi.org/10.1029/2008gb003327

Team, R. C. (2013). R: A Language and Environment for Statistical Computing. Vienna, Austria: R Foundation for Statistical Computing; 2019. 3. McMurdie PJ, Holmes S. phyloseq: an R package for reproducible interactive analysis and graphics of microbiome census data. *PLoS One*, *8*, e61217.

Terhaar, J., Lauerwald, R., Regnier, P., Gruber, N., & Bopp, L. (2021). Around one third of current Arctic Ocean primary production sustained by rivers and coastal erosion. *Nature Communications 2021 12:1*, *12*(1), 1–10. https://doi.org/10.1038/s41467-020-20470-z

Tesi, T., Muschitiello, F., Smittenberg, R. H., Jakobsson, M., Vonk, J. E., Hill, P., Andersson, A., Kirchner, N., Noormets, R., & Dudarev, O. (2016). Massive remobilization of permafrost carbon during post-glacial warming. *Nature Communications*, *7*(1), 13653.

Thomson, S. N., Reiners, P. W., Hemming, S. R., & Gehrels, G. E. (2013). The contribution of glacial erosion to shaping the hidden landscape of East Antarctica. *Nature Geoscience 2013 6:3*, *6*(3), 203–207. https://doi.org/10.1038/ngeo1722

Toggweiler, J. R., Dixon, K., & Bryan, K. (1989). Simulations of radiocarbon in a coarse-resolution world ocean model: 1. Steady state prebomb distributions. *Journal of Geophysical Research: Oceans*, *94*(C6), 8217–8242. https://doi.org/10.1029/JC094IC06P08217

Torres, M. E., Mix, A. C., & Rugh, W. D. (2005). Precise δ13C analysis of dissolved inorganic carbon in natural waters using automated headspace sampling and continuous-flow mass spectrometry. *Limnology and Oceanography: Methods*, *3*(8), 349–360.

Treat, C. C., Marushchak, M. E., Voigt, C., Zhang, Y., Tan, Z., Zhuang, Q., Virtanen, T. A., Räsänen, A., Biasi, C., & Hugelius, G. (2018). Tundra landscape heterogeneity, not interannual variability, controls the decadal regional carbon balance in the Western Russian Arctic. *Global Change Biology*, *24*(11), 5188–5204.

Turetsky, M. R., Abbott, B. W., Jones, M. C., Anthony, K. W., Olefeldt, D., Schuur, E. A. G., Grosse, G., Kuhry, P., Hugelius, G., Koven, C., Lawrence, D. M., Gibson, C., Sannel, A. B. K., & McGuire, A. D. (2020). Carbon release through abrupt permafrost thaw. *Nature Geoscience*, *13*(2), 138–143. https://doi.org/10.1038/s41561-019-0526-0

Turetsky, M. R., Abbott, B. W., Jones, M. C., Walter Anthony, K., Olefeldt, D., Schuur, E. A. G., Koven, C., McGuire, A. D., Grosse, G., Kuhry, P., Hugelius, G., Lawrence, D. M., Gibson, C., & Sannel, A. B. K. (2019). Permafrost collapse is accelerating carbon release. *Nature 2021 569:7754*, *569*(7754), 32–34. https://doi.org/10.1038/d41586-019-01313-4

Ulrich, M., Grosse, G., Strauss, J., & Schirrmeister, L. (2014). Quantifying wedge-ice volumes in Yedoma and thermokarst basin deposits. *Permafrost and Periglacial Processes*, *25*(3), 151–161.

Van Everdingen, R. O. (1998). *Multi-Language Glossary of Permafrost and Related Ground-Ice Terms in Chinese, English, French, German, Icelandic, Italian, Norwegian, Polish, Romanian, Russian, Spanish, and Swedish*. International Permafrost Association, Terminology Working Group.

Venturelli, R. A., Siegfried, M. R., Roush, K. A., Li, W., Burnett, J., Zook, R., Fricker, H. A., Priscu, J. C., Leventer, A., & Rosenheim, B. E. (2020). Mid-Holocene grounding line retreat and readvance at Whillans Ice Stream, West Antarctica. *Geophysical Research Letters*, *47*(15). https://doi.org/https://doi.org/10.1029/2020GL088476

Vinšová, P., Kohler, T. J., Simpson, M. J., Hajdas, I., Yde, J. C., Falteisek, L., Žárský, J. D., Yuan, T., Tejnecký, V., Mercl, F., Hood, E., & Stibal, M. (2022). The biogeochemical legacy of arctic subglacial sediments exposed by glacier retreat. *Global Biogeochemical Cycles*, *36*(3). https://doi.org/10.1029/2021GB007126

Vonk, J. E., Tank, S. E., Mann, P. J., Spencer, R. G. M., Treat, C. C., Striegl, R. G., Abbott, B. W., & Wickland, K. P. (2015). Biodegradability of dissolved organic carbon in permafrost soils and aquatic systems: A meta-analysis. *Biogeosciences*, *12*(23), 6915–6930. https://doi.org/10.5194/bg-12-6915-2015

Vonk, J., Sanchez-Garcia, L., van Dongen, B. E., Alling, V., Kosmach, D., Charkin, A., Semiletov, I. P., Dudarev, O. V, Shakhova, N., Roos, P., Eglinton, T. I., Andersson, A., & Gustafsson, O. (2012). Activation of old carbon by erosion of coastal and subsea permafrost in Arctic Siberia. *Nature*, *489*(7414), 137–140. https://doi.org/10.1038/nature11392

Vonk, Jorien E, Mann, P. J., Davydov, S., Davydova, A., Spencer, R. G. M., Schade, J., Sobczak, W. V, Zimov, N., Zimov, S., & Bulygina, E. (2013). High biolability of ancient permafrost carbon upon thaw. *Geophysical Research Letters*, *40*(11), 2689–2693.

Vonk, Jorien E, Semiletov, I. P., Dudarev, O. V, Eglinton, T. I., Andersson, A., Shakhova, N., Charkin, A., Heim, B., & Gustafsson, Ö. (2014). Preferential burial of permafrost-derived organic carbon in Siberian-Arctic shelf waters. *Journal of Geophysical Research: Oceans*, *119*(12), 8410–8421. https://doi.org/10.1002/2014jc010261

Wacker, L., Fahrni, S. M., Hajdas, I., Molnar, M., Synal, H.-A., Szidat, S., & Zhang, Y. L. (2013). A versatile gas interface for routine radiocarbon analysis with a gas ion source. *Nuclear Instruments and Methods in Physics Research Section B: Beam Interactions with Materials and Atoms*, *294*, 315–319.

Wadham, J. L., De'Ath, R., Monteiro, F. M., Tranter, M., Ridgwell, A., Raiswell, R., & Tulaczyk, S. (2013). The potential role of the Antarctic Ice Sheet in global biogeochemical cycles. *Earth and Environmental Science Transactions of The Royal Society of Edinburgh*, *104*(1), 55–67. https://doi.org/10.1017/S1755691013000108

Wadham, J. L., Hawkings, J. R., Tarasov, L., Gregoire, L. J., Spencer, R. G. M., Gutjahr, M., Ridgwell, A., & Kohfeld, K. E. (2019). Ice sheets matter for the global carbon cycle. *Nature Communications 2019 10:1*, *10*(1), 1–17. https://doi.org/10.1038/s41467-019-11394-4

Wagner, A., Lohmann, G., & Prange, M. (2011). Arctic river discharge trends since 7 ka BP. *Global and Planetary Change*, *79*(1–2), 48–60. https://doi.org/10.1016/J.GLOPLACHA.2011.07.006

Wakeham, S. G., McNichol, A. P., Kostka, J. E., & Pease, T. K. (2006). Natural-abundance radiocarbon as a tracer of assimilation of petroleum carbon by bacteria in salt marsh sediments. *Geochimica et Cosmochimica Acta*, *70*(7), 1761–1771. https://doi.org/10.1016/j.gca.2005.12.020

Waldrop, M. P., Chabot, C. L., Liebner, S., Holm, S., Snyder, M. W., Dillon, M., Dudgeon, S. R., Douglas, T. A., Leewis, M.-C., & Walter Anthony, K. M. (2023). Permafrost microbial communities and functional genes are structured by latitudinal and soil geochemical gradients. *The ISME Journal*, 1–12.

Walinsky, S. E., Prahl, F. G., Mix, A. C., Finney, B. P., Jaeger, J. M., & Rosen, G. P. (2009). Distribution and composition of organic matter in surface sediments of coastal Southeast Alaska. *Continental Shelf Research*, *29*(13), 1565–1579. https://doi.org/10.1016/j.csr.2009.04.006

Walter Anthony, K., Daanen, R., Anthony, P., Schneider von Deimling, T., Ping, C.-L., Chanton, J. P., & Grosse, G. (2016). Methane emissions proportional to permafrost carbon thawed in Arctic lakes

since the 1950s. *Nature Geoscience*, *9*(9), 679–682.

Walter Anthony, K., Schneider von Deimling, T., Nitze, I., Frolking, S., Emond, A., Daanen, R., Anthony, P., Lindgren, P., Jones, B., & Grosse, G. (2018). 21st-century modeled permafrost carbon emissions accelerated by abrupt thaw beneath lakes. *Nature Communications*, *9*(1), 1–11.

Wanninkhof, R. (2014). Relationship between wind speed and gas exchange over the ocean revisited. *Limnology and Oceanography: Methods*, *12*(6), 351–362. https://doi.org/10.4319/LOM.2014.12.351

Ward, C. P., Nalven, S. G., Crump, B. C., Kling, G. W., & Cory, R. M. (2017). Photochemical alteration of organic carbon draining permafrost soils shifts microbial metabolic pathways and stimulates respiration. *Nature Communications 2017 8:1*, *8*(1), 1–8. https://doi.org/10.1038/s41467-017-00759-2

Wei, B., Jia, G., Hefter, J., Kang, M., Park, E., Wang, S., & Mollenhauer, G. (2020). Comparison of the U37K', LDI, TEX86H, and RI-OH temperature proxies in sediments from the northern shelf of the South China Sea. *Biogeosciences*, *17*(17), 4489–4508. https://doi.org/10.5194/BG-17-4489-2020

Wei, B., Mollenhauer, G., Hefter, J., Grotheer, H., & Jia, G. (2020). Dispersal and aging of terrigenous organic matter in the Pearl River Estuary and the northern South China Sea Shelf. *Geochimica et Cosmochimica Acta*, *282*, 324–339.

Wei, B., Mollenhauer, G., Hefter, J., Kusch, S., Grotheer, H., Schefuß, E., & Jia, G. (2021). The nature, timescale, and efficiency of riverine export of terrestrial organic carbon in the (sub)tropics: Insights at the molecular level from the Pearl River and adjacent coastal sea. *Earth and Planetary Science Letters*, *565*, 116934. https://doi.org/10.1016/J.EPSL.2021.116934

Wei, B., Mollenhauer, G., Kusch, S., Hefter, J., Grotheer, H., Schefuß, E., Geibert, W., Ransby, D., & Jia, G. (2023). Anthropogenic perturbations change the quality and quantity of terrestrial carbon flux to the coastal ocean. *J. Geophys. Res. Biogeosciences*.

Weiss, R. F., & Price, B. A. (1980). Nitrous oxide solubility in water and seawater. *Marine Chemistry*, *8*(4), 347–359.

Werner, R. A., & Brand, W. A. (2001). Referencing strategies and techniques in stable isotope ratio analysis. *Rapid Communications in Mass Spectrometry*, *15*(7), 501–519. https://doi.org/10.1002/RCM.258

White, H. K., Reddy, C. M., & Eglinton, T. I. (2005). Isotopic constraints on the fate of petroleum residues sequestered in salt marsh sediments. *Environ Sci Technol*, *39*(8), 2545–2551. https://doi.org/10.1021/es048675f

White, H. K., Reddy, C. M., & Eglinton, T. I. (2008). Radiocarbon-based assessment of fossil fuel-derived contaminant associations in sediments. *Environ Sci Technol*, *42*(15), 5428–5434. https://doi.org/10.1021/es800478x

Wickham, H., Averick, M., Bryan, J., Chang, W., D'Agostino McGowan, L., Francois, R., Grolemund, G., Hayes, A., Henry, L., & Hester, J. (2019). Ooms j. *Robinson D., Seidel DP, Spinu V., Takahashi k., Vaughan D., Wilke C., Woo K., and Yutani H*, 1686.

Wickland, K. P., Waldrop, M. P., Aiken, G. R., Koch, J. C., Jorgenson, M. T., & Striegl, R. G. (2018). Dissolved organic carbon and nitrogen release from boreal Holocene permafrost and seasonally frozen soils of Alaska. *Environmental Research Letters*, *13*(6). https://doi.org/https://doi.org/10.1088/1748-

9326/aac4ad

Wild, B., Andersson, A., Bröder, L., Vonk, J., Hugelius, G., McClelland, J. W., Song, W., Raymond, P. A., & Gustafsson, Ö. (2019). Rivers across the Siberian Arctic unearth the patterns of carbon release from thawing permafrost. *Proceedings of the National Academy of Sciences*, *116*(21), 10280–10285. https://doi.org/10.1073/PNAS.1811797116

Winterfeld, M., Mollenhauer, G., Dummann, W., Kohler, P., Lembke-Jene, L., Meyer, V. D., Hefter, J., McIntyre, C., Wacker, L., Kokfelt, U., Tiedemann, R., Köhler, P., Lembke-Jene, L., Meyer, V. D., Hefter, J., McIntyre, C., Wacker, L., & Kokfelt, U. (2018). Deglacial mobilization of pre-aged terrestrial carbon from degrading permafrost. *Nat Commun*, *9*(1), 3666. https://doi.org/10.1038/s41467-018-06080-w

Włodarska-Kowalczuk, M., Mazurkiewicz, M., Górska, B., Michel, L. N., Jankowska, E., & Zaborska, A. (2019). Organic carbon origin, benthic faunal consumption, and burial in sediments of Northern Atlantic and Arctic Fjords (60–81 N). *Journal of Geophysical Research: Biogeosciences*, *124*(12), 3737–3751.

Woodcroft, B. J., Singleton, C. M., Boyd, J. A., Evans, P. N., Emerson, J. B., Zayed, A. A. F., Hoelzle, R. D., Lamberton, T. O., McCalley, C. K., & Hodgkins, S. B. (2018). Genome-centric view of carbon processing in thawing permafrost. *Nature*, *560*(7716), 49–54.

Wörmer, L., Lipp, J. S., Schröder, J. M., & Hinrichs, K.-U. (2013). Application of two new LC–ESI–MS methods for improved detection of intact polar lipids (IPLs) in environmental samples. *Organic Geochemistry*, *59*, 10–21.

Woszczyk, M., Bechtel, A., Püttmann, W., & Rzodkiewicz, M. (2021). Effects of environmental history and post-depositional processes on the organic matter record of Lake Łebsko, Poland. *Organic Geochemistry*, *155*, 104209.

Yager, P., Sherrell, R., Stammerjohn, S., Ducklow, H., Schofield, O., Ingall, E., Wilson, S., Lowry, K., Williams, C., Riemann, L., Bertilsson, S., Alderkamp, A.-C., Dinasquet, J., Logares, R., Richert, I., Sipler, R., Melara, A., Mu, L., Newstead, R., … van Dijken, G. (2016). A carbon budget for the Amundsen Sea Polynya, Antarctica: Estimating net community production and export in a highly productive polar ecosystem. *Elementa: Science of the Anthropocene*, *4*, 15. https://doi.org/10.12952/JOURNAL.ELEMENTA.000140

Young, N. E., Briner, J. P., Maurer, J., & Schaefer, J. M. (2016). 10Be measurements in bedrock constrain erosion beneath the Greenland Ice Sheet margin. *Geophysical Research Letters*, *43*(22), 11,708-11,719. https://doi.org/10.1002/2016GL070258

Yumashev, D., Hope, C., Schaefer, K., Riemann-Campe, K., Iglesias-Suarez, F., Jafarov, E., Burke, E. J., Young, P. J., Elshorbany, Y., & Whiteman, G. (2019). Climate policy implications of nonlinear decline of Arctic land permafrost and other cryosphere elements. *Nature Communications 2019 10:1*, *10*(1), 1–11. https://doi.org/10.1038/s41467-019-09863-x

Zeebe, R. E., & Wolf-Gladrow, D. (2001). *CO2 in seawater: equilibrium, kinetics, isotopes* (Issue 65). Gulf Professional Publishing.

Zemp, M., Huss, M., Thibert, E., Eckert, N., McNabb, R., Huber, J., Barandun, M., Machguth, H., Nussbaumer, S. U., Gärtner-Roer, I., Thomson, L., Paul, F., Maussion, F., Kutuzov, S., & Cogley, J. G. (2019). Global glacier mass changes and their contributions to sea-level rise from 1961 to 2016.

Nature, *568*(7752), 382–386. https://doi.org/10.1038/s41586-019-1071-0

Zhang, B., Wu, X., Tai, X., Sun, L., Wu, M., Zhang, W., Chen, X., Zhang, G., Chen, T., Liu, G., & Dyson, P. (2019). Variation in Actinobacterial Community Composition and Potential Function in Different Soil Ecosystems Belonging to the Arid Heihe River Basin of Northwest China. *Frontiers in Microbiology*, *10*, 2209. https://doi.org/10.3389/FMICB.2019.02209/

Zhang, J., Quay, P. D., & Wilbur, D. O. (1995). Carbon isotope fractionation during gas-water exchange and dissolution of CO2. *Geochimica et Cosmochimica Acta*, *59*(1), 107–114. https://doi.org/10.1016/0016-7037(95)91550-D

Zhang, X., Bianchi, T. S., Cui, X., Rosenheim, B. E., Ping, C., Hanna, A. J. M., Kanevskiy, M., Schreiner, K. M., & Allison, M. A. (2017). Permafrost organic carbon mobilization from the watershed to the Colville River Delta: Evidence from 14C ramped pyrolysis and lignin biomarkers. *Geophysical Research Letters*, *44*(22), 11491–11500. https://doi.org/https://doi.org/10.1002/2017GL075543